THE UNIVERSITY *of* EDINBURGH

This thesis has been submitted in fulfilment of the requirements for a postgraduate degree (e.g. PhD, MPhil, DClinPsychol) at the University of Edinburgh. Please note the following terms and conditions of use:

This work is protected by copyright and other intellectual property rights, which are retained by the thesis author, unless otherwise stated.
A copy can be downloaded for personal non-commercial research or study, without prior permission or charge.
This thesis cannot be reproduced or quoted extensively from without first obtaining permission in writing from the author.
The content must not be changed in any way or sold commercially in any format or medium without the formal permission of the author.
When referring to this work, full bibliographic details including the author, title, awarding institution and date of the thesis must be given.

Measuring Redox Potential in 3D Breast Cancer Tumour Models using SERS Nanosensors

Lauren E. Jamieson

Thesis presented for the degree of

Doctor of Philosophy

The University of Edinburgh

September 2015

Supervisors: Dr Colin J. Campbell

Professor David J. Harrison

dare to dream ...

Declaration of Authorship

I declare that:

- this thesis is my own composition;
- the work presented in this thesis is my own work and where others were involved this is stated and I made a significant contribution to this work and;
- this work has not been submitted for any other degree or professional qualification.

In this thesis the results of research carried out in the School of Chemistry at the University of Edinburgh under the supervision of Dr Colin J. Campbell (University of Edinburgh) and Professor David J. Harrison (University of St Andrews) is described.

Lauren E. Jamieson

University of Edinburgh

September 2015

Signed: _____

Date: _____

Acknowledgements

Firstly I would like to extend my thanks to my supervisor, Dr Colin Campbell, who gave me the opportunity to work on this incredibly interesting and exciting research project. Colin provided invaluable support, advice, encouragement and inspiration throughout the course of my PhD and for that I am incredibly grateful. Thanks must also be extended to my second supervisor, Professor David Harrison, for his insight, advice, inspiration and expertise.

Support and advice both academically and non academically was received from all members of the Campbell group – Kate, Jing, Patrick, Lina, Sarah, Anna-Maria, Vicky, Hannah, Sam and Sophie – and for that my thanks to them. Particular thanks to Kate who provided much of the training received at the start of my PhD and was always on hand to answer my many questions and share frustrations/chocolate with. For general office entertainment thanks also to the Mount group (Andrew, Richard, Justin, Damion, Simon) and Martin.

For teaching a chemist how to do biology thanks must be given to Peter Mullen and Dr Carol Ward who trained me in cell culture and provided cells and general advice.

My gratitude goes to Professor Eleanor Campbell and her research group, particularly Andre and Oleg, for Raman instrument use and general assistance. Massive thanks must be extended to Dave for his microscopy support and expertise for fluorescence measurements and general words of wisdom, typically 'what have you got that's not going to work this time?' and also to Pierre for photothermal OCT work. Steve and Christian must be thanked for TEM sample preparation and support and Alan for SEM and HIM support.

A special thanks to Aleksandra who collaborated in much of this work and her research supervisors Dr Kamilla Malek and Professor Malgorzata Baranska who provided the opportunity to work at Jagiellonian University in Krakow. Not only was Aleksandra a top research partner but also a top tour guide, Polish teacher and stretch partner and my time in Krakow was one of the highlights of my PhD.

To the spectroscopy community and friends I've made, my extreme gratitude for keeping the science spark alive when I needed it most. Particularly thanks to Caryn for her support,

encouragement and friendship, without which the write up process wouldn't have gone nearly as smoothly.

Thanks to the University of Edinburgh for providing funding for carrying out my PhD research. For providing funding for additional opportunities thanks must be made to a Neil Campbell Travel Award (University of Edinburgh); a QualityNano Transnational Access grant; SPIE Biophotonics South America registration fee waiver; a University of Edinburgh Conference Grant; a RSC Travel Grant; an ICAVS 8 Student Grant; and IRDG funding for attending the Martin & Willis student meeting.

Outwith science there are many people to thank who have helped preserve my sanity throughout completion of my PhD. City of Edinburgh Trampoline Club for providing countless numbers of hours of brain switch off time and teaching me how to fly. Thanks particularly to my trampolining girls Lauren J, Kayleigh, Lauren M and Kirsty for both trampoline related and non trampoline related science time out. Particular thanks must go to Lauren J for her help, support and encouragement over the years.

For providing a further countless number of brain switch off hours thanks to Spinal Chord who also taught me what it feels like to fly. Both trampolining and circus have taught me valuable life lessons without which the PhD process would not have gone nearly so smoothly. Particular thanks must go to Rodolfo for his friendship and support and giving me the opportunity to fulfill my circus dreams, and to Sunday Dinner Club (Mags, Heather, Laura, Gillian) who are always there to help and support in all aspects of life and provide hilarious banter and true inspiration.

Finally and most importantly I would like to thank my mum, dad and all my family. Without ongoing support from my mum and dad none of this would have been possible. This work is dedicated to them.

Abstract

Cellular redox potential is incredibly important for the control and regulation of a vast number of processes occurring in cells. Disruption of the fine redox balance within cells is has been associated with disease. Of particular interest to my research is the redox gradient that develops in cancer tumours, in which the internal regions are further from vascular blood supply and therefore become starved of oxygen and hypoxic. This makes treatment of these areas a lot more challenging, as radiotherapy approaches rely on the presence of oxygen and, with a poor vascular blood supply, drugs delivered through the blood stream will have poor access to these regions.

Currently, there is limited knowledge regarding the quantitative nature of this redox gradient in cancerous tumours. To aid the development of drugs and therapies to overcome this problem, a system that enables quantitative mapping of redox potential through a tumour would be a vital tool. In this work redox sensitive molecules attached to gold nanoparticles (NPs) are delivered to cells and give signals using surface enhanced Raman scattering (SERS). Redox potential changes are monitored quantitatively by ratiometric changes in signal intensity of selected signals in the SER spectra acquired. Multicellular tumour spheroids (MTS) are used as a three dimensional (3D) *in vitro* tumour model, in which the 3D architecture and gradients observed in tumours *in vivo* develop.

As redox potential is pH dependent and pH is another important physiological characteristic in its own right, a SERS pH sensor was developed and ultimately a system that multiplexes intracellular pH and redox measurement by SERS. Initially, simultaneous redox potential and pH measurements were performed in monolayer culture before extending this to MTS. Photothermal optical coherence tomography (OCT) was used to investigate overall 3D NP distribution in the MTS models. It was possible to control NP delivery to MTS to localise NPs to various regions. Redox potential and pH could then be measured using a fibre optic Raman probe, and spatial response to drug treatment monitored. Intracellular NP localisation was investigated using transmission electron microscopy (TEM), scanning electron microscopy (SEM), helium ion microscopy (HIM) and confocal fluorescence microscopy (CFM) and attempts were made to control NP delivery to particular intracellular compartments.

Lay Summary

Balance is of fundamental importance to all aspects of life. Take, for example, my other passion – come night-time I swap my lab coat for sequins and lycra and swing from the ceiling circus style. While tied by my feet to two pieces of fabric, legs pulled apart about 10 m in the air, keeping my balance is of vital importance – literally a matter of life or death. The importance of balance here is clear. Not so clear to the humble onlooker is the fight for balance existing in every individual cell in my body – again this comes down to a matter of life or death. Inside each cell there are millions and millions of chemical reactions that exist in a delicately balanced state. Of particular importance to my research is the balance between oxidising and reducing species – a characteristic referred to as redox potential. This balance essentially arises from the need for oxygen to survive. Just like a car needs oxygen to burn fuel and produce energy, cells need oxygen to burn our fuel, the food we eat, and produce energy for cells to function. For the car, the detrimental effects of oxygen in the atmosphere are observed when, over time, the car rusts. For our cells, the detrimental effects of oxygen come from the production of reactive oxygen species (ROS) that can damage cells and are associated with disease progression. ROS are also highly implicated in the ageing process and the cosmetics industry markets antioxidant products claimed to 'mop up' ROS and make you look '10 years younger'. Our cells have their own antioxidants that help remove these ROS and keep everything in a balanced state. It is when this balance is disturbed that it can often become a matter of life or death.

While it is the loss of redox balance as a result of accumulation of excessive ROS and oxidative stress that is the most documented side of the scale when it comes to disease development, my research is particularly interested in the other side of the scale. Hypoxia, a characteristic of lack of oxygen, is particularly important in cancer. A cancer tumour is a rapidly growing mass of cells and, as the mass grows, cells towards the centre become further from the body's regular blood supply that carries oxygen, as well as other nutrients, to cells. Therefore, these central areas often become starved of oxygen and hypoxic, which is important when considering treatment options as, for example, radiotherapy relies on the presence of oxygen. There is currently limited information available about how these gradients are characterised.

My research aims to quantify redox potential gradients in models of tumours grown in the laboratory, called multicellular tumour spheroids (MTS). A technique called surface enhanced Raman scattering (SERS) is used to perform measurements. Raman scattering detects the presence of bond vibrations in molecules. Molecules that are sensitive to redox potential are attached to gold nanoparticles (spherical gold particles with nanometer scale diameter) and delivered to cells. Attachment to gold causes an enhancement in the normally weak Raman scattering effect from the molecules. These molecules are sensitive to the redox environment around them in the cell and SER spectra acquired from regions of the cell containing these sensors display a ratiometric response to changing redox environment allowing redox potential to be measured in distinct regions of the cell. This technique was used to establish redox potential gradients in MTS as a model of cancer tumours, providing vital information for further drug and therapy development and a platform for drug and therapeutic testing.

Contents

Declaration of Authorship iii

Acknowledgements iv

Abstract vi

Lay Summary vii

List of Figures xv

List of Equations xx

List of Tables xxi

Abbreviations xxiii

Chapter 1 Introduction **1**

1.1. Intracellular Redox Potential 1

1.1.1. Oxygen Dependence and ROS 1

1.1.2. Redox Couples 3

1.1.2.1. Glutathione 6

1.1.2.2. Other Important Redox Couples 7

1.1.3. Compartmentalisation 9

1.1.4. Involvement of Redox Potential in Cellular Processes and Disease 12

1.1.5. The Hallmarks of Cancer and Redox Potential Implication 14

1.2. Measuring Intracellular Redox Potential 18

1.2.1. Measuring Glutathione Concentration 18

1.2.2. Fluorescent Dyes 20

1.2.3. Glutathione Reductase Crystals 20

1.2.4. Reduction-Oxidation Sensitive Green Fluorescent Proteins (roGFPs) 21

1.3. SERS Nanosensors 22

1.3.1. Raman Scattering and Surface Enhanced Raman Scattering 22

1.3.2. Vibrational Spectroscopy in Biology and Medicine 27

1.3.3. Using SERS to Measure Intracellular Redox Potential 30

1.4. Multicellular Tumour Spheroids (MTS) – from 2D to 3D – A New Challenge for SERS Nanosensors 33

1.4.1. From Monolayer to MTS – A More Realistic Model 33
1.4.2. Methods for Growing MTS 35
1.4.2.1. Spontaneous Aggregation 36
1.4.2.2. Hanging Drop 36
1.4.2.3. Gyratory Methods and Spinner Flasks 37
1.4.2.4. Non Adhesive Plates/Liquid Overlay 37
1.4.2.5. Microcarrier Beads 37
1.4.2.6. Scaffolds 38
1.4.2.7. Microwells and Microfluidics 38
1.4.3. Current Techniques for Chemical Analysis of MTS 38
1.4.3.1. Advances in Instrument Technology to Analyse MTS 39
1.4.3.2. Measuring Oxygen Concentration and Hypoxia 43
1.4.3.3. pH and Nutrient Concentration 45
1.4.3.4. Proteins 46
1.4.3.5. Localisation of and Cellular Response to Drugs 49
1.4.4. SERS – A New Method for Quantitative Analysis of MTS Characteristics 50
1.5. Project Aims 53

Chapter 2 Experimental Methods 54
2.1. Cell Culture Procedures 54
2.1.1. General Cell Culture Procedures 54
2.1.2. Haemocytometry 55
2.1.3. 3D Cell Culture – Multicellular Tumour Spheroids (MTS) 55
2.1.4. Setting MTS in Collagen Matrix 55
2.1.5. Hypoxyprobe 56
2.1.6. MTT Assay 57
2.1.7. Drug Treatment 57
2.1.7.1 Staurosporine 57
2.1.7.2 TNFα 57
2.1.8. Fluorescence Staining 58
2.1.8.1. LysoSensor™ Green DND-153 58
2.1.8.2. DiD 58

2.1.8.3. NucBlue® Live ReadyProbes® Reagent 58
2.1.8.4. Tetramethylrhodamine methyl ester (TMRM) 58
2.2. SERS Experiments 59
2.2.1. Instrumentation 59
2.2.2. Nanoparticles 60
2.2.3. Nanoparticle Functionalisation 62
2.2.3.1. 150 nm Nanoparticles 62
2.2.3.2. 50 nm Nanoparticles 70
2.2.3.3. Nanoparticles Synthesised Using Frens Procedure 71
2.2.4. SERS of Functionalised Nanoparticles 71
2.2.5. Redox Probe Calibration 71
2.2.6. pH Calibration 72
2.2.6.1. Buffer Preparation 72
2.2.6.2. Calibration Renishaw inVia 72
2.2.6.3. Calibration Ocean Optics QE65 Pro 73
2.2.6.4. Calibration WITec 73
2.2.7. Intracellular SERS Measurements 73
2.2.7.1. Renishaw inVia 73
2.2.7.2. WITec 74
2.2.7.2.1. MBA-NP pH Measurements 74
2.2.7.2.2. Multiplexed MBA-NP and AQ-NP Measurements 74
2.2.7.3. Ocean Optics QE65 Pro for MTS Measurements 75
2.2.7.4. New Renishaw inVia 75
2.3. Microscopy and Other Related Techniques 76
2.3.1. Transmission Electron Microscopy (TEM) 76
2.3.2. Helium Ion Microscopy (HIM) 77
2.3.3. Scanning Electron Microscopy (SEM) 77
2.3.4. Confocal Fluorescence Microscopy (CFM) 77
2.3.5. Photothermal Optical Coherence Tomography (OCT) 79
2.3.6. UV-visible Absorption Spectroscopy 80
2.3.7. Bright Field Microscopy for General Cell Culture 80
2.3.8. Microplate Reader 80

2.3.9. Fluorescence Spectroscopy CANLS1-NQ-NS Washing 80
2.3.10. Slide Reader 80
2.4. Data Processing 81
2.4.1. pH Calibration 81
2.4.2. AQ-NP Calibration for Multiplexing 81
2.4.3. Standard Spectral Processing for Renishaw and Ocean Optics Spectra 81
2.4.4. Investigation of Intracellular pH in Endothelial Cells 82
2.4.5. Simultaneous MBA-NP and AQ-NP Measurements 82
2.4.6. Statistics 83
2.4.7. New Renishaw inVia System 83
2.4.8. Automated processing 83
2.4.9 Confocal Fluorescence Microscopy 83

Chapter 3 From Monolayer to MTS 85
3.1. Cell Morphology 85
3.2. The Current 'Gold Standard' for Redox Measurement in MTS – Hypoxyprobe™ 87
3.3. Nanosensor Uptake 89
3.4. SERS – From Monolayer to MTS 99
3.4.1. Preparation of NQ-NPs 99
3.4.2. SERS of NQ-NPs in MCF7 Cells in Monolayer Culture 99
3.4.3. SERS of NQ-NPs in MCF7 Cells in MTS 102
3.4.4. Preparation of AQ-NPs 106
3.4.5. SERS of AQ-NPs in MCF7 Cells in Monolayer Culture 108
3.4.6. SERS of AQ-NPs in MCF7 Cells in MTS 111
3.5. Moving Forward 114

Chapter 4 Developing a SERS pH Sensor 116
4.1. Finding a pH Sensor 117
4.1.1. *Para*mercaptobenzoic Acid as a SERS pH Sensor 119
4.1.1.1. MBA-NP Calibration: Renishaw inVia 122
4.1.1.2. MBA-NP Calibration: Ocean Optics QE65 Pro 126

4.1.1.3. MBA-NPs Calibration: WITec 131
4.1.1.4. MBA-NPs Calibration Comparison 132
4.1.2 Other SERS pH Sensors 134
4.1.2.1. 4-Mercaptopyridine as a SERS pH Sensor 135
4.1.2.2. 4-Aminobenzenethiol as a SERS pH Sensor 138
4.1.2.3. Mercaptonitrobenzoic Acid as a SERS pH Sensor 140
4.2. Intracellular pH Measurements in Monolayer Culture Using MBA-NPs 142
4.2.1. pH Changes During Apoptosis 143
4.2.2. Monitoring Intracellular pH in Endothelial Cells using MBA-NPs and Response to Changing pH of Extracellular Environment and Tumour Necrosis Factor-α 146
4.3. Conclusions 151

Chapter 5 Simultaneous Intracellular Redox Potential and pH Measurements in Monolayer Culture and MTS 152
5.1. Simultaneous Intracellular Redox Potential and pH Measurements in Live Cells in Monolayer Culture Using SERS Nanosensors 152
5.2. Simultaneous Intracellular Redox Potential and pH Measurements in Live Cells in MTS Using SERS Nanosensors – Ocean Optics and Photothermal OCT 160
5.2.1. Photothermal OCT – Visualising and Controlling 3D NP Distribution in MTS 161
5.2.2. Raman Fibre Optic Probe – Determining pH and Redox Potential in Different MTS Regions 165
5.2.3. Raman Fibre Optic Probe – Response of pH and Redox Potential Gradients to Drug Treatment 173
5.3. Simultaneous Intracellular Redox Potential and pH Measurements in Live Cells in MTS Using SERS Nanosensors – Renishaw inVia 179

Chapter 6 Tracking and Controlling Nanoparticle Uptake Into Cellular Compartments 188
6.1. Increasing Nanoparticle Uptake Into Cytosol vs Endosomes and

Analysis by TEM 188
6.2. Confocal Fluorescence Microscopy in Reflection Mode as a New Method for Tracking Intracellular Nanoshell Location in Live Cells 195
6.2.1. Technique Development 195
6.2.2. Targeting Nuclei and Mitochondria and Analysis using CFM 200

Chapter 7 Conclusions 203

References 207

Appendices 215

Appendix 1 Redox Calibrations 215
Appendix 2 Poster 217
Appendix 3 Publication 1
Chemical analysis of multicellular tumour spheroids
Appendix 4 Publication 2 (conference proceedings paper)
Monolayer to MTS: using SEM, HIM, TEM and SERS to compare morphology, nanosensor uptake and redox potential in MCF7 cells
Appendix 5 Publication 3
SERS-based monitoring of the intracellular pH in endothelial cells: the influence of the extracellular environment and tumour necrosis factor-α
Appendix 6 Publication 4
Simultaneous intracellular redox potential and pH measurements in liver cells using SERS nanosensors

List of Figures

Figure 1.1 Mitochondrial electron transport chain

Figure 1.2 ROS Lewis structures

Figure 1.3 ROS regulation in signaling pathways

Figure 1.4 Redox couples in cells

Figure 1.5 Biosynthesis of glutathione

Figure 1.6 Thioredoxin redox couple

Figure 1.7 Structure of cysteine and cystine

Figure 1.8 Structure of $NAD(P)^+$ and NAD(P)H

Figure 1.9 Steady state potentials of redox couples in intracellular compartments

Figure 1.10 Endoyctic pathway

Figure 1.11 Redox potential control in the cell cycle

Figure 1.12 Oxidative stress in disease

Figure 1.13 Hallmarks of cancer

Figure 1.14 Tumour cell organisation and gradients

Figure 1.15 Glutathione recycling assay

Figure 1.16 Structure of oxidised and reduced RF1

Figure 1.17 Hydrocyanine dye for ROS concentration determination

Figure 1.18 roGFP structure

Figure 1.19 Raman scattering

Figure 1.20 Raman spectrometer schematic

Figure 1.21 SERS enhancement mechanism

Figure 1.22 Structure of reduced and oxidised NQ and AQ on NPs

Figure 1.23 SERS for intracellular redox potential measurement

Figure 1.24 MTS organisation and gradients

Figure 1.25 Methods for MTS growth

Figure 1.26 Imaging MTS

Figure 1.27 Hypoxyrprobe™ staining of MTS

Figure 1.28 AQUA for quantitative immunofluorescence

Figure 3.1 TEM of MCF7 cells in monolayer culture and MTS

Figure 3.2 HIM of MCF7 cells in monolayer culture and MTS

Figure 3.3 Hypoxyprobe™ stained MCF7 and BT474 MTS

Figure 3.4 TEM of NPs in MCF7 cells after 24 hr incubation

Figure 3.5 MTT assay for NP treated MCF7 cells

Figure 3.6 Nanoparticle uptake by endocytosis

Figure 3.7 TEM of NPs in MCF7 cells after 24 hr incubation and 6 days growth in monolayer culture

Figure 3.8 TEM of NPs in MCF7 cells after 24 hr incubation and 6 days growth as MTS

Figure 3.9 HIM of NPs

Figure 3.10 HIM images of NPs interacting with MCF7 cells

Figure 3.11 SEM images of NPs in MCF7 cell MTS

Figure 3.12 Haematoxylin stained MTS sections for NP detection

Figure 3.13 UV-Vis and Raman of NQ-NPs

Figure 3.14 Redox potential from MCF7 cells determined by SERS using NQ-NPs with and without serum during incubation

Figure 3.15 SER spectrum of NQ-NPs in monolayer cell culture

Figure 3.16 Mapping redox potential in MTS with NQ-NPs

Figure 3.17 Redox potential from SERS measurements using NQ-NPs in monolayer culture and MTS

Figure 3.18 SER spectra of NQ-NPs in MTS

Figure 3.19 AQ-NP appearance and UV-Vis spectra under different functionalisation conditions

Figure 3.20 AQ-NP SER spectrum

Figure 3.21 Redox potential in MCF7 cells determined by SERS using NQ-NPs and AQ-NPs

Figure 3.22 SER spectra of AQ-NPs in monolayer culture

Figure 3.23 MCF7 cells incubated with AQ-NPs

Figure 3.24 Mapping redox potential in MTS with AQ-NPs

Figure 3.25 Comparing redox potential from SERS of AQ-NPs in monolayer culture, AQ-NPs in MTS and NQ-NPs in MTS

Figure 4.1 Henderson-Hasselbalch plots at different pKa

Figure 4.2 MBA-NP equilibrium and SER spectra at high and low pH

Figure 4.3 Background Raman spectra from quartz and gold

Figure 4.4 Slide preparation for SERS pH calibrations
Figure 4.5 MBA-NP calibration peak intensity ratio plots Renisahw inVia
Figure 4.6 MBA-NP calibration peak position Renishaw inVia
Figure 4.7 MBA-NP calibration plot Renishaw inVia
Figure 4.8 MBA-NP calibration peak intensity ratio plots Ocean Optics
Figure 4.9 MBA-NP calibration Ocean Optics calibration comparison
Figure 4.10 MBA-NP calibration plots Ocean Optics
Figure 4.11 MBA-NP calibration plot WITec
Figure 4.12 MBA-NP calibration plots instrument comparison
Figure 4.13 Automated vs manual data processing for MBA-NP spectra
Figure 4.14 4MP-NP equilibrium and SER spectra at high and low pH
Figure 4.15 4MP-NP calibration peak intensity ratio plots Ocean Optics
Figure 4.16 4MP-NP calibration peak intensity ratio plot Renishaw
Figure 4.17 4ABT-NP equilibrium and SER spectra at high and low pH
Figure 4.18 4ABT-NP calibration peak intensity ratio plots Ocean Optics
Figure 4.19 NBA-NP equilibrium and SER spectra at high and low pH
Figure 4.20 NBA-NP calibration peak intensity ratio plots Ocean Optics
Figure 4.21 MCF7 cell morphology upon STS treatment
Figure 4.22 Monitoring pH changes in MCF7 cells upon STS treatment using MBA-NPs
Figure 4.23 Optimising MBA-NP incubation time in EA.hy926 cells
Figure 4.24 SERS maps of pH in EA.hy926 cells measured using MBA-NPs and response to application of external buffers at different pH
Figure 4.25 Calibration plots for pH measurements in EA.hy926 cells
Figure 4.26 SERS maps of pH in EA.hy926 cells measured using MBA-NPs after TNF-α treatment.

Figure 5.1 AQ-NP equilibrium, representative SER spectra at highly oxidising and reducing conditions and calibration curve
Figure 5.2 Peak fitting for AQ-NP calibration
Figure 5.3 SERS maps for simultaneous pH and redox potential in EA.hy926 cells
Figure 5.4 Peak fitting for multiplexed AQ-NP and MBA-NP spectra
Figure 5.5 Cluster SER spectra for simultaneous pH and redox measurement using MBA-NP and AQ-NP

Figure 5.6 AQ-NP half wave potential dependence on pH

Figure 5.7 Schematic of photothermal OCT setup

Figure 5.8 Photothermal OCT for detection of NPs in MTS

Figure 5.9 Determining NP distribution in MTS using photothermal OCT

Figure 5.10 Targeting NPs to different areas of MTS and detection of distribution using photothermal OCT

Figure 5.11 Experimental setup for SERS measurements from MTS using fibre optic probe

Figure 5.12 Multiplexed MBA-NP and AQ-NP spectra from fibre optic SERS measurement in MTS

Figure 5.13 Radial pH changes in MTS measured by SERS using a fibre optic probe and targeted MBA-NPs

Figure 5.14 Radial redox potential changes in MTS measured by SERS using a fibre optic probe and targeted NQ-NPs

Figure 5.15 pH adjusted vs not pH adjusted redox potential measurements in MTS

Figure 5.16 Radial redox potential changes in MTS measured by SERS using a fibre optic probe and targeted AQ-NPs

Figure 5.17 Radial pH changes in MTS measured by SERS using a fibre optic probe and targeted MBA-NPs response to STS treatement

Figure 5.18 Radial redox potential changes in MTS measured by SERS using a fibre optic probe and targeted NQ-NPs response to STS treatment

Figure 5.19 Average MBA-NP and NQ-NP spectral changes for radial pH and redox potential differences in MTS before and after STS treatment

Figure 5.20 Average MBA-NP and NQ-NP spectral changes for radial pH and redox potential differences in MTS STS time course

Figure 5.21 Experimental setup for SERS measurements from MTS using Renishaw inVia

Figure 5.22 Depth scans of MBA-NP spectral changes in MTS processed using Wire 4.1 and intensity at point 1425 cm^{-1}

Figure 5.23 Depth scans of MBA-NP spectral changes in MTS processed using Wire 4.1 and maximum intensity of 14-- cm^{-1}, width and area

Figure 5.24 Intensity maps of MBA-NP maps in MTS

Figure 5.25 Depth scans of NQ-NP spectral changes in MTS processed using Wire 4.1 and ratiometric intensity of 1635 cm^{-1} and 1582 cm^{-1} signals

Figure 6.1 NQ, AQ, aminoNQ and CANLS1 structures

Figure 6.2 % NP uptake into cytosol relative to endosomes under varying conditions

Figure 6.3 TEM images of NPs undergoing endocytosis in cells

Figure 6.4 Structures of molecules uses to functionalise NPs for increased release from endosomes

Figure 6.5 % NP uptake into cytosol relative to endosomes for NPs functionalised with various molecules to increase release from endosomes

Figure 6.6 NPs in agarose imaged by reflection using CFM

Figure 6.7 NPs in cells imaged by reflection using CFM

Figure 6.8 Time course uptake of NPs in cells imaged by reflection using CFM and fluorescence to analyse uptake to vesicles relative to cytosol

Figure 6.9 Uptake of NPs into lysosomes analysed by reflection and fluorescence using CFM

Figure 6.10 CANLS1, NLS2 and SBTPP structures

Figure 6.11 Analysing uptake of CANLS1-NPs to nuclei using CFM

Figure 6.12 Analysing uptake of NLS2-NPs to nuclei using CFM

Figure 6.13 Analysing uptake of SBTPP-NPs to mitochondria using CFM

List of Equations

Equation 1.1 Redox environment of a cell

Equation 1.2 Nernst equation

Equation 1.3 Standard equilibrium

Equation 1.4 Reaction quotient from standard equilibrium

Equation 1.5 Substituted Nernst equation at 25 °C

Equation 1.6 Substituted Nernst equation at 37 °C

Equation 1.7 Nernst equation for glutathione

Equation 1.8 GSSG/GSH equilibrium

Equation 2.1 Cell concentration determined from haemocytometry

Equation 4.1 Henderson Hasselbalch equation

Equation 4.2 Weak acid equilibrium

Equation 4.3 Boltzmann equation for curve fitting

Equation 4.4 Boltzmann equation for curve fitting rearranged for x

Equation 4.5 Equation for pH determination MBA-NP Renishaw inVia

Equation 4.6 Equation for pH determination MBA-NP Ocean Optics 1

Equation 4.7 Equation for pH determination MBA-NP Ocean Optics 2

Equation 4.8 Equation for pH determination MBA-NP Ocean Optics 3

Equation 4.9 Equation for pH determination MBA-NP Ocean Optics 4

Equation 4.10 Overall equation for pH determination MBA-NP Ocean Optics

Equation 4.11 Equation for pH determination MBA-NP WITec

List of Tables

Table 1.1 Microscopy techniques to visualise MTS

Table 1.2 Enabling technologies for chemical analysis of MTS

Table 2.1 Summary of Raman instruments used

Table 2.2 Summary of nanoparticles used

Table 2.3 Excitation and emission settings for fluorescent dyes

Table 3.1 Statistics for redox potential in MCF7 cells in monolayer culture measured with NQ-NPs incubated with and without serum

Table 3.2 Statistics for redox potential in MCF7 cells in monolayer culture and MTS measured with NQ-NPs

Table 3.3 Statistics for redox potential in MCF7 cells in monolayer culture measured with NQ-NPs and AQ-NPs

Table 3.4 Statistics for redox potential in MCF7 cells in monolayer culture and MTS measured with AQ-NPs and MTS measured with NQ-NPs

Table 4.1 MBA-NP SERS assignments

Table 4.2 Apparent pKa and adjusted R^2 MBA-NP calibration Renishaw inVia

Table 4.3 Apparent pKa and adjusted R^2 MBA-NP calibration Ocean Optics

Table 4.4 Apparent pKa and adjusted R^2 MBA-NP calibration Ocean Optics comparison

Table 4.5 Apparent pKa and adjusted R^2 MBA-NP calibration comparison

Table 4.6 Automated vs manual data processing for MBA-NP spectra

Table 4.7 4MP-NP SERS assignments

Table 4.8 Apparent pKa and adjusted R^2 4MP-NP calibration

Table 4.9 4ABT-NP SERS assignments

Table 4.10 Apparent pKa and adjusted R^2 4ABT-NP calibration

Table 4.11 NBA-NP SERS assignments

Table 4.12 pH changes in MCF7 cells measured by MBA-NP upon STS treatment

Table 5.1 Simultaneous intracellular pH and redox potential measurements

Table 5.2 Radial pH changes in MTS measured by SERS using a fibre optic probe and targeted MBA-NPs

Table 5.3 Radial redox potential changes in MTS measured by SERS using a fibre optic probe and targeted NQ-NPs

Table 5.4 Radial redox potential changes in MTS measured by SERS using a fibre optic probe and targeted AQ-NPs

Table 5.5 Radial pH changes in MTS measured by SERS using a fibre optic probe and targeted MBA-NPs response to STS treatement

Table 5.6 Radial redox potential changes in MTS measured by SERS using a fibre optic probe and targeted NQ-NPs response to STS treatment

Table 6.1 % NP uptake into cytosol relative to endosomes under varying conditions

Table 6.2 % NP uptake into cytosol relative to endosomes for NPs functionalised with various molecules to increase release from endosomes

Abbreviations

NP	nanoparticle
SERS	surface enhanced Raman scattering
3D	three dimensional
TEM	transmission electron microscopy
SEM	scanning electron microscopy
HIM	helium ion microscopy
ROS	reactive oxygen species
ATP	adenosine triphosphate
DNA	deoxyribonucleic acid
NADH	nicotinamide dinucleotide hydride
NAD	nicotinamide dinucleotide
$FADH_2$	flavin adenine dinucleotide hydride
FAD	flavin adenine dinucleotide
Cyt c	cytochrome complex
ADP	adenosine diphosphate
Pi	inorganic phosphate
MnSOD	manganese superoxide dismutase
CAT	catalase
Prx3	peroxiredoxin 3
JNK	c-Jun N-terminal kinase
ATF	activating transcription factor
MEK	mitogen-activated protein kinase kinase
Erk	extracellular signal regulated kinase
NADPH	nicotinamide dinucleotide phosphate hydride
NADP+	nicotinamide dinucleotide phosphate
GSSG	oxidised glutathione
GSH	reduced glutathione
Trx1	thioredoxin 1
Trx2	thioredoxin 2
roGFP	reduction-oxidation sensitive green fluorescent proteins

PrSH	protein thiol
PrSSG	protein S-glutathione
Cys	cysteine
RNA	ribonucleic acid
PDT	photodynamic therapy
RB	retinoblastoma-associated protein
TP53	tumour protein p53
VEGF-A	vascular endothelial growth factor-A
PPP	pentose phosphate pathway
DTNB	5,5′-dithiobis(2-nitrobenzoic acid)
TNB	5-thio-2-nitrobenzoic acid
GR	glutathione reductase
NEM	N-ethylmaleimide
2VP	2-vinylpyridine
M4VP	1-methyl-4-vinyl-pyridinium trifluoromethane sulfonate
HPLC	high performance liquid chromatography
RF1	Redoxfluor-1
YFP	yellow fluorescent protein
UV	ultraviolet
IR	infrared
CCD	charge-coupled device
HOMO	highest occupied molecular orbital
LUMO	lowest unoccupied molecular orbital
FTIR	Fourier transform infrared
ATR	attenuated total reflection
QCL	quantum-cascade laser
PCA	principle component analysis
PLS	partial least-squares
CARS	coherent anti-Stokes Raman spectroscopy
SRS	stimulated Raman spectroscopy
SORS	spatially offset Raman spectroscopy
TRS	transmission Raman spectroscopy
TERS	tip enhanced Raman spectroscopy

SERRS	surface enhanced resonance Raman spectroscopy
SESORS	surface enhanced spatially offset Raman spectroscopy
NIR	near infrared
NQ	1,8-diaza-4,5-dithian-1,8-di(2-chloro-[1,4]-naphthoquinone-3-yl)octane
AQ	N-[2-({2-[(9,10-dioxo-9,10-dihydroanthracen-2-yl)formamido]ethyl}disulfanyl)ethyl]-9,10-dioxo-9,10-dihydroanthracene-2-carboxamide
DFT	density functional theory
MTS	multicellular tumour spheroid
2D	two dimensional
ECM	extracellular matrix
PEG	polyethylene glycol
PDMS	polydimethylsiloxane
PCL	poly(ɣ-caprolactone)
OCT	optical coherence tomography
OPT	optical projection tomography
LSM	light sheet microscopy
SPIM	single plane illumination microscopy
HIF	hypoxia inducible factor
MRS	magnetic resonance spectroscopy
PET	positron emission tomography
PtPFPP	Pt(II)-tetrakis(pentafluorophenyl)porphine
PLIM	phosphorescence lifetime imaging
BCECF	2′,7′-Bis-(2-Carboxyethyl)-5-(and-6)-Carboxyfluorescein
STIM	scanning transmission ion microscopy
PIXE	proton-induced X-ray emission
SXFM	scanning X-ray fluorescence microscopy
MDR1	multidrug resistance gene
AQUA	automated quantitative analysis
iTRAQ	isobaric tags for relative and absolute quantification
MALDI	matrix assisted laser desorption/ionisation
TOF	time of flight
ESI-Q	electrospray ionisation quadrupole

GLUT-1	glucose transporter 1
CAIX	carbonic anhydrase IX
MSI	mass spectrometry imaging
LC-MS	liquid chromatography mass spectrometry
MS	mass spectrometry
CRI	confocal Raman imaging
FLIM	fluorescence lifetime imaging microscopy
DOX	doxorubicin
HTS	high throughput screening
DMEM	Dulbecco's modified eagle's medium
FCS	foetal calf serum
HAT	hypoxanthine-aminopterin-thymidine
PBS	phosphate buffered saline
T/EDTA	trypsin/ethylenediaminetetraaceticacid
DMSO	dimethyl sulfoxide
EtOH	ethanol
NaOH	sodium hydroxide
MBA	*para*mercaptobenzoic acid
NR	nanorod
STS	staurosporine
TNFα	tumour necrosis factor α
TMRM	tetramethylrhodamine methyl ester
CFM	confocal fluorescence microscopy
CANLS1	fluorescein-aminohexanoic acid-PKKKRKVC
NLS2	CGGPKKKRKVGG
SBTPP	4-sulfanylbutylphenylphosphanium bromide
4MP	4-mercaptopyridine
4ATP	4-aminobenzenethiol
NBA	nitrobenzoic acid
TG	1-thio-glucose
PLA	polyarginine
2AET	cysteamine
PEG800	poly(ethylene glycol) methyl ether thiol

PEG6	O-(2-Mercaptoethyl)-O′-methyl-hexa(ethylene glycol)
PLL	poly-L-lysine
SF	serum free
CTAB	cetrimonium bromide
ANOVA	analysis of variance
DMF	dimethylformamide
2ABT	2-aminobenzenethiol
CASP3	caspase-3
R6G	rhodamine 6G
IHC	immunohistochemistry

Chapter 1

Introduction

"Life is like riding a bicycle. To keep your balance you must keep moving." – **Albert Einstein**

1.1 Intracellular Redox Potential

The redox potential within a cell is a measure of how oxidising or reducing the intracellular environment is. Intracellular redox potential exists as a finely controlled balance between reactive oxygen species (ROS) and antioxidant enzymes and small molecules that exist as redox couples. Cellular redox potential is an incredibly important factor within cells involved in the regulation of numerous essential processes. Disruption of redox potential is associated with hundreds of diseases including cancer.[1] For this reason, being able to measure and understand intracellular redox potential could be essential for monitoring disease states, along with guiding development of and monitoring response to drugs and therapy.

1.1.1 Oxygen Dependence and ROS

Oxygen is essential for energy production in cells and therefore for cell survival. Oxygen is the final electron acceptor in the electron transport chain in the mitochondria, which generates adenosine triphosphate (ATP) to fuel cell function (Figure 1.1).[2] Therefore, without oxygen, cells would not survive. However, the need for oxygen and, in particular, its proximity to many available electrons in the electron transport chain (Figure 1.1), leads to the production of ROS, which cause oxidative stress and damage to cells. ROS include hydrogen peroxide (H_2O_2), the superoxide radical ($O_2^{\bullet-}$), singlet oxygen ($^1O_2$) and the hydroxyl radical ($\bullet OH$) (Figure 1.2).[1] While ROS are primarily generated endogenously, they can also be generated from exogenous sources such as UV light, ionising radiation and pathogens such as viruses. ROS contribute significantly to the intracellular redox environment and ROS generation is the primary factor leading to oxidative stress and the need for antioxidants to counteract this. If, however, ROS levels become too high or antioxidant levels too low, oxidative stress has been associated with disease progression.[1,3]

In particular, ROS can cause damage to DNA and subsequently lead to mutations and cancer progression. Thus, it is important that antioxidants such as glutathione are present to help deplete ROS levels. Despite the negative effects of ROS, they also have essential functions in, for example, various signaling pathways as signaling molecules regulating cellular processes such as those illustrated in Figure 1.3.

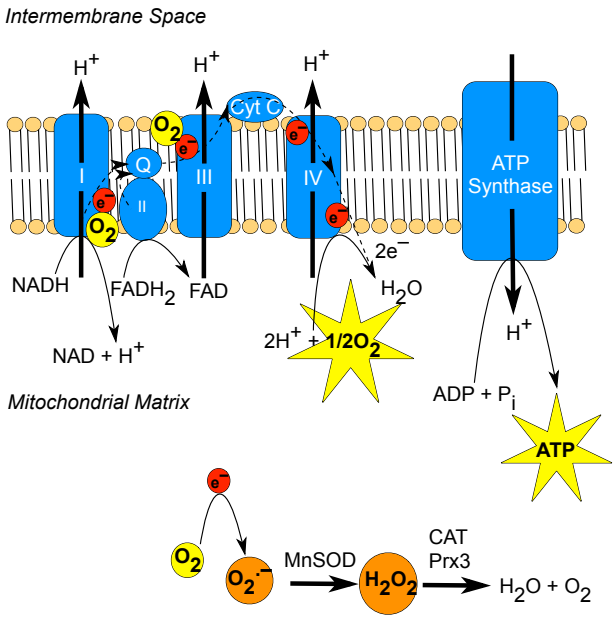

Figure 1.1 illustrates the processes taking part in the electron transport chain in the mitochondria in cells, where electrons (e^-) are transported through a series of transmembrane complexes (I, II, III and IV) and electron carriers (quinone (Q) and cytochrome C (Cyt C)) to finally reduce oxygen (O_2). This is the final stage in cellular respiration, where oxygen acts as the final electron acceptor and produces energy in the form of adenosine triphosphate (ATP) from adenosine diphosphate (ADP) and inorganic phosphate (P_i), using the transmembrane protein ATP synthase and the hydrogen ion (H^+) transmembrane gradient. Electrons are donated to the electron transport chain from nicotinamide adenine dinucleotide hydride (NADH) and flavin adenine dinucleotide hydride ($FADH_2$). The presence of oxygen close to free electrons can also lead to the production of reactive oxygen species (ROS). An example of ROS production to produce the superoxide anion ($O_2^{\cdot-}$) and subsequently hydrogen peroxide (H_2O_2) by the enzyme manganese superoxide dismutase (MnSOD) is shown. Hydrogen peroxide can subsequently be converted to water (H_2O) and oxygen (O_2) by catalase (CAT) and peroxiredoxin 3 (Prx3) (adapted from Finkel[4]).

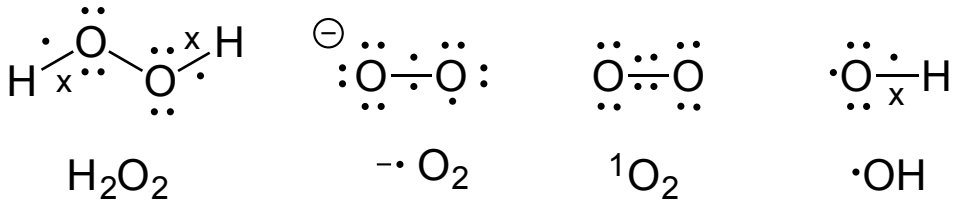

Figure 1.2 shows the Lewis structures of some examples of reactive oxygen species – hydrogen peroxide (H_2O_2), superoxide radical ($O_2^{-\bullet}$), singlet oxygen ($^1O_2$) and hydroxyl radical (•OH) – where electrons from oxygen are represented by a circle, and electrons from hydrogen are represented by a cross.

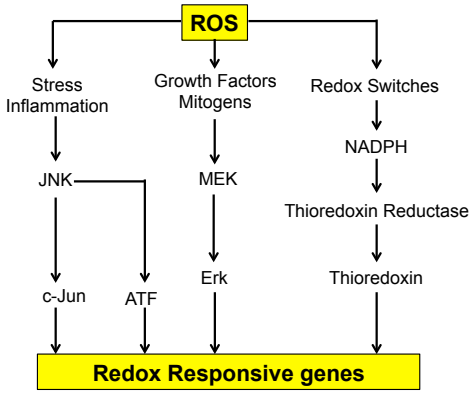

Figure 1.3 illustrates the importance of reactive oxygen species (ROS) in the regulation of signaling pathways in cells by indicating some of the pathways in which ROS control redox responsive genes. The stress inflammation pathway activates c-Jun N-terminal kinase (JNK) and activating transcription factor (ATF); the growth factor mitogens pathway activates mitogen-activated protein kinase kinase (MEK)/extracellular signal regulated kinase (Erk); and redox switches can activate thioredoxin reductase and thioredoxin via NADPH. (Adapted from Waris *et al.*[1])

1.1.2 Redox Couples

While there are many redox couples contributing to the overall intracellular redox potential and removal of ROS, there are a few particularly significant couples that contribute largely to overall redox potential. These couples can demonstrate the regulation of redox potential as a result of the balance between the reduced and oxidised forms of the species and the redox coupled interplay between different couples. The most important of these to specifically consider is glutathione/glutathione disulfide, while others such as thioredoxin, cysteine/cystine, protein sulfhydryls and $NAD(P)^+$/NAD(P)H also make a significant

contribution to the overall intracellular redox potential. Figure 1.4 demonstrates how these important redox couples can interconnect with one another in cells to regulate overall redox potential.[5]

In reality, this interplay of redox couples spans a huge number of redox active enzymes and molecules existing within cells. Therefore, in order to provide a completely accurate redox potential value for a particular compartment within a cell, the sum of the relative contributions of all the redox active molecules would be required, as demonstrated in Equation 1.1, where E_i is the half wave potential for a particular redox couple and $[\text{reduced species}]_i$ is the concentration of the reduced species of that couple present.[6]

$$\text{redox environment} = \sum_{i=1}^{n\,(\text{couple})} E_i \times [\text{reduced species}]_i \qquad (1.1)^{6}$$

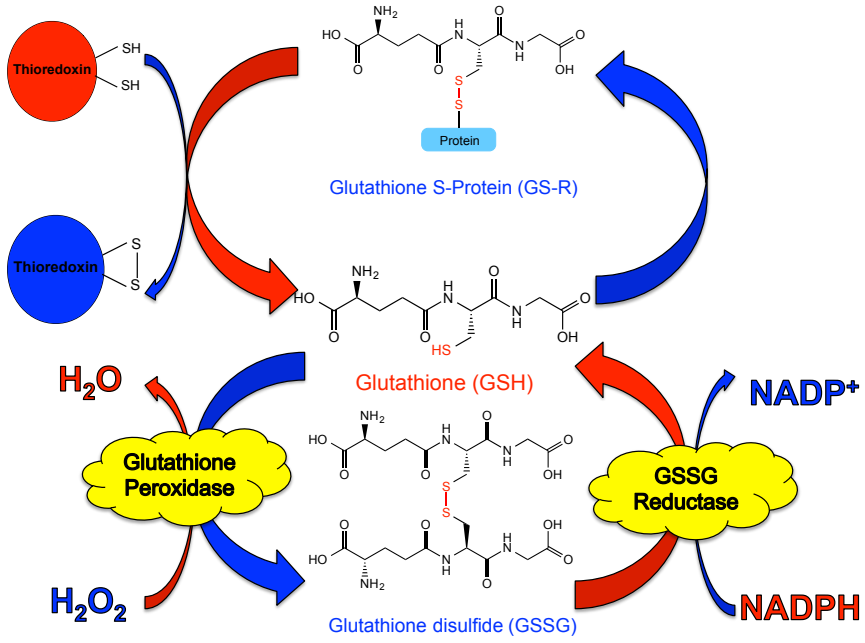

Figure 1.4 illustrates how redox couples in the cell can interplay in redox processes to contribute to overall cellular redox potential, using some of the main redox couples to demonstrate this (adapted from Filomeni *et al.*[5]). Red arrows represent reductive processes, blue arrows represent oxidative processes and yellow bubbles represent enzymes that catalyse the redox process.

The Nernst equation, given in Equation 1.2, is used to calculate the half wave potential for a particular species, where R is the gas constant (8.314 J K^{-1} mol^{-1}), T is temperature (K), n is the number of electrons involved in the redox process, F is the Faraday constant (9.6485×10^4 C mol^{-1}) and Q is the reaction quotient, which for a standard equation, illustrated in Equation 1.3, is given in Equation 1.4.[6] It is important to note here that the Nernst equation for calculating the redox contribution from a particular species is pH dependent as the standard reduction potential, ΔE, applies to standard biochemical conditions i.e. pH 7.[7] Typically, standard pH conditions refer to a pH of 0 as this gives an activity of 1. However, for a biological environment, using a standard cellular pH of 7 is typical. If conditions in the biological environment were to vary from this, an adjustment would have to be made to account for this. This adjustment comes in the ΔE^{θ} term, which changes with changing pH. Theoretically, for a one electron process, this varies by 59.2 mV per pH unit.[7]

$$\Delta E = \Delta E^{\theta} - \frac{RT}{nF} \ln Q \tag{1.2}$$

[6]

$$aA + bB \rightleftharpoons cC + dD \tag{1.3}$$

$$Q = \frac{[C]^c[D]^d}{[A]^a[B]^b} \tag{1.4}$$

Substituting constants into the Nernst Equation and converting ln to $\log_{10}$, gives Equation 1.5 at 25°C (298.15 K) and Equation 1.6 at 37 °C (310 K).[6]

$$\Delta E = \Delta E^{\theta} - \frac{59.1 \text{ mV}}{n} \log Q \tag{1.5}$$

[6]

$$\Delta E = \Delta E^{\theta} - \frac{61.5\ mV}{n} \log Q \qquad (1.6)^{6}$$

It would be impossible to determine the concentration of reduced and oxidised forms of every redox couple in a cell and the relative contribution of each couple to the overall redox potential and therefore the overall intracellular redox potential. For this reason, overall intracellular redox potential is often simplified as a measure of the redox potential contribution from the glutathione redox couple, as this is the largest contributor to intracellular redox potential. Equation 1.7 shows how the concentration of the oxidised, [GSSG], and reduced, [GSH], forms of glutathione can be substituted into the Nernst equation to give an approximation of the overall intracellular redox potential, where the standard half wave potential of the glutathione redox couple (Equation 1.8) is –240 mV.[6]

$$\Delta E = -240 - \frac{59.1}{2} \log\left(\frac{[GSH]^2}{[GSSG]}\right) mV \qquad (1.7)^{6}$$

$$GSSG + 2H^{+} + 2e^{-} \rightleftharpoons 2GSH \qquad (1.8)^{6}$$

1.1.2.1 Glutathione

Glutathione is the primary redox buffer inside cells, cytosolic glutathione concentrations ranging from about 1-11 mM.[6] In contrast, the concentration of extracellular glutathione is low and the primary redox couple found in the extracellular environment is cysteine/cystine. Glutathione is a tripeptide synthesised from L-glutamate, L-cystein and glycine by the enzymes ɣ-glutamylcysteine synthetase and glutathione synthetase (Figure 1.5).[8]

The biosynthesis of glutathione is primarily carried out in the cytosol and it can be transported into other intracellular compartments. There are, however, pools of glutathione found in some organelles independent of cytosolic glutathione biosynthesis. One example is in the nucleus, in which protein sulfhydryls are kept at critical redox potential values buffered by glutathione.[6]

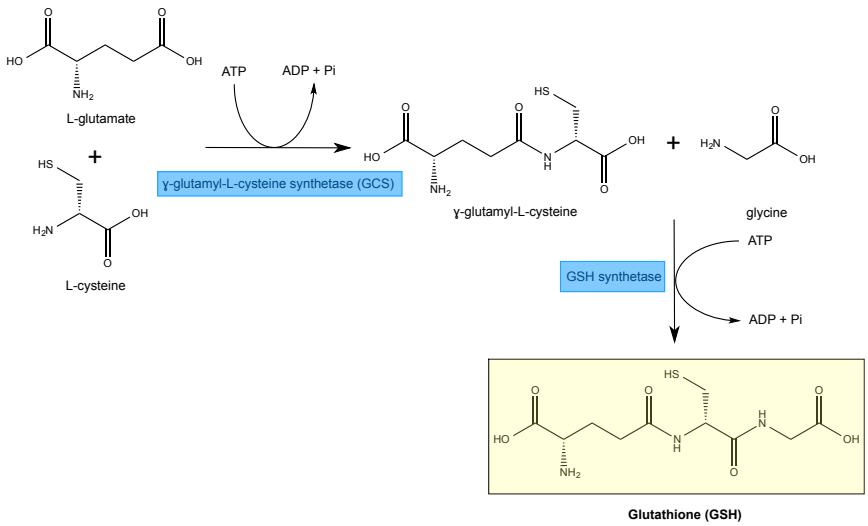

Figure 1.5 illustrates the steps in the cellular biosynthesis of glutathione from L-glutamate, L-cysteine and glycine, catalysed by the enzymes ɣ-glutamylcysteine synthetase and glutathione synthetase.[8]

1.1.2.2 Other Important Redox Couples

While glutathione is the primary contributor to intracellular redox potential, there are many other important redox couples that interplay greatly with glutathione and each other to influence the overall redox environment. Thioredoxins are proteins with a low molecular weight, which can exist in the disulfide or reduced sulfhydryl forms.[9] Intracellular thioredoxin concentrations are about 100 to 1000 times less than glutathione.[6] While glutathione forms intermolecular disufide bonds between different molecules, thioredoxin tends to form intramolecular disulfide bonds, the enzyme thioredoxin reductase catalysing the reduction of the disulfide to the dithiol using NADPH as the electron source (Figure 1.6).

In mammals, two types of thioredoxin are found – thioredoxin 1 (Trx1) in the cytoplasm and nucleus and thioredoxin 2 (Trx2) in the mitochondria.[9] The standard half wave potential of the disulfide of Trx1 has been estimated to be approximately –230 mV and experiments using redox Western blot have estimated the steady state potential of Trx1 in the cytoplasm at –280 mV, more reducing than the glutathione redox couple. The steady state potential of Trx1 in the nucleus has been estimated to be more reducing. As would be expected, Trx2 has been shown to have a much more negative half wave potential of about –330 mV (pH 7.6), which is consistent with mitochondrial function. Steady state potential of Trx2 in the mitochondria has been shown to vary from about –360 mV to –340 mV. The mitochondria

are expected to be the most reducing compartment in cells, as a result of the extensive electron transfer activity being carried out.[6]

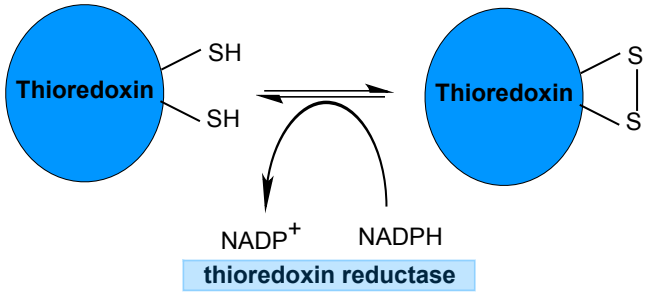

Figure 1.6 illustrates the activity of thioredoxin reductase in the intramolecular reduction of the disulfide to dithiol form of thioredoxin using NADPH.[6]

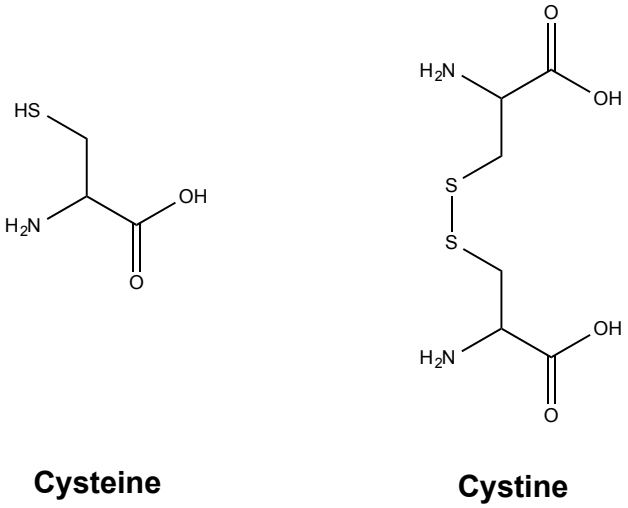

Figure 1.7 shows the structure of cysteine and cystine.

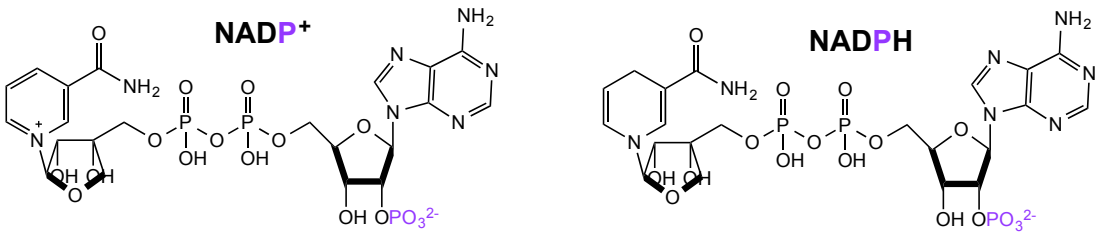

Figure 1.8 shows $NADP^+$/NADPH and NAD^+/NADH redox couple structures where the purple PO_3^{2-} is substituted by hydrogen (H) in NAD^+/NADH.

The low molecular weight thiol/disulfide cysteine/cystine (Figure 1.7) is the main contributor to plasma potential, plasma having a potential of around –80 mV, which becomes more oxidising with ageing, chemotherapy, cardiovascular disease and smoking.[9,10] Cysteine/cystine is also one of the amino acids found in all proteins in the body and these proteins all make a contribution to overall intracellular redox potential via the redox state of their, often conserved, cysteine amino acids.

The final major contributors to intracellular redox potential to be considered are the nicotinamide adenine dinucleotide (NAD^+/NADH) and nicotinamide adenine dinucleotide phosphate ($NADP^+$/NADPH) systems (Figure 1.8). On average, the [NADPH]:[$NADP^+$] ratio is close to 100:1, while that for [NADH]:[NAD^+] is generally between 1:10 and 1:100.[6] These ratios reflect the major roles of the two couples, NADPH/$NADP^+$ is involved primarily in reductive biosynthesis, whereby NADPH provides the electron source for reduction, while NADH/NAD^+ is primarily involved in oxidative catabolic reactions, in which NAD^+ acts as an electron sink accepting electrons. Importantly, NADPH is also the major source of electrons for reduction of glutathione disulfide to glutathione, aiding reduction of oxidative stress. It is important to note that these intracellular ratios reflect steady state values for the couples that, particularly in this case, lie far from equilibrium. Cytosolic binding sites favouring binding of the reduced or oxidised form of the couples are thought to be involved in maintaining the steady state potential required.

1.1.3 Compartmentalisation

Another important characteristic of intracellular redox potential is that it is highly compartmentalised in cells, the different organelles within a cell being regulated at varying redox potentials allowing them to carry out their respective functions efficiently. The particular redox potential that different organelles are regulated at is poorly understood due to a lack of techniques allowing this to be measured, a lot of techniques involving disruption of the cell to measure an overall redox potential. However, some techniques have been applied that have allowed a closer study of redox potential changes between different organelles, including targeted reduction-oxidation sensitive green fluorescent proteins (roGFPs) (see Section 1.2.4).[11]

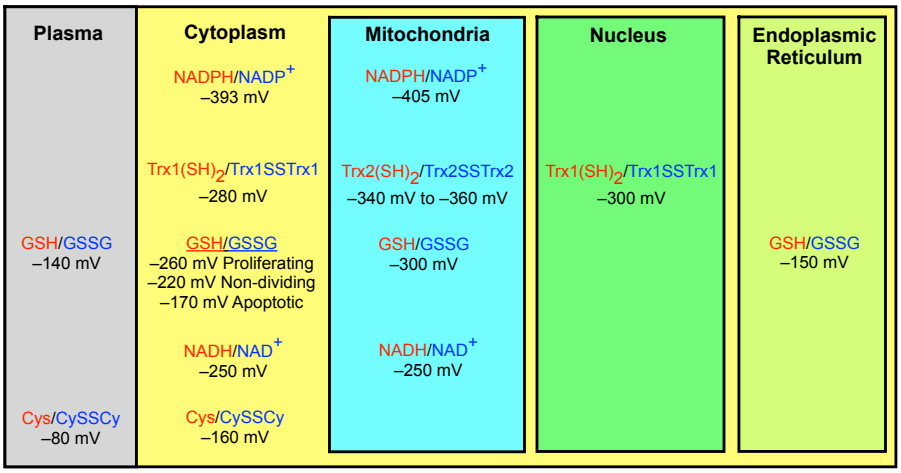

Figure 1.9 illustrates estimated steady state potentials of various redox couples in different compartments of the cell reported by Kemp *et al.*[9] (adapted from Kemp *et al.*[9]) These estimates are generally not grounded in sound scientific evidence and there is a need for techniques to more accurately measure intracellular redox potential. The steady state potential is the redox contribution from that particular redox couple, taking into account the relative concentrations from the reduced and oxidised form of that couple, and the standard half cell potential of that couple. Overall redox potential in each compartment would take into account relative contributions from each redox couple.

The cytosol is generally the largest component of a cell and the cytosolic redox potential, determined from glutathione measurements, is typically less than –200 mV in cells with nuclei and mitochondria.[9] Most redox couples are present in all of the intracellular organelles, but the concentration varies between compartments (Figure 1.9). In some compartments, the concentration of a particular redox couple is dependent on the rate of transfer of that species across a membrane into that organelle from the cytosol.[9] However, in some cases, there is also a transport independent contribution to the concentration, as the redox active molecule is also synthesised in that organelle. While it is difficult to put absolute values on redox contribution from different redox couples in different organelles, attempts have been made to collate such information.

The most redox active compartment in the cell is the mitochondria, the site where respiration occurs, carrying electrons to O_2 along the electron transport chain[2]. This large volume of electron transport activity gives rise to an environment more reductive than that in the cytosol and other organelles.[11]

The nuclear environment is also thought to be a more reductive environment than the cytosol from evidence available. Achieving accurate measurement of GSSG and GSH concentrations in the nucleus is difficult, due to potential changes as a result of the measurement process. However, protein thiol (PrSH) and protein S-glutathione (PrSSG) concentrations, measured by high performance liquid chromatography (HPLC) of GSH produced from reduction of nuclear and cytosolic protein fractions with dithiothreitol (DTT), revealed a higher ratio of PrSH:PrSSG than in the cytosol.[11] The more reducing redox environment of the nucleus is important for functions such as maintaining the integrity of DNA against oxidative damage and regulating transcription factors.[3]

On the other hand, the endoplasmic reticulum and export system in the cell tends to be a more oxidising environment than the cytosol.[9,11] This allows for the correct folding and processing of proteins, including the addition of the necessary disulfide bonds, an essential aspect to protein folding and obtaining the correct conformation for export and function.[11]

Another particularly oxidising environment is found in peroxisomes, lysosomes and endosomes, in which the oxidative environment is used for digestion of their contents.[11] The endocytic pathway is involved in the uptake and digestion of cargo such as proteins into cells and cycles through various endocytic vesicles as shown in Figure 1.10. Initial consideration may suggest that these vesicles would exhibit a reducing environment, as the reduction of protein disulfides is thought to aid digestion of proteins.[12] This is in contrast to the oxidising environment of the endoplasmic reticulum to allow introduction of disulfides into proteins when processing for secretion. However, research has confirmed that endosomes and lysosomes exhibit an oxidising environment. One study by Austin *et al.*[12] used roGFPs (see Section 1.2.4) fused to marker proteins of different endocytic compartments – recycling endosomes, lysosomes and late endosomes – to measure redox state in these compartments. Control conditions fused roGFPs to mitochondrial and endoplasmic reticulum proteins. Results confirmed that endocytic and lysosomal compartments were in a similar oxidation state to endoplasmic reticulum, with roGFP between 94% and 96% oxidised in the various endocytic compartments, consistent with 95.8% in endoplasmic reticulum and in contrast to 8.3% in mitochondria. This gave an estimate that endocytic compartments were at a minimum –240 mV compared to –318 mV in mitochondria.

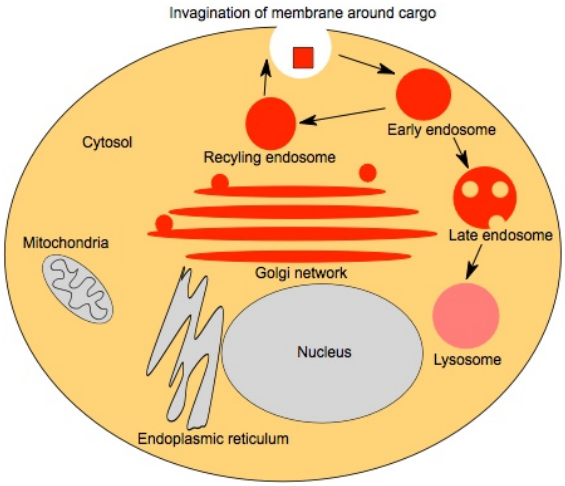

Figure 1.10 illustrates the stages of the endocytic pathway in cells (adapted from Casey *et al.*[13]). Cargo is introduced into the cell by invagination of the membrane around the cargo and progresses to an early endosome. The endosome can then progress to a recycling endosome and release contents into the extracellular environment, or progress to a late endosome and subsequently lysosome.

1.1.4 Involvement of Redox Potential in Cellular Processes and Disease

Intracellular redox potential is a critical factor controlling and regulating a vast number of cellular processes. Fundamentally, cell growth, proliferation and death can be linked to redox potential control as illustrated in Figure 1.11. In general, hypoxic conditions stimulate cell proliferation and as cellular redox potential shifts to more positive potentials, proliferation decreases and differentiation increases until, under oxidative stress, apoptosis, programmed cell death, occurs and at very oxidising potentials necrosis, uncontrolled cell death, can also occur.[6,14] Redox potential has also been suggested to be a major controlling factor in a wide range of other cellular processes, including DNA, RNA and protein synthesis, enzyme activation and a huge number of signal transduction pathways.[3,15] Redox signaling largely operates through sulfur switches, whereby sulfur can exist in the disulfide or sulfhydryl form depending on the redox state of the cell. For example, these sulfur switches are often in the form of conserved cysteine residues in proteins, whereby formation of the disulfide form, usually intramolecularly between two cysteine residues, changes the conformation of a protein and can lead to activation or inhibition.[5,9]

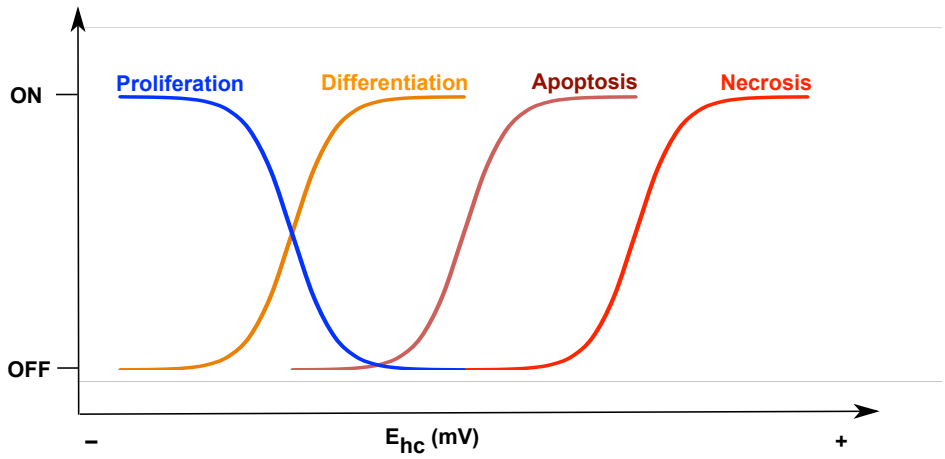

Figure 1.11 illustrates how cell cycle can be controlled by redox potential (adapted from Schafer *et al.*[6]). At more reducing intracellular redox potential values (left hand side), proliferation is favoured (switched 'ON'). As the intracellular redox potential increases, proliferation decreases and is eventually switched 'OFF' while differentiation becomes switched 'ON'. Moving to even more oxidative potentials apoptosis is switched 'ON' and finally at the most oxidising potentials necrosis is switched 'ON'.

Having seen how redox potential can be associated with a variety of cellular processes, it can be imagined that, when this regulation and fine balance is disrupted, problems will result. Oxidative stress is associated with the onset of a huge number of diseases including cardiovascular[10] and neurodegenerative diseases (Figure 1.12). ROS accumulation and oxidative stress are also associated with ageing.[1] At the other side of the redox scale, hypoxia is associated with disease and in particular cancer. When tumours develop, the centre of the tumour becomes depleted in oxygen due to poor access by blood vessels and thus the central regions of tumours become hypoxic.[16] As conventional methods for cancer treatment such as radiotherapy[16] and photodynamic therapy (PDT)[17], rely on the presence of oxygen, this makes these central regions very resistant to therapy. On a related note, vascular drug delivery during chemotherapy relies on good access to the affected areas. Therefore, it is more difficult for these drugs to reach regions with limited, poor or no vasculature.[18]

Figure 1.12 illustrates the many disease states that oxidative stress has been associated with (adapted from http://www.oxidativestressresource.org[19]).

1.1.5 The Hallmarks of Cancer and Redox Potential Implication

As already discussed, redox potential has an important role to play in a number of disease states. It is incredibly significant to consider its role in cancer. To do so, first it is important to condider how cancer can be characterised. Hanahan *et al.*[20] published a review paper in which they discuss 'The Hallmarks of Cancer' as the defining features in the development of cancer. Figure 1.13 illustrates the six primary 'capabilities' developed by a cell as it progresses to a cancerous state.

The first of these characteristics is 'sustaining proliferative signaling', which involves the breakdown of a cell's ability to regulate growth and division cycles by careful control of signaling molecules such as growth factors. Cancer cells evade the healthy regulation mechanism in a number of ways, including by producing growth factors themselves; stimulating nearby cells to increase growth factor production; increasing the number of growth factor receptors, thus becoming 'hyperresponsive'; and becoming 'constitutively active' or independent of the need for growth factor regulation.[20]

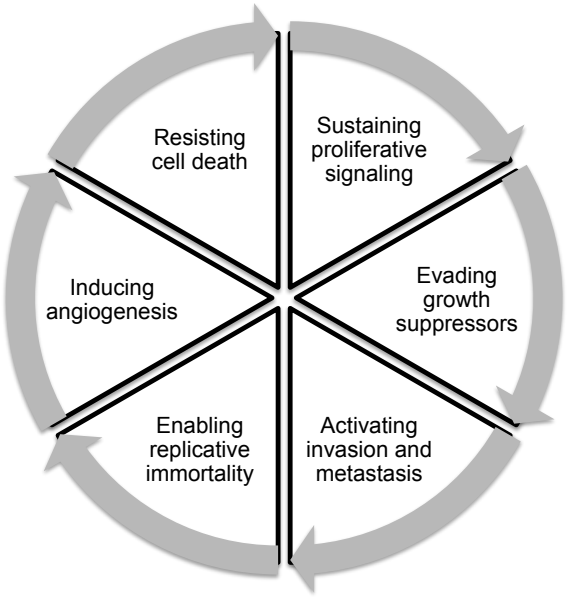

Figure 1.13 illustrates the six primary 'Hallmarks of Cancer', defining features in the development of cancer, as defined by Hanahan *et al.*[20] (adapted from Hanahan *et al.*[20]).

The second of these characteristics is the ability to 'evade growth suppressors'. This characteristic relies on cancer cells' ability to evade the mechanisms in place to reduce proliferation by tumour suppressor genes. In particular, retinoblastoma-associated (RB) and tumour protein p53 (TP53) can downregulate proliferation in response to signals from outside the cell for growth inhibition (RB) and intracellular stress and abnormality signals (TP53). In cancer cells, there can be defects in the pathways producing RB and TP53, leading to the usual tumour suppressing mechanisms not operating properly.[20]

The third characteristic is the cells' ability to 'resist cell death'. While defects in cells such as DNA damage and signaling imbalances would normally lead to apoptosis to remove the affected cells, cancer cells develop the ability to resist this process and survive. Again, the tumour suppressor TP53 is involved in signaling for apoptosis and the loss of its function in cancerous cells is the major cause of a cell's ability to evade apoptosis.[20]

The next characteristic is 'enabling replicative immortality'. Usually, cells will only undergo a certain number of replicative cycles before they enter senescence, a nonproliferative but viable state, and finally crisis, at which point the cells die. Cancer cells can, however, acquire the ability to come out of this crisis state in a proliferative and viable state. It is thought that

this capability is largely derived from the hugely increased activity of telomerase in these cancerous cells, an enzyme that adds telomeres, hexanucleotide repeats, to the end of chromosomes. These telomeres protect the ends of chromosomes, but in normally functioning cells, there is only a certain number of these repeats, which become progressively smaller with successive cell cycles and therefore determine the number of cycles a cell can progress through. The hugely increased activity of telomerase can counteract this mechanism of controlling how many cell cycles occur before cell death.[20]

The next characteristic of cancerous cells is the ability to 'induce angiogenesis'. As tumours develop, new blood vessels are required to supply nutrients and oxygen to the tumour tissue. Angiogenesis is stimulated in cancerous cells by proangiogenic factors such as vascular endothelial growth factor-A (VEGF-A). Blood vessels in tumours are, however, very erratic, not well organised and leaky, so they are not as efficient as regular blood vessels.[20]

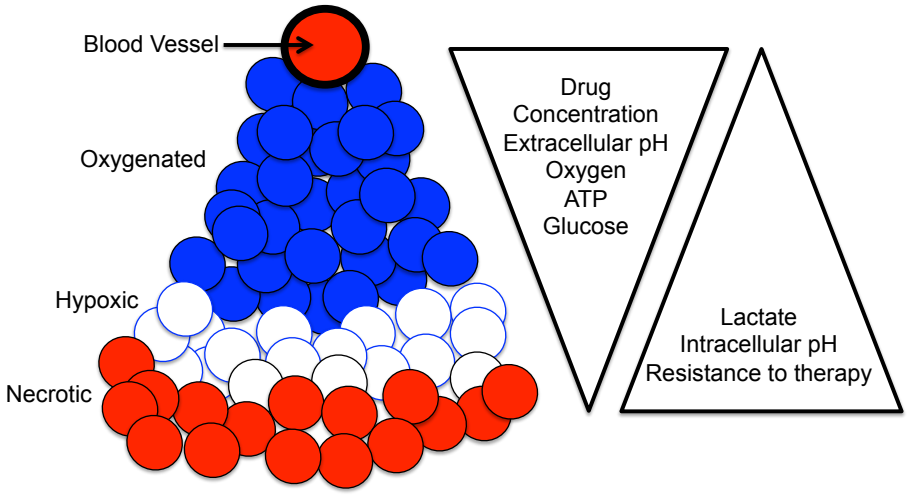

Figure 1.14 illustrates the organisation of cells within a tumour where regions further from blood supply can become depleted of oxygen and hypoxic. As well as gradients in oxygen concentration, gradients in other features establish as shown, with increasing therapy resistance going further from blood vessels. Eventually cells become necrotic. Blue spheres represent oxygenated cells, white spheres represent hypoxic cells and red spheres represent necrotic cells.[16]

Finally, the last characteristic is the cancer cells' ability to 'activate invasion and metastasis'. This allows the cancer cells to spread within the tissue and to other parts of the body and it is thought that loss of the cell-to-cell adhesion molecule E-Cadherin is one of the major contributors to the cells' ability to carry out invasion and metastasis.[20]

Briefly considering how redox potential could be important within these 'Hallmarks of Cancer', areas where it could have a significant contribution emerge immediately. For example, it has already been discussed how redox potential is important in cell cycle regulation, whereby hypoxic conditions promote proliferation and oxidising conditions promote cell death.[6] Relating this to cancer development, it could be suggested that hypoxic conditions could favour cancer development, as this links into the characteristics of 'sustaining proliferative signalling' and 'resisting cell death'. Hypoxia Inducible Factor-1α (HIF-1α) is also activated in hypoxic conditions, which in turn is involved in the activation of VEGF and in turn the promotion of angiogenesis.[21]

Another important aspect to consider in cancer development is the development of a 'tumour microenvironment'.[20] As a tumour develops, it develops its own microenvironment. When angiogenesis is induced, it has already been discussed that the vasculature that results is very disorganised and poor at performing its function.[16] As a result, a gradient develops as blood supply diminishes towards the centre of tumours and therefore oxygen and nutrient supply is deficient in these regions. This creates a hypoxic environment centrally in tumours (Figure 1.14).

There is also a proposed decrease in pH nearer the centre of tumours, primarily due to increased lactate production by anaerobic respiration.[22] The high rate of anaerobic respiration and tendency towards the pentose phosphate pathway (PPP)[23] in tumour cells is an important phenomenon, named the Warburg effect.[24] Interestingly, research has shown that where tumour cells are not oxygen or energy deficient, the intracellular pH is neutral to alkaline and the extracellular pH is lower. In normal cells, extracellular pH is, in contrast, higher than intracellular pH. This difference can be primarily attributed to the Na^+/H^+ exchanger, the main pH regulator in cells, which can become activated by various growth factors involved in tumour angiogenesis.[16,25] In addition to poor vasculature leading to poor access for vascular drugs, this hypoxic environment is very resistant to therapy.

1.2. Measuring Intracellular Redox Potential

The importance of intracellular redox potential in the regulation of a huge number of cellular processes and the role of redox potential dysregulation in disease development has been established. In order to gather information about intracellular redox potential to explore how it regulates cellular processes and how it can become dysregulated in disease, techniques are required for the measurement of intraceullular redox potential. A variety of techniques have been established, although they all have drawbacks, as will be discussed.

1.2.1 Measuring Glutathione Concentration

One of the first methods used to investigate intracellular redox potential was the glutathione recycling assay. This allows the concentrations of glutathione and glutathione disulfide to be measured, but in order to do so, requires the cells to be lysed so is not suitable for live intracellular measurements. This technique also relies on glutathione being the major intracellular redox couple, as it reports redox potential only depending on glutathione and glutathione disulfide concentrations. Overall, this gives a good rough estimate of intracellular redox potential, but in order to get a more accurate value, contributions from all the other redox active couples in the cell would need to be considered. The assay also does not take into account compartmentalisation in the cell, instead only giving an overall cellular potential.[26]

The assay works by measuring both total GSSG + GSH concentration and GSSG concentration. As illustrated in Figure 1.15, 5,5′-dithiobis(2-nitrobenzoic acid) (DTNB) reacts with GSH to form GSTNB and 5-thio-2-nitrobenzoic acid (TNB), which is yellow in colour. In the presence of glutathione reductase (GR) and NADPH, GSTNB is then reduced back to GSH (by reaction with GSH to produce GSSG and TNB and reduction of GSSG with GR), which is recycled back into the reaction. By measuring the rate of formation of TNB by its absorbance at 405 nm, the concentration of GSH can be determined, as this is proportional. GSSG is also reduced to GSH by GR and therefore can be measured in this reaction. This assay will therefore determine total GSH + GSSG concentration. However, by initially masking GSH in the sample with a masking reagent, GSSG concentration can also be determined. These masking reagents mask the thiol of GSH and include N-ethylmaleimide (NEM) and 2-vinylpyridine (2VP). However, this masking reaction provides a further source

of error in these experiments, as it is relatively slow, which provides time for autooxidation of GSH to GSSG during this process. The use of 1-methyl-4-vinyl-pyridinium trifluoromethane sulfonate (M4VP) was later reported as a better masking reagent as masking is completed in 2 minutes compared to 20-60 minutes with NEM and 2VP.[26]

High performance liquid chromatography (HPLC) techniques have also been used to determine GSSG and GSH concentrations from cell lysates but again this is only giving redox potential values based on glutathione and over the whole cell.[27]

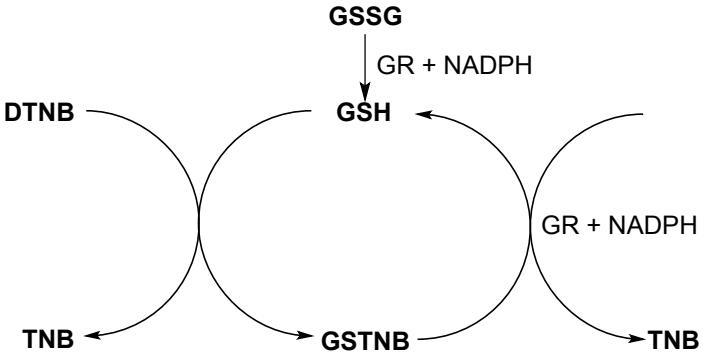

Figure 1.15 illustrates the processes involved in the glutathione recycling assay, where 5,5′-dithiobis(2-nitrobenzoic acid) (DTNB) reacts with glutathione (GSH) to produce 5-thio-2-nitrobenzoic acid (TNB) and GSTNB. The rate of TNB production is measured by absorbance at 405 nm. GSTNB reacts with GSH to produce GSSG, which is reduced back to GSH by glutathione reductase (GR) and NADPH. Initially, GSSG from the sample is also reduced to GSH, by GR and NADPH, therefore total GSSG and GSH concentration is determined. By masking GSH initially, GSSG concentration can be determined. (adapted from Shaik *et al*.[26]).

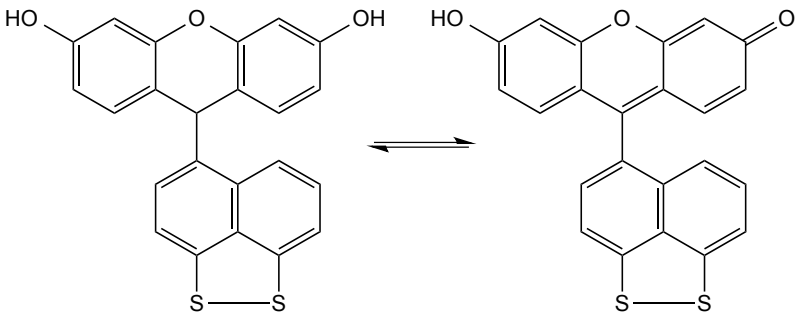

Figure 1.16 shows the structure of the fluorescent dye Redoxfluor-1 (RF1) in its reduced and oxidised forms.[28] RF1 reports reversibly on intracellular redox state.

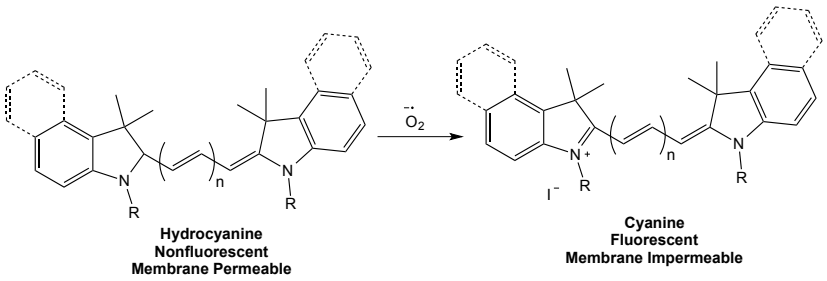

Figure 1.17 shows the structure of non-fluorescent hydrocyanine, which reacts with oxygen radicals to produce fluorescent cyanine, irreversibly reporting on oxygen radical concentration in cells (adapted from Kundu *et al.*[29]).

1.2.2 Fluorescent Dyes

Another technique for the characterisation of the redox environment in cells is the use of fluorescent dyes that report on the redox state of cells. One example of such a dye, which can reversibly report on intracellular redox state, is Redoxfluor-1 (RF1) (Figure 1.16).[28] This redox reporter has the advantage that it reports reversibly on redox state. However, this technique only reports on whether the redox potential of the intracellular environment is above or below a particular potential – the half wave potential of the reporter molecule. While this fluorescent dye has the advantage that it reports reversibly on redox environment, many fluorescent dyes operate by covalent interaction, so also have the disadvantage that they cannot measure reversible changes. A lot of fluorescent dyes also only report on concentrations of particular oxidants. Hydrocyanine dyes are an example of irreversible redox reporters that only report on the concentration of specific ROS such as oxygen radicals (Figure 1.17).[29]

1.2.3 Glutathione Reductase Crystals

Another technique, with the same disadvantage as fluorescent dyes in that it only reports on whether the redox potential of the intracellular environment is above or below a particular potential, is the use of glutathione reductase crystals. Glutathione reductase crystals are yellow in their oxidised form and dark orange in their reduced form. At intracellular conditions of pH 7.4 and 37 °C, the half wave potential of the glutathione reductase crystals is –270 mV. After microinjection of these crystals into the cytosol of human fibroblast cells, the crystals turn from yellow to dark orange and therefore the only conclusion that can be drawn is that the environment was more reducing than –270 mV.[30]

1.2.4 Reduction-Oxidation Sensitive Green Fluorescent Proteins (roGFPs)

The current 'gold standard' technique for measuring intracellular redox potential is roGFPs. Various roGFPs have been engineered with specific cysteine residues, which exist as a redox couple (Figure 1.18). Depending on the oxidation state of these residues, the fluorescence excitation maxima of the roGFP changes and therefore the ratio of reduced to oxidised roGFP can be determined and from that the redox potential of the environment.[31,32]

This technique has many advantages over previously developed redox monitoring techniques, one of the main advantages being that it can be performed *in vivo* in real time to reversibly monitor redox potential. The engineered roGFPs can also be designed to target particular organelles such as the cytosol, mitochondria, nucleus and peroxisomes and thus can be used to measure redox potential in particular compartments and compare the differences between compartments. Essentially, the roGFPs do not interfere with any processes occurring in the cells. While roGFPs have many advantages in comparison to other techniques used previously for intracellular redox monitoring, they are not perfect. It has

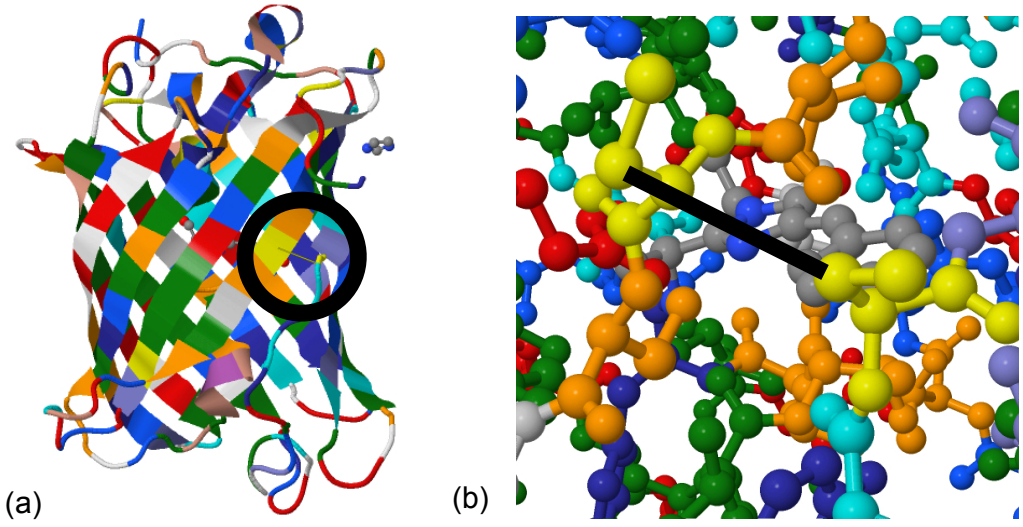

Figure 1.18 (a) illustrates the structure of an oxidised reduction-oxidation sensitive green fluorescent protein (roGFP) (roGFP1-R7) with engineered cysteine residues (yellow), sensitive to redox environment, highlighted (black circle) and (b) shows a ball and stick model of the cysteine residues (yellow) in reduced roGFP (roGFP1-R8), where black line represents where the disulfide bond would form in the oxidised form (colour coded by amino acid) (adapted from http://www.rcsb.org[33]).[34]

been suggested that they might primarily respond to the effects of glutathione and not all redox active molecules present in cells. This was discussed in relation to an earlier developed yellow fluorescent protein (YFP), whereby cytosolic measurements of redox potential using the YFP agreed largely with those determined from GSSG/GSH concentrations and there was no reaction between reduced thioredoxin and the oxidised YFP.[35] The half wave potential of roGFP1 is approximately –291 mV and that of roGFP2 is approximately –280 mV, making measuring the redox potential of significantly oxidised compartments such as the endoplasmic reticulum and peroxisomes difficult using any of these probes, although current developments are attempting to address this issue.[31,32]

1.3 SERS Nanosensors

Using SERS nanosensors for the measurement of intracellular redox potential makes use of Raman scattering, a technique that probes the vibrational states of molecules, whereby vibrational signals from signaling molecules are enhanced by attachment to, or in the environment of, metal nanoparticles (NPs).

1.3.1 Raman Scattering and Surface Enhanced Raman Scattering

Raman scattering was discovered by C.V. Raman in 1928, who observed the scattering effect in a series of liquid and vapour samples.[36] Raman scattering probes the vibrational modes of a molecule. In spectroscopy, energy is absorbed or emitted by a molecule, as the molecule moves between energy states. Depending on the type of radiation involved, this can probe different transitions within a molecule – ultraviolet (UV) and visible radiation can probe electronic transitions, infrared (IR) radiation can probe vibrational transitions and far IR and microwaves can probe rotational transitions. In IR spectroscopy, as a molecule transitions between vibrational energy levels, the absorbance or emission of radiation is observed in the spectrum. In addition to absorbance and emission of incident radiation, radiation can also be scattered by a molecule. It is this scattering of radiation that is measured in Raman scattering.[37,38]

The majority of scattered radiation does not change in frequency and this is known as Rayleigh scattering. However, about 1 in 10^7 of the photons scattered by a molecule changes in energy.[37] These photons can either lose energy to the molecule and therefore emerge with

less energy, known as Stokes scattering, or gain energy from the molecule and therefore emerge with more energy, known as anti-Stokes scattering. This scattering effect can probe both rotational and vibrational energy levels, depending on the incident radiation used. However, it is vibrational Raman scattering that is being used in this project. Figure 1.19 illustrates the process of Raman scattering pictorially, whereby molecules are excited to virtual energy states transiently before they emit radiation again. As discussed, most of this radiation is emitted at the same frequency, but some radiation is scattered at lower and higher frequencies, whereby the difference between incident and scattered radiation corresponds to the vibrational energy. Figure 1.19 also compares the processes of IR absorption and Raman scattering, which can both measure the same bond vibrations, but by absorption/emission or scattering respectively. As most scattered radiation is scattered elastically by Rayleigh scattering, on comparison of absorbance and Raman cross sections, the Raman effect is very weak compared to IR absorbance.[37,38]

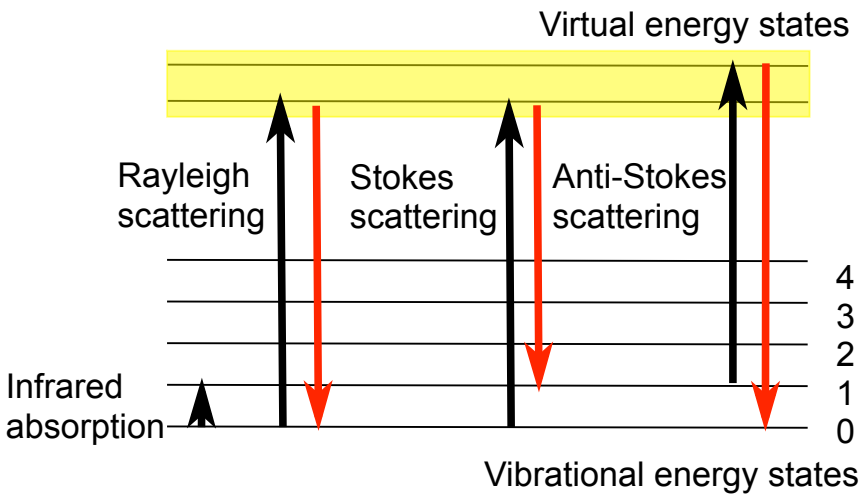

Figure 1.19 illustrates the Raman scattering process in comparison to infrared (IR) absorption. In IR spectroscopy, radiation is absorbed by a molecule, causing an increase in vibrational energy state. In Raman scattering, energy is absorbed by a molecule, promoting the molecule to a virtual energy state, followed by emission of the radiation. The majority of radiation is emitted with the same frequency as the incident radiation, Rayleigh scattering, but about 1 in 10^7 photons are scattered with lower or higher frequency, Stokes and anti-Stokes scattering respectively. The difference in energy between incident and emitted radiation in these cases correspond to the difference in vibrational energy levels in the same manner as IR spectroscopy.

While regular IR spectroscopy gives signal intensity many orders of magnitude greater than for vibrational Raman scattering, as a result of a larger absorbance cross section compared to scattering cross section, it has major drawbacks for analysis of biological systems. Biological samples are typically aqueous and water is strongly IR active. The three vibrational bands of water, at approximately 3300 cm^{-1}, 2200 cm^{-1} and 1650 cm^{-1}, strongly dominate the IR absorbance spectrum of aqueous samples.[39] In particular the vibrational band at approximately 1650 cm^{-1} appears in the region of particular interest for biological samples, overlapping with the protein amide-I band at approximately 1655 cm^{-1} and complicating analysis. In contrast, water has low cross section for Raman scattering, making analysis of aqueous samples easier.[40] Raman scattering is also compatible with samples in almost any state, whereby IR spectroscopy often requires more careful and specific sample preparation.[41] In addition to the need to often minimise water content in samples for IR spectroscopy, there is a need for more careful sample preparation, as, often complete regions of the IR spectrum will be absorbed by a neat sample, unless path length is limited to below approximately 100 μm.[42] While this is a problem in transmission and reflectance IR spectroscopy, due to large volumes of the sample being illuminated, attenuated total reflectance (ATR) IR spectroscopy only illuminates small regions of the sample and therefore sample preparation is minimised.

It is also important to note that the selection rules for IR spectroscopy require that the dipole moment of the molecule changes during the vibration, while those for Raman require that the polarisability changes.[37] This leads to different vibrational modes being observed using the different techniques and is the reason why water signals are observed strongly in IR spectra but only weakly in Raman spectra. Despite the drawbacks of IR spectroscopy, it has still been used extensively and successfully for analysis of biological samples, as will be discussed with examples in Section 1.3.2. Likewise, the benefits of Raman over IR spectroscopy have been exploited for application to biology and medicine, as will be discussed in Section 1.3.2. The basic setup for Raman is illustrated in Figure 1.20 and involves sample illumination using a monochromatic laser, focused onto the sample of interest, most typically through a fibre optic probe or microscope, and then collection of scattered radiation onto a CCD, which produces a spectrum.[43]

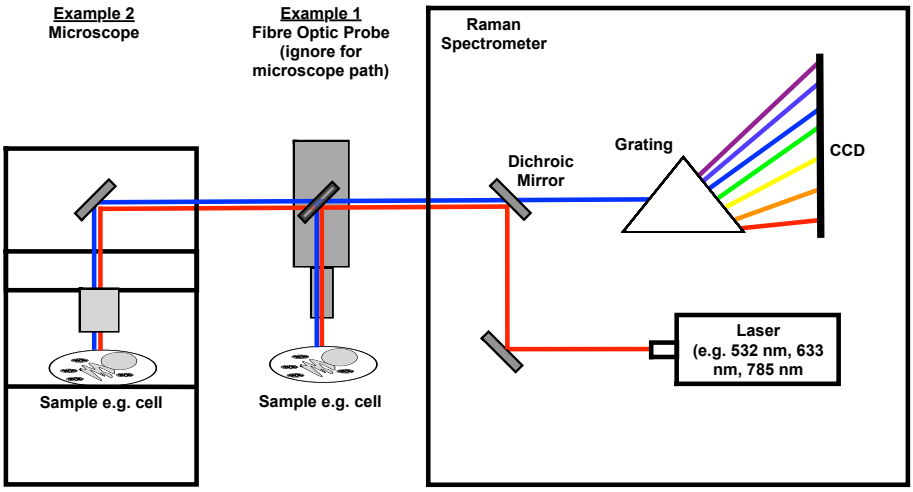

Figure 1.20 illustrates the basic instrumental setup for a Raman spectrometer where monochromatic laser light (from a laser with wavelength e.g. 532 nm, 633 nm and 785 nm), can be focused onto a sample of interest commonly via a fibre optic probe or microscope before collection of scattered radiation through a dichroic mirror, grating (to separate wavelengths) and onto a CCD (adapted from Fenn *et al.*[43]).

As discussed, the Stokes and anti-Stokes signals from Raman scattering, which give the information on vibrational modes of the molecule being investigated, are very weak, the majority of scattered radiation having the same energy as the incident radiation.[38] SERS overcomes this problem by increasing signal intensity as a result of surface plasmon resonance from roughened metal surfaces to which the molecules being probed can be in close proximity or attached. This enhancement effect was first observed by Fleischmann *et al.*[44] in 1974, who noticed an abnormally large enhancement in Raman signal from pyridine attached to roughened silver electrodes. SERS was first explained by Van Duyne *et al.*[45], who were the first to characterise this enhancement and term it SERS.[46]

Surface plasmon resonance on the roughened metal surface is key to this enhancement. Metals, such as gold and silver, consist of a lattice of positive ions and plasma of delocalised electrons. In the presence of incident radiation at the resonant frequency of these electrons, an electromagnetic field is created that enhances scattering from molecules attached to or in close proximity to the surface.[37,47] Gold and silver are particularly useful metals for this technique, as their plasmon resonance frequencies lie in the near infrared (NIR) or visible range used for Raman scattering.[47] The exact value of surface plasmon resonance depends on a number of properties, including the size, shape and degree of aggregation of the

nanoparticles.[48] For example, increasing the size of spherical gold nanoparticles redshifts their surface plasmon resonance, as does aggregation of the nanoparticles.[49] Aggregation of nanoparticles can also result in 'hotspots' between particles, regions where localised electric field is enhanced even further. As well as nanoparticles composed of a single metal, nanoparticles can consist of multiple materials. For example, metal nanoshells have a dielectric core, such as silica, and a metal shell, such as gold.[50] In this case as well as changing the overall size of the nanoshell, the core:shell ratio can be altered to change the surface plasmon resonance. A redshift in surface plasmon resonance is observed as the shell thickness is decreased resulting in an increase in the core:shell ratio.

Electromagnetic enhancement is thought to be the primary source of enhancement in SERS. Figure 1.21 illustrates pictorially how a metal NP behaves in response to an electric field, as an example to illustrate the electromagnetic enhancement process. Free electrons move in the opposite direction to the field creating an oscillation of electrons otherwise known as a surface plasmon. This creates areas of high electric field intensity on the surface of these NPs, resulting in enhancement of Raman signals from any molecules in close enough proximity to the surface.

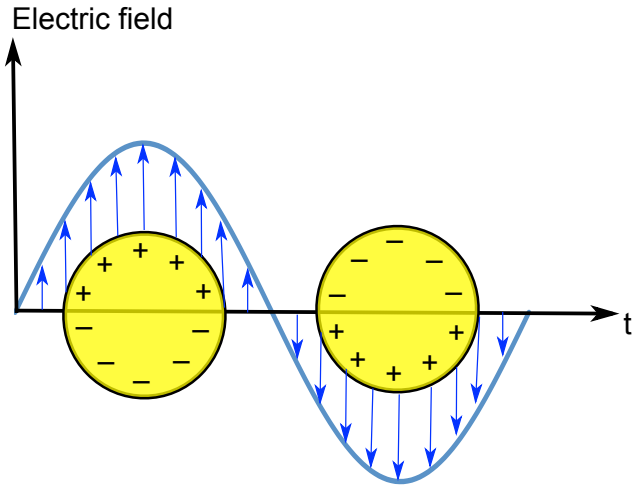

Figure 1.21 illustrates how the free electrons in metal NPs (yellow spheres) respond to the application of an external electric field (blue line and arrows). This results in surface plasmons – the name given to the oscillation of these electrons – and creates regions of high intensity electric field at the surface of NPs leading to enhancement of Raman signal intensity for molecules in close proximity of attached to the surface (adapted from Hammond *et al.*[51]).

While this electromagnetic effect is thought to be the primary contributor to the enhancement of signals in SERS, the exact mechanism taking place is a subject of debate and it is also thought that there is a chemical source of enhancement, whereby the molecule being probed is bonded to the metal surface. This chemical source is a result of charge transfer in the molecule being investigated from the highest occupied molecular orbital (HOMO) to the lowest unoccupied molecular orbital (LUMO) of the electronic energy levels. Such a transition would normally require higher energy radiation that used. However bonding to the metal surface provides a lower energy pathway to this excited state via the Fermi level of the metal.[52]

1.3.2 Vibrational Spectroscopy in Biology and Medicine

There have been a lot of recent advances in the use of vibrational spectroscopy research for application in biology and medicine. Both IR and Raman spectroscopy have advanced rapidly for applications in analysis of biological material including tissue *in vivo*, excised tissue, tissue sections, blood, serum and single cells.[53] One of the major advantages of IR and Raman spectroscopy over, for example, fluorescence staining and immunohistochemistry techniques is that it is a label free method, detecting native biochemical markers of cells and tissue via characteristic bond vibrations. Another major advantage and area of extensive research is the potential for increased objectivity and automation in histopathology and cytology with a movement towards spectropathology as the ultimate goal.[53] Standard clinical practice requires analysis of tissue sections by a pathologist for disease determination. Attempts are being made to move towards more automated disease diagnosis in tissue sections using vibrational spectroscopy. In 2004 Diem *et al.*[54] gave a concise overview of vibrational spectroscopy in cells and tissue over a ten year period. Since then the field has continued to expand in all directions.

Baker *et al.*[55] recently presented an overview on the analysis of biological materials using Fourier transform IR (FTIR) spectroscopy, which addressed one of the major factors required for translation of this technique to the clinical setting; the requirement for standardised protocols for sample preparation, data acquisition and data processing. Considerations in sample preparation depend on the type of sample (fixed cells or tissue, live cells or biofluids) and include considerations such as sample thickness and substrate. As mentioned, water contribution in IR spectra limits use for analysis of aqueous samples such as live cells.

However, developments have been made using microfluidics and spectral data processing methods for water removal, which allow live cells to be analysed. FTIR can be performed in transmission, transflection and attenuated total reflection (ATR) modes, all of which have advantages and drawbacks. Light source is another important consideration in FTIR spectroscopy as, in order to obtain greater lateral and spatial resolution in microspectroscopy, synchrotron radiation was required due to diffraction limitations using a globar source.[56] Recent advances have helped overcome resolution with globar sources[57] and for particular applications, new techniques such as the use of quantum-cascade lasers (QCL) have been applied. The final challenge for FTIR spectroscopy for biological analysis is spectral processing. Spectra from biological samples are complex and require both preprocessing of spectra and often chemometric techniques for extracting discriminatory information. This includes multivariate analysis techniques such as principle component analysis (PCA), partial least-squares (PLS) and cluster analysis[58]. High reliance on spectral processing can be a drawback, due to computational demands, standardisation of processing techniques and over processing of data during the analysis process.

FTIR has, however, been widely applied successfully to biological samples yielding significant results for disease detection. It has been investigated widely as a replacement for standard histopathologic techniques that are time consuming and rely on the subjective opinion of a pathologist, and has successfully discriminated cell types and pathology in tissue sections.[58,59] FTIR spectroscopy has also been successfully applied for cyto-pathological detection in single cells.[60] The effects of drugs on single cells have also been successfully investigated.[61] Recent advances have addressed the use of FTIR for blood serum analysis with potential for rapid and easy disease diagnosis, as serum samples can be quickly and easily obtained from patients.[62,63] A particularly exciting study has demonstrated the use of FTIR spectroscopy for detection of malaria in blood samples using minimal sample preparation and allowing quick and easy detection with portable devices and no need for scientist input. Clinical trials are now being carried out in Thailand using this technique.[64,65]

Raman spectroscopy has also been used extensively in similar applications to IR spectroscopy. The major advantage of Raman over IR spectroscopy is that minimal sample preparation is required and, due to the reduced water signals, it can be easily applied

directly to tissue and live cells in an aqueous environment.[66,67] There has been exciting development in clinical applications of Raman spectroscopy in both excised and *in vivo* tissue samples in addition to tissue sections and single cells.[68] Studies have demonstrated the application of endoscopic Raman methods to allow direct tissue measurements for objective disease diagnosis.[69] A particularly exciting recent development, in which Raman spectroscopy was used in real time for assessment of tumour margins for determining tissue to be excised in a brain tumour operation was featured on the BBC news.[70] While these direct Raman measurements do not have the same need for sample preparation as with IR spectroscopy, there remains a need for similar reliance on data processing for determination of discriminatory signatures. Raman spectroscopy has also been applied for histopathological analysis of tissue sections in a similar manner to IR spectroscopy. In this case, the same considerations have to be made with regards to sample preparation, acquisition and processing including consideration of sample substrate and wavelength of laser.[71] Substrates such as calcium fluoride that minimise background are desirable. However, cost must be taken into consideration when clinical translation is the ultimate goal. Raman spectroscopy has been successfully applied for histopathology and cytology with studies showing ability to discriminate malignancies in lymph nodes[72] and for cervical cancer screening and diagnosis[73]. Raman spectroscopy has also been applied for monitoring drug interactions in single cells.[74]

The primary disadvantage of Raman spectroscopy for clinical translation is that Raman scattering is a weak effect. Signals of interest can be enhanced using the SERS techniques, which has been applied *in vivo*, *ex vivo* and *in vitro* for detection and treatment of disease; and characterisation of biological samples with minimal reliance on multivariate data analysis techniques by simplifying spectra acquired through enhancement of particular signals of interest producing sharp discriminatory bands.[75,76] Compared to Raman spectroscopy, SERS also provides the potential for multiplexed analysis of biological material, potentially detecting multiple disease markers simultaneously, as SERS provides sharp signals potentially allowing targeted detection of multiple specific disease markers. The much stronger SERS signals also mean shorter acquisition times and lower laser power can be employed, minimising damage to cells and tissue. Generally, NPs are targeted to specific molecules or disease markers for detection *in vitro*, *ex vivo* and *in vivo*. Unfunctionalised NPs have also been exploited for detection of intracellular enzyme

activity.[77] Examples of SERS for *in vitro* analysis of biological material include glucose sensing[78], important for diabetes, and multiplexed detection of multiple phenotypic markers in breast cancer cells by NPs with antibody markers for each phenotype.[79] Applications of SERS *in vivo* have also included multiplexed detection for imaging in living mice.[80] SERS has already demonstrated a huge potential for disease detection. It has many advantages over spontaneous Raman. However, one disadvantage is that it is invasive, in that it requires delivery of NPs to cells. However, many studies have shown that NPs, particularly gold NPs, are biologically inert with low toxicity and they are already employed in biological applications such as dental prosthetics.[50]

The latest developments in Raman spectroscopy for biomedical application delve into more specifically developed technologies such as non linear techniques, coherent anti-Stokes Raman spectroscopy (CARS) and stimulated Raman spectroscopy (SRS), spatially offset Raman spectroscopy (SORS), transmission Raman spectroscopy (TRS), tip enhanced Raman spectroscopy (TERS), surface enhanced resonance Raman spectroscopy (SERRS) and surface enhanced spatially offset Raman spectroscopy (SESORS).[66,75,81] These technologies provide various platforms for overcoming previous pitfalls for Raman spectroscopy in the characterisation of biological material.

1.3.3 Using SERS to Measure Intracellular Redox Potential

NPs and, in particular, metal NPs have been used extensively for a variety of biological applications in addition to SERS. This includes the use of NPs to deliver, for example, drugs, DNA and RNA into cells; using NPs for imaging purposes in biological systems[82–84] including NPs fluorescently labeled for imaging purposes[85]; and even the use of NPs in cancer therapy, whereby they convert absorbed NIR light into heat for destruction of tumours[86–89].[90,91]

Gold NPs are used in this project; they enhance signals from signaling molecules and as such are used as detectors in biological environments. Gold is a particularly good metal to use in biology as it is inert and non-toxic to biological systems.[92] In particular, gold NPs of approximately 150 nm diameter with a 125 nm silica core are used in the majority of this work. Changing the diameter of the NPs and the core to shell ratio can alter the plasmon resonance, the wavelength at which the particles are resonant. For example, an increasing

core:shell ratio redshifts the plasmon resonance, moving it to an increased wavelength.[50] A NIR resonance is ideal for the application of these NPs as it falls within the wavelength of radiation used for Raman spectroscopy, and NIR is lower energy than visible radiation and therefore damage to cells is minimised upon laser illumination. The 150 nm diameter NPs used have a plasmon resonance between 780 nm and 820 nm, which is ideal for performing SERS in cells.

The NPs are functionalised with redox active molecules. These molecules have been developed to cover the redox potential values estimated to be found in intracellular environments. The molecules exist as redox couples, whereby the number of molecules reduced or oxidised changes in response to the environment to report on intracellular redox potential in a ratiometric manner. Ratiometric biological nanosensors have been widely employed for accurate and quantitative analysis of cellular characteristics such as pH, Ca^{+} ion concentration, oxygen, reactive oxygen and nitrogen species, redox potential and antioxidants.[93] The two redox active molecules used in this project are 1,8-diaza-4,5-dithian-1,8-di(2-chloro-[1,4]-naphthoquinone-3-yl)octane (NQ)[94,95] (Figure 1.22(a)) and N-[2-({2-[(9,10-dioxo-9,10-dihydroanthracen-2-yl)formamido]ethyl}disulfanyl)ethyl]-9,10-dioxo-9,10-dihydroanthracene-2-carboxamide (AQ)[96,97] (Figure 1.22(b)). Density functional theory (DFT) calculations and spectroelectrochemistry have previously been carried out on both of these molecules.[94–97] By analysing spectra of the molecules under different redox potential values and comparing these to DFT calculations, particular peaks were observed to change in response to redox potential. In the case of NQ, this was the peak at approximately 1645 cm^{-1}, corresponding to C=O stretching the oxidised species, and at approximately 1577 cm^{-1}, corresponding to symmetric ring breathing observed in both species. In the case of AQ, this was the peaks at approximately 1669 cm^{-1}, corresponding to quinone C=O stretching in the oxidised species, and at approximately 1606 cm^{-1}, corresponding to amide stretching with symmetric ring breathing observed in both species. Recently, in our group, a library of modified quinone redox probes have been developed[98] to cover a wide redox scale.[92,94,96,97]

Therefore, by recording spectra of NQ-NPs and AQ-NPs in cells and taking the ratio of the signals indicated, the redox potential of the environment can be determined from these calibration experiments using normalisation equations and the Nernst equation. Figure 1.23 illustrates the basic setup for intracellular redox potential measurement using SERS.[94,97]

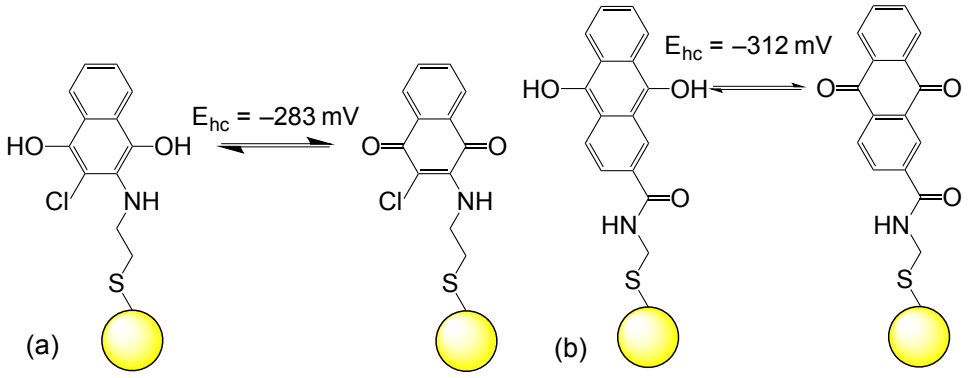

Figure 1.22 (a) shows the structure of reduced and oxidised redox active quinone molecule NQ attached to a NP (yellow sphere) and the half cell potential of the process and (b) illustrates the same information for anthraquinone AQ.

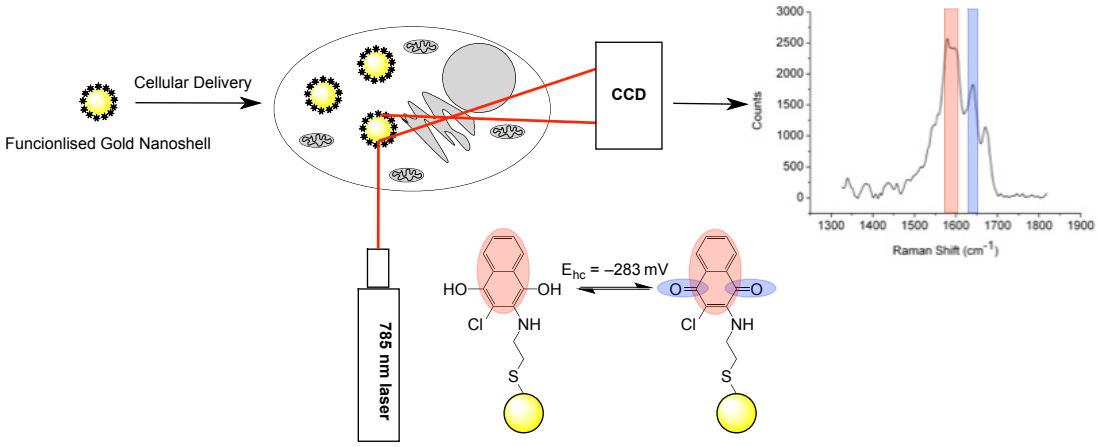

Figure 1.23 illustrates the procedure to carry out surface enhanced Raman scattering (SERS) in cells using SERS nanosensors to determine intracellular redox potential. Functionalised nanoparticles (NPs) (in this example a nanoshell (yellow) functionalised with redox sensitive quinone NQ (black stars)) are delivered into cells before recording SER spectra from the cells. Intracellular redox potential is calculated from the resultant SER spectra with the help of calibration data, by taking the ratio of a redox sensitive (blue) and non-redox sensitive (red) peaks. An example of a NQ-NP spectrum is shown where blue shading corresponds to the C=O stretch vibration and red shading corresponds to the ring breathing vibration (adapted from Auchinvole *et al.*[95]).

1.4 Multicellular Tumour Spheroids (MTS) – from 2D to 3D – A New Challenge for SERS Nanosensors

Conventional two dimensional (2D) monolayer cell culture could be considered the 'gold standard' technique for *in vitro* cellular experiments. However, the need for a model that better mimics the three dimensional (3D) architecture of tissue *in vivo* has led to the development of multicellular tumour spheroids (MTS) as a 3D tissue culture model. MTS mimic the environment of *in vivo* tumours in which, for example, oxygen and nutrient gradients develop, protein expression changes and cells form a spherical structure with regions of proliferation, senescence and necrosis. MTS are becoming increasingly common as a tool for investigating tumour physiology and drug development, as a model that better mimics tissue *in vivo*. However, analysis of these 3D models is more complicated, with the addition of important spatial information to be resolved and increased z penetration required when imaging. Chemical analysis and imaging techniques are constantly being improved for measurement of, for example, oxygen concentration, hypoxia, pH, nutrient concentration, proteins and drug delivery as will be discussed extensively in section 1.4.3.[99] There is room for vast improvement in techniques for measuring these characteristics quantitatively in MTS and the SERS nanosensors introduced in section 1.3.3 have great potential for use in this area. The importance of MTS in cell culture experiments along with currently established methods for chemical analysis of these structures will be discussed, to illustrate the scope for new techniques to be developed for analysis.

1.4.1 From Monolayer to MTS – A More Realistic Model

In traditional monolayer culture, cells are grown on a flat surface in a Petri dish or flask where their primary physical contacts are with the substrate on which they are growing and the culture medium surrounding them, with very little cell-cell interaction.[100] *In vivo*, cells are in a 3D environment in which the major physical contact is cell-cell interactions with surrounding cells, and cell-matrix interactions with the extracellular matrix (ECM). This 3D environment introduces complexity that is not observed in traditional monolayer cell culture. As a result, drugs and disease therapies that prove effective in the monolayer cell culture models often fail to carry this efficacy forward into *in vivo* trials.[101] While tissue explants grown in culture provide a step between monolayer cell culture and the *in vivo* environment, access to such samples is limited. There is therefore a need for an *in vitro*

model of tumour biology that mimics better the 3D environment that exists *in vivo* without the added ethics, health, safety, cost, availability and EU or US legislation limitations encountered when using animal models or explanted tissue.

MTS have become increasingly used for the study of cell function and testing of drugs, as they satisfy the requirement for a more complex and physiologically relevant cell culture model.[102–105] In particular, MTS are used for the study of cancer, as an *ex vivo* model of cancer tumours. Importantly, the blood supply to a tumour *in vivo* is poor, due to rapidly proliferating cells producing cellular masses in which the central regions may be far from the well organised vasculature of the body. Cancer cells are capable of signaling for the formation of new blood vessels, via proteins such as vascular endothelial growth factor (VEGF)[20]. However, the resulting vasculature is disorganised and leaky so does not effectively deliver oxygen and nutrients to the tumour. As a result, concentration gradients develop in factors such as oxygen, nutrients and pH (Figure 1.24).[16] The concentration gradients developed in tumours *in vivo* are mimicked by MTS where a radial structure develops with a necrotic core, surrounding quiescent cells and an outer proliferating layer (Figure 1.24).[106]

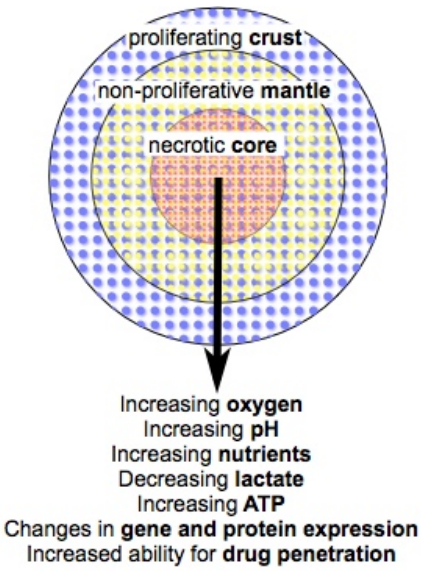

Figure 1.24 summarises multicellular tumour spheroid (MTS) organisation and radial changes that are established. As MTS grow they can develop a non-proliferative mantle and eventually a necrotic core (adapted from Lin, R. *et al*.[107]).

The microenvironments[20] that develop in cancer tumours give rise to local heterogeneity in aspects including gene expression and regulation; cell differentiation, proliferation, viability and death; drug metabolism; and response to stimuli (Figure 1.24).[108] This combination of factors leads to increased complexity when considering drug and therapy treatments *in vivo* compared to simple monolayer cell culture assays. For example, increased resistance to cytotoxic drugs and ionising radiation is found in tumours *in vivo* as a consequence of the microenvironment that develops.[16,109] This makes the use of MTS in drug and therapy development increasingly important as they mimic better the *in vivo* environment of tumours in comparison to traditional monolayer culture models.

1.4.2 Methods for Growing MTS

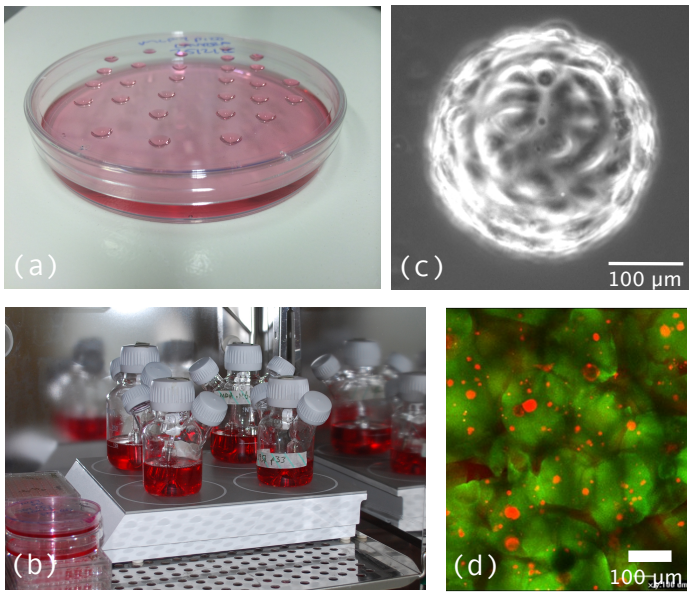

Figure 1.25 Examples of methods of multicellular tumour spheroid (MTS) formation: (a) MTS being grown using the basic hanging drop technique, by pipetting drops of cell suspension onto the lid of a Petri dish where MTS grow; (b) MTS growing in spinner flasks, by transferring cell suspension into a flask where liquid is constantly spun during growth; (c) MTS growing on a microcarrier bead, a solid bead that can be made from e.g. dextran or cellulose; and (d) cells (red, CellTracker™) growing in a 3D scaffold of alginate gel (green), an example of the start of MTS growth in a scaffold of NovaMatrix-3D™ (images courtesy of Peter Mullen (University of St Andrews) (b), and Dr S Langdon (University of Edinburgh) (d)).

A variety of techniques have been developed for the formation of MTS. The basic requirement for MTS formation is that adhesions between cells is stronger than that between cells and the substrate they are grown on.[107] The first examples of multicellular spheroid growth were performed by Holtfreter[110] who was studying gastrulation, and Moscona and Moscona[111] who demonstrated the aggregation of isolated chick chondrogenic and myogenic cells.[5] These initial studies formed non-tumour multicellular spheroids with the advantage that they better mimic the *in vivo* 3D environment. While this project focuses on MTS as an *in vitro* cancer tumour model, the techniques discussed are equally applicable to non-tumour spheroids.

Depending on the culture technique and cell type employed, spheroids are formed in varying quantities, over various time periods and with varying degrees of homogeneity and the particular technique used is likely to be guided by the particular application being employed. For example, using spinner flasks allows large quantities of MTS to be formed, but these often lack homogeneity, while using the hanging drop technique allows much more homogenous and uniform MTS formation, but is difficult to perform on a large scale.[100,107] Figure 1.25 illustrates some of the techniques employed for MTS formation. In this work the particular technique used was the hanging drop technique as it required no specialist equipment or setup (only Petri dishes), and therefore was cheap and easy to carry out. It allowed production of MTS of uniform size and shape, and while it makes large scale production of MTS difficult, this was not required for this work.

1.4.2.1 Spontaneous Aggregation

The simplest method for the formation of MTS is spontaneous aggregation, whereby the cells spontaneously cluster to form cell aggregates that grow in 3D. Technically, these are cell aggregates rather than MTS and only a few cell lines grow in this way – MDA-MB-435 human breast cancer cells being one example.[100] Due to these limitations, a variety of other more complex methods have been developed.

1.4.2.2 Hanging Drop

In its simplest form, the hanging drop method involves growing MTS from drops of cell suspension in culture media suspended from the lid of a Petri dish (Figure 1.25(a)). Cells

aggregate in the drops, which remain in place by surface tension and then grow into MTS.[107] More recent technologies have developed multiwell plates for the growth of MTS using the hanging drop method including the Perfecta3D™ Hanging Drop Plates[112], whereby the new design allows for easier treatment, media exchange and handling of the MTS. Growing MTS using this method allows for the formation of MTS of uniform size, although it is difficult to culture large numbers of MTS in this way.[102]

1.4.2.3 Gyratory Methods and Spinner Flasks

A popular method for formation of large numbers of MTS is the spinner flask method (Figure 1.25(b)). This involves putting a suspension of cells in media into a flask that is constantly kept stirring. Due to the constant motion, cells are not given the chance to adhere to surfaces in the flask and therefore aggregate together and grow to form MTS. Similarly gyratory methods involve placing the cell suspension in flasks that are put into incubators where they are rotated by gyratory motions. Both of these techniques allow for larger quantities of MTS to be formed however the drawback is that the MTS formed are heterogeneous in size and shape and the constant rotary motion could mechanically alter the MTS.[100,107]

1.4.2.4 Non Adhesive Plates/Liquid Overlay

Another popular method for MTS formation involves growing cells in plates with substrates that limit cell adhesion. This relies on the cell-cell adhesion being stronger than the cell-substrate adhesion, encouraging cells to aggregate and form MTS rather than adhere to the substrate on the plate. Using substrates such as agarose[113], polyethylene glycol (PEG) and polydimethylsiloxane (PDMS) to coat the bottom of plates allows for this type of MTS formation.[99]

1.4.2.5 Microcarrier Beads

Microcarrier beads are 100-400 μM diameter[100], solid beads on which cells are grown in 3D (Figure 1.25(c)). They can be produced from various materials including dextran and cellulose. Microcarrier beads are available at a low cost commercially and tend to allow spheroid formation from primary cells and transformed cell lines as well as cell types that are normally difficult to grow such as endothelial cells. As the beads form the central regions

of these cultures there is less likelihood that a necrotic core will develop and therefore these models are more representative of healthy cells growing *in vivo* as opposed to cancer tumour cell lines.[114]

1.4.2.6 Scaffolds

Scaffolds are extracellular matrix (ECM) mimics that can either be synthetic e.g. polyglycolic acid or naturally derived e.g. type I collagen and Matrigel® (Figure 1.25(d)). They are 3D matrices, which allow cells to attach, proliferate and differentiate and guide cells to produce 3D MTS structures.[2] 3D Biotek have developed culture kits based on the biodegradable scaffold poly(ɣ-caprolactone) (PCL).[115]

1.4.2.7 Microwells and Microfluidics

A relatively recent advancement in the growth of uniform MTS on a large scale is the use of microwells and microfluidics, enabled by the development of microprinting techniques including photolithography and soft lithography.[107] Arrays of wells are printed into materials such as polyethylene glycol (PEG), polydimethylsiloxane (PDMS) and agarose, which are nonadherent to cells.[116] Thousands of wells can be printed in a single substrate with a defined diameter. When a cell suspension is added to such a printed substrate in a plate, cells settle into the wells such that each well contains an equal number of cells that then form MTS homogenous in size and shape. Size and geometry of MTS formed can be controlled by well shape and size. Recently, many systems have been developed on microfluidic chips patterned with microwells and microchannels, such that MTS can be formed in arrays and, for example, drugs can be delivered to these systems.[99,101]

1.4.3 Current Techniques for Chemical Analysis of MTS

MTS have been established as an important tool for investigating tumour characteristics and response to drugs and therapy. Techniques for chemical analysis of MTS have required advances in instrument technology to provide the desired spatial resolution and depth penetration required as well as development of assays to monitor variation in oxygen, hypoxia, pH, nutrients and protein expression. The following section discusses current techniques developed to allow such chemical analysis of MTS.

1.4.3.1 Advances in Instrument Technology to Analyse MTS

In the simplest form, standard histological methods are used to visualise MTS, but this involves fixing and sectioning the samples, which introduces artefacts and does not allow the observation of dynamic processes. Conventional histological dyes also have low spatial resolution.[108] New instrumentation has allowed MTS to be analysed *in situ*.

Confocal microscopy can be used to view MTS with z resolution, but penetration depths are limited and may not allow full z penetration through MTS. Efforts have been made to improve resolution and penetration depth of confocal microscopy to achieve the best images, including the use of borosilicate glass bottoms on dishes as opposed to polystyrene, a water immersion microscope objective instead of a dry objective and increased laser power/light output at deeper image depths.[117] While better resolution and increased z penetration was observed, the z penetration was still limited to 350 μM with this technique, meaning it was unable to visualise the entire depth of a MTS.

Two and multi photon microscopy have been used for imaging 3D samples as they can give an increase in penetration depth in comparison to one photon confocal microscopy, as it uses NIR radiation that can penetrate deeper into tissue than shorter wavelength visible radiation, that gets absorbed more readily.[118] Samples are probed with laser pulses of longer wavelengths but high intensities to stimulate multi photon excitation.[119] High intensities are required to increase the chance of non-linear multi photon excitations and the laser is generally operated by using long wavelength femto-second pulses of high intensity to decrease phototoxicity and photobleaching.[120] Increased z penetration and contrast are achieved and excitation in the surrounding sample is reduced, as multiple photons absorbed simultaneously are required to cause the excitation, likely only at the point of interest where there is high enough intensity to allow this. Therefore photobleaching and phototoxcity are minimised in the surrounding sample.[118–121]

Recent advances in microscopy to view MTS involve the use of optical coherence tomography (OCT) (Figure 1.26(b)), optical projection tomography (OPT) (Figure 1.26(c)) and light sheet microscopy (LSM) (Figure 1.26(d)) to map MTS. In OCT, back scattered or back reflected light is detected to provide cross sectional images through a 3D sample.[122] In

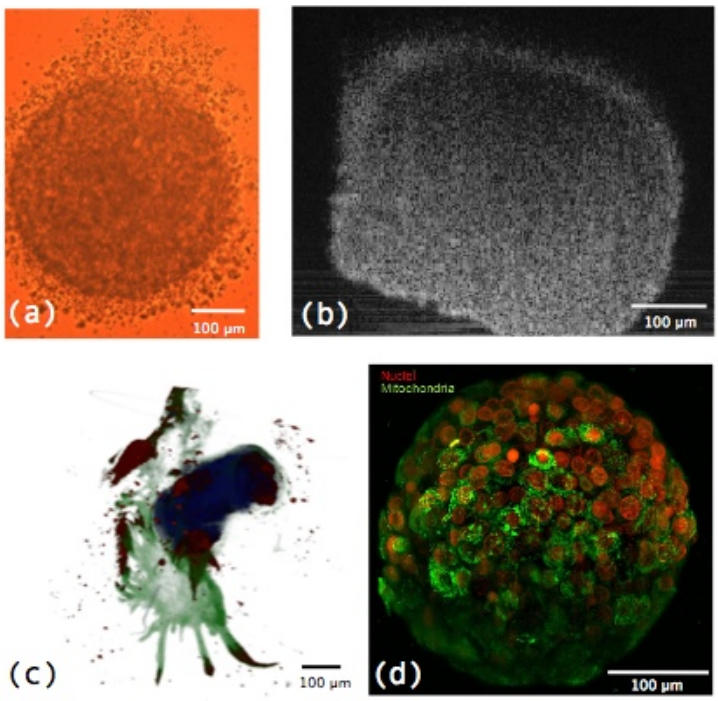

Figure 1.26 (a) MTS imaged using a light microscope; (b) a cross section through the centre of an MTS using OCT; (c) an OPT image of an MTS derived from a primary cancer specimen where blue core = implanted MTS, green = outgrowth into culture in collagen and red = positive immunoreactivity for Her2; and (d) LSM image of a MTS[108] (images courtesy of Dr Pierre Bagnaninchi (Univeristy of Edinburgh) (b), Prof. David Harrison (University of St Andrews) (c) and reproduced with permission from Dr Nariman Ansari (Goethe University Frankfurt) (d)).

OPT, the sample is rotated and straight line projections are taken through it to generate 3D images.[123,124] The advantage of OCT and OPT are that much larger sample volumes can be imaged, but resolution is much lower than that which can be obtained from sectioned samples viewed through standard high resolution microscopes or by using confocal microscopy.[125]

A more recent and very useful microscopy advancement for the analysis of MTS is light sheet microscopy (LSM) or single plane illumination microscopy (SPIM). This involves using a light sheet, a plane of light, to illuminate a sample as opposed to a single point. As well as providing an image of a whole specimen slice at once and therefore reducing acquisition time, this technique reduces the light exposure of areas of the sample and therefore reduces photobleaching and phototoxicity.[108] It is an ideal technique for analysis of MTS, as it allows

whole sections through MTS to be observed at once and z stacks to be built into a 3D image with better z resolution than confocal microscopy (Figure 1.26(d)). A disadvantage of this technique is the general need to embed samples in a transparent gel material, usually agarose or low melting point agarose. Embedding in such materials can impact growth, placing mechanical restraints on specimens and making growth time course experiments inaccurate. Recently, Desmaison *et al.*[126] developed a sample holder allowing MTS to be mounted in hydrogel and a time course experiment of MTS growth to be performed.

Further advances have recently been made to LSM including the use of self-reconstructing Bessel beams and two-photon fluorescence excitation, which produced an increase of nearly two fold in axial resolution and 5-10 fold increase in contrast, in comparison to linear Bessel beam excitation, and 3-5 fold increase in z penetration depth in comparison to Gaussian beam linear excitation.[127,128] Very recently, LSM has been performed using an Airy beam to provide further advances, in particular allowing a larger field of view with high contrast and high resolution.[129]

It is worth mentioning some additional microscopy techniques that can reveal morphological characteristics of MTS compared to monolayer culture. Transmission electron microscopy (TEM) has been used to visualise cell-cell[130] and cell-ECM[131] interactions in MTS, while scanning electron microscopy (SEM) reveals high magnification and high resolution information about the surface characteristics of MTS, including visualisation of cell-cell interactions and the morphology of cells[132–134]. Both techniques require cells to be fixed and processed and SEM only reveals surface topology, with samples often coated in gold removing a lot of surface detail. Helium ion microscopy (HIM) removes the need for coating and provides increased resolution compared to SEM.[135] Table 1.1 summarises the microscopy techniques used when analysing MTS along with their advantages and limitations.

Table 1.1 summarises microscopy techniques used to visualise MTS along with advantages and limitations of each technique.

Microscopy technique	Advantages	Limitations
Standard	Simple	No z depth Primarily fixed and sectioned samples
Confocal	z depth possible	Limited to a maximum of 350 μM z depth
Two and multi-photon	Increased z depth and contrast Photobleaching and phototoxicity to surrounding sample minimised	z depth still limited
OCT	Can image whole MTS	Resolution is poorer
OPT	Can image whole MTS	Resolution is poorer
LSM	Can image whole MTS Acquisition time reduced Photobleaching and phototoxcity reduced	Samples typically embedded in a transparent gel which can impact growth
TEM	High resolution to visualise cell-cell and cell-ECM interactions	Limited field of view Involves fixing and processing samples
SEM	High resolution and high magnification of surface characteristics	Involves fixing samples Only reveals surface information Samples often gold coated which removes surface detail
HIM	Increased resolution compared to SEM for revealing surface characteristics No requirement for coating	Involves fixing samples Only reveals surface information

1.4.3.2 Measuring Oxygen Concentration and Hypoxia

A significant characteristic of MTS in comparison to monolayer cultures, which is particularly relevant to this project, is the variation in oxygen concentration, mimicking *in vivo* tumours. As tumours and MTS grow, the central regions become increasingly depleted in oxygen (and hypoxic) and eventually cells may die, creating a necrotic core.[136] Hypoxia in tumours is incredibly significant, as it can induce pro-survival signalling, leading to metabolic changes and resistance to therapy.[16,20,137,138]

It is desirable to chemically analyse variations in oxygen concentration and hypoxia through MTS. Oxygen concentration and hypoxia are highly interlinked, but not identical characteristics. Oxygen concentration is singularly a measurement of the level of oxygen present, while hypoxia is a more complex characteristic that can be defined in several ways, including nitroreductase activity[139], HIF activation[21] and expression of HIF associated genes[140], to name a few. This distinction is important, since a hypoxic phenotype (HIF stabilisation, glycolytic metabolism) is a characteristic of many cancers irrespective of oxygen concentration (Warburg Effect).[24] When considering chemical analysis of MTS, some techniques have been developed specifically to measure hypoxia as a function of, for example, nitroreductase activity, while other techniques directly measure oxygen concentration. Intracellular redox potential is another characteristic highly interlinked with oxygen concentration and hypoxia.

One of the first methods developed for measuring hypoxia uses small molecules such as 2-nitroimadazole that are metabolised under hypoxic conditions and subsequently detected.[141] An example is the commercially available Hypoxyprobe-1™ (PimonidazoleHCl)[142] (Figure 1.27(a)), in which the metabolised product in hypoxic regions is detected by an antibody and subsequently visualised by either a fluorescent tag[143] or colorimetric detection (Figure 1.27(b) and (c)).

This technique is limited to distinguishing cells below and above a hypoxic limit without giving truly quantitative information. Autoradiography was used in initial detection methods for these probes and extension to magnetic resonance spectroscopy (MRS) and positron emission tomography (PET) allowed non-invasive detection of hypoxia in living

systems.[144–150] Hypoxyprobe-1™ has been used to visualise distributions of hypoxia in MTS, giving good spatial resolution, but its use is limited to fixed sections.[136,151]

Direct measurement of oxygen concentration can be achieved using oxygen microelectrodes. These have been miniaturised to give increased spatial resolution of oxygen measurements both *in vivo* and *ex vivo*. The main disadvantage is that this is an invasive technique with the risk that the oxygen electrodes perturb their immediate environment and thus distort values obtained.[139,152]

Recent advances have been made to develop increasingly efficient O_2 sensing probes such as new cell-penetrating phosphorescent probes, based on conjugates of Pt(II)-tetrakis(pentafluorophenyl)porphine (PtPFPP) dyes.[153] The Pt probe was conjugated with glucose, which minimised aggregation and self-quenching for measurements in aqueous media and was used to perform high resolution phosphorescence lifetime based imaging (PLIM) of O_2 in PC12 MTS. Nanoprobes have also been used *in vivo* to measure reactive oxygen species (ROS) concentrations and hypoxia and these techniques could potentially be applied to MTS models and, with the use of more advanced instrument technologies, allow live 3D imaging through the MTS.[154]

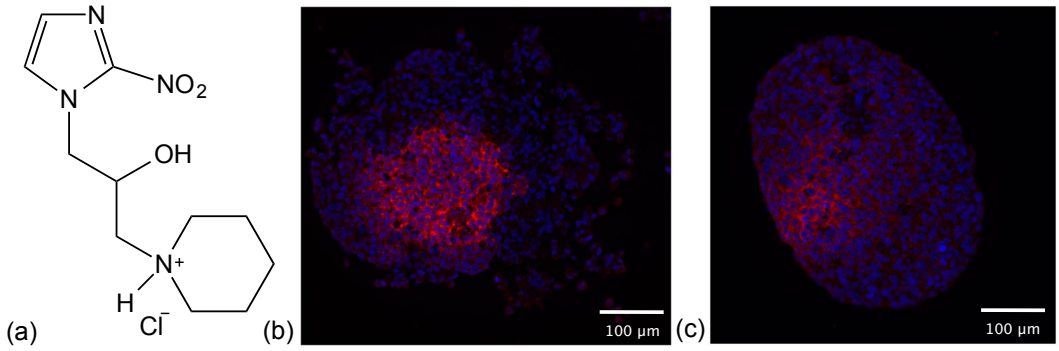

Figure 1.27 shows the structure of Hyproxyprobe™ (a), a commercially available hypoxia probe, consisting of a 2-nitroimidazole based molecule that is metabolised under hypoxic conditions and subsequently detected. Two fluorescent images of MTS stained with Hypoxyprobe-1™ (pink) where cell nuclei are stained with DAPI (blue) are shown in (b) and (c) (images courtesy of Peter Mullen).

1.4.3.3 pH and Nutrient Concentration

Lactate accumulation is common in areas of low oxygen due to increased glycolysis, utilisation of the pentose phosphate pathway (PPP) and decreased oxidative phosphorylation.[23] Therefore, decreasing oxygen concentration and hypoxia tends to correlate with an increase in lactate accumulation and decreasing pH. Gradients in nutrient concentration including glucose and ATP that are intimately linked to changes in metabolic pathways can also correlate with pH and oxygen gradients.

Methods for measuring pH and nutrient concentrations in MTS are limited and primarily based on monolayer techniques. Significantly, studies of pH in tumour cells have revealed that intracellular and extracellular pH differ significantly, intracellular pH becoming neutral to alkaline and extracellular pH acidic.[16,25] This intra- and extracellular trend is attributed to ion pumps exporting protons from inside to outside cells that can become activated by certain growth factors that promote tumour angiogenesis, often associated with requirement for increased blood supply in areas of lower oxygen. This gradient of lower extracellular to intracellular pH is the opposite of that observed under normal tissue conditions. Detection of differences between intra- and extracellular environment would require sufficient subcellular resolution to allow these environments to be distinguished accurately, without the risk of averaging intra- and extracellular environments.

Most methods to detect pH in culture employ fluorescence and can also be used in MTS, for example the intracellular monitoring dye BCECF.[155] One of the commonly used techniques to monitor nutrient and pH variations in MTS is bioluminescence imaging. Walenta *et al*.[156] used the technique of bioluminescence of cryosectioned non-proliferating Rat 1 aggregates and MR1 MTS to determine variations in ATP, glucose and lactate. While bioluminescence imaging reveals detailed information about nutrient gradients in MTS with high spatial resolution, the resolution was not sufficient to distinguish intra- and extra-cellular compartments. The actual resolution achieved in this study was approximately 40 μM to 20 μM dependent on magnification used, therefore the signal from intra- and extracellular spaces were averaged and not distinguished.

The more recent use of nanoprobes for pH imaging *in vivo* also has potential in live MTS. This technique is based on pH sensitive fluorescent probes conjugated to nanoprobes that

can also be antibody-targeted to specific cells. Live cell imaging is possible but there is the drawback of limited range of pH detection.[154] SERS has been used to measure intracellular pH using gold NPs functionalised with pH active molecules in monolayer culture.[157–161] This technique could be extended to MTS and has the potential for multiplexing to allow numerous characteristics, such as pH and redox, to be measured simultaneously.[162] This is the major topic of this project.

^{1}H magnetic resonance chemical shift imaging of MTS incubated with imidazole was used to provide information on pH variations in MTS with 32 × 32 μm resolution. While this resolution is not enough to distinguish intra- and extracellular pH variations it revealed a 0.6 pH unit difference between central and peripheral regions of the MTS.[163]

Spectroscopic imaging techniques have been used to map changes in chemical, elemental and nutrient concentrations in MTS. DLD-1 MTS have been analysed by scanning transmission ion microscopy (STIM), proton-induced X-ray emission (PIXE) mapping, scanning X-ray fluorescence microscopy (SXFM) and FTIR spectroscopy. STIM revealed useful information regarding cell density where lower density was observed in central regions relating to the necrotic core. PIXE revealed elemental maps giving information on elemental density of P, S, Cl, K and Fe. Cu and Zn distribution were mapped using SXFM while FTIR spectroscopy revealed detailed information regarding the distribution of different biomolecules such as proteins, lipids and DNA as well as lactate.[164]

1.4.3.4 Proteins

Primarily as a result of the gradients of, for example, oxygen that develop in MTS, protein expression is often altered. Standard techniques for measuring protein expression such as Western blotting can be difficult to perform with MTS samples, due to the requirement for large numbers of cells, although this problem has been addressed to some extent by techniques such as in-cell Westerns.[101] To overcome this problem, multiple MTS for the same conditions can be used. An example study using Western blotting shows that the multidrug resistance (MDR1) gene is hypoxia responsive and regulated by hypoxia inducible factor-1 (HIF-1).[165] Both immunohistochemistry and immunofluorescence can be used to detect and quantify protein expression using specific antibodies. For example, proteins involved in cell-cell and cell-ECM interactions and components of ECM such as cadherins, integrins and

collagens respectively can be immunochemically stained. It is also possible to perform quantitative immunofluorescence, for example using automated quantitative analysis (AQUA), which allows quantitation of a target signal e.g. Her2 in Figure 1.28 in cells stained for cytokeratin (tumour cells).[166] While spatial information can be acquired using these techniques, there is the need to fix samples. A similar technique that is also often used and based on fluorescence is flow cytometry of trypsinised samples. While this is simple and can provide quantitative data, it removes the majority of spatial information.[167,168]

Bioluminescence has also been used to detect protein expression, protein-protein interactions and enzyme activity by employing different versions of the luciferase bioluminescence assay.[169,170] This is a promising technique, as it has the potential to provide spatial information by live imaging of intact MTS. In comparison to fluorescence, bioluminescence has the advantage of a lower background and therefore better sensitivity, a larger range over which quantitative signal can be obtained and less perturbation by coloured compounds.[101]

Nanoprobes can be used for the detection of particular enzymes to analyse their expression. For example, a nanoprobe was developed to detect the activity of caspase-3, an enzyme involved in apoptosis, whereby nanoparticles were conjugated with a caspase-3 substrate and scattering colour varied as individual nanoparticles were released by the enzyme, acting to digest the substrate.[154] This technique was used *in vivo*, but has the potential for spatial analysis of differences in enzyme expression in MTS.

A novel demonstration of spatially resolved protein expression information was performed by McMahon,[171] whereby MTS layers were progressively trypsinised to isolate the outer proliferating layer, middle peri-necrotic layer and necrotic core. Mass spectrometry using isobaric tags, for relative and absolute quantification (iTRAQ), approach with matrix assisted laser desoption/ionisation time of flight time of flight (MALDI-TOF-TOF) and electrospray ionisation quadrupole TOF (ESI-Q-TOF) was used to analyse the protein content of each layer and compare and contrast. This new approach was also complemented with traditional techniques including immunohistological staining using GLUT-1 and CAIX antibodies. While this technique does not provide highly resolved spatial information, it is the first technique to demonstrate spatial changes in protein expression through MTS.

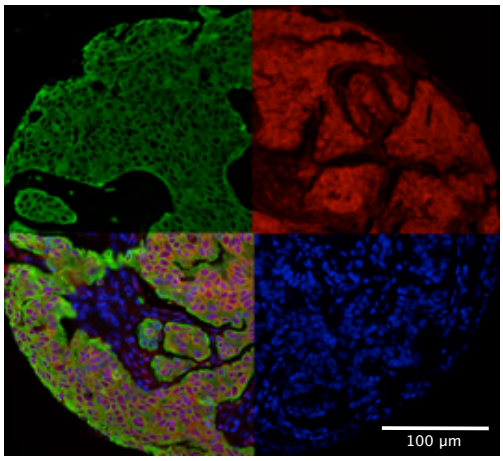

Figure 1.28 Quantitative immunofluorescence using AQUA to quantify target signal (Her2, red, top right) in cells marked for cytokeratin (i.e. tumour cells, green, top left) in MTS. Nuclei are stained with DAPI (blue, bottom right). All fluorescent signals are combined in the bottom left image (image courtesy of Prof David Harrison).

Another recent and promising technique based on mass spectrometry that derives spatial information on proteins in MTS is mass spectrometry imaging (MSI). Matrix assisted laser desorption/ionisation (MALDI) has been used to analyse frozen or fixed tissue sections for spatial imaging of protein and peptides as well as other species such as lipids and small molecules.[172] Typically, frozen tissue sections are analysed[173]. However, this technique has also been performed on formalin-fixed, paraffin-embedded tissue sections[174]. To limit analyte spreading during preparation, matrix-free MSI has also been developed.[175] In addition to tissue sections, MALDI imaging has been performed on sectioned MTS embedded in collagen to give information on protein variations through the structure. Proteins were identified using MALDI-TOF-TOF and nanoflow liquid chromatography mass spectrometry (LC-MS)/MS of lysates from MTS and cytochrome C and histone H were both detected as two of the species mapped. This technique is useful as it provides spatially resolved information without the need for specific stains such as those used in immunohistochemistry and immunofluorescence. However, it still requires samples to be fixed or frozen and sectioned and therefore live samples cannot be analysed.

Another emerging and promising technique for chemical analysis of MTS is Raman imaging. This technique is a label free and non-invasive technique for probing differences in chemical composition. Raman imaging probes the vibrational modes of molecules giving information

on the chemical composition of the area being probed in a spatially resolved manner. This technique has been predominantly investigated in monolayer culture but recently it has been shown to be useful for the analysis of 3D MTS culture also.[176] While still in its initial stages of research, this technique is very promising for live and label free chemical imaging of MTS.

The techniques of MSI and confocal Raman imaging (CRI) have been combined to provide enhanced chemical information, combining information on integrity of cells and protein levels using CRI and small molecule location using MSI.[177] In this example, MTS were fixed, processed and sectioned for analysis. While CRI has potential for live cell imaging of whole MTS, MSI is only possible on sectioned samples.

1.4.3.5 Localisation of and Cellular Response to Drugs

The development of the MTS model and techniques to chemically analyse and characterise MTS has provided a more realistic *ex vivo* model of cancer.[104,105] In addition to increasing insight into physiological characteristics of MTS, this provides a platform for more effective testing of drug candidates and therapies.[151] Therefore, screening of drug candidates on MTS gives more reliable results, saving time and money in later stages of drug trials. Recent developments in high throughput screening (HTS) have allowed MTS to be used in place of monolayer culture, allowing drug candidates to be better selected for efficacy.[102,132,178] For example, Tung *et al*.[102] report on the use of a 384 hanging drop array plate to allow easy formation of large numbers of MTS, and allows drug testing. They showed that A431.H9 cells responded with significantly different cytotoxicity in monolayer culture and MTS, grown using their 384 hanging drop array plate, to anticancer drugs. Cells grown as MTS showed significantly more resistance to 5-fluorouracil (5-FU), a cell proliferation inhibitor, compared to monolayer culture. However, the cytotoxin tirapazamine (TPZ), which is triggered by hypoxia, proved to be more cytotoxic in MTS compared to monolayer culture. This response could be explained due to the increased hypoxic regions in MTS compared to monolayer culture, triggering the drug action.

The interesting technique of biodynamic imaging has been used to analyse cellular response to drugs toxic to mitochondria and B-Raf Inhibitors.[179] This is an optical technique that monitors dynamic changes in cells over time and how these changes vary when treated with a particular drug. Biodynamic imaging detects dynamic light scattering using low-coherence

digital holography to elucidate information on intracellular motions. Such motions include dynamic processes in cells including organelle movement and cytoskeletal changes that are often affected by drug treatment. The effect of drugs affecting the mitochondria and Raf kinase inhibitors on two colon cancer cell lines was investigated using this biodynamic imaging technique.[179]

Nanomedicine is a rapidly advancing area of cancer research. It is apparent that, when developing promising nanoparticle based techniques for cancer therapy, imaging technologies capable of successfully visualising the 3D MTS structure are essential. As already discussed, the advances in instrument technology, primarily with OCT, OPT and LSM, allow successful 3D images of MTS to be formed. Fluorescent LSM would be particularly useful for monitoring nanoparticle uptake if nanoparticles could be fluorescently labelled. Studies have investigated the use of techniques such as fluorescence lifetime imaging microscopy (FLIM) to examine the distribution of doxorubicin (DOX) functionalised iron oxide nanoparticles, whereby native DOX released from the nanoparticles had a different fluorescence lifetime to DOX conjugated to the nanoparticles, allowing distinction between released and conjugated DOX to be investigated.[180] In another study, 3D multiphoton fluorescence microscopy was successfully employed to investigate the uptake of quantum dots and DOX encapsulated in micelles.[134]

MALDI imaging has also been used to monitor drug uptake in MTS. Both the drug irinotecan and its metabolites were imaged by MALDI in HCT116 colon cancer MTS at various time points to investigate uptake and metabolism of the drug.[181] Raman imaging also has potential for use in drug uptake studies in MTS.[176]

1.4.4 SERS – A New Method for Quantitative Analysis of MTS Characteristics

It has been widely established that MTS are a vital *in vitro* tool for investigation of tumour physiology and response to drugs and therapy. There is a need for these models due to the limitations of monolayer culture in displaying the complex characteristics found *in vivo* as a result of their 2D rather than 3D nature. This includes characteristics such as lack of cell-cell and cell-ECM interactions and failure to develop the gradients found in tumours where

central regions become deprived of oxygen and nutrients, an incredibly important characteristic, as limited penetration to these areas by drugs and lack of oxygen lead to resistance to many therapies. However, the increasing use of the more physiologically relevant MTS model has led to the requirement of more sophisticated imaging and chemical analysis techniques to characterise the physiological environment of these MTS and monitor responses to drugs and therapy, particularly for use in HTS methods.

New techniques have been developed for improved analysis of a variety of chemical characteristics of MTS moving from traditional flow cytometry, immunohistochemical, immunofluorescence, bioluminescence imaging and western blotting to newer techniques such as nanoprobes and Raman imaging. Enabling technologies are summarised in Table 1.2.

However, there is huge room for improvement in analytical techniques to monitor the physiological environment within MTS in a spatially resolved and quantitative manner. This important information could reveal essential characteristics of tumours and therefore aid the development of effective drugs and therapy. For this reason it would be incredibly useful for the SERS technique used by our group to monitor intracellular redox potential quantitatively to be extended for use in MTS.

Table 1.2 summarises the enabling technologies discussed for chemical analysis of MTS along with their uses and limitations.

Enabling Technology	Use	Limitations
Hypoxia probes e.g Hypoxyprobe™	Hypoxia detection	Sample has to be fixed and sectioned Only detects above/below a certain hypoxic limit
Oxygen microelectrodes	Measure oxygen concentration	Invasive so can perturb environment
Cell penetrating phosphorescent probes	O_2 sensing	Delivery of probes to cells

Nanoprobes	ROS detection pH detection Enzyme activity	Delivery of nanoprobes to cells
Fluorescent dyes	pH detection	Limited pH detection range
Bioluminescence imaging	pH and nutrient detection Protein expression Protein-protein interactions Enzyme activity	Intra- and extra-cellular compartments cannot be distinguished
^{1}H magnetic resonance chemical shift imaging	pH detection	Intra- and extra-cellular compartments cannot be distinguished
Spectroscopic imaging	Cell density (STIM) Element density (PIXE and SXFM) Protein, lipid, DNA and lactate distribution (FTIR)	Samples have to be frozen and sectioned
Western Blotting	Protein expression	Spatial information lost
Immunohistochemistry and immunofluorescence	Protein expression	Samples have to be fixed and processed
Flow cytometry	Protein expression	Spatial information limited
Mass spectrometry	Protein expression	Spatial resolution possible but limited
Mass spectrometry imaging	Protein expression Lipid and small molecule expression Drug uptake and metabolism	Samples have to be frozen and sectioned

1.5 Project Aims

The main aim of my project is to extend the technique of measuring cellular redox potential using SERS nanosensors from monolayer cell culture into MTS. It has been established that MTS are an important tool in cell culture, mimicking the *in vivo* environment more closely than traditional monolayer culture techniques, and there is a significant need to develop new techniques for chemical analysis of MTS, including redox potential measurements. The wide application of vibrational spectroscopy techniques for important biomedical applications has also been established and in particular the application of SERS to monitor intracellular redox potential, an incredibly important physiological parameter. The MTS will be used as a model of tumour microenvironment, whereby the aim is to establish a quantitative model of how redox potential changes through MTS. Initially, establishing uptake of nanosensors into MTS will be required before moving towards recording SER spectra from functionalised NPs in MTS. Once spectra can be reliably recorded, investigation will be required to relate spatial position of the functionalised NPs in the MTS to SERS spectra recorded in order to build up a picture of how redox potential changes through the MTS. When this quantitative model of redox potential variation has been established, it could be used to monitor changes in response to drug delivery or other types of cancer therapy and ultimately perhaps to help combat the problem of resistance in hypoxic regions by guiding therapy.

Chapter 2

Experimental Methods

"What is the recipe for successful achievement? To my mind there are just four essential ingredients: Choose a career you love, give it the best there is in you, seize your opportunities, and be a member of the team." – **Benjamin Franklin Fairless**

2.1 Cell Culture Procedures

2.1.1 General Cell Culture Procedures

The majority of cellular work was carried out using MCF7 human breast cancer cells. Cells were cultured in Dulbecco's modified eagle's medium (DMEM; Gibco; 31885-023), supplemented with penicillin/streptomycin (10,000 units/ml) and 10% heat-inactivated foetal calf serum (FCS) (for serum free (SF) medium FCS was not added). Cells were incubated at 37 °C and 5% CO_2 in a humidified incubator. HCT116 colorectal cancer cells and HCT116p53–/– colorectal cancer cells were cultured in the same manner. EAhy926 endothelial cells were cultured in DMEM supplemented with 10 % heat-inactivated FCS (no FCS for SF medium)y, 2 mM L-glutamine, penicillin/streptomycin and 2 % HAT.

When passaging cells, old media was removed and cells were washed with phosphate buffered saline (PBS). Cells were trypsinised by addition of trypsin/ethylenediaminetetraaceticacid (T/EDTA) and incubation at 37 °C and 5% CO_2 in a humidified incubator for 5-10 mins. Detached cells were re-suspended in fresh medium and pelleted by centrifugation at 1,200 rpm for 5 minutes. Pelleted cells were resuspended and appropriate volumes of cell suspension were seeded for continued growth.

When freezing cells for storage, cells were trypsinised as when passaging and the pelleted cells were resuspended in freeze mixture (10% DMSO in 90% heat-inactivated FCS). Aliquots of the resuspended cells were pipetted into labeled cryovials and stored at –80 °C

When thawing cells from storage at –80 °C, the cryovial was removed from the freezer, the outside wiped with 70% EtOH and the sample was left to thaw before transferring to a pre-

labelled universal container containing medium. The sample was pelleted by centrifugation at 1,200 rpm for 5 minutes, before resuspending the pellet and seeding for continued growth as required.

2.1.2 Haemocytometry

Haemocytometry was used to determine cell concentrations. An aliquot of cells (10 µl) from cells resuspended after trypsinising and pelleting, as when passaging cells, was mixed with 0.2% trypan blue (10 µl) on parafilm and then pipetted into a Bright Line™ Haemocytometer for cell counting.

Equation 2.1 was used to determine cell concentration where C = cell concentration (cells/ml), N = number of cells and Q = number of quadrants counted (5).

$$\mathrm{C} = \frac{N}{Q} \times 2 \times 10^4 \tag{2.1}$$

2.1.3 3D Cell Culture – Multicellular Tumour Spheroids (MTS)

MTS were prepared using the hanging drop technique. Cells were grown in monolayer culture as normal. Cells were trypsinised, pelleted by centrifugation and resuspended in 0.5 ml of medium. 20 µl drops of cell suspension were pipetted onto the lid of a plastic Petri dish and approximately 5-10 ml of medium were added to the bottom of the dish. The lid containing hanging drops was placed on the Petri dish and MTS were grown in the drops over a period of, in general, 6 days.

2.1.4 Setting MTS in Collagen Matrix

Keeping everything on ice, collagen solution was prepared from collagen stock (25%), acetic acid (45%), 10X Culture Media (10%), NaOH (10%) and FCS (10 %), to the volume required (typically a total of 1-10 ml). MTS were transferred via pipette into the desired volume of collagen in a glass bottomed imaging dish and collagen was allowed to set in a humidified incubator at 37 °C and 5% CO_2 for approximately 1 hour.[182]

2.1.5 Hypoxyprobe

MTS were removed from hanging drops and incubated with 100 μM Hypoxyprobe™ (www.hypoxyprobe.com) for 45-60 mins. Hypoxyprobe solution was removed and MTS were fixed in 4% paraformaldehyde. MTS were paraffin embedded and sectioned at the Division of Pathology Laboratories, Western General Hospital. Immunohistochemistry (IHC) was then performed on sectioned MTS mounted on slides at St Andrew's University. Slides were placed in a metallic rack and de-waxed in xylene (3 × 5 mins followed by rehydration in 100% (× 2), 80% and 50% alcohol (2 min each) washing in running water (2 min). Antigen retrieval (to break the cross linking of proteins formed during fixing, to allow binding of primary antibody) was then performed by placing slides into pre-heated sodium citrate/citric acid buffer (prepared from 18 ml of 0.1 M citric acid and 82 ml of 0.1 M sodium citrate made up to 1 l with Elga (lab purified) water) in a pressure cooker and heating on high for 8 mins in a microwave (reaches a temperature of *ca* 120 ºC. Upon removal from the microwave cold water was added and slides cooled for 20 mins. Slides were then washed in PBS/Tween 20 (PBS/T) (500 ml PBS and 500 μl Tween 20) (2 × 5 mins) followed by treatment in 3% hydrogen peroxide (10 ml 30% H_2O_2 and 90 ml Elga water) (10 mins) and further washes in PBS/T (2 × 5 mins). Slides were then removed and excess solution blotted off on tissue before marking around sections with a hydrophobic Immedge pen. Dako Total Protein blocking solution was then dropped onto the marked areas for 10 mins before blotting off onto tissue. Primary antibody (anti-pimonidazole mouse IgG1 monoclonal antibody (Mab1)) (1:8000) was then added to marked areas and slides incubated for 1 hr in a black slide box. Following incubation slides were washed again in PBS/T (2 × 5 mins) and then incubated with Dako Mouse Envision labeled polymer (30 mins) followed by further PBT/T washing (2 × 5 mins). Marked sections were then incubated with DAB solution (20 μl DAB chromagen and 1 ml DAB substrate buffer) (20 mins). Sections were washed in water. Slides were then placed into haematoxylin followed by washing in running water (2 mins) then transfer to Scott's tap water (3.5 g sodium bicarbonate, 20 g magnesium sulphate dissolved and made up to 1 l with Elga water) (1 min) followed by further washing in running water (2 mins). Slides were dehydrated in 50% alcohol (30 s), 80% alcohol (30 s), 100% alcohol (2 × 2 mins) followed by xylene (3 × 5 mins). Slides were mounted in DPX and left to dry before imaging.

2.1.6 MTT Assay

Cells were plated in a 96-well plate and incubated overnight in a humidified incubator at 37 °C and 5% CO_2 to ensure adhesion. Cells were washed with PBS and serum free (SF) medium (80 μl) was added for 1-2 hr before addition of bare NP (20 μl, final concentration 730 fM), NQ-NP (20 μl, final concentration 730 fM), AQ-NP (20 μl, final concentration 730 fM), MBA-NP (20 μl, final concentration 730 fM), nanorods (NR) (20 μl, final concentration 224 pM) and untreated as required and overnight incubation. (Note: the concentration of NPs/NR is expressed as the number of moles of particles in one litre throughout this work, converted from the number of particles per ml, as supplied, using Avogadro's constant). The following day, cells were washed with PBS and phenol red free medium (90 μl) and 3-(4,5-dimethylthiazol-2-yl)-2,5-diphenyltetrazolium bromide solution (10 μl, 5 mg/ml) were added. After incubation for 4 hr, the solution was removed and solubilizing solution (10 % TRITON X-100, 0.1 M HCL in IPA) (100 μl) was added. A BIOTEK Syntergy HT microplate reader was used to measure absorbance while shaking at 570 nm and 690 nm.

2.1.7 Drug Treatment

2.1.7.1 Staurosporine

For cells in monolayer culture, cells, treated overnight with MBA-NPs before washing and adding 2 ml SF medium, were treated with 20 μl of 100 μM STS in SF medium (final STS concentration 1 μM) and Raman measurements were taken after over a period of 1 hr from plates upon initial treatment with STS (0-1 hr), after 1 hr treatment with STS (1-2 hr), after 2 hr treatment with STS (2-3 hr), after 4 hr treatment with STS (4-5 hr), after 5 hr treatment with STS (5-6 hr) and after 6 hr treatment with STS (6-7 hr).

For MTS, medium was removed from hanging drops and replaced with 20 μl of 10 μM STS over various time points.

2.1.7.2 TNFα

Medium was replaced with medium containing 10 ng/ml TNFα followed by 12 hr incubation before NP incubation.

2.1.8 Fluorescence Staining

2.1.8.1 LysoSensor™ Green DND-153

Medium was removed and replaced with pre-warmed phenol red free medium containing 1 μM LysoSensor (1 ml) followed by incubation for 30 min in a humidified incubator at 37 °C and 5% CO_2. Medium was removed and replaced with phenol red free media before imaging cells.

2.1.8.2 DiD

Medium was removed and the coverslip was covered with 100 μl of 5 μM DiD in pre-warmed phenol red free media followed by incubation in a humidified incubator at 37 °C and 5% CO_2 for approximately 5 mins. Medium was removed and cells were washed with PBS (3 × 10 mins) before replacing with phenol red free media before imaging cells.

Where cells were stained with both Lysosensor and DiD, Lysosensor staining was performed initially followed directly by DiD staining as detailed for the individual stains.

2.1.8.3 NucBlue® Live ReadyProbes® Reagent

Medium was removed and replaced with pre-warmed phenol red free medium containing 2 drops per ml of NucBlue (1 ml per well) followed by incubation for 20-30 mins at room temperature. Medium was removed and replaced with phenol red free medium before imaging cells.

2.1.8.4 Tetramethylrhodamine methyl ester (TMRM)

Medium was removed and replaced with pre-warmed phenol red free media containing 100 nM TMRM (1 ml per well) followed by incubation for 20-30 mins at room temperature. Medium was removed and replaced with phenol red free media before imaging cells.

2.2 SERS Experiments

2.2.1 Instrumentation

SERS spectra were recorded using four different Raman instruments:

1) A Reinshaw inVia confocal Raman Microscope and Spectrometer (old model) with a 785 nm diode laser with a maximum of 10 mW power at the sample, along with 50 × (NA 0.45) Olympus long working distance air objective to focus laser light onto samples (10 × long working distance air objective was also available) and Wire 3.4. software. For non-mapping experiments, point focus was used, with a laser spot size diameter of *ca.* 2 μm. For mapping experiments line focus was used, with beam profile at the sample of dimensions *ca.* 3 μm × 25 μm. Mapping steps were 5 μm in x × 3.56 μm bins in y along the line (rough maps to find signals), or 1 μm in x × 1.19 μm bins in y along the line (final maps for data). This spectrometer was the only one available when this project work began and therefore was used for all of the initial experiments in Chapter 3 and parts of Chapter 4.
2) An Ocean Optics QE65 Pro Spectrometer with fibre optic probe and 785 nm laser with 350 mW power, with Spectra Suite software. This spectrometer did not allow mapping (no microscope attached), and was therefore used for single point measurements. When focused the laser spot from the fibre optic probe was on the order of 1 mm. This spectrometer was used predominantly in Chapter 5, where spatial information was gained from NP targeting rather than microscopically mapping, and in parts of Chapter 4 for calibrations.
3) A WITec system, with a He-Ne laser (632.8 nm) (also 532 nm and 785 nm lasers used in initial experiments) with 10 mW power at the sample and equipped with an immersive objective with magnification of 60 × (NA 1.0), and an air objective with magnification of 20 × and WITec Project 2.06 software. For non-mapping experiments (calibration in Chapter 4) the 20 × objective was used. For mapping experiments (Chapter 4 Section 4.2.2 and Chapter 5 Section 5.2) the 60 × objective was used for point mapping, with a spatial resolution of *ca.* 0.4 μm and mapping step sizes of 1 μm in both x and y. This spectrometer was situated in Jagiellonian University, Krakow, where work was carried out in collaboration.

4) A Renishaw inVia confocal Raman Microscope and Spectrometer (new model) with a 785 nm diode laser with a maximum of 10 mW power at the sample, along with a 5 × (NA 0.12) long working distance objective to focus laser light onto samples (20 × and 50 × objectives were also available but short working distance) and Wire 4.1 software. This spectrometer was used for some preliminary mapping experiments (Chapter 5 Section 5.3), as it was only available in the final months of this work. Depth mapping experiments were carried out using a point focus with both no pinhole, pinhole and pinhole with high confocality, and z steps of 20 μm or 50 μm. Mapping in xy was carried out using a point focus, with spatial resolution of *ca.* 4 μm, and mapping step sizes of 20 μm in both x and y.

A summary of instruments, their specifications/settings and the sections of this work in which they were used, is given in Table 2.1 for ease of reference.

2.2.2 Nanoparticles

The majority of SERS experiments were carried out using aqueous suspensions of NPs (2.2 × 10^9 particles/ml, 3.65 pM) purchased from Nanospectra Biosciences that had a 150 nm diameter with a 125 nm silica core and 25 nm gold shell and were resonant at approximately 780 nm, as stated when supplied, and confirmed by UV-Vis spectroscopy on arrival.

For some targeting experiments, 50 nm gold NPs were used purchased from Sigma-Aldrich (3.5 × 10^{10} particles/ml, 58.1 pM) that had a diameter 50 nm and were resonant at 535-539 nm.

Gold nanorods (NR) (6.73 × 10^{11} particles/ml, 1.12 nM) were purchased from Nanopartz and had a diameter 10 nm, length 38 nm, resonance at 780 nm and were CTAB coated.

For work carried out in Jagiellonian University, NPs were prepared according to the Frens procedure.[183] In this synthesis, Au ions are reduced by citrate ions. Previous measurements using UV-visible absorbance spectroscopy, Dynamic Light Scattering and AFM determined the size of NPs to be 40 nm, and resonance to be 527 nm.[184]

Table 2.1 summarises the different Raman spectrometers used in this work along with their specifications/settings and the sections of the work in which they were used.

	Spectrometer	Laser Wavelength (nm)	Spectral Resolution (cm^{-1})	Objective	Point/Line Focus	Mapping Step Size (x μm × y μm)	Centre (cm^{-1})	Illumination time (s)	Illumination power (%)	Section
1	**Renishaw inVia (old)**	785	*ca.* 1	50 ×	Point	N/A	1580 (NQ),1600 (AQ)	30	10	Figure 3.12(b) Figure 3.19
					Line	1 × 1.19	1580 (NQ),1600 (AQ)	30	10	3.4
					Point	N/A	1400	30	10	4.1.1.1
					Point	N/A	1400	30	10	4.1.2.1
					Line	1 × 1.19	1400	30	10	4.2.1
2	**Ocean Optics QE65 Pro**	785	*ca.* 2-4	N/A	N/A	N/A	Full range	30	100	4.1.1.2
								30	100	4.1.2.1
								30-60	100	4.1.2.2
								30-60	100	4.1.2.3
								30	100	5.2
3	**WITec**	633	*ca.* 1.5-2	20 ×	Point	N/A	Full range	0.04	100	4.1.1.3
				60 ×	Point	1 × 1	Full range	0.04	100	4.2.2
						1 × 1	Full range	0.03	100	5.1
4	**Renishaw inVia (new)**	785	*ca.* 1	5 ×	Point High Confocality	20 (z)	1400	60	10	Figure 5.22(a)
					Point	20 (z)	1400	30	10	Figure 5.22(b)
					Point High Confocality	20 (z)	1400	60	10	Figure 5.23
					Point	20 × 20	1400	1	50	Figure 5.24
					Point, no pinhole	20 (z)	1580	1	50	Figure 5.25(a)
					Point, no pinhole	50 (z)	1580	0.5	50	Figure 5.25(b) Figure 5.25(c)

Table 2.2 summarises the different nanoparticles used in this work by abbreviation used, along with their characteristics and the sections of the work in which each was used.

Nanoparticle	Size	Absorption Maxima	Sections used
NP	150	*ca.* 780	Chapter 3
			4.1.1.1
			4.1.1.2
			4.1.2
			4.2.1
			5.2
			5.3
			6.1
			6.2.1
			6.2.2
NP50	50	*ca.* 535-539	6.2.2
NR	10 (diameter)	*ca.* 780	Figure 3.5
	× 38 (length)		
NP40	40	*ca.* 527	4.1.1.3
			4.2.2
			5.1

A summary of the different nanoparticles used in this work by abbreviation used, along with characteristics (size and absorption maxima), and the Sections each was used in, is given in Table 2.2. Unless otherwise stated, NP refers to 150 nm NPs, as these were used primarily in this work.

2.2.3 Nanoparticle Functionalisation

2.2.3.1 150 nm Nanoparticles

For NQ-NPs, NPs were functionalised overnight with 100 μM NQ in 10% EtOH solution. The 100 μM NQ solution was prepared by firstly dissolving a small (*ca.* 1 mg) mass of NQ in EtOH, to make a 1 mM NQ solution. This solution was heated and sonicated for 30 mins to dissolve NQ, due to its poor solubility. The solution was then filtered through cotton wool, followed by a further 10 mins heating and sonicating. The solution was filtered through

cotton wool again, and then passed through a 0.22 μm filter. 100 μl of this solution was then mixed with 900 μl of tissue culture grade water to make the 100 μM NQ in 10% EtOH solution. 1 ml of NPs were centrifuged (5500 rpm, 10 mins) and all but 200 μl of the water was removed leaving the NP pellet at the bottom of the centrifuge tube. The 100 μM NQ solution was added and the resultant solution was left overnight in the dark. Functionalised NQ-NPs were washed 3 times with water. To do this NQ-NPs were centrifuged (5500 rpm, 10 mins) and all but 200 μl of solution was removed and replaced with tissue culture grade water (400 μl after first and second washes and 1 ml after third wash). UV-Vis spectra were recorded before and after washing steps.

For AQ-NPs, NPs were functionalised overnight with 100 μM AQ in 1% DMSO solution. The 100 μM AQ solution was prepared by firstly dissolving a small (*ca.* 2 mg) mass of NQ in DMSO, to make a 10 mM AQ solution. 30 μl of this solution was then diluted to 3 ml with tissue culture grade water. The solution was then filtered through cotton wool twice, and then passed through a 0.22 μm filter. 1 ml of NPs were centrifuged (5500 rpm, 10 mins) and all but 200 μl of the water was removed leaving the NP pellet at the bottom of the centrifuge tube. 1 ml of 100 μM AQ solution was added and the resultant solution was left overnight in the dark. Functionalised AQ-NPs were washed 2-3 times with water. To do this AQ-NPs were centrifuged (5500 rpm, 10 mins) and all but 200 μl of solution was removed and replaced with tissue culture grade water (400 μl for all but last wash where 1 ml was used). UV-Vis spectra were recorded before and after washing steps.
Previous to establishing this procedure as the optimal functionalisation conditions, functionalisation was investigated by overnight incubation of NPs with 100 μM AQ solution in 10% acetone, 10% DMF, 5% DMF, 1% DMF and 0.1% DMF.

For paramercaptobenzoic acid NPs (MBA-NPs), NPs were functionalised overnight with 100 μM pMBA in 10% EtOH solution. The 100 μM MBA solution was prepared by firstly dissolving a small (*ca.* 1 mg) mass of MBA in EtOH, to make a 1 mM MBA solution. The solution was then filtered through cotton wool twice, and then passed through a 0.22 μm filter. 100 μl of this solution was then mixed with 900 μl of tissue culture grade water to make the 100 μM MBA in 10% EtOH solution. 1 ml of NPs were centrifuged (5500 rpm, 10 mins) and all but 200 μl of the water was removed leaving the NP pellet at the bottom of the centrifuge tube. The 100 μM MBA solution was added and the resultant solution was left

overnight in the dark. Functionalised MBA-NPs were washed 3 times with water. To do this MBA-NPs were centrifuged (5500 rpm, 10 mins) and all but 200 μl of solution was removed and replaced with tissue culture grade water (400 μl after first and second washes and 1 ml after third wash). UV-Vis spectra were recorded before and after washing steps.

For 4-mercaptopyridine NPs (4MP-NPs), NPs were functionalised overnight with 100 μM 4MP in 10% EtOH solution. The 100 μM 4MP solution was prepared by firstly dissolving a small (*ca.* 1 mg) mass of 4MP in EtOH, to make a 1 mM 4MP solution. The solution was then filtered through cotton wool twice, and then passed through a 0.22 μm filter. 100 μl of this solution was then mixed with 900 μl of tissue culture grade water to make the 100 μM 4MP in 10% EtOH solution. 1 ml of NPs were centrifuged (5500 rpm, 10 mins) and all but 200 μl of the water was removed leaving the NP pellet at the bottom of the centrifuge tube. The 100 μM 4MP solution was added and the resultant solution was left overnight in the dark. Functionalised 4MP-NPs were washed 3 times with water. To do this 4MP-NPs were centrifuged (5500 rpm, 10 mins) and all but 200 μl of solution was removed and replaced with tissue culture grade water (400 μl after first and second washes and 1 ml after third wash). UV-Vis spectra were recorded before and after washing steps.

For 4-aminobenzenethiol NPs (4ABT-NPs), NPs were functionalised overnight with 100 μM 4ABT in 10% EtOH solution. The 100 μM 4ABT solution was prepared by firstly dissolving a small (*ca.* 1 mg) mass of 4ABT in EtOH, to make a 1 mM 4ABT solution. The solution was then filtered through cotton wool twice, and then passed through a 0.22 μm filter. 100 μl of this solution was then mixed with 900 μl of tissue culture grade water to make the 100 μM 4ABT in 10% EtOH solution. 1 ml of NPs were centrifuged (5500 rpm, 10 mins) and all but 200 μl of the water was removed leaving the NP pellet at the bottom of the centrifuge tube. The 100 μM 4ABT solution was added and the resultant solution was left overnight in the dark. Functionalised 4ABT-NPs were washed 3 times with water. To do this 4ABT-NPs were centrifuged (5500 rpm, 10 mins) and all but 200 μl of solution was removed and replaced with tissue culture grade water (400 μl after first and second washes and 1 ml after third wash). UV-Vis spectra were recorded before and after washing steps.

For nitrobenzoic acid NPs (NBA-NPs), NPs were functionalised overnight with 100 μM NBA in 10% EtOH solution. The 100 μM NBA solution was prepared by firstly dissolving a

small (*ca.* 1 mg) mass of NBA in EtOH, to make a 1 mM NBA solution. The solution was then filtered through cotton wool twice, and then passed through a 0.22 μm filter. 100 μl of this solution was then mixed with 900 μl of tissue culture grade water to make the 100 μM NBA in 10% EtOH solution. 1 ml of NPs were centrifuged (5500 rpm, 10 mins) and all but 200 μl of the water was removed leaving the NP pellet at the bottom of the centrifuge tube. The 100 μM NBA solution was added and the resultant solution was left overnight in the dark. Functionalised NBA-NPs were washed 3 times with water. To do this NBA-NPs were centrifuged (5500 rpm, 10 mins) and all but 200 μl of solution was removed and replaced with tissue culture grade water (400 μl after first and second washes and 1 ml after third wash). UV-Vis spectra were recorded before and after washing steps.

For aminoNQ-NPs, NPs were functionalised overnight with 100 μM aminoNQ in 10% EtOH solution. The 100 μM aminoNQ solution was prepared by firstly dissolving a small (*ca.* 1 mg) mass of aminoNQ in EtOH, to make a 1 mM aminoNQ solution. The solution was then filtered through cotton wool twice, and then passed through a 0.22 μm filter. 100 μl of this solution was then mixed with 900 μl of tissue culture grade water to make the 100 μM aminoNQ in 10% EtOH solution. 1 ml of NPs were centrifuged (5500 rpm, 10 mins) and all but 200 μl of the water was removed leaving the NP pellet at the bottom of the centrifuge tube. The 100 μM aminoNQ solution was added and the resultant solution was left overnight in the dark. Functionalised aminoNQ-NPs were washed 3 times with water. To do this aminoNQ-NPs were centrifuged (5500 rpm, 10 mins) and all but 200 μl of solution was removed and replaced with tissue culture grade water (400 μl after first and second washes and 1 ml after third wash). UV-Vis spectra were recorded before and after washing steps.

For CANLS1-NQ-NPs, NPs were functionalised overnight with 100 μM NQ and 229 μM CANLS1 in 10% EtOH solution. A 1 mM NQ solution was prepared by firstly dissolving a small (*ca.* 1 mg) mass of NQ in EtOH, to the correct concentration. This solution was heated and sonicated for 30 mins to dissolve NQ, due to its poor solubility. The solution was then filtered through cotton wool, followed by a further 10 mins heating and sonicating. The solution was filtered through cotton wool again, and then passed through a 0.22 μm filter. A 558 μM CANLS1 solution was prepared by dissolving a small (*ca.* 2 mg) mass of CANLS1 in tissue culture grade water. The same heating, sonicating and filtering steps as for NQ were followed. 100 μl of the 1 mM NQ solution, 400 μl of tissue culture grade water and 500 μl of

the 558 μM CANLS1 solution were mixed to make a 100 μM NQ and 229 μM CANLS1 solution in 10% EtOH. 1 ml of NPs were centrifuged (5500 rpm, 10 mins) and all but 200 μl of the water was removed leaving the NP pellet at the bottom of the centrifuge tube. The NQ/CANLS1 solution was added and the resultant solution was left overnight in the dark. CANLS1-NQ-NPs were washed numerous times with water until it was determined by fluorescence spectroscopy that excess CANLS1 had been removed. To do this CANLS1-NQ-NPs were centrifuged (5500 rpm, 10 mins) and all but 200 μl of solution was removed and replaced with tissue culture grade water. Fluorescence spectra of the resultant CANLS1-NQ-NP solution and the removed solution after washing steps were recorded to determine when all excess CANLS1 had been removed. Fluorescence spectra were recorded using 490 nm excitation and emission at *ca.* 520 nm was monitored as described in Section 2.3.9. As CANLS1 exhibits an emission at 520 nm, loss of fluorescence at this wavelength indicated loss of excessCANLS1 during washing steps. UV-Vis spectra were recorded before and after washing steps.

For 1-thio-glucose NPs (TG-NPs), NPs were functionalised overnight with both 1 mM and 100 μM TG in aqueous solution. 10 mM 1-thio-glucose was prepared by hydrolysis of 1-thio-glucose tetraacetate by Patrick Thomson. The solution was then filtered through cotton wool twice, and then passed through a 0.22 μm filter. 100 μl of this solution was then mixed with 900 μl of tissue culture grade water to make the 1 mM TG solution, or 10 μl of this solution was mixed with 990 μl of tissue culture grade water to make the 100 μM TG solution. For each concentration of TG, 1 ml of NPs were centrifuged (5500 rpm, 10 mins) and all but 200 μl of the water was removed leaving the NP pellet at the bottom of the centrifuge tube. The required TG solution was added and the resultant solution was left overnight in the dark. Functionalised TG-NPs were washed 3 times with water. To do this TG-NPs were centrifuged (5500 rpm, 10 mins) and all but 200 μl of solution was removed and replaced with tissue culture grade water (400 μl after first and second washes and 1 ml after third wash). UV-Vis spectra were recorded before and after washing steps.

For polyarginine NPs (PLA-NPs), NPs were functionalised overnight with 50 μM PLA hydrochloride in aqueous solution. The 50 μM PLA solution was prepared by firstly dissolving a small (*ca.* 1 mg) mass of PLA in tissue culture grade water, to make a 100 μM PLA solution. The solution was then filtered through cotton wool twice, and then passed

through a 0.22 μm filter. 500 μl of this solution was then mixed with 500 μl of tissue culture grade to make the 50 μM aqueous PLA solution. 1 ml of NPs were centrifuged (5500 rpm, 10 mins) and all but 200 μl of the water was removed leaving the NP pellet at the bottom of the centrifuge tube. The 50 μM PLA solution was added and the resultant solution was left overnight in the dark. Functionalised PLA-NPs were washed 3 times with water. To do this PLA-NPs were centrifuged (5500 rpm, 10 mins) and all but 200 μl of solution was removed and replaced with tissue culture grade water (400 μl after first and second washes and 1 ml after third wash). UV-Vis spectra were recorded before and after washing steps.

PLA hydrochloride had molecular weight 5000-15000 g mol^{-1} and 10000 g mol^{-1} was used for concentration calculation.

For cysteamine NPs (2AET-NPs), NPs were functionalised overnight with 100 μM 2AET in 10% EtOH solution. The 100 μM 2AET solution was prepared by firstly dissolving a small (*ca.* 1 mg) mass of 2AET in EtOH, to make a 1 mM 2AET solution. The solution was then filtered through cotton wool twice, and then passed through a 0.22 μm filter. 100 μl of this solution was then mixed with 900 μl of tissue culture grade water to make the 100 μM 2AET in 10% EtOH solution. 1 ml of NPs were centrifuged (5500 rpm, 10 mins) and all but 200 μl of the water was removed leaving the NP pellet at the bottom of the centrifuge tube. The 100 μM 2AET solution was added and the resultant solution was left overnight in the dark. Functionalised 2AET-NPs were washed once with water. To do this 2AET-NPs were centrifuged (5500 rpm, 10 mins) and all but 200 μl of solution was removed and replaced with 1 ml of tissue culture grade water. UV-Vis spectra were recorded before and after washing steps.

For poly(ethylene glycol) methyl ether thiol NPs (PEG800-NPs), NPs were functionalised overnight with 100 μM PEG800 in aqueous solution. The 100 μM PEG800 solution was prepared by firstly dissolving a small (*ca.* 1 mg) mass of PEG800 in tissue culture grade water, to make a 1 mM PEG800 solution. The solution was then filtered through cotton wool twice, and then passed through a 0.22 μm filter. 100 μl of this solution was then mixed with 900 μl of tissue culture grade water to make the 100 μM PEG800 aqueous solution. 1 ml of NPs were centrifuged (5500 rpm, 10 mins) and all but 200 μl of the water was removed leaving the NP pellet at the bottom of the centrifuge tube. The 100 μM PEG800 solution was added and the resultant solution was left overnight in the dark. Functionalised PEG800-NPs

were washed once with water. To do this PEG800-NPs were centrifuged (5500 rpm, 10 mins) and all but 200 μl of solution was removed and replaced with 1 ml of tissue culture grade water. UV-Vis spectra were recorded before and after washing steps.

For O-(2-Mercaptoethyl)-O'-methyl-hexa(ethylene glycol) NPs (PEG6-NPs), NPs were functionalised overnight with 100 μM PEG6 in aqueous solution. The 100 μM PEG6 solution was prepared by firstly dissolving a small (*ca.* 10 mg) mass of PEG6 in tissue culture grade water, to make a 10 mM PEG6 solution. 300 μl of this solution was then added to 2700 μl of tissue culture grade water to make a 1 mM PEG6 solution. The solution was then filtered through cotton wool twice, and then passed through a 0.22 μm filter. 100 μl of this solution was then mixed with 900 μl of tissue culture grade water to make the 100 μM PEG6 aqueous solution. 1 ml of NPs were centrifuged (5500 rpm, 10 mins) and all but 200 μl of the water was removed leaving the NP pellet at the bottom of the centrifuge tube. The 100 μM PEG6 solution was added and the resultant solution was left overnight in the dark. Functionalised PEG6-NPs were washed 3 times with water. To do this PEG6-NPs were centrifuged (5500 rpm, 10 mins) and all but 200 μl of solution was removed and replaced with tissue culture grade water (400 μl after first and second washes and 1 ml after third wash). UV-Vis spectra were recorded before and after washing steps.

For PEG6-NQ-NPs, NPs were functionalised overnight with 100 μM NQ and 100 μM PEG6 in 10% EtOH solution. The 1 mM NQ and 1 mM PEG6 solutions in EtOH were prepared in the same way as for NQ-NP and PEG6-NP functionalization respectively. 100 μl of 1mM NQ solution and 100 μl of 1 mM PEG6 solution were then mixed with 800 μl of tissue culture grade water to make the 100 μM NQ and 100 μM PEG6 in 10% EtOH solution. 1 ml of NPs were centrifuged (5500 rpm, 10 mins) and all but 200 μl of the water was removed leaving the NP pellet at the bottom of the centrifuge tube. The 100 μM NQ and 100 μM PEG6 in 10% EtOH solution was added and the resultant solution was left overnight in the dark. Functionalised PEG6-NQ-NPs were washed 3 times with water. To do this PEG6-NQ-NPs were centrifuged (5500 rpm, 10 mins) and all but 200 μl of solution was removed and replaced with tissue culture grade water (400 μl after first and second washes and 1 ml after third wash). UV-Vis spectra were recorded before and after washing steps.

For CANLS1-NPs, NPs were functionalised overnight with 10 μM CANLS1 in aqueous solution. A stock solution of 100 μM CANLS1 was prepared by dissolving a small mass of CANLS1 in tissue culture grade water. The solution was then filtered through cotton wool twice, and then passed through a 0.22 μm filter. 100 μl of this solution was then mixed with 900 μl of tissue culture grade water to make the 10 μM CANLS1 aqueous solution. 1 ml of NPs were centrifuged (5500 rpm, 10 mins) and all but 200 μl of the water was removed leaving the NP pellet at the bottom of the centrifuge tube. The 10 μM CANLS1 solution was added and the resultant solution was left overnight in the dark. Functionalised CANLS1-NPs were washed 3 times with water. To do this CANLS1-NPs were centrifuged (5500 rpm, 10 mins) and all but 200 μl of solution was removed and replaced with tissue culture grade water (400 μl after first and second washes and 1 ml after third wash). UV-Vis spectra were recorded before and after washing steps.

For NLS2-NPs, NPs were functionalised overnight with 10 μM NLS2 in aqueous solution. A stock solution of 100 μM NLS2 was prepared by dissolving a small mass of NLS2 in tissue culture grade water. The solution was then filtered through cotton wool twice, and then passed through a 0.22 μm filter. 100 μl of this solution was then mixed with 900 μl of tissue culture grade water to make the 10 μM NLS2 aqueous solution. 1 ml of NPs were centrifuged (5500 rpm, 10 mins) and all but 200 μl of the water was removed leaving the NP pellet at the bottom of the centrifuge tube. The 10 μM NLS2 solution was added and the resultant solution was left overnight in the dark. Functionalised NLS2-NPs were washed 3 times with water. To do this NLS2-NPs were centrifuged (5500 rpm, 10 mins) and all but 200 μl of solution was removed and replaced with tissue culture grade water (400 μl after first and second washes and 1 ml after third wash). UV-Vis spectra were recorded before and after washing steps.

For 4-sulfanylbutylphenylphosphanium bromide NPs (SBTPP-NPs), NPs were functionalised overnight with 100 μM SBTPP in aqueous solution. 100 μM SBTPP was prepared by dissolving a small mass of SBTPP (*ca.* 5mg) in tissue culture grade water. The solution was then filtered through cotton wool twice, and then passed through a 0.22 μm filter. 1 ml of NPs were centrifuged (5500 rpm, 10 mins) and all but 200 μl of the water was removed leaving the NP pellet at the bottom of the centrifuge tube. The 100 μM SBTPP solution was added and the resultant solution was left overnight in the dark. Functionalised

SBTPP-NPs were washed once with water. To do this SBTPP-NPs were centrifuged (5500 rpm, 10 mins) and all but 200 μl of solution was removed and replaced with tissue culture 400 μl tissue culture grade water. UV-Vis spectra were recorded before and after washing steps. SBTPP was synthesised by Patrick Thomson.

2.2.3.2 50 nm Nanoparticles

For CANLS1-NPs, NPs were functionalised overnight with 10 μM CANLS1 in aqueous solution. A stock solution of 100 μM CANLS1 was prepared by dissolving a small mass of CANLS1 in tissue culture grade water. The solution was then filtered through cotton wool twice, and then passed through a 0.22 μm filter. 100 μl of this solution was then mixed with 900 μl of tissue culture grade water to make the 10 μM CANLS1 aqueous solution. 1 ml of NPs were centrifuged (5500 rpm, 10 mins) and all but 200 μl of the water was removed leaving the NP pellet at the bottom of the centrifuge tube. The 10 μM CANLS1 solution was added and the resultant solution was left overnight in the dark. A UV-Vis spectrum of the functionalized CANLS1-NPs was recorded recorded.

For NLS2-NPs, NPs were functionalised overnight with 10 μM NLS2 in aqueous solution. A stock solution of 100 μM NLS2 was prepared by dissolving a small mass of NLS2 in tissue culture grade water. The solution was then filtered through cotton wool twice, and then passed through a 0.22 μm filter. 100 μl of this solution was then mixed with 900 μl of tissue culture grade water to make the 10 μM NLS2 aqueous solution. 1 ml of NPs were centrifuged (5500 rpm, 10 mins) and all but 200 μl of the water was removed leaving the NP pellet at the bottom of the centrifuge tube. The 10 μM NLS2 solution was added and the resultant solution was left overnight in the dark. A UV-Vis spectrum of the functionalized NLS2-NPs was recorded recorded.

For SBTPP-NPs, NPs were functionalised overnight with 100 μM SBTPP in aqueous solution. 100 μM SBTPP was prepared by dissolving a small mass of SBTPP (*ca.* 5mg) in tissue culture grade water. The solution was then filtered through cotton wool twice, and then passed through a 0.22 μm filter. 1 ml of NPs were centrifuged (5500 rpm, 10 mins) and all but 200 μl of the water was removed leaving the NP pellet at the bottom of the centrifuge tube. The 100 μM SBTPP solution was added and the resultant solution was left overnight in the dark. Functionalised SBTPP-NPs were washed once with water. To do this SBTPP-NPs

were centrifuged (5500 rpm, 10 mins) and all but 200 μl of solution was removed and replaced with tissue culture 400 μl tissue culture grade water. UV-Vis spectra were recorded before and after washing steps. SBTPP was synthesised by Patrick Thomson.

2.2.3.3 Nanoparticles Synthesised Using Frens Procedure

A stock solution of MBA at the concentration of 1 mM was prepared by diluting an appropriate mass of the solid in ethanol. A stock solution of AQ at the concentration of 100 μM was prepared by diluting an appropriate mass of the solid in DMSO to a concentration of 10 mM and diluting the resultant solution with PBS to 100 μM.

MBA-NP and AQ-NP solutions were prepared by mixing 100 μl of the 1 mM solution of MBA and 400 μl of 100 μM solution of AQ respectively with 1 ml of the gold colloid. After 5 min, mixtures were centrifuged for 10 min at 3000 rpm. For MBA-NPs supernatant was removed and NPs were re-dissolved in PBS.

2.2.4 SERS of Functionalised Nanoparticles

Functionalised NPs were dried onto a glass coverslip or glass bottomed imaging dish. SER spectra of the dried NPs were recorded by focusing on the NPs using the Renishaw inVia Raman microscope with point laser (785 nm) and 30 s acquisition time at 10% laser power (and appropriate centre for the nanosensor – 1580 cm^{-1} for NQ-NP, 1600 cm^{-1} for AQ-NP, 1400 cm^{-1} for MBA-NP).

2.2.5 Redox Probe Calibration

SERS spectroelectrochemistry of NQ-NPs was carried out by Jing Jiang and Craig Auchinvole as described by Auchinvole *et al.*[95,185]. SERS spectroelectrochemistry for AQ-NPs was carried out by Jing Jiang as described by Jiang *et al.*[96,97]. Calibration plots and equations are detailed in Appendix 1. The half wave potential of AQ at different pH values was determined by cyclic volatammetry by Jing Jiang as described by Jiang *et al.*[97] and agreed with theoretical predictions.

2.2.6 pH Calibration

2.2.6.1 Buffer Preparation

One series of buffers for pH calibration were prepared, at room temperature, as follows. Actual pH values were measured using a Fisherbrand Hydrus 400 pH meter with Mettler Toledo InLab® Routine Pro pH electrode.

pH 5.8: KH_2PO_4 (4.17 g) and K_2HPO_4 (0.435 g) were dissolved to 500 ml (measured pH = 5.77).
pH 6.5: KH_2PO_4 (3.4 g) and NaOH (0.30 g) were dissolved to 500 ml (measured pH = 6.47).
pH 6.6: NaH_2PO_4 (2.18 g), Na_2HPO_4 (3.375 g) and NaCl (2.13 g) were dissolved to 500 ml (measured pH = 6.82).
pH 6.8: KH_2PO_4 (3.48 g) and NaOH (0.47 g) were dissolved to 500 ml (measured pH = 6.83).
pH 7.0: A pH 7.0 buffer tablet (Fischer Scientific) was dissolved to 100 ml (measured pH = 7.00).
pH 7.2: A pH 7.2 buffer tablet was dissolved to 100 ml (measured pH = 7.20).
pH 7.4: KH_2PO_4 (3.40 g) and NaOH (0.79 g) were dissolved to 500 ml (measured pH = 7.49)
pH 7.6: KH_2PO_4 (3.40 g) and NaOH (0.85 g) were dissolved to 500 ml (measured pH = 7.59).
pH 7.8: Na_2HPO_4 (32.85 g) and NaH_2PO_4 (1.17 g) were dissolved to 500 ml (measured pH = 8.12).

Another set of pH buffers were prepared, at room temperature, by firstly dissolving appropriate masses of solid analytes in deionised water to make 0.1 M solutions of sodium hydroxide, sodium phosphate, disodium hydrogen phosphate and phosphate acid purchased from Sigma-Aldrich and of analytical grade. Appropriate volumes of each of these solutions were mixed to prepare buffer solutions and pH was measured using a pH meter.

2.2.6.2 Calibration Renishaw inVia

For the calibration experiments in Chapter 4 (section 4.1) , poly-L-lysine (PLL) solution (*ca.* 20 μl, 0.1 mg/ml) was deposited on the surface of a quartz slide or a gold 'chip' (cut glass slide coated with a thin layer of gold) glued onto a larger slide using Araldite. After *ca.* 2 hrs PLL solution was removed and MBA-NPs, 4MP-NPs or 2AET-NPs (*ca.* 20 μl) was dried onto the surface where PLL had been attached. Sticky wells were stuck to the slides to allow

buffer exchange between measurements. Buffers were added to the well before the laser was focused on NPs on the surface and SER spectra recorded (30 s acquisition, 10% laser power). After measurements for one buffer were complete, the buffer solution was removed, surface washed with water and a new buffer added.

2.2.6.3 Calibration Ocean Optics QE65 Pro

For dried NP measurements the procedure detailed in section 2.2.6.2 was followed for sample preparation and the laser spot was focused on an area of NPs and SER spectra acquired with 30 s acquisition time.

For solution calibrations, 2AET-NPs or NBA-NPs (20 μl) were mixed with the desired buffer (20 μl) on a gold 'chip' and pH of the mixture was recorded using a SevenGo Duo pro™ SG68 multi-parameter handheld meter (pH/ion/oxygen) with InLab® Micro pH electrode. SER spectra were then acquired from the solution with 30 s or 60 s acquisition.

2.2.6.4 Calibration WITec

Solutions of MBA-NPs were mixed with buffers in the pH range 0-12 (5:1 v/v) and solutions were placed in a 96 well plate. Three spectra for each pH were acquired directly from the wells using freshly prepared samples for each repeat and a 20 × air objective.

2.2.7 Intracellular SERS Measurements

2.2.7.1 Renishaw inVia

For cells in monolayer culture, 1×10^5 cells were plated on a coverslip in a 6 well plate or in a glass bottomed imaging dish of the same size. In general, the next day, growth medium was removed, cells washed with PBS and medium without FCS (SF media) added. After about 1 hour, functionalised NPs were added at a concentration of approximately 170 fM and cells were incubated overnight. The following day, medium was removed and cells washed before adding fresh medium (with FCS) and performing SERS measurements.

For MTS, cells were split into 25 cm^3 flasks (1:10 split of cells at approximately 90% confluence). Cells were incubated overnight before removing medium, washing and changing to serum free media. After about 1 hour, functionalised NPs were added at a concentration of approximately 170 fM and cells were incubated overnight. The following

day, cells were trypsinised and resuspended before forming hanging drops for MTS formation as detailed previously.

When performing SERS measurements in cells, a line focus laser was used. A rough map was firstly performed over a cell with an X step of 5.0 μm and a Y step of 3.56 μm and 2 or 3 s acquisition time at 50% laser power. Where a signal was observed in the resulting spectra, coordinates were noted and a more detailed map with an X step of 1 μm and a Y step of 1.19 μm and 30 s acquisition time at 10% laser power was recorded. This generated 147 spectra in just under 4 minutes.

2.2.7.2 WITec

2.2.7.2.1 MBA-NP pH Measurements

Medium was replaced with SF media containing MBA-NP solution in a 10:1 ratio (v/v) (100 fM). Incubations were carried out for 0.5, 1, 2, 4 and 12 hrs before washing cells with PBS and addition of buffers of pH 3.93, 6.21, 7.20 (PBS control), 8.60 and 11.35. SER maps were collected immediately from 5 cells under each condition. Only live and healthy cells were measured as determined by qualitative analysis of morphological features *e.g.* shape, adhesion. Integration time was 0.04 s with a single accumulation and laser power 10 mW with a spectral range of 0-2400 cm^{-1} recorded using a 600 g mm^{-1} grating. Maps were acquired using raster scans over single cells using a 60 × immersion objective and mapping step of 1 μm using a computer-controlled x,y-stage. Total mapping time for a single cell was *ca.* 5 min.

2.2.7.2.2 Multiplexed MBA-NP and AQ-NP Measurements

Cells were grown in plastic wells with glass bottom. 24 h after passaging medium was replaced by SF medium and left for 1 hour. Then, 200 μl of MBA-NP solution and 400 μl of AQ-NP solution were added to the SF medium in the wells and left for approximately 2 hours. Media was removed, cells washed with PBS and SERS measurements were carried out immediately. Integration time was 0.03 s with a single accumulation and laser power 10 mW with a spectral range of 0-2400 cm^{-1} recorded using a 600 g mm^{-1} grating. Maps were acquired using raster scans over single cells using a 60 × immersion objective and mapping step of 1 μm using a computer-controlled x,y-stage. Total mapping time for a single cell was *ca.* 5 min.

2.2.7.3 Ocean Optics QE65 Pro for MTS Measurements

For delivery of NPs (MBA-NPs, AQ-NPs, NQ-NPs or MBA-NPs and AQ-NPs) to different regions of MTS, different protocols were followed. In all cases, medium for cells growing in monolayer culture was exchanged for serum free (SF) medium for 1-2 hrs. For uniform distribution of NPs through MTS, cells in monolayer culture were then incubated overnight with NPs at a concentration of *ca.* 170 fM (for the combination of MBA-NPs and AQ-NPs 170 fM of both was added) before formation of hanging drops the following day and addition of 5 μl of medium every other day. For NP delivery to central regions of MTS the same protocol was followed. However, on the second day of MTS growth, 5 μl of medium was removed and 10 μl of cell suspension not treated with NPs was added. For NP delivery to intermediate and outer regions of MTS, MTS were grown from cells initially not treated with NPs. For delivery to intermediate region, 5 μl of cell suspension from cells incubated overnight with NPs (using the same procedure as previously, exchanging for serum free media and overnight incubation with NPs at concentration *ca.* 170 fM) was added on the second day of growth. For delivery to the outer region, 5 μl of cell suspension from cells incubated overnight with NPs (as previously) was added on the fifth day of growth. Spectra were collected on the sixth day of growth.

On the sixth day of growth, MTS in medium were pipetted onto a gold-coated glass slide. 5 consecutive SER spectra were collected from 3 MTS under each condition by focusing the laser spot on the MTS and using an acquisition time of 30 s.

2.2.7.4 New Renishaw inVia

MTS were prepared with a uniform distribution of MBA-NPs and AQ-NPs and only NQ-NPs by following the same procedure as in section 2.2.7.3 and set in collagen as described in section 2.1.4 in glass bottomed imaging dishes. A long distance 5 × air objective was used for all measurements. Depth scans were performed through the centre of MTS using using a 785 nm laser and 1400 cm^{-1} centre for MBA-NPs and AQ-NPs condition and 1580 cm^{-1} for NQ-NP condition. For MTS with MBA-NPs and AQ-NPs 20 μm (for high confocality) and 50 μm (for standard confocality) z step size were used and either 60 s or 30 s acquisition with 10% laser power. For xy map of the same condition 20 μm steps in x and y were used with 1 s acquisition and 50% laser power. For NQ-NP MTS depth scans 20 μm step size with 1 s

acquisition and 50% laser power and 50 μm step size with 0.5 s acquisition and 50% laser power were used with no pinhole.

2.3 Microscopy and Other Related Techniques

2.3.1 Transmission Electron Microscopy (TEM)

Monolayer cultured cells or MTS were fixed in 0.5% gluteraldehyde in 0.1 M sodium cacodylate or PBS for about 2 hours. Cells in monolayer culture were scraped and transferred to an eppendorf tube where they were pelleted by centrifugation before removing fixative and adding PBS. MTS were fixed in an eppendorf tube before removing excess fixative and adding PBS.

For cell preparation for TEM experiments for nanoparticle uptake investigation, medium was exchanged for SF media (as with SERS experiments) and cells were incubated overnight with 170 fM bare NPs, NQ-NPs, AQ-NPs, aminoAQ-NPs, CANLS1-NQ-NPs, TG-NPs, PLA-NPs, PEG800-NPs, 2AET-NPs, PEG6-NPs or PEG6-NQ-NPs as required. The following days cells were washed with PBS and fixed for monolayer culture preparation or grown into MTS for MTS experiments followed by 6 days growth and then fixing as described. For chloroquine treatment, cells were incubated overnight in SF media with 170 fM NQ-NPs and 1 μM chloroquine followed by washing and fixation steps.

Preparation of fixed samples for TEM was carried out by Steve Mitchell at the School of Biological Science, University of Edinburgh, and also personally at University of St Andrew's with the help of Christian Hacker (John Lucocq group). The procedure for the latter is detailed below. Samples prepared by Steve were examined on a Philips CM120 BioTwin transmission electron microscope (Philips Electron Optics, Eindhoven, The Netherlands) and images taken on a Gatan Orius CCD camera (Gatan, Oxon, UK).

Osmium tetroxide solution was prepared by mixing 1 part 4% osmium tetroxide, 1 part 6% potassium ferrocyanide, 1 part 0.4 M sodium cacodylate and 1 part dH_2O. Excess PBS supernatant was removed from the samples and osmium solution (100 – 200 μl per sample) was added and cells incubated for 10-15 minutes. Osmium solution was removed and the samples were washed with distilled water (3 x 5 min). Using a glass vial rotator for subsequent steps, 50% ethanol was added to the samples and they were transferred into

small glass vials. After 10 mins, 50% ethanol was removed and 70% ethanol added to each sample, making sure the sample did not dry out during exchange. A further series of graded ethanol steps were carried out (80%, 90%, 95% and 2 x 100%) with 10 min incubation per step. Following this 2 x 15 min propylenoxide incubations were carried out, before adding a 1:1 mix of epoxy resin in propylenoxide and incubating overnight with a sealed lid. The next morning, lids were removed from the vials and the samples were incubated for a further 3 hr on the rotator until the propylenoxide had evaporated. Cell fragments were taken out, gently blotted on filter paper, placed inside the PVC lids and fresh epoxy resin added. After a further 4 hours incubation, the blotting of fragments was repeated and the fragments were placed in PVC capsules for making the final blocks and filled with fresh epoxy resin. Capsules were placed in oven at 60 °C for 24 hr. 70 nm sections were taken using a diamond knife. Sections were positioned on copper grids and stained with lead citrate before examining and photographing with a Jeol JEM transmission electron microscope connected to a digital camera.

2.3.2 Helium Ion Microscopy (HIM)

Monolayer cultured cells grown on a coverslip and incubated overnight with functionalised NPs as described in section 2.3 or MTS grown with NPs as described in section 2.3 were fixed in 0.5% gluteraldehyde in 0.1 M sodium cacodylate or PBS. Samples were mounted on a sticky carbon stub and analysed using a Zeiss Orion Plus Helium Ion Microscope running at 30 kV with 10 μm aperture, an Everhart Thornley detector and charge neutralization achieved using an electron flood gun.

2.3.3 Scanning Electron Microsocpy (SEM)

Samples were prepared as for SEM and analysed using a Zeiss Ultra SEM.

2.3.4 Confocal Fluorescence Microscopy (CFM)

Cells were plated onto coverslips overnight (1-2.5 × 10^5 cells) in a 6 well plate. Phenol red free medium was used for CFM experiments. The following day, NP incubation was carried out as required and the day after, fluorescent staining was performed, followed by imaging.

Table 2.3 tabulates excitation lasers and emission filters used for the fluorescent stains (and reflection for NPs) used in this project.

Stain	Excitation laser (nm)	Emission filter (nm)
Reflection (NPs)	488	478-483 (Figure 6.11-6.13) 478-498 (Figure 6.8-6.9) 480-500 (Figure 6.6))
Reflection (NPs)	594	590-599 (Figure 6.7)
Lysosensor	488	502-597
DiD	633	645-749
NucBlue	405	413-478
TMRM	514	525-665

For bare NP and AQ-NP overnight incubation, medium was exchanged for SF media for 1-2 hrs before incubation with 170 fM bare NPs or AQ-NPs as required. For time course experiment staining was performed first followed by addition of NPs at a concentration of 170 fM immediately before acquiring images at 504 s intervals. For CANLS1, NLS2 and SBTPP NP overnight incubation, media was exchanged for SF media for 1-2 hrs before incubation with 340 fM CANLS1/NLS2/SBTPP-NPs (150 nm) or 340 fM NLS and 5.33 pM CANLS1/NLS2/SBTPP-NPs (50 nm). For overnight incubation, cells were washed the following day followed by fluorescence staining as required (see Section 2.1.8), and medium was replaced with phenol red free medium before transferring coverslips to holders for imaging.

Live cells were imaged in coverslip holders in media at 37 °C and 5 % CO_2 (with the exception of non cell samples, which were imaged under normal room conditions) using a Leica SP5 Confocal microscope, Leica LASAF software and a HCX PLAPO ×63/1.40-0.6 Oil CS objective or HCX PLAPO ×40/1.25 Oil PH3 CS objective. Table 2.3 documents excitation laser wavelength and emission filter wavelengths used for each stain in the project.

For reflection imaging of NPs in agar (Figure 6.6), equal volumes of agarose and bare NPs (150 nm) were mixed and set between a glass slide and coverslip. The agarose was heated in a microwave for *ca.* 1 min before mixing a small *ca.* 100 μl volume with an equal volume of bare NPs (150 nm). Then a small (*ca.* 50 μl) volume of the mixture was pipetted onto a glass

slide and a coverslip was placed on top before the agar set. Reflection from NPs was imaged as detailed above and in Table 2.3.

2.3.5 Photothermal Optical Coherence Tomography (OCT)

Photothermal OCT experiments were carried out by Pierre Bagnaninchi (University of Edinburgh) who provided the following procedure:

"The system used in this study was similar to the system used by Pai *et al.*[186]. The custom system is built around a commercial OCT engine (Callisto, Thorlabs) which consist of a spectrometer and a superluminescent laser diode (SLD) light source centred at λ_o= 930 nm with a FWHM bandwidth of 90 nm, providing a resolution of 5 μm in tissue.
The light beam was then collimated out of a single mode fibre onto a pair of galvanometers (Thorlabs), to form a custom laser scanning head (LSH) that raster the beam into an inverted microscope (SPi95, Brunel). Two *f*=50 mm double achromats in a telecentric configuration were used as the imaging lens. As opposed to conventional OCT the system was in a common path configuration where the first reflection from the sample was used as a reference. The common path configuration resulted in increased phase stability rejecting common noise more efficiently. Control and acquisition algorithms were written in labview and matlab. Spectra were collected at a rate of 1200 spectra per second. In depth intensity and phase information along the depth axis, Z, were retrieved by fast Fourier transform of the spectra after resampling in the k-space.

In order to introduce the excitation infrared laser (785nm), the illumination path of the inverted microscope was used. The excitation laser was modulated by an optical shutter operated at 330 mHz frequency, heating the gold nanocages at their absorption peak on and off. Thus producing a phase modulated at the excitation laser modulation frequency due to the local variation in temperature induced by the plasmonics photothermal effect.
The photothermal effect was measured by recording successive B scans (N=64) at the same location with an acquisition frequency of 3 Hz. A typical photothermal in depth mts cross-section dataset consisted in 64 time-lapse images (400x512 pixels (x,z)). Considering the small size of the mts, images were cropped down to 256 pixel in z to speed up image processing. The time varying phase in each pixel was then Fourier transformed and filtered in the spectral domain with a bandpass filter corresponding to the excitation laser frequency.

The amplitude was plotted as a heat map showing the distribution of the gold NPs in the mts. In addition, the mean intensity over successive Bscan was calculated to produce spheroids images. Finally, an overlay was built by combining the two using the thresholded mean intensity picture as a mask for the photothermal map. All pictures presented were 1.5mm in x by 0.625mm in z (depth)."

2.3.6 UV-visible Absorbance Spectroscopy

Solutions of NPs were measured using a Varian Cary 50 Bio UV/Visible Spectrophotometer to obtain their UV-Vis spectra. Solutions were measured in a 0.5 ml micro cuvette from 200-900 nm with baseline correction and fast scanning.

For work carried out at Jagiellonian University, electronic absorption spectra of NP solutions were measured using a UV-Vis-NIR Perkin Elmer spectrophotometer (model Lambda 35). Solutions were measured in quartz cells with 1 cm path length from 200-1100 nm with a resolution of 2 nm.

2.3.7 Bright Field Microscopy for General Cell Culture

Samples were viewed using a Meiji Techno TC5500 Inverted Epi-Fluorescence Microscope.

2.3.8 Microplate reader

A BIOTEK Syntergy HT microplate reader was used to measure absorbance while shaking at 570 nm and 690 nm for MTT assay results.

2.3.9 Fluorescence Spectroscopy CANLS1-NQ-NPs Washing

Fluorescence spectra were recorded using a Jobin Yvon Spex Fluoromax spectrofluorometer with excitation 490 nm and emission *ca.* 520 nm to analyse decrease in fluorescence at 520 nm after sequential washing of CANLS1-NQ-NPs in order to determine successful removal of excess CANLS1.

2.3.10 Slide Reader

Hypoxyprobe stained MTS sections were imaged using a Leica SCN400 slide reader and Leica SCN400 Client software.

2.4 Data Processing

2.4.1 pH Calibration

Spectra acquired from the Renishaw inVia system were analysed using Origin 9 software. Smoothing was performed 4 times using a Savitzky-Golay algorithm (9 point). An 8 point baseline was subtracted and peak heights were determined using the peak finding function and the 1st derivative method.

Spectra acquired from the Ocean Optics QE65 Pro system were analysed using Origin 9 software. An 8 point baseline was subtracted and peak heights were determined using the peak finding function and the 1st derivative method.

For spectra acquired on the WITec system, the relative intensity of bands corresponding to COO^- stretching (approximately 1400 cm^{-1}) and aromatic ring stretching (approximately 1590 cm^{-1}) were calculated using OPUS software and plotted against pH.

Origin 9 was used to fit a Boltzmann equation to calibration plots in each case. For intracellular pH experiments in section 4.2.2, following calculation of relative intensities of bands of interest using OPUS software, Gnuplot software was used to fit a curve to calibration data.

2.4.2 AQ-NP Calibration for Multiplexing

Analysis was performed using Origin 9. After smoothing (9 points, Savitzky-Golay) and manual baseline subtraction (8 points), two peaks were fitted in the region from 1500 cm^{-1} to 1800 cm^{-1} using the GaussAmp function. Peak centres were fixed to approximately 1606 cm^{-1} (C=C stretching) and 1667 cm^{-1} (C=O stretching), y0 was fixed to 0, and peak widths were fixed to 10 (for representative peak fitting see Fig S2). A calibration curve was generated by plotting the relative intensity of the fitted peak at 1667 cm^{-1} against that at 1606 cm^{-1} and Origin 9 was using to fit a Boltzmann equation to the calibration curve.

2.4.3 Standard Spectral Processing for Renishaw and Ocean Optics Spectra

Spectra acquired from the Renishaw inVia system were analysed using Origin 9 software. Smoothing was performed 4 times using a Savitzky-Golay algorithm (9 point smoothing). A

baseline was subtracted (8 points, spline, manually selected), and peak heights were determined using the peak finding function. Ratio of signal intensities of peaks of interest was used along with Boltzmann fitted equations from calibration experiments to determine the pH corresponding to each individual spectrum.

Spectra acquired from the Ocean Optics QE65 Pro system were analysed using Origin 9 software. An 8 point baseline was subtracted and peak heights were determined using the peak finding function and the 1st derivative method. Ratio of signal intensities of interest was used along with Boltzmann fitted equations from calibration experiments to determine the pH corresponding to each individual spectrum.

2.4.4 Investigation of Intracellular pH in Endothelial Cells

WITec Project 2.06 software was used to perform hierarchical k-means cluster analysis of SERS maps. Routine procedures were performed for cosmic ray removal and smoothing using a Savitzky-Golay algorithm (13 poins) in the region 200-1800 cm^{-1}. Cluster analysis was performed on each individual cell map. Classes were selected by comparing spectral profiles of their mean spectra. Analysis was started from 10-12 classes and where mean spectra were identical in the marker band region classes were merged. Mean SER spectra were used to calculate pH by comparison to calibration data.

2.4.5 Simultaneous MBA-NP and AQ-NP measurements

Hierarchical k-means cluster analysis of SERS maps was performed by using WITec Project 2.06 software. The spectra were analysed in the region of 400-1800 cm^{-1} after a routine procedure for cosmic ray removal and smoothing (13 points) using a Savitzky-Golay algorithm.

Spectra of resultant clusters were analysed using Origin 9 software. An 8 point baseline was subtracted from all spectra in the region 1000-1800 cm^{-1}. For spectra with only MBA signals, peak heights were determined using the peak finding function and the 1st derivative method. For spectra with both MBA and AQ signals, three peaks were fitted in in the region from 1500 cm^{-1} to 1800 cm^{-1} using the GaussAmp function. Peak centres were fixed to

approximately 1587 cm^{-1} and width 7 (MBA ring breathing), 1606 cm^{-1} and width 10 (AQ C=C stretching) and 1667 cm^{-1} and width 10 (AQ C=O stretching) and y0 was fixed to 0. Relative intensities of the signals at 1667 cm^{-1} and 1606 cm^{-1} were used to determine redox potential.

2.4.6 Statistics

Where data sets were compared for significant difference, Origin 9 software was used to perform One-Way ANOVA on data sets with significance at the 0.05 level.

2.4.7 New Renishaw inVia System

For depth and map scans, spectra were processed using Wire 4.1 software. Cosmic ray removal was performed using a width of features algorithm (width parameter 7, height parameter 15) followed by smoothing using a Savitsky-Golay algorithm (window size 9, polynomial order 3) and baseline subtraction. For MTS containing MBA-NPs and AQ-NPs spectra were normalised from 0 to 1 in the region of interest and for depth scans maps of intensity at point 1425 cm^{-1} were created using the mapping review feature or maximum intensity of signal between 1390 cm^{-1} and 1430 cm^{-1} as well as signal width and area was extracted manually from peak picking. For xy map maps of intensity at points of interest (1425 cm^{-1}, 1373 cm^{-1}, 1588 cm^{-1}) were created using the mapping review feature. For MTS containing NQ-NPs maps of intensity at points of interest (1635 cm^{-1} and 1582 cm^{-1}) were created using the mapping review feature along with ratio map of 1625 cm^{-1}/1582 cm^{-1} signal intensity.

2.4.8 Automated processing

Automated data processing for calibration of MBA-NPs and determination of pH from SER spectra of MBA-NPs in cells was developed and carried out by Kate Fisher.[187]

2.4.9 Confocal Fluorescence Microscopy

Image J was used to process initial results from CFM. Channels were split and manually filtered qualitatively before merging channels and extracting images.

For quantitative measurement Image-Pro Premier 3D 64 bit was used for image processing. Cell areas were extracted by selecting regions of interest in order to eliminate background reflection outwith the cell. Isosurfaces were created for each channel as well as colocalisation of reflection and fluorescence channels. Isosurfaces were manually filtered qualitatively and volumes for each isosurface extracted to allow determination of percentage of overlayed versus total reflection signal.

Chapter 3

From Monolayer to MTS

"Be so good they can't ignore you." – **Steve Martin**

Chapter 1 has outlined the importance of MTS as a more realistic *in vitro* model of the *in vivo* cellular environment and, in particular, as a model for cancer tumours and the resultant gradients that are commonly established in various important characteristics such as oxygen, nutrient and lactate concentration, as well as gene and protein expression. As discussed, the aim of this research was to establish quantitative information regarding this gradient, in particular with respect to redox potential, in MTS using SERS NPs previously developed for application in live monolayer cell culture.

In this chapter, the importance of 3D as opposed to 2D cell culture is further explored using imaging techniques, in particular TEM, SEM and HIM, to visualise the important differences in cell morphology and organisation of cells. Protocols for growing MTS and delivery of the SERS NPs were established, using these same imaging techniques to confirm NP uptake firstly in the particular cell type used in this research in monolayer culture and subsequently in the MTS models. Hypoxyprobe™ was used in attempt to visualise hypoxia in the MTS grown and act as a point of comparison when developing the SERS technique. Initial SERS measurements were then carried out and compared between monolayer and MTS culture highlighting areas for development.

3.1 Cell Morphology

To further emphasise the importance of MTS as an *in vitro* cell culture model in place of monolayer culture, imaging techniques were used to visualise some of the key morphological differences between the two culture techniques. In particular, the 3D as opposed to 2D environment and the presence of cell-cell and cell-ECM contacts in MTS were visualised. Figure 3.1 shows TEM images of cells grown in monolayer culture and as MTS. This high-resolution technique, which allows detailed subcellular features to be visualised, clearly shows the introduction of many cell-cell contacts in MTS compared to monolayer culture. This is apparent from the densely packed cells in Figure 3.1(b) from MTS, compared

to the individual cell in Figure 3.1(a) from monolayer culture, with some of the cell-cell contacts in MTS indicated by arrows in Figure 3.1(b).

In TEM preparation, samples need to be sectioned, so visualisation of the 3D environment was not possible. To achieve this, HIM was used. HIM is a relatively new technique that works in a similar way to SEM but uses helium ions in place of electrons for imaging samples.[135] A helium ions source, in comparison to an electron source, allows for better image resolution and contrast. This is because a helium ion beam can be focused onto a smaller probe size and excitation volume is reduced, as a result of higher source brightness and the shorter de Broglie wavelength of helium ions.[188] There is also an increase in secondary electrons produced per helium ion compared to electron – 2 to 8 compared to only 1 – providing higher contrast. In addition sample coating that can remove many of the surface features of the samples, and is commonly used in SEM to reduce charging at the sample surface, is not required for HIM.[189] Accumulation of positive charge from the helium ion beam can easily be charge neutralised using a low voltage electron beam, and therefore insulating samples can be imaged without the need for sample coating.

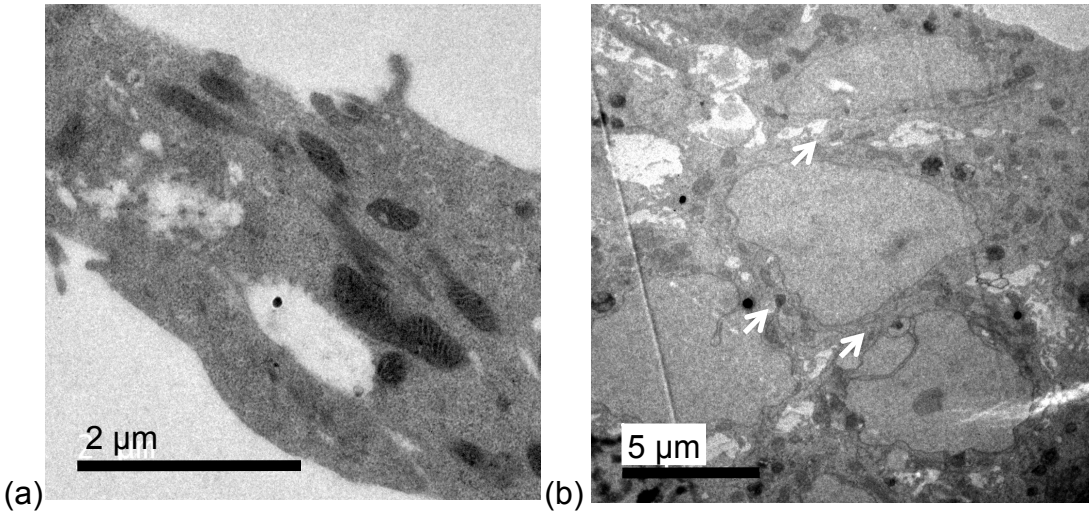

(a) (b)

Figure 3.1 shows TEM images of MCF7 cells in monolayer culture (a) and MTS (b) where differences in cell morphology can be visualised. Primarily, the presence of many more densely packed cells with many cell-cell contacts in MTS (b) were observed compared to the individual cell in monolayer culture (a). Some of these cell-cell contacts are indicated by arrows.

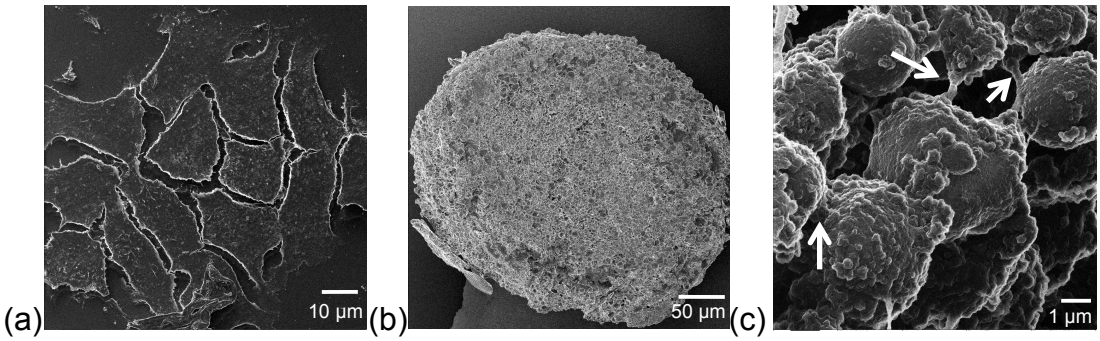

Figure 3.2 shows HIM images of MCF7 cells growing in monolayer culture (a) and as MTS with a larger field of view to image a whole MTS (b) and smaller field of view to image more detailed cell-cell interactions in MTS (c). The main features observed in MTS compared to monolayer culture, is the 3D environment and multiple cell-cell interactions. The flat nature of cells growing in monolayer culture is visualised in (a) compared to the 3D nature of cells growing as MTS, particularly apparent in (c). Many cell-cell contacts are also apparent in (c) and some are indicated by arrows.

Figure 3.2 shows HIM images of cells grown in monolayer culture and as MTS. The contrast between environments is clear – monolayer cultured cells appear very flat (Figure 3.2(a)), primarily in contact with the coverslip that they were growing on and previously, what would have been culture medium. In MTS, cells appear much more 3D (Figure 3.2(b) and (c)) with mainly cell-cell and cell-ECM contacts. Some of the cell-cell contacts apparent in the higher magnification MTS image are highlighted in Figure 3.2(c) with arrows. Figure 3.2(b) is a lower magnification image of the MTS, allowing the full MTS structure to be visualized as a spherical mass of cells, with a diameter of *ca.* 500 µm. The gradients being investigated arise from the 3D radial environment in MTS, in comparison to the flat monolayer culture cells with a generally uniform environment.

3.2 The Current 'Gold Standard' for Redox Measurements in MTS – Hypoxprobe™

Currently, the 'gold standard' technique for monitoring intracellular redox potential in MTS is small molecule probes such as Hypoxyprobe™, as discussed in Chapter 1 Section 1.4.3.2. This is a 2-nitroimidazole derivative (see Figure 1.27(a) for structure), which is metabolised in hypoxic regions (nitro group reduced to amine), and the metabolised product is detected using IHC. This technique, however, has many limitations. Samples must be fixed and

sectioned and therefore live cell measurement is not possible. It also only acts as an on/off 'switch', indicating whether the environment was above or below a particular hypoxic limit and does not provide quantitative information. Essentially, it is only reporting two states – above a certain hypoxic limit or redox potential or below this limit. These probes have, however, had use in applications considering radiotherapy resistance, as this limit correlates well with that for radioresistance.[190] The scope for development of new techniques for monitoring redox potential in live MTS quantitatively is large. This could provide a vital platform for drug and therapy development and monitoring response to treatment.

To provide a point of comparison, MCF7 cell MTS were grown and stained with Hypoxyprobe™ (Figure 3.3(a)). The majority of work in this project uses MCF7 breast cancer cells, as they were readily available and known to form MTS easily. Therefore, these cells provided a model system for improvement of analysis of intracellular redox potential in MTS. Interestingly, MCF7 cells did not show any positive stain for Hypoxyprobe™ in contrast to positive control BT474 (also breast cancer) MTS (Figure 3.3(b)). MCF7 cell MTS were noticeably smaller than the large BT474 cell MTS, which could have been a contributing factor. Lack of staining for Hypoxyprobe™ serves to further emphasise the need for more quantitative analysis techniques as this indicator only stains if cells reach a particular hypoxic state. It is likely that gradients exist in the MTS, but that the MTS have not yet grown to the extent of developing an extreme hypoxic core that would be detected by Hypoxyprobe™.

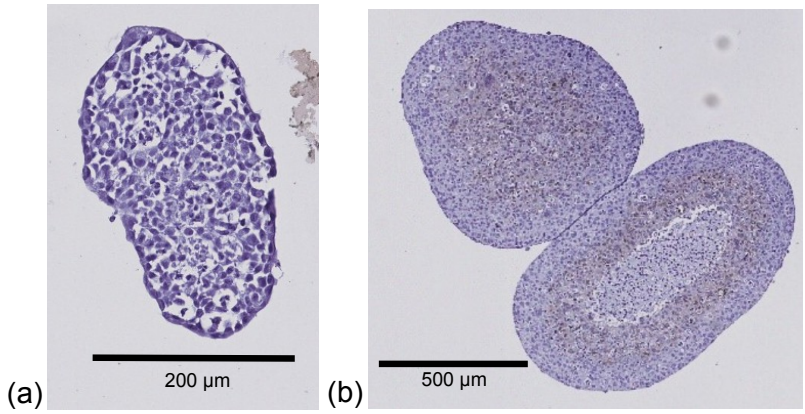

Figure 3.3 shows MCF7 cell MTS stained with Hypoxyprobe™ (a) and positive control BT474 cell MTS stained with Hypoxyprobe™ (positive control BT474 section provided by Peter Mullen, University of St Andrews).

3.3 Nanosensor Uptake

Before moving onto SERS measurements, it was important to confirm uptake of nanosensors into MCF7 cells for the first time and confirm that they were not toxic to the cells. It was also necessary to establish a technique for uptake of nanosensors into MTS.

Primarily, TEM was used to confirm nanosensor uptake. For the standard monolayer culture, cells were incubated overnight with 150 nm nanosensors, as described in Chapter 2 Section 2.2.3.1. The following day, when cells would usually be taken for SERS measurements, they were fixed and processed for TEM as described in Chapter 2 Section 2.3.1. Figure 3.4 shows examples of TEM images for nanosensor uptake in monolayer cultured MCF7 cells. This confirmed uptake. Interestingly, some nanosensors were found on the outside of cells attached to the cell membrane as in Figure 3.4(a). This was not expected, as the cells were washed multiple times before fixing to remove NPs outside cells. However, it is possible that these NPs were in the process of being taken up into cells and therefore attached to the cell membrane. It was also apparent that some NPs were present inside vesicles in the cells, as in Figure 3.4(c). Ideally all NPs would be found in the cytosol, as this is the environment being probed in this work.

Previous work with these NPs revealed no cytotoxicity to NIH/3T3 mouse fibroblast cells.[92] This was confirmed in the MCF7 cell line using the MTT assay as described in Chapter 2 Section 2.1.6. Results are shown in Figure 3.5, revealing that bare NPs, NQ-NPs and AQ-NPs had no toxic effect on MCF7 cells when cells were incubated overnight with these NPs.

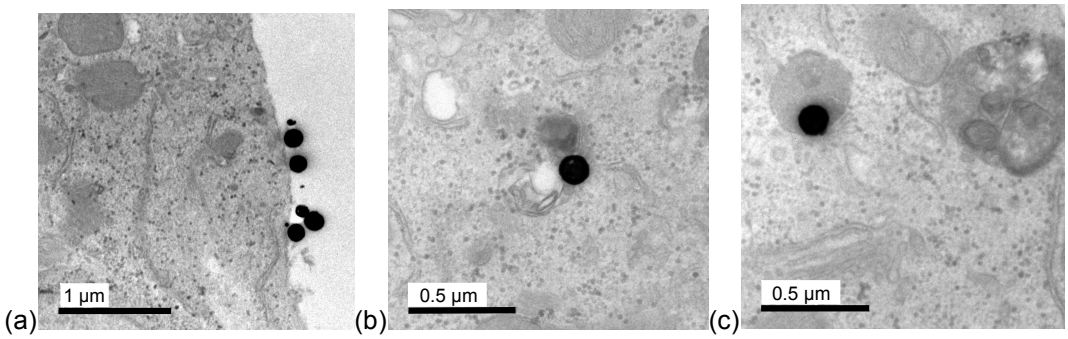

Figure 3.4 (a)-(c) illustrate TEM images obtained for MCF7 cells grown in monolayer culture and incubated with NQ-NPs overnight before fixing. NQ-NPs were visible on the outside of cells (a), in the cytosol (b) and inside vesicles in the cells(c).

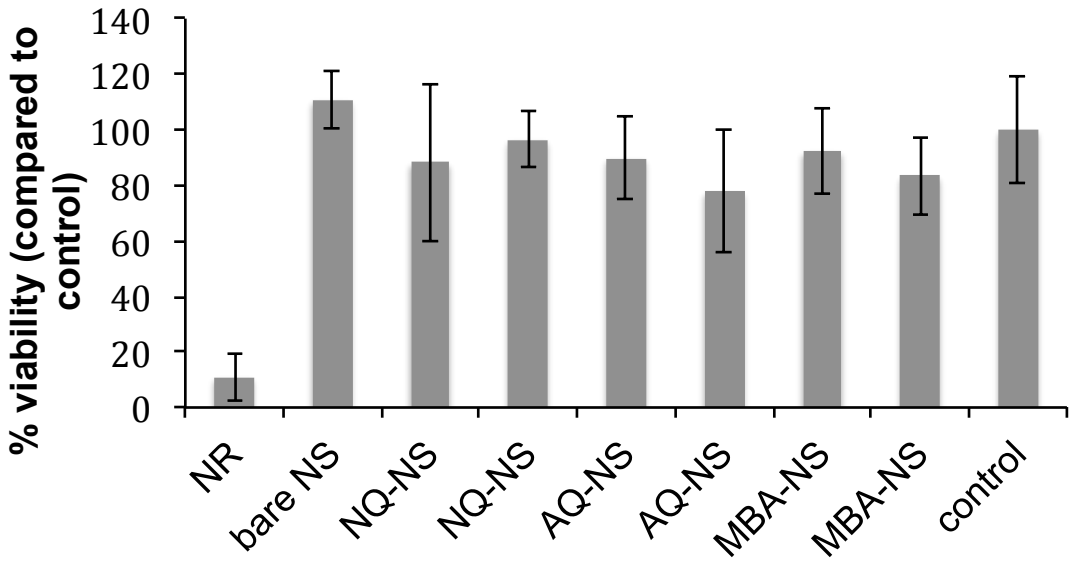

Figure 3.5 shows cytotoxicity results for MCF7 cells treated with NPs functionalised with different molecules and nanorods (NRs) overnight. % viability compared to control was assessed and only displayed cytotoxic effect for NRs. This was expected as NRs were coated with CTAB, which is toxic to cells.

The exact mechanism of NP uptake into cells, and transport within cells is not fully understood. Therefore, attempts to increase the number of NPs delivered to the cytosol relative to vesicles proves challenging. It has been suggested that the primary mode of uptake of NPs to cells is through various forms of endocytosis.[191] During endocytosis, the material, in this case NP, entering the cell is internalised into an early endosome as shown in Figure 3.6. There are various forms of endocytosis, with some of the primary mechanisms illustrated in Figure 3.6. Clatharin-dependent and caveolin-dependent endocytosis are receptor mediated processes, with the binding of NPs to the surface of the cell initiating the process. It is possible that the redox active molecules functionalised onto the NPs used in this work could allow binding to cell surface receptors to mediate these endocytosis mechanisms. Macropinocytosis is a form of fluid-phase uptake where the cell engulfs extracellular fluid by pinching off its plasma membrane. This can occur when NPs interact by hydrophobic or electrostatic interaction with the outer membrane, the most probable mechanism for the NPs used in this work.

Following uptake into an early endosome via any of these processes, the early endosome can then progress to a recycling endosome, and the contents of this can then be excreted from the cell. Alternatively, the early endosome can mature to a late endosome then lysosome, at which point it can be released into the cytosol, and potentially transported to various organelles as illustrated in Figure 3.6. The typical time course of endocytosis from internalisation to lysosome is less than one hour[192], and therefore for the experiments in this project, in which the typical incubation time with NPs was 24 hrs, it would be expected that NPs, if taken up via endocytosis, would have progressed to lysosomes and been released into the cytosol. However, it was reported by Salvati *et al.*[193] that NPs accumulate in lysosomes, which would explain why some NPs could still be observed within vesicles in the TEM images. It is possible that some NPs may be taken up directly into cells (Figure 3.6), but this is unlikely to be the primary uptake mechanism unless NPs are particularly small or have been modified to promote this uptake mechanism. Even in this case, NPs can end up inside vesicle structures as demonstrated in Figure 3.6.

Many studies have reported modifying NPs with, for example, small molecules or peptides, to either initiate release from vesicles, or to promote direct uptake pathways that avoid endocytosis. For example, Guarnieri, D. *et al.*[194] used the membranotropic peptide gH625 to modifiy the surface of polystyrene nanoparticles, which consequently evaded endocytosis, and were taken up directly into cells via membrane translocation. Understanding and modifying uptake mechanisms of NPs into cells does, however, remain an area of much difficulty and uncertainty. Chapter 6 will investigate in more detail some of the methods investigated for increasing the proportion of NPs delivered to the cytosol, and decrease the number retained in vesicles. Chapter 6 will also introduce quantitative measurement of the number of NPs in the cytosol relative to vesicles, and attempts will be made to modify this. This includes investigating how uptake can vary between cell lines, and modifying NPs with different small molecules and peptides.

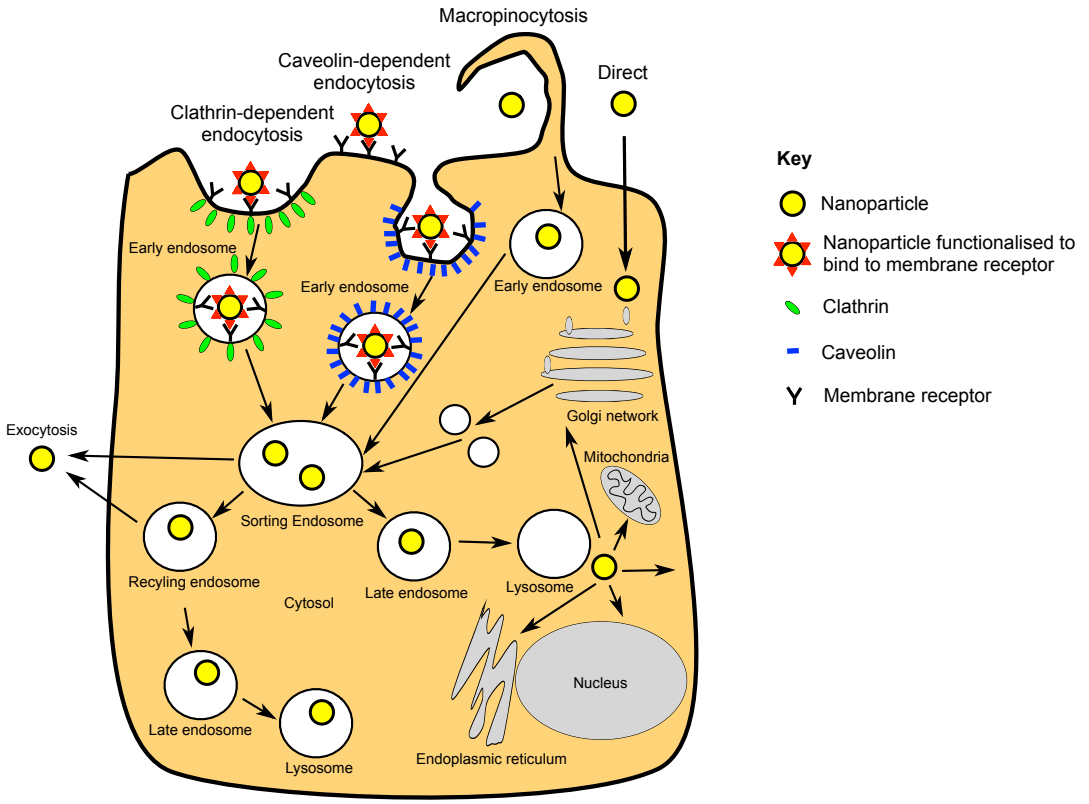

Figure 3.6 illustrates some of the primary uptake mechanisms for NPs into cells. The main mechanism is via endocytosis, which can take many forms. These include clatharin-dependent and caveolin-dependent endocytosis that are receptor mediated processes, and macropinocytosis, where NPs interact with the cell surface via hydrophobic or electrostatic interaction and are engulfed in a fluid-phase uptake process. In all cases, NPs are taken up into an early endosome, which can either progress to a recycling endosome, and contents are released by exocytosis, or progress to a late endosome and lysosome, eventually potentially escaping into the cytosol.

For the purpose of this chapter, the next stage was to deliver NPs to MTS. When moving from monolayer culture to MTS, it was proposed that incubation with NPs could still be performed in monolayer culture overnight, before culturing the resultant cell suspension in hanging drops to form MTS over a subsequent number of days, usually six. This method was simple, but relied on the NPs remaining in cells for prolonged periods of time, which had not been previously investigated. Therefore, an experiment in monolayer culture was carried out to confirm that NPs remained in cells over these prolonged time periods, by incubating cells with NPs overnight before washing the next day and allowing growth for a

subsequent six days before fixing cells for TEM. Figure 3.7 shows representative images of NPs in MCF7 cells after this time period and confirmed NPs remained in cells. Again, as with overnight incubation, some were found inside vesicles.

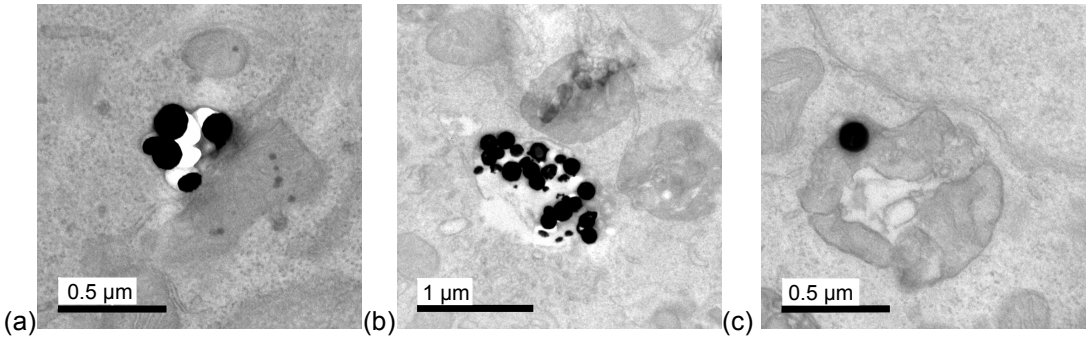

Figure 3.7 (a)-(c) illustrate TEM images obtained for MCF7 cells grown in monolayer culture and incubated with NQ-NPs for 24 hours followed by a further six days growth in monolayer culture before fixing.

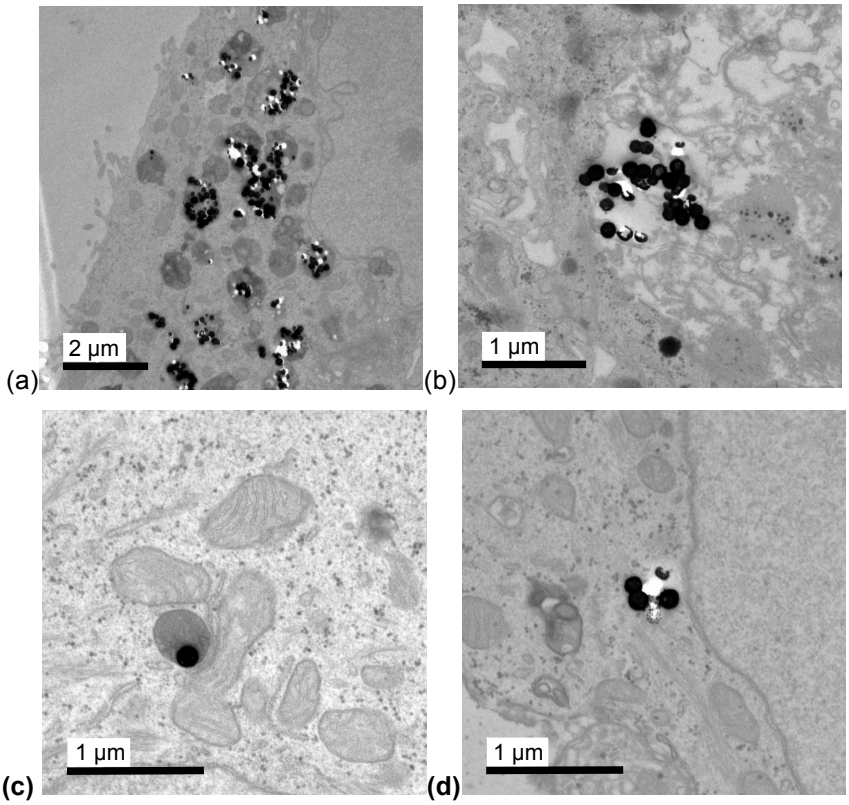

Figure 3.8 (a)-(d) illustrate TEM images obtained for MCF7 cells grown in monolayer culture and incubated with NQ-NPs for 24 hours followed by a further six days growth as MTS before fixing.

Finally, MTS were grown from the cell suspension formed from trypsinising monolayer cultured cells incubated overnight with NPs, at the same concentration as for previous experiments in monolayer culture (170 fM NPs). While initially attempts were made to form MTS using the spinner flask method, this was replaced with a simple hanging drop method, due to equipment and cost limitations. Cell suspension was cultured in 20 μl drops on the lid of a Petri dish, as detailed in Chapter 2 Section 2.1.3, which resulted in formation of MTS. Figure 3.8 shows TEM images of these MTS after a further six days growth, following formation of hanging drops. Clearly NPs were still present and again a proportion of these were observed inside vesicles as opposed to the cytosol.

HIM was also used to investigate uptake of NPs. As this technique is highly surface sensitive it was not useful for confirming uptake of NPs in MTS, in which very few NPs would be expected to be present on the surface of MTS. Even in sectioned samples, HIM was so surface sensitive that only blade marks where the sample had been cut could be seen. Despite washing steps before fixing, NPs were still present on the surface of cells grown in monolayer culture and could be visualised by HIM. Dried NPs were also imaged to investigate if there were any significant differences in appearance between unfunctionalised NPs (Figure 3.9(a)), NQ-NPs (Figure 3.9(b)) and AQ-NPs (Figure 3.9(c)). No significant difference was observed.

When imaging NPs interacting with cells, it was predominantly NPs interacting with the surface of cells that could be seen. However, in some cases, for example the two on the left in Figure 3.10(c) and some areas of Figure 3.10(e and f), some NPs could be seen just below the surface. Interestingly, NPs functionalised with different reporter molecules appeared to interact differently with cells. AQ is more hydrophobic than NQ and NPs functionalised with AQ appeared to aggregate much more, appearing in clumps on the surface of cells (Figure 3.10(e-f)), while NPs functionalised with NQ tended to be more dispersed (Figure 3.10(a-d)). Clumps of AQ-NPs were also found outside cells in what appeared to be ECM (Figure 3.10(g-h)).

.

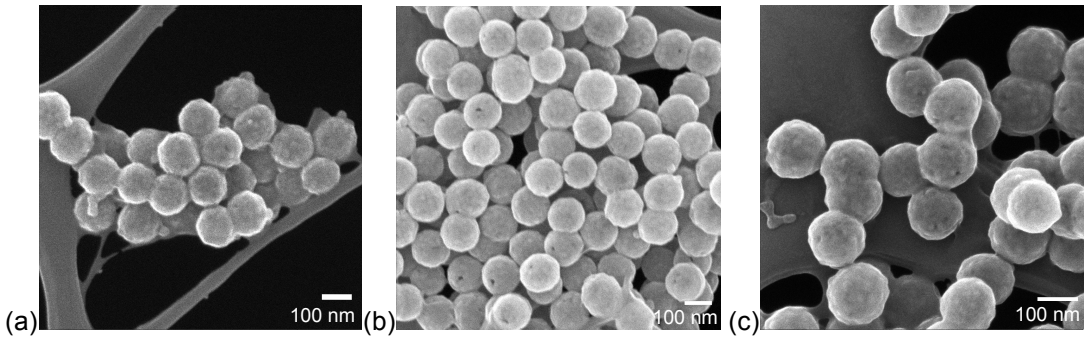

Figure 3.9 shows HIM pictures of unfunctionalised NPs (a), NQ-NPs (b) and AQ-NPs (c)

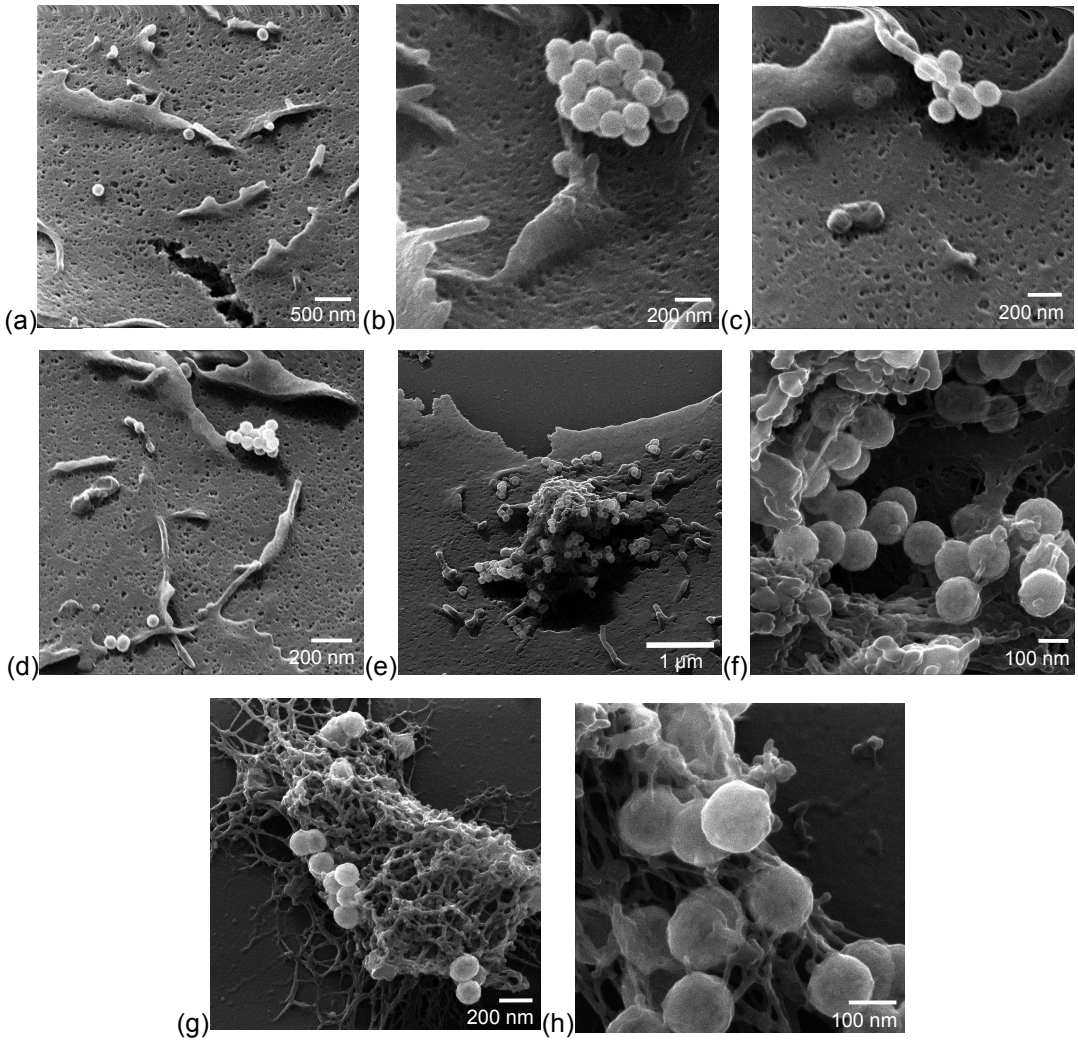

Figure 3.10 shows HIM images of functionalised NPs interacting with MCF7 cells in monolayer culture – (a-d) are NQ-NPs and (e-h) are AQ-NPs. In some cases the interaction is with some extracellular material (g and h).

While HIM did not provide any useful information to confirm NP uptake in MTS, SEM was used to visualise NPs in MTS. This was possible as backscattered electrons can be used to image samples in SEM in addition to secondary electrons.[195] Backscattered electrons allow visualisation of features just below the surface of samples as opposed to only surface features visualised by secondary electrons. Figure 3.11(a and c) show regions of MTS imaged with secondary electrons and Figure 3.11(b and d) show the same regions imaged with backscattered electrons. Firstly, the difference in image resolution between SEM and HIM is apparent. Secondly, backscattered electron detection confirmed the presence of NPs in MTS.

So far, these high resolution techniques have failed to provide spatial information regarding NP distribution in MTS. It was hypothesised that NPs may be predominantly present in the central areas of MTS, as incubation was carried out prior to MTS formation from the resultant cell suspension, which aggregated and grew radially into MTS. Therefore, it was thought that the NPs would remain near the central regions of MTS as new cells grew radially from there. However, Salvati *et al.*[193] demonstrated that NPs were divided equally between daughter cells during cell division, suggesting that NPs could become distributed throughout the whole MTS as it grew by cell division. Immunohistochemistry (IHC) analysis of MTS sections with and without NPs and stained with haematoxylin and Hypoxyprobe™ revealed uniform distribution of NPs through MTS (Figure 3.12). In MTS grown from cells containing NPs, dark haematoxylin stained 'speckles' are clearly visible and not present in MTS with no NPs. This suggests that these 'speckles' of haematoxylin stain, are a result of the haematoxylin associating with the NPs inside the cells. Haematoxylin is standardly used as a DNA stain as it binds to negatively charged compounds.[196] It is possible that haematoxylin could be associating with the NPs as a result of a charge effect, if the NPs had a negative surface charge.

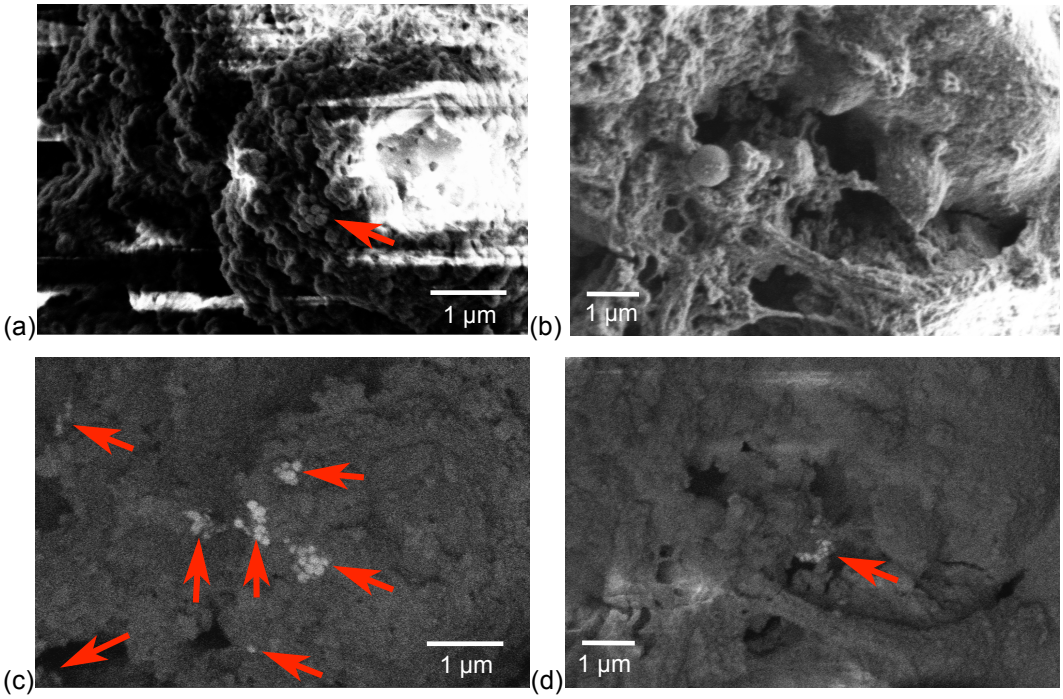

Figure 3.11 shows SEM images of regions of MCF7 cell MTS where the same area was imaged with secondary (a and c) and backscattered (b and d respectively) electrons. Red arrows point to areas where NPs are visible.

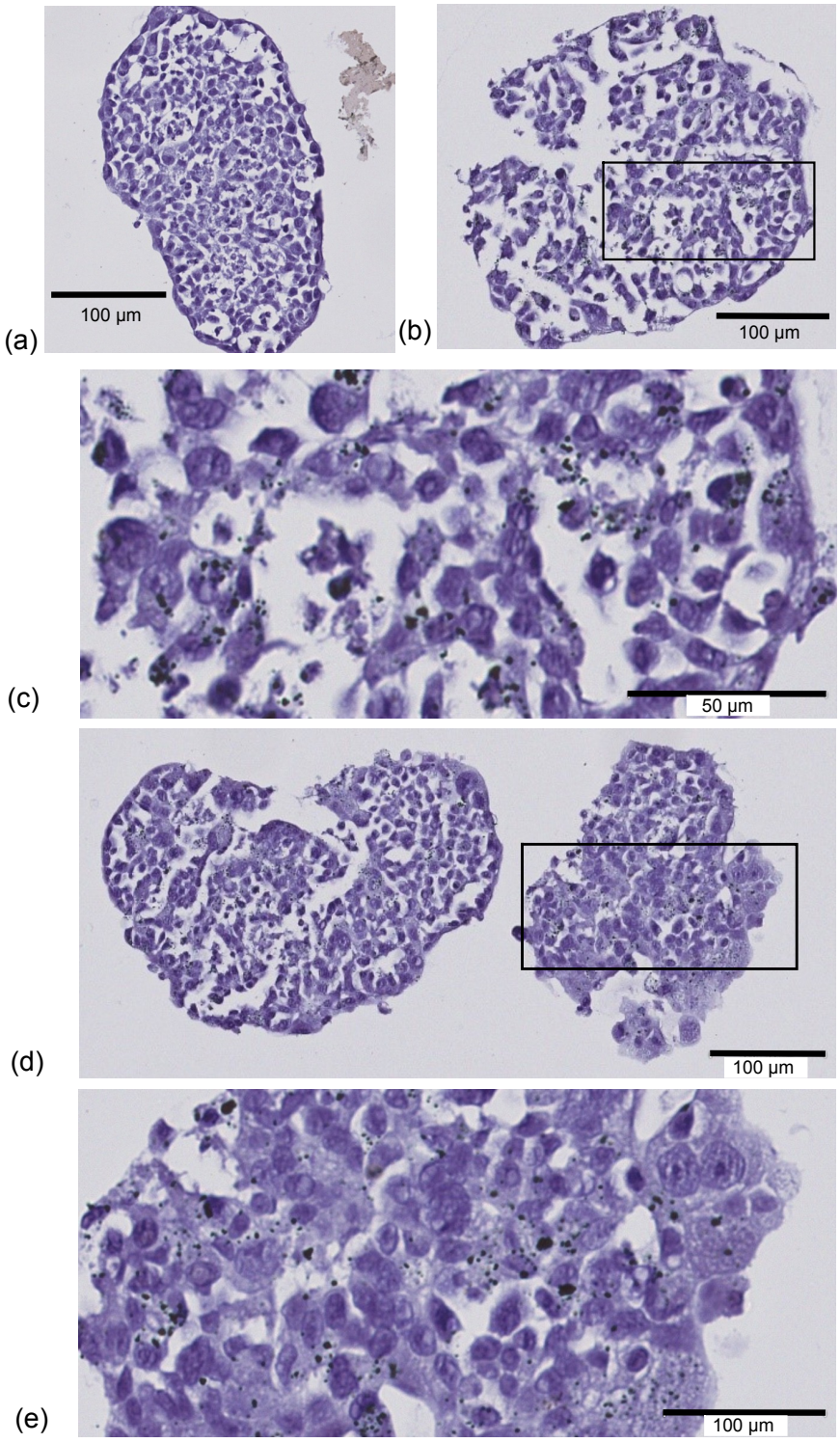

Figure 3.12 shows images of paraffin embedded and sectioned MTS stained with Hypoyprobe™ and haematoxylin. Control MTS stained with haematoxylin but without NPs (a) did not display the same dark 'speckles' as MTS stained with haematoxylin with NPs present (b-e). These dark 'speckles' were therefore attributed to NPs. Magnified areas of (b) and (d) are shown in (c) and (e) respectively with boxes highlighting magnified areas.

3.4 SERS – From Monolayer to MTS

3.4.1 Preparation of NQ-NPs

NPs were successfully functionalised with NQ as described in Chapter 2 Section 2.2.3.1. UV-visible absorbance spectra of the functionalised NPs before and after washing (Figure 3.13(a)) showed a slight drop in absorbance as a result of NP loss in the washing steps, and, importantly, removal of excess NQ was seen by the absorbance decrease between 200 nm and 300 nm. SERS of the dried functionalised NPs (Figure 3.13(b)) showed the characteristic NQ signals at approximately 1577 cm^{-1} (ring breathing) and 1645 cm^{-1} (C=O stretching). NQ, when not functionalised onto NPs, gives no Raman signal, and therefore it could be concluded that this was a SER spectrum, confirming NP functionalisation.

3.4.2 SERS of NQ-NPs in MCF7 Cells in Monolayer Culture

MCF7 cells were plated and incubated with NQ-NPs for 24 hours, as described in Chapter 2 Section 2.2.7.1, before carrying out SERS on the cells. Cells were incubated with NQ-NPs in medium containing 10% FCS and medium containing no FCS. From previous results, reported by Ochsenkühn *et al.*[92], the standard procedure uses FCS free media during incubation with NPs as experiments carried out in NIH-3T3 mouse fibroblast cells showed that NQ-NPs were taken up free into the cytosol in this case but were found in vesicles and with protein coats also when FCS was used during incubation with NQ-NPs, attributed to proteins from the FCS coating the NPs. Using FCS free media also led to an increased uptake of NQ-NPs.[92] Bonifacio *et al.*[197] also reported, for *ex vivo* serum and plasma samples, when filtration was carried out to remove most of the proteins in these samples, SER spectra showed a significant increase in intensity. This supports the finding that serum proteins, present in FCS for *in vitro* cell experiments, can interact and interfere with SERS nanosensors.

Results from incubation with and without FCS in the culture medium agreed, with a mean of –261 mV without FCS during incubation and –260 mV with FCS during incubation, when all spectra under each condition were averaged. A one-way ANOVA confirmed that means were not significantly different at the 0.05 level. Figure 3.14 illustrates a boxplot of redox potential values calculated under each condition, with statistical values given in Table 3.1.

Figure 3.15 shows a representative spectrum from cellular measurements giving a redox potential of –261 mV.

Each spectrum containing a SERS response from NQ-NPs was processed as described in Chapter 2 Section 2.4.3, by firstly smoothing followed by subtraction of a baseline and peak finding to extract the intensities of the peaks at approximately 1580 cm^{-1} and 1630 cm^{-1}, which were converted to a redox potential value as described in Appendix 1. Briefly, the 1630 cm^{-1} peak, corresponding to the C=O stretch frequency of NQ, increases in intensity relative to the 1580 cm^{-1} ring breathing peak, as the redox potential of the environment becomes more oxidising. This is because the C=O stretch peak at 1630 cm^{-1} is only present in the oxidised form of NQ, while the ring breathing peak at 1580 cm^{-1} is present in both oxidised and reduced forms of NQ. Therefore, increasing relative intensity of the peak at 1630^{-1} to 1580 cm^{-1} corresponds to a greater proportion of NQ in oxidised as opposed to reduced form, which reflects on the redox potential of the environment. Taking this ratio and comparing to calibration experiments (Appendix 1), an absolute redox potential value was generated for any NQ-NP spectrum.

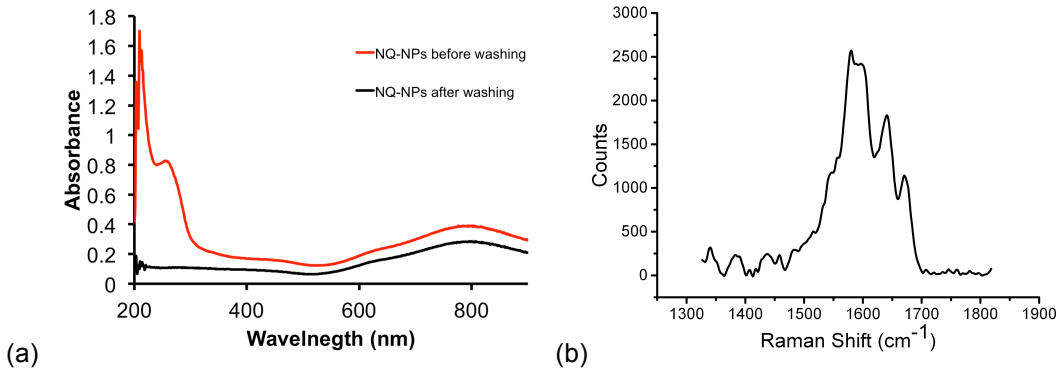

Figure 3.13 (a) illustrates the UV-visible absorbance spectrum of NQ-NPs (150 nm nanoshells described in Chapter 2 Section 2.2.2 with a plasmon resonance at *ca.* 785 nm, functionalised with NQ as described in Chapter 2 Section 2.2.3.1) before (red line) and after (black line) washing steps following functionalisation and (b) illustrates the SER spectrum of dried NQ-NPs confirming functionalisation.

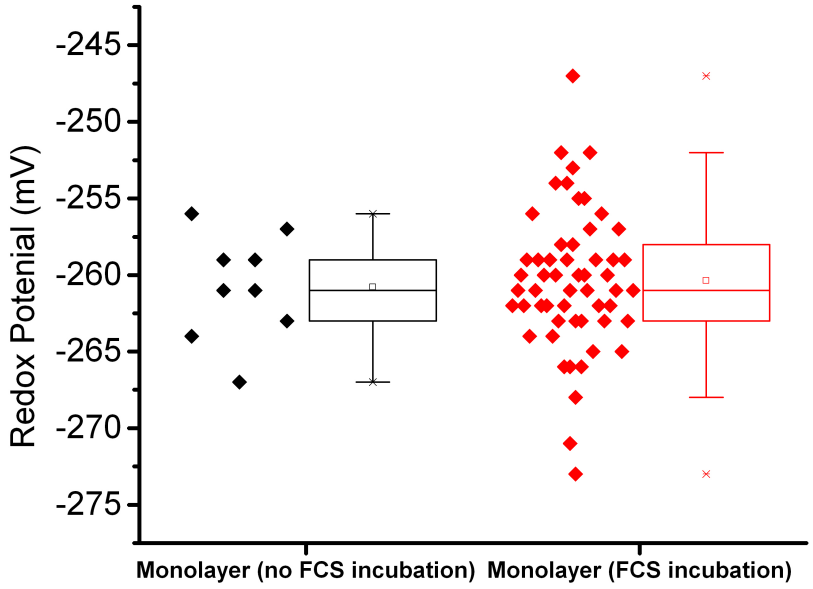

Figure 3.14 illustrates the distribution of redox potential values calculated using SERS of NQ-NPs in MCF7 cells in monolayer culture, where incubation was carried out with and without FCS in the culture medium. A one-way ANOVA confirmed that means were not significantly different at the 0.05 level.

Table 3.1 illustrates the statistics for redox potential values calculated using SERS of NQ-NPs in MCF7 cells in monolayer culture, where incubation was carried out with and without FCS in the culture medium.

	Monolayer NQ-NPs without FCS	**Monolayer NQ-NPs with FCS**
n	9	55
Mean (mV)	–261	–260
Standard Deviation (mV)	3.5	4.6
Maximum (mV)	–256	–247
3rd Quartile (mV)	–259	–258
Median (mV)	–261	–261
1st Quartile (mV)	–263	–263
Minimum (mV)	–267	–273

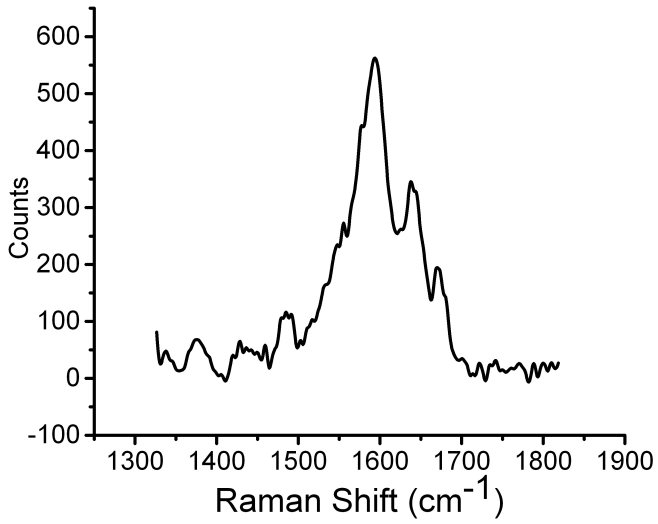

Figure 3.15 shows a representative NQ-NP spectrum from measurements performed in MCF7 cells in monolayer culture. This particular spectrum gives a redox potential value of –261 mV.

3.4.3 SERS of NQ-NPs in MCF7 Cells in MTS

After applying the previously established technique to MCF7 cells in monolayer culture, work began to expand this technique to MTS. It was hypothesised that the location of the NQ-NPs in the MTS would depend on the point at which the NQ-NPs were added during MTS growth. One option for the addition of NQ-NPs to MTS was to incubate the cells for 24 hours with NQ-NPs in monolayer culture, as previously, before growing MTS from the resultant cell suspension when trypsinised. It could be hypothesised that using this procedure the location of NQ-NPs would be expected to be in the central regions of the MTS. Further work could investigate adding NQ-NPs at various points during MTS growth to control the location of NQ-NPs in the MTS. Future work discussed in Chapter 5 will focus largely on establishing the distribution of NPs in MTS and how this changes when NPs are added at different points in MTS growth. Figure 3.12 has already suggested a uniform NP distribution in MTS grown from cells originally incubated overnight with NPs in monolayer culture before MTS formation. Salvati *et al.*[193] also demonstrated that NPs were divided equally between daughter cells during cell division, supporting the results that NPs would be distributed throughout MTS if grown in this manner.

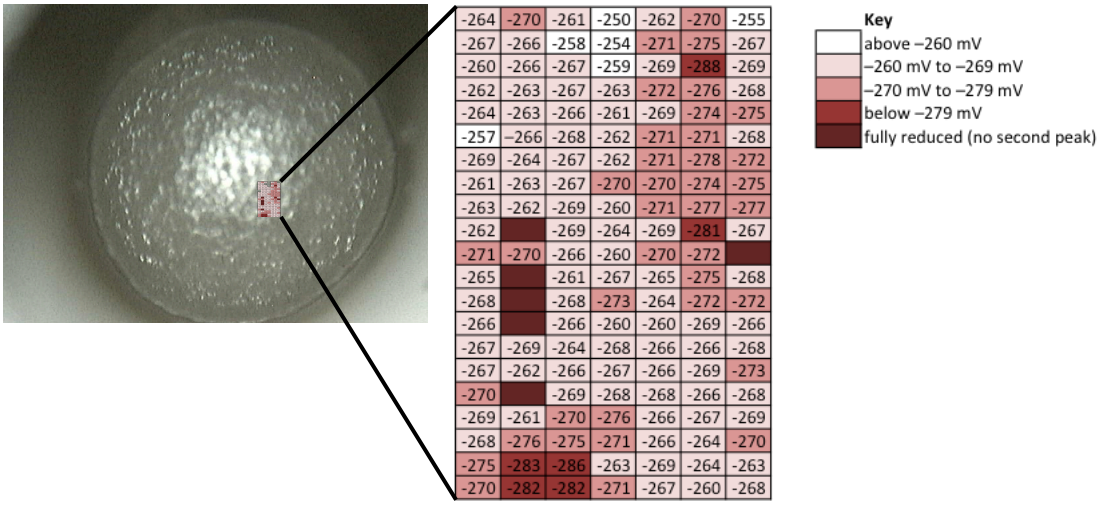

Figure 3.16 shows a white light image of a single MTS (× 10) and an illustration of the initial method used for MTS mapping where a small region (7 × 25 μm) of the MTS was mapped. An example of the redox potential values obtained from a single map are shown.

SER spectra of NQ-NPs in MTS were obtained successfully. Initially, spectra were obtained by mapping small regions of MTS (Figure 3.16), grown using the hanging drop method, from cells incubated with NQ-NPs in monolayer culture as detailed in Chapter 2 Section 2.2.7.1. The number of spectra obtained for a single map was much greater than that for monolayer experiments, possibly due to the additional z direction from which out of focus signals could be obtained. Figure 3.17 illustrates the distribution of redox potential values obtained from a single map of NQ-NPs in MTS compared to the previously obtained values in monolayer culture and Table 3.2 gives the statistics.

The mean redox potential of –268 mV was lower than that for monolayer culture (–260 mV), which would be expected due to the contribution from the more central hypoxic regions of the MTS. The standard deviation for MTS was also larger, again as expected due to the development of gradients spanning a wide range of potentials. Many of the spectra did not have a clear peak for the C=O stretch (at between 1630 cm^{-1} and 1648 cm^{-1}) and therefore, instead of recording the intensity of the peak corresponding to the oxidised species, the intensity of the largest noise peak in this region was probably being recorded. For this reason, many of the spectra could have been at the fully reduced limit of NQ-NPs and therefore the mean redox potential would have been even more reduced. The fully reduced limits of NQ-NPs corresponds to spectra where the C=O stretching signal at *ca.* 1630 cm^{-1} is

no longer observed. This signal may still be present at a low intensity under the other signals in the spectrum. However, when the peak intensity cannot be extracted for this peak, it is beyond the limits of this sensor. This peak disappears with decreasing redox potential of the environment, as less NQ molecules exist in the oxidised form with the C=O stretching frequency. Appendix 1 gives more detailed results from calibration of NQ-NS, where the changing intensity of the C=O stretching frequency peak can be observed relative to redox potential. At the other extreme, NQ-NPs could reach their measurable limit at the oxidising end. This occurs when the C=O stretching signal no longer increases significantly with increasing redox potential, corresponding to all NQ-NPs becoming oxidised.

There were some cases where this C=O stretch signal was not measureable and therefore the redox potential was definitely below the reduced limit of the NQ-NPs. Figure 3.18(a) shows an example of this case. Figure 3.18(b) shows the spectrum giving the most oxidised redox potential reported for this particular map. However, the signal-to-noise ratio was low, further highlighting the noise problem discussed. Due to the large number of spectra at the fully reduced limit of NQ-NPs, there was a need to use a new sensor molecule that could report on more reducing potential values.

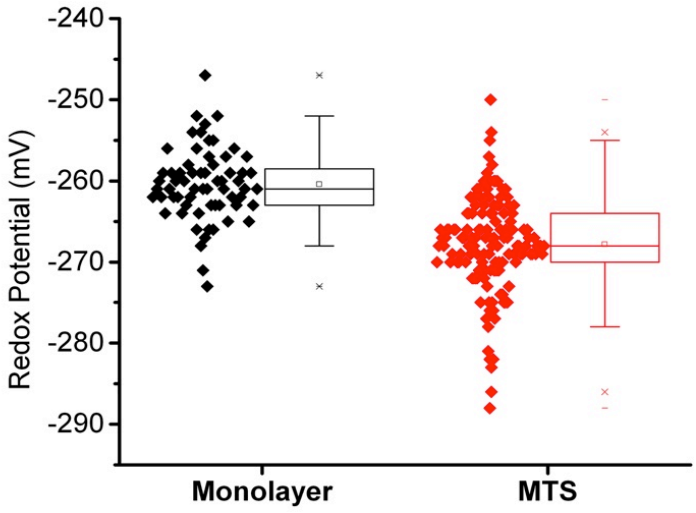

Figure 3.17 illustrates the distribution of redox potential values calculated using SERS of NQ-NPs in MCF7 cells in MTS for a single map, compared to values obtained for MCF7 cells in monolayer culture, from Section 3.4.2.

Table 3.2 presents the statistics for redox potential values calculated using SERS of NQ-NP in MCF7 cells in MTS for a single map, compared to values obtained for MCF7 cells in monolayer as discussed previously.

	NQ-NPs monolayer	NQ-NPs MTS
n	64	141
Mean (mV)	–260	–268
Standard Deviation (mV)	4.5	5.9
Maximum (mV)	–247	–250
3rd Quartile (mV)	–259	–264
Median (mV)	–261	–268
1st Quartile (mV)	–263	–270
Minimum (mV)	–273	–288

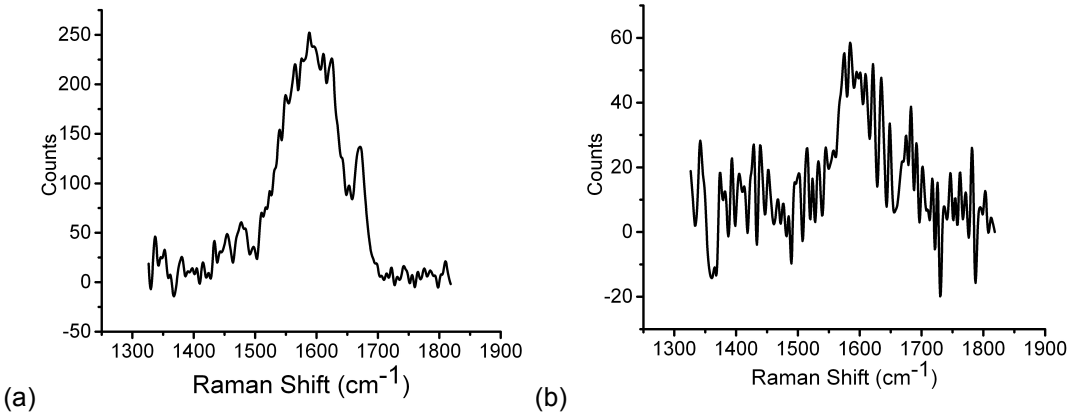

Figure 3.18 shows examples of spectra obtained from SERS mapping of NQ-NPs in a single MTS. An example of a spectrum that reported a fully reduced redox potential is shown in (a) and the spectrum that reported the most oxidised potential from this set of measurements of –250 mV is shown in (b), however this example also illustrates the low signal-to-noise ratio exhibited by some spectra.

3.4.4 Preparation of AQ-NPs

Results from SERS of NQ-NPs in MTS revealed the need for NPs to measure more reducing potentials as many of the spectra of NQ-NPs in MTS were fully reduced.

Preparation of AQ-NPs was complicated by solubility issues and initially a suitable procedure for functionalisation had to be established. AQ is not soluble in water or ethanol so functionalisation could not be carried out in either of these solvents. While it is recommended by the supplier (Nanospectra Bioscience) that these are the only solvents that should be used with the NPs, a different solvent had to be used to allow functionalisation. To attempt to minimise any negative effect the solvent might have on the integrity of the NPs, the solvent was used in a low percentage in water.

Initially, 10% acetone was used, but UV-visible absorbance and Raman spectroscopy revealed unsuccessful functionalisation. Subsequently, 10% DMF was used during functionalization. However, notable aggregation of NPs was observed by eye and under the Raman microscope (Figure 3.19(a)) and there was a huge loss of NPs during washing (Figure 3.19(b)). However Raman spectra revealed successful functionalisation. Results were similar using 5% DMF (Figure 3.19(c-d) and 1% DMF (Figure 3.19(e-f)), although loss of NPs and aggregation improved slightly. Using 0.1 % DMF allowed fewer washes to be carried out with less NP aggregation (Figure 3.19(g)) and loss of NPs reduced further (Figure 3.19(h)). Similar results to 0.1 % DMF were observed using 1% DMSO but with slightly less NP aggregation still (Figure 3.19(i)) and slightly less NP loss during washing steps (Figure 3.19(j)). 1% DMSO was used in subsequent functionalisations. Successful funtionalisation was confirmed for 1% DMSO by SERS of dried AQ-NPs (Figure 3.20) where the characteristic peaks were present at approximately 1600 cm^{-1} and 1670 cm^{-1}. Again, no Raman spectrum is observed for AQ before functionalization. For AQ-NPs, the 1600 cm^{-1} peak corresponds to a ring breathing peak present in both reduced and oxidised AQ, while the 1670 cm^{-1} corresponds to the C=O stretching frequency, present in only the oxidised form of AQ. This sensor behances in an analogous manner to NQ-NPs, but with a more reducing half cell potential, allowing it to measure more reducing redox potential values.

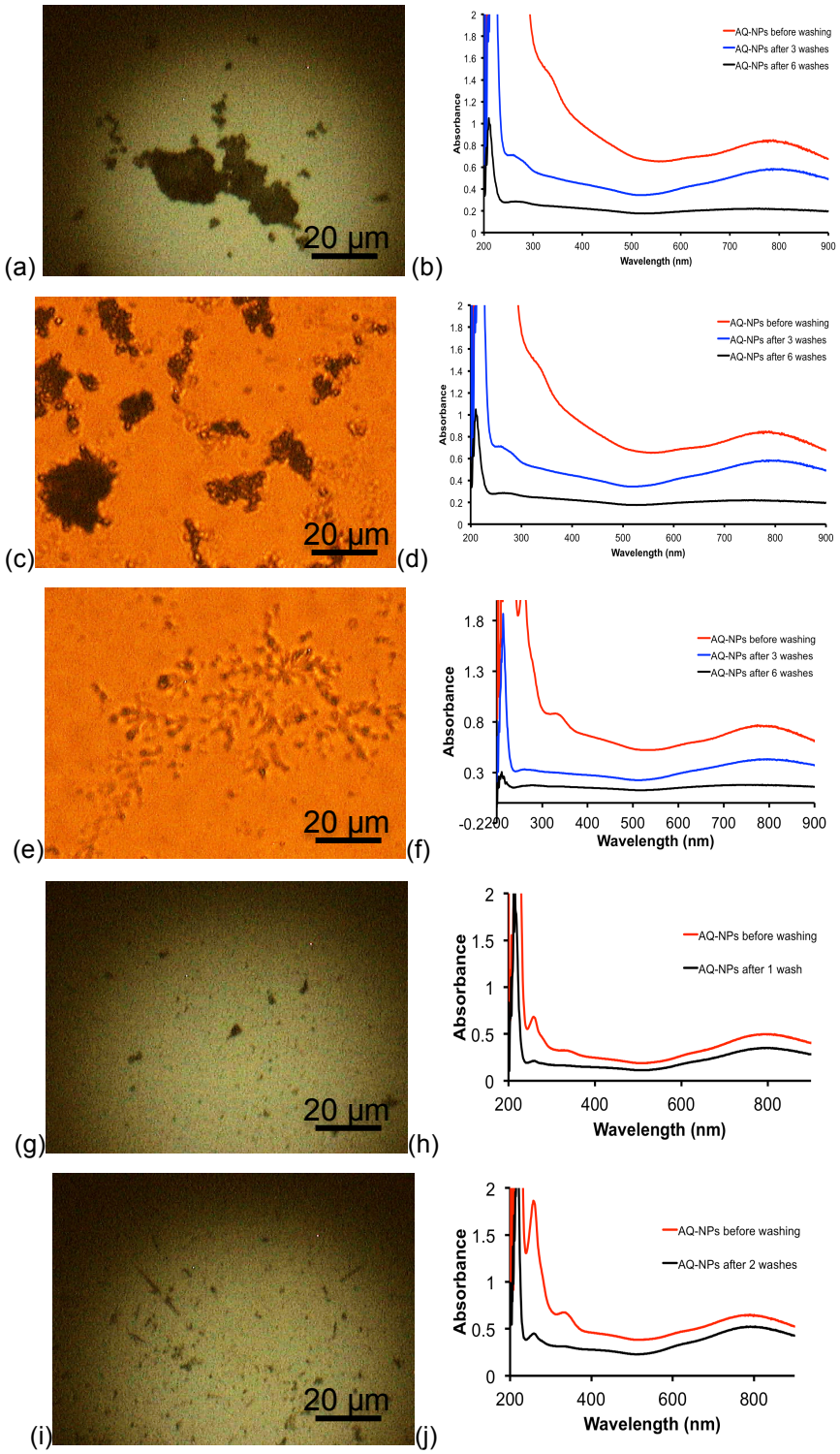

Figure 3.19 shows white light images (× 50) of AQ-NPs under the Raman microscope and UV-visible absorbance spectra before and after washing steps for a range of functionalisation solvents: (a) and (b) for 10% DMF; (c) and (d) for 5% DMF; (e) and (f) for 1% DMF; (g) and (h) for 0.1% DMF; and (i) and (j) for 1% DMSO. A reduction in aggregation and reduced loss of NPs during washing steps was observed progressing through these solvents.

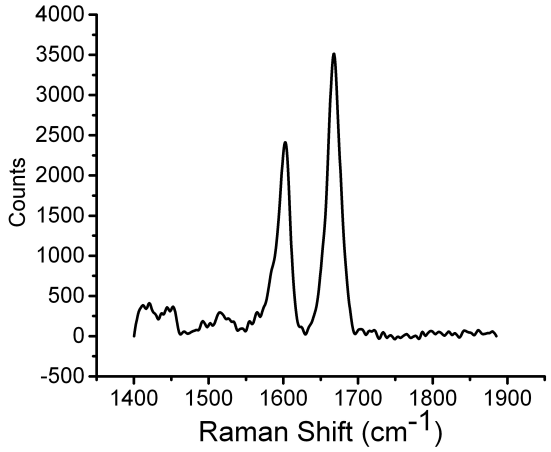

Figure 3.20 illustrates the Raman spectrum of dried AQ-NPs (functionalised in 1% DMSO), confirming successful functionalisation.

3.4.5 SERS of AQ-NPs in MCF7 Cells in Monolayer Culture

After NPs were successfully functionalised with AQ, cells were incubated with AQ-NPs, following the same procedure used for NQ-NPs. Results from 6 processed maps of AQ-NPs in monolayer culture gave a total of 93 spectra for processing. Of these 93 spectra, 66 illustrated that AQ had been fully oxidised and 27 spectra gave measurable potentials. The limit of measurement of AQ at the oxidised side is –240 mV, which would suggest that 66 spectra gave a potential more oxidising than –240 mV. However, as this is near the limit for measurement from AQ, measurements may not be accurate and the redox potential value probably was not as oxidised as –240 mV. Similar to NQ-NPs, the signal at 1670 cm^{-1} changes in intensity with redox potential relative to the signal at 1600 cm^{-1}, and calibration experiments (Chapter 2 Section 2.2.5, Appendix 1) allowed the peak intensity ratio to be converted to a redox potential value. The limits of measurement for a probe correspond to the 'edges' of measurement, where all redox probe molecules become oxidised or reduced. Near these limits, calculation of redox potential from peak ratio becomes less accurate.

Of the 27 spectra giving measurable potentials, the mean potential was –261 mV, which agrees with values calculated using NQ-NPs. Standard deviation was large at 13 mV and values were very spread out in comparison to those from NQ-NPs, as illustrated in the boxplots in Figure 3.21 and statistics in Table 3.3. AQ appeared to be a less accurate sensor than NQ. Figure 3.22(a) illustrates an example of a spectrum of fully oxidised AQ-NPs and Figure 3.22(b) illustrates the spectrum that gave the most reduced potential of –289 mV.

A final point to note was that it was harder to find SERS signals from AQ-NPs than NQ-NPs and the signals obtained tended to be low intensity and the redox potential determined from these was therefore less accurate and more subject to error from noise. It was noticed that AQ-NPs tended to aggregate more during washing after functionalisation and this could be a reason why signals were more difficult to find. This could have been a result of the different solvent being used during functionalisation or use of a different, more hydrophobic, molecule for functionalisation. This observation is consistent with previous HIM results. Images of cells that contained AQ-NPs appeared to have dark regions, as indicated in Figure 3.23, that tended to correlate well with regions of SERS AQ-NP signal. It is possible that this is clumps of NPs being visualised in the cell.

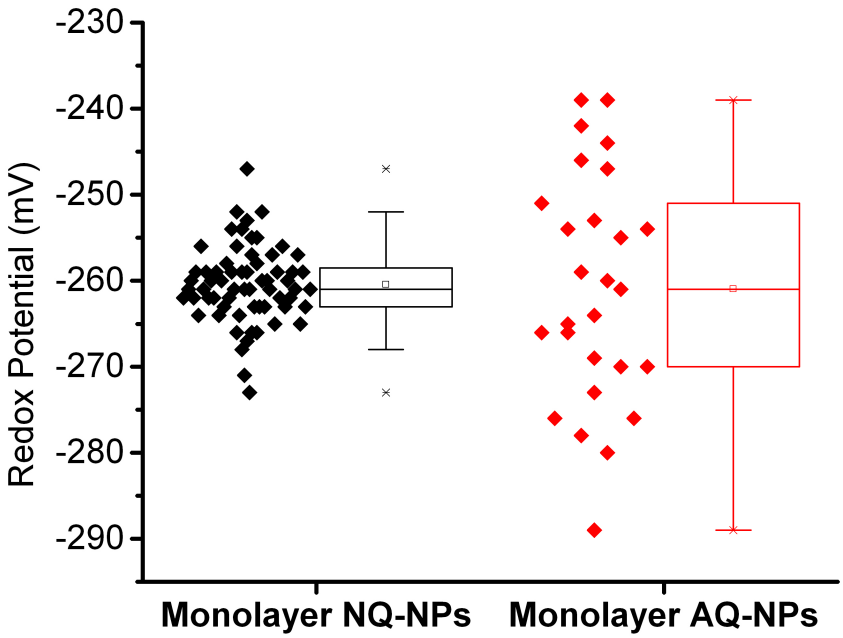

Figure 3.21 illustrates the distribution of measurable redox potential values calculated using SERS of AQ-NPs in MCF7 cells in monolayer culture, compared to values obtained using NQ-NPs for MCF7 cells in monolayer culture as discussed previously.

Table 3.3 presents the statistics for measurable redox potential values calculated using SERS of AQ-NPs in MCF7 cells in monolayer culture, compared to values obtained using NQ-NPs for MCF7 cells in monolayer culture as discussed previously.

	NQ-NPs monolayer	**AQ-NPs monolayer**
n	64	27
Mean (mV)	–260	–261
Standard Deviation (mV)	4.5	13
Maximum (mV)	–247	–239
3rd Quartile (mV)	–259	–251
Median (mV)	–261	–261
1st Quartile (mV)	–263	–270
Minimum (mV)	–273	–289

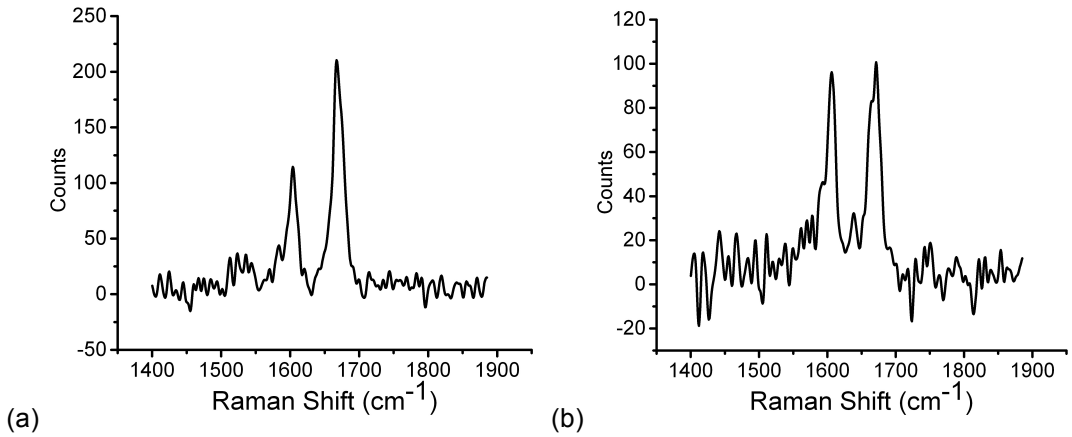

Figure 3.22 shows examples of spectra obtained from SERS mapping of AQ-NPs in monolayer culture. An example of a spectrum outside the limit of the AQ-NP measurable redox potential range at the oxidized side (a) and the spectrum that gave the most reduced potential of –289 mV is shown in (b).

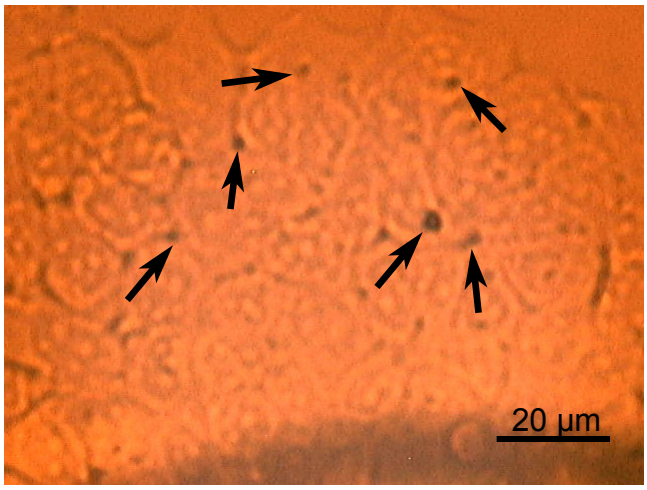

Figure 3.23 shows a white light image (× 50) of MCF7 cells in monolayer culture and incubated with AQ-NPs. Arrows indicate dark regions thought to be AQ-NP aggregates.

3.4.6 SERS of AQ-NPs in MCF7 Cells in MTS

AQ-NPs were used to measure redox potential in MTS. As with NQ-NPs, MCF7 cells were incubated with AQ-NPs overnight in monolayer culture before harvesting cells into a cell suspension that was used to form hanging drops for MTS formation as detailed in Chapter 2. Results gave potentials ranging from fully oxidised to fully reduced AQ-NPs and a range of measurable potential values in between. As with NQ-NPs in MTS, more spectra were obtained from AQ-NPs in MTS than in monolayer culture. It would be expected that redox potential values in MTS would be a lot more varied due to the differing environments as a result of more distance from nutrients and oxygen going further to the centre of the MTS. More reducing potentials were also determined from the SER spectra in the MTS. The most reduced potential of AQ-NPs in MCF7 cells in monolayer culture was –289 mV, with the majority of spectra indicating fully oxidised AQ. In MTS, there was a significant number of spectra indicating fully reduced AQ and a lot more with measurably highly reduced potentials. This would support the hypothesis that the internal environment of MTS is hypoxic. However, there is no information available to relate a particular redox potential value to its position in the MTS yet and this is an area of focus for future work and will be addressed in Chapter 5.

Initially, SERS was performed on MTS with AQ-NPs after six days of growth as MTS. Figure 3.24 shows one example of a map that gave a huge variety of redox potential values and examples of spectra that were fully oxidised, fully reduced and of measurable potential.

From 11 Raman maps of MTS, 179 spectra were analysed. Of these spectra, 20 were fully oxidized (outside the measurable redox potential range of AQ-NPs at the oxidised side) and 75 were fully reduced (outside the measurable redox potential range of AQ-NPs at the reduced side. Of the 84 spectra with measurable redox potential values, the mean redox potential was –314 mV. Figure 3.25 compares the results obtained from AQ-NPs in monolayer culture and MTS and also compares these to the results obtained from NQ-NPs in MTS. Table 3.4 compares statistics. Spectra from AQ-NPs in MTS were generally more reduced than those in monolayer culture, with a mean potential of –314 mV compared to –261 mV (significantly different at the 0.05 level, confirmed by a one-way ANOVA). The standard deviation was also much larger for MTS compared to monolayer culture: 46 mV

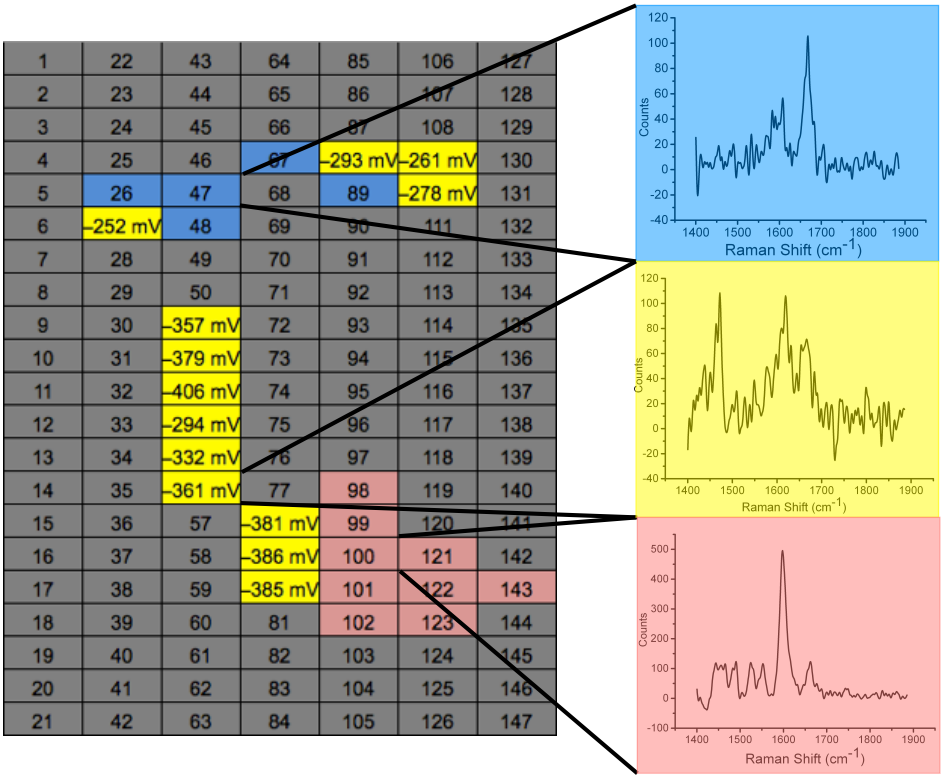

Figure 3.24 illustrates a single map obtained from SERS of AQ-NPs in MCF7 cells grown as MTS where cells were incubated with AQ-NPs in monolayer culture before forming MTS for 6 days of growth. Red indicates fully reduced AQ-NP, yellow indicates spectra where signals were measurable and the potential value is given, blue indicates fully oxidised AQ-NP and grey indicates spectra where there was no measurable SERS signal.

compared to 13 mV. This agrees with the trend observed from NQ-NP measurements where MTS gave a more reduced mean redox potential and higher standard deviation, consistent with the expected results due to increased hypoxic regions and development of varied gradients in MTS. Results from AQ-NPs and NQ-NPs in MTS were also significantly different at the 0.05 level by one-way ANOVA with AQ-NPs, giving a more reduced mean redox potential of –314 mV, compared to –268 mV. This can, however, be explained as NQ-NPs cannot measure potentials as reduced as AQ-NPs and therefore it is probable that NQ-NPs had reached the limit of their detection range at the reduced end while AQ-NPs allowed the lower potentials to be measured.

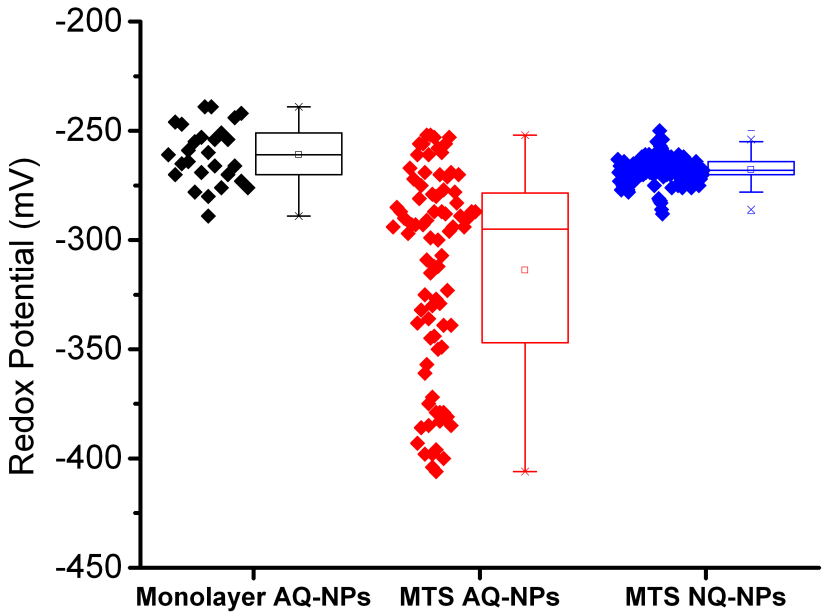

Figure 3.25 illustrates the distribution of measurable redox potential values calculated using SERS of AQ-NPs in MCF7 cells in monolayer culture compared to MTS and the values obtained using NQ-NPs in MTS.

Table 3.4 illustrates the statistics for measurable redox potential values calculated using SERS of AQ-NPs in MCF7 cells in monolayer culture, MTS and the values obtained using NQ-NPs in MTS.

	AQ-NPs monolayer	AQ-NPs MTS	NQ-NPs MTS
n	27	84	141
Mean (mV)	–261	–314	–268
Standard Deviation (mV)	13	46	5.9
Maximum (mV)	–239	–252	–250
3rd Quartile (mV)	–251	–279	–264
Median (mV)	–261	–295	–268
1st Quartile (mV)	–270	–347	–270
Minimum (mV)	–289	–406	–288

3.5 Moving Forward

This chapter has provided a more visual comparison between monolayer culture and MTS in terms of cell morphology, using TEM and HIM to emphasise the need for realistic 3D cell culture techniques. The current 'gold standard' technique for MTS redox potential measurement, Hypoxyprobe™, was used in the attempt to visualise hypoxic regions of MCF7 MTS, but did not show positive staining, further highlighting the need for a more quantitative technique allowing increased redox discriminations as well as live cell measurements to be made.

When moving the SERS nanosensor technique into MTS, the initial steps required confirmation of nanosensor uptake in MTS models. Initially, uptake of nanosensors into MCF7 cells in monolayer culture was confirmed using TEM, followed by confirming that nanosensors remained in cells in monolayer culture and subsequently MTS for up to 6 days. It was observed that a significant proportion of nanosensors were found inside vesicles and one aim of further work was to promote uptake into the cytosol (Chapter 6). HIM showed interesting differences in the interaction of NPs functionalised with different molecules with cells, such as increased clustering of AQ-NPs in comparison to NQ-NPs, and SEM confirmed uptake of NPs into MTS. However, while TEM and SEM confirmed uptake of NPs into MTS, they did not give information on the distribution of NPs within the MTS and future work will investigate monitoring spatial distribution of NPs in the 3D MTS structures (Chapter 5). IHC

already gave an indication that growing MTS from cells initially incubated overnight with NPs resulted in a uniform distribution of NPs through the MTS.

Initial SERS measurements were performed in MCF7 cells in monolayer culture and MTS. NQ-NPs gave a mean redox potential of –260 mV in monolayer cultured MCF7 cells. Initial attempts at measurement in MTS involved mapping small regions of MTS. Therefore, spatial information was not obtained, but instead, an average measurement from a MTS. Again, gaining spatial information is one of the primary goals of subsequent research (Chapter 5). However, from this overall picture, a significantly more reduced mean potential and larger standard deviation of values was obtained, consistent with the development of hypoxic regions and gradients in MTS. Due to a large proportion of NQ-NP spectra reaching the fully reduced state of NQ, another redox probe, AQ-NPs, capable of monitoring more reduced potentials was used. Results in monolayer culture agreed with those obtained for NQ-NPs. Results in MTS showed a similar trend of a more reduced mean and higher standard deviation. The results, however, spanned a wider range of potential values than expected, ranging from fully oxidised to fully reduced AQ-NPs. It was hypothesised that this wide range could be a result of pH not being considered as it could not be assumed that pH was at a standard value of 7.2, as pH also varies through MTS. Therefore, future work will aim to establish a method of measuring both pH and redox potential by SERS to allow appropriate corrections to be made. Firstly, a SERS pH sensor will be investigated (Chapter 4) before multiplexing this with redox measurements (Chapter 5).

Chapter 4

Developing a SERS pH Sensor

"The way I see it, if you want the rainbow, you gotta put up with the rain." – **Dolly Parton**

Initial attempts at measuring cellular redox potential in MTS using SERS nanosensors revealed a wide and somewhat sporadic distribution of potential values, spanning ranges outwith those expected with redox probes and revealing potential values from fully oxidised to fully reduced, therefore covering a range of more than 200 mV. When examining these results, it was necessary to consider possible factors that could influence the redox values obtained. Of particular importance was the need to include a pH measurement in order to allow pH adjusted redox potential values to be obtained. Calibration of redox sensors was performed at pH 7.2 and therefore only in a cellular environment with pH 7.2 could the equation be used to give an accurate redox potential value.[95,97] Outside this pH, an adjustment would have to be made to take the actual cellular pH into consideration. In theory, the half wave potential of a molecule should change by 59.2 mV per pH unit[7] (from the Nernst equation) and therefore, if experimentally confirmed, this would allow a correction for pH to be made.

In monolayer culture, cellular pH should be close to 7.2 for healthy cells, but in MTS a pH gradient is expected to develop and is therefore a vital characteristic to measure in parallel with redox potential. The combination of measurements allows accurate adjustments to be made to the redox measurements and also allows a deeper understanding of the MTS microenvironment. Regulation of pH is important in various cellular processes, such as cell volume regulation and inflammation, as will be discussed.[157] Fluorescent techniques have previously been employed to measure cellular pH and allow for appropriate adjustments to be made.[96] However, fluorescent techniques are not ideal and drawbacks include poor photostability and photobleaching.[93] If wavelengths in the visible range are used, there is also the presence of cell autofluorescence masking reporter signal. These techniques also involve the introduction of a fluorescent dye into cells, which could potentially modify cell behavior. Therefore, an improvement would be to use SERS to make both measurements. While this still involves the introduction of a foreign material into the cell, if both pH and redox

potential are measured using the same technique, it limits the number of species being introduced into the cell, as well as allowing both measurements to be carried out simultaneously on one instrument. Gold NPs have also been shown to be inert and non toxic to cell.[92]

4.1 Finding a pH Sensor

Previous studies have developed SERS pH sensors, the most studied of which is *para*mercaptobenzoic acid (MBA).[92,158–160] Other molecules used in SERS pH sensing include 4-mercaptopyridine (4MP)[198–200], 4-aminobenzenethiol (4ABT)[201] and 2-aminobenzenethiol (2ABT)[202]. SERS pH sensors report on pH in an analogous manner to how SERS redox sensors report on redox potential. Particular Raman peaks change in intensity in response to pH, as a result of protonation and deprotonation of the reporter molecule, in this case. Calibration experiments for SERS pH sensors involve recording Raman spectra of NPs functionalised with the reporter molecule in the presence of buffers of different pH. In theory, the resultant calibration curves should be consistent with a Henderson-Hasselbalch curve[203], given by Equation 4.1, where HA is the protonated (weak acid) and A^- the conjugate base, which exists in the equilibrium shown in Equation 4.2. In SERS experiments, generally the ratio of a pH sensitive (indicative of protonation state) to a non pH sensitive (reference) peak is taken. If the pH sensitive peak increases with increasing pH, this ratio will relate to the proportion of the molecule in the deprotonated form and (1–ratio) will relate to the proportion of the molecule in the protonated form. Taking ratio/(1–ratio) will be equal to $[A^-]/[HA]$.

$$\mathrm{pH} = \mathrm{pKa} + \log\frac{[A^-]}{[HA]} \qquad (4.1)[203]$$

$$HA \rightleftharpoons A^- + H^+ \qquad (4.2)[203]$$

The pKa of the molecule is the pH at which $[A^-]/[HA] = 1$ i.e. when the concentration of A^- and HA are equal.[203] Below this pH, more molecules are protonated than deprotonated. Therefore, the higher the pKa, the more difficult it is to deprotonate the molecule i.e. the less acidic the weak acid is. Figure 4.1 shows Henderson-Hasselbalch curves, plotting the normalised concentration of conjugate base against pH, for different pKa values. From these

plots, it can be seen that for any particular molecule, the range at which it will be able to report on pH depends on its pKa. The range covers about 2 pH units, 1 either side of the pKa, but would be most accurate over 1 pH unit, 0.5 either side of the pKa, as this is where the most rapid change in the curve occurs. For example, for a molecule with pKa = 7.0 (red line), pH could be detected between pH 6 and 8 but most accurately between pH 6.5 and 7.5. This is important when considering a SERS pH sensor for use for cellular pH measurements, as a molecule with a pKa that gives a suitable detection range is required. The standard pH in biological environments is pH 7.0-7.4[204] and therefore a molecule with a pKa similar to this would be ideal. Even in extreme intracellular conditions, it is unlikely that the pH would be outside the range of detection of a molecule with pKa 7.0. It is important to note that the pKa for molecules on gold NPs tend to differ significantly from the pKa of the same molecule in solution and therefore using the pKa's of particular molecules as a guide would not be particularly useful. In addition to an appropriate pKa to give a desirable pH detection range, there are other factors important to consider when selecting an appropriate molecule for pH detection by SERS. The molecule would ideally give a strong SERS intensity from both the pH sensitive and reference peak in order to minimise error in measurement. It is possible to use computational calculations to estimate changes in SERS spectra of functionalised NPs with pH. However, in general, experimental results were predominantly relied on.

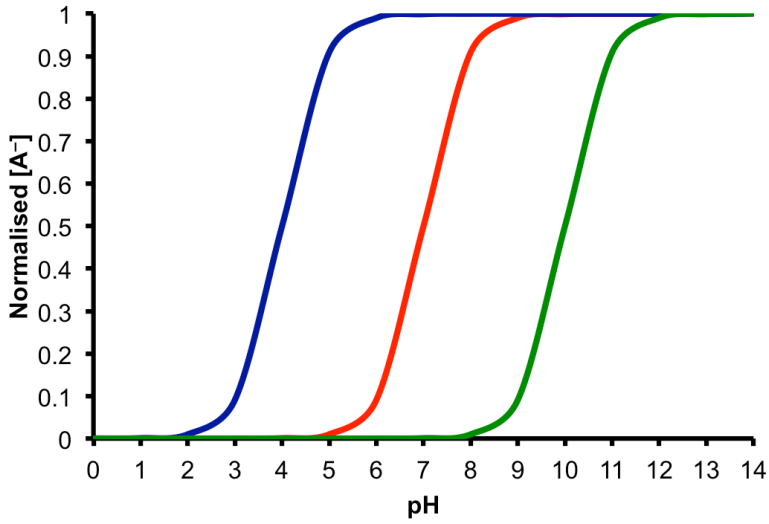

Figure 4.1 illustrates Henderson-Hasselbalch curves for pKa=4.0 (blue line), pKa=7.0 (red line) and pKa=10.0 (green line). Normalised concentration of [A^-] is plotted against pH. Concentration is normalised between 0 and 1, where 0 corresponds to all molecules being protonated (HA), and 1 corresponds to all molecules being deprotonated (A^-).

4.1.1 *Para*mercaptobenzoic Acid as a SERS pH Senosr

MBA has been well documented as a pH sensitive SERS reporter.[92,158–160] MBA functionalised NPs (Figure 4.2(a)) (MBA-NPs) have pH responsive peaks in their SER spectra (Figure 4.2(b)), most significantly signals at approximately 1400 cm^{-1} (represented using 14-- cm^{-1}) and approximately 1700 cm^{-1} (represented using 17-- cm^{-1}), assigned to COO^- stretching and C=O stretching respectively. The COO^- stretching mode peak intensity increases with increasing pH, due to increased MBA deprotonation and the C=O stretching mode peak intensity increases with decreasing pH. The intense peaks at approximately 1080 cm^{-1} and approximately 1590 cm^{-1} are attributed to pH independent aromatic ring vibrations and can therefore be used as reference peaks. Table 4.1 summarises MBA-NP Raman peaks of interest for pH sensing along with assignments. MBA has a large cross section for Raman scattering, making it a good choice as a SERS sensor. However, the drawback of this molecule is that the pH sensitive peaks are much weaker than the reference peaks and therefore measurements are more subject to error, as these less intense peaks are more subject to noise and changes in response to pH are only small intensity differences.

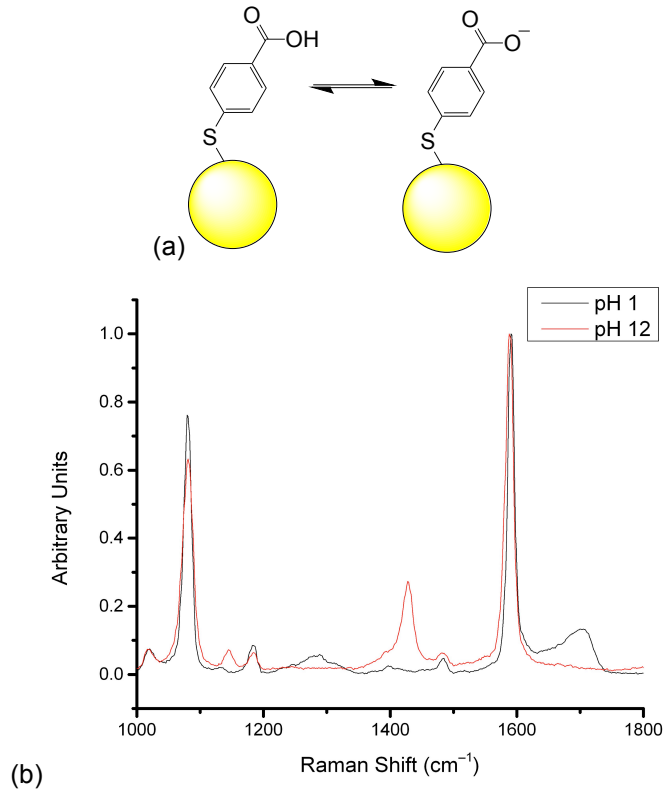

Figure 4.2 (a) illustrates the equilibrium between protonated and deprotonated MBA-NPs where the yellow spheres represent NPs and (b) illustrates representative MBA-NP spectra at high and low pH.

Table 4.1 summarises the main SERS peaks found in MBA-NP spectra.[92,158–160]

Wavenumber (cm^{-1})	Assignment	pH sensitive?
1079	ring breathing	no
1390-1430	COO^- symmetric stretch	yes
1590	ring breathing	no
1700	C=O stretch	yes

Calibration of MBA-NPs was generated by plotting relative intensity of selected signals against pH. As discussed, the expected sigmoid is centred around the pKa of the MBA-NPs and in theory should display a Henderson-Hasselbalch curve[203]. Calibration of MBA-NPs was performed on three different instruments – a Renishaw inVia Raman spectrometer; an Ocean Optics QE65 Pro spectrometer; and a WITec Raman spectrometer (see Chapter 2 Section 2.2.1 for instrumental details). This was because all three instruments were used to perform intracellular measurements using the nanosensors for different parts of the project and, while in theory the resultant calibration curve should not differ between instruments, calibrations were performed on all three instruments to confirm this and to produce a calibration curve for use with the appropriate instruments.

For calibration experiments, MBA-NPs were dried onto a surface to allow buffers to be exchanged between measurements. Initially, glass slides were used, but the background Raman signal from the glass made this difficult. Quartz slides have much lower signal than glass and were used for some experiments. However, there was still background from the slide present (Figure 4.3(a)). Finally glass slides coated with a thin layer of gold were used and gave almost no background (Figure 4.3(b)). MBA-NPs that were dried straight onto the slides tended to wash off easily when buffers were exchanged between measurements. For this reason poly-L-lysine (PLL) at a concentration of 1 mg/ml was firstly used to coat the slide for about 2 hrs, before MBA-NPs were then dried onto the slide as described in Chapter 2. Adhesive wells were stuck to the slides to contain solutions and allow buffer exchange between measurements. When buffers were exchanged, the slide was washed with distilled water before replacing with the next buffer. In order to minimise the area coated with gold due to cost considerations, a small gold 'chip' was glued onto a larger slide using Araldite before proceeding to attach the NPs to the chip. Figure 4.4 summarises this process.

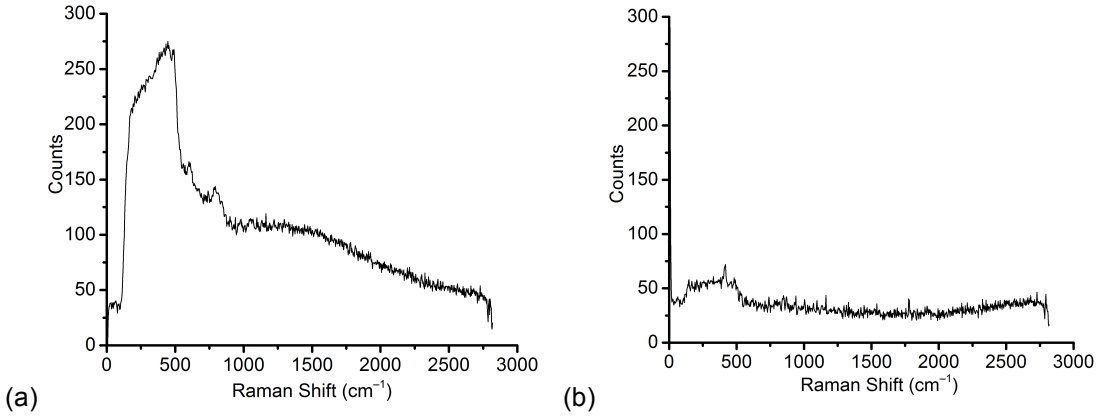

Figure 4.3 (a) illustrates the average of 20 Raman spectra of the background from a quartz slide (a) and a gold slide (b).

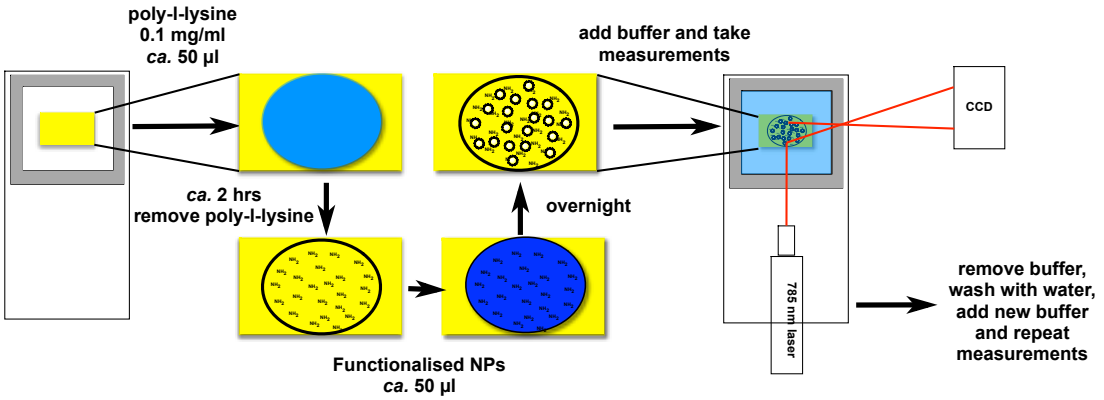

Figure 4.4 illustrates the steps involved in preparing a slide (white) with an adhesive well (grey) and gold slide (yellow) adhered with Araldite glue, for pH calibration of functionalized NPs.

Finally, after plotting relative intensity of selected peaks against pH, Origin 9.0 was used to fit a Boltzmann curve. The general form of the Boltzmann equation is given in equation 4.3 and rearranged for x in equation 4.4. In this case, y is the ratio of the selected peaks and x is the pH. Therefore, Equation 4.4 can subsequently be used to determine an unknown pH from a ratio of signal intensities. Parameters are A1 (initial y value); A2 (final y value); x0 (the centre of the curve i.e. x value at the midpoint of the curve, which translates to pKa in this case); and dx, the time constant.[205] For comparison, Henderson-Hasselbalch curves expected from theory were also plotted with pKa = x0.

$$y = A2 + \frac{A1 - A2}{1 + exp^{\frac{x-x0}{dx}}} \qquad (4.3)^{205}$$

$$x = \left(ln\left(\frac{A1 - A2}{y - A2}\right) - 1\right)dx + x0 \quad (4.4)^{205}$$

4.1.1.1 MBA-NP Calibration: Renishaw inVia

Initially, calibrations were carried out on a Renishaw inVia system, as described previously. When plotting peak intensity ratios vs pH, various ratios were investigated (Figure 4.5). Due to the limited spectral range when performing a static scan on the Renishaw inVia system (approximately 500 cm^{-1}), the 1590 cm^{-1} peak was used for reference in this case, as both pH responsive peaks and the 1590 cm^{-1} peak could be recorded within a static scan. It was also noticed when analysing results that the centre of the pH responsive peaks shifted with changing pH, particularly the peak at 14-- cm^{-1}, which shifted from approximately 1390 cm^{-1} at lower pH to approximtately 1430 cm^{-1} at higher pH (Figure 4.6(a) and (b)). When plotted against pH, the centre of the peak at approximately 1700 cm^{-1} showed no significant trend with pH (Figure 4.6(c)).

In addition to plotting peak intentiy ratios vs pH for the maximum peak intensity at 14-- cm^{-1} and 17-- cm^{-1} relative to the maximum peak intensity at 1590 cm^{-1} (Figure 4.5(a) and (b) respectively), the intensity at a set wavenumber of 1426 cm^{-1} and 1701 cm^{-1} relative to the maximum peak intensity at 1590 cm^{-1} vs pH (Figure 4.5(c) and (d) respectively) was plotted for comparison. Peak fits (black lines) where a set wavenumber was used were closer to the Henderson Hasselbalch curves (red lines) and adjusted R^2 values were higher (Table 4.1). However, error bars were significantly larger, so maximum peak intensity was preferred. Graphs plotting the peak intensity ratio of the two pH responsive peaks were also plotted (Figure 4.5(e) and (f)), but as both peaks respond in this case, it is preferable not to use these calibrations. Larger error bars in this case also indicate decreased accuracy in comparison to using a plot relative to a non pH responsive peak. In Figure 4.5(e), where the ratio of the peak at 14-- cm^{-1} to that at 17-- cm^{-1} was plotted, the fitted curve was almost identical to the Henderson Hasselbalch curve. This was also the case in Figure 4.5(c) for the ratio of 1426 cm^{-1} peak intensity to that at 1590 cm^{-1}. In Figure 4.5(f), the curve fit did not match well with the Henderson Hasselbalch curve. However, this was for two pH responsive peaks, which decreases accuracy. In Figure 4.5(a), (b) and (d), fitted curves were slightly stretched from the expected Henderson Hasselbalch plots. This behaviour has been seen previously when redox calibrations were carried out and was attributed to surface absorption characteristics. This

was explained using a modified Nernst equation, in this case including an α parameter to account for differences as a result of differing orientations of surface absorbed molecules.[98]

Table 4.2 details the apparent pKa values (determined from the x0 term of the Boltzmann fit) and adjusted R^2 values for all plots including peak centre of the 14-- cm^{-1} signal. The apparent values ranged from 7.6 to 8.8 with the exception of the 17-- cm^{-1}/14-- cm^{-1} plot that did not fit well with theory and gave an apparent pKa of 3.2. For the Renishaw system, the 14-- cm^{-1}/1590 cm^{-1} plot was used for calibration purposes. Figure 4.7 plots the 14-- cm^{-1} peak relative to the 1590 cm^{-1} peak against pH without normalisation. A Boltzmann fit gave adjusted R^2 of 0.9652 and apparent pKa of 8.2. From the calibration plot pH values between approximately 6 and 10 should be able to be measured accurately from this before the gradient of the curve decreases significantly making measurements less accurate. Equation 4.5 is the rearranged Boltzmann fit for the curve allowing pH to be determined from 14-- cm^{-1}/1590 cm^{-1} peak intensity ratio.

Table 4.2 details the apparent pKa determined from x0 and adjusted R^2 values from the Boltzmann fits for plots of peak intensity ratios and peak centre against pH given in Figure 4.5 and 4.6 respectively.

Plot	Apparent pKa	Adjusted R^2
14-- cm^{-1}/1590 cm^{-1}	8.2	0.98595
17-- cm^{-1}/1590 cm^{-1}	7.6	0.90590
1426 cm^{-1}/1590 cm^{-1}	8.4	0.99854
1701 cm^{-1}/1590 cm^{-1}	7.8	0.93656
14-- cm^{-1}/17-- cm^{-1}	8.8	0.99520
17-- cm^{-1}/14-- cm^{-1}	3.2	0.84766
14-- Peak Centre	7.9	0.99055

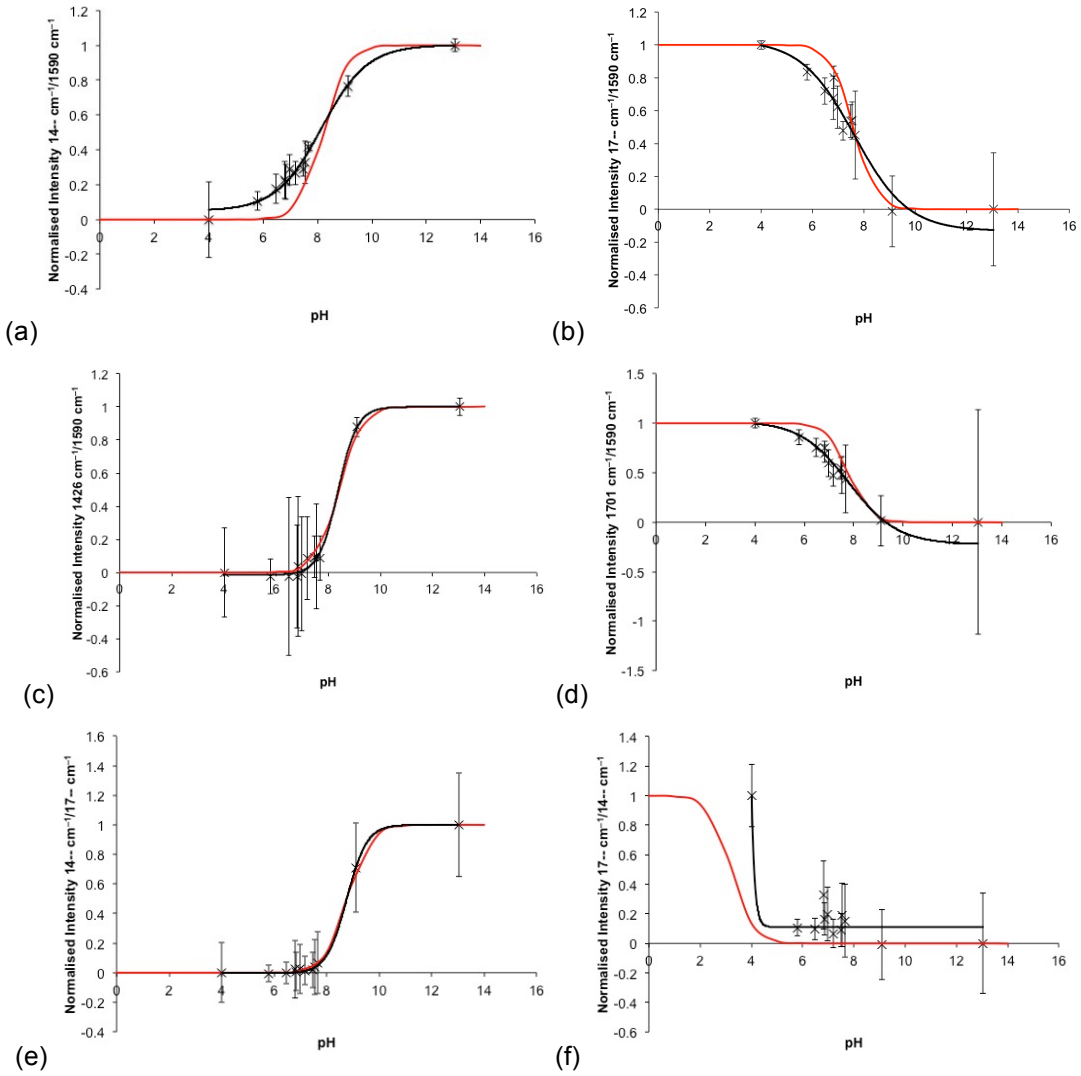

Figure 4.5 illustrates graphs that plot normalised peak intensity ratios against pH for various peak combinations for the calibration of MBA-NPs on a Renishaw inVia spectrometer. Black lines are the Boltzmann fit to plotted points and red lines are the theoretical Henderson Hasselbalch curves with pKa determined from the Boltzmann fit as equal to x0. Maximum intensities for the peaks at 14-- cm^{-1} and at 17-- cm^{-1}, which are pH sensitive, divided by peak intensity for the signal at approximately 1590 cm^{-1}, which is not pH sensitive are given in (a) and (b) respectively. Intensity ratios of the peak intensity at set values of 1426 cm^{-1} and 1701 cm^{-1} divided by peak intensity at 1590 cm^{-1} are given in (c) and (d) respectively. Maximum intensity for the signal at 14-- cm^{-1} divided by that for the signal at 17-- cm^{-1} and the inverse are given in (e) and (f) respectively.

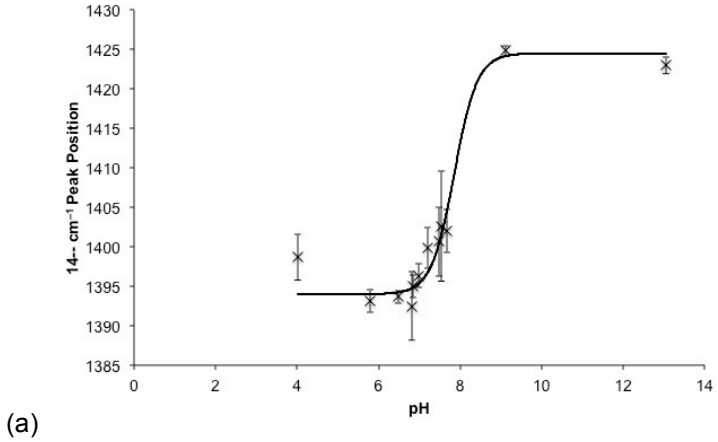

(a)

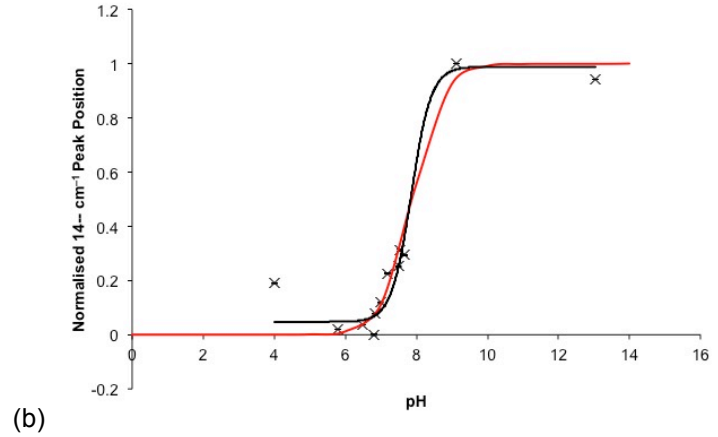

(b)

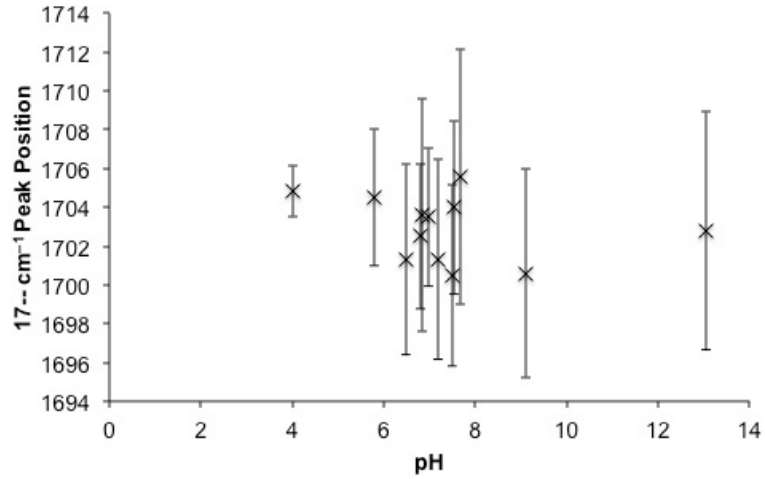

(c)

Figure 4.6 investigates the dependence of pH sensitive peak centre on pH for MBA-NPs calibrated on a Renishaw inVia spectrometer. The peak centre of the signal at 14-- cm^{-1} (a) was pH sensitve ranging from approximately 1390 cm^{-1} at low pH to 1430 cm^{-1} at high pH. The normalised plot in (b) compares the Boltzmann fitted line (black) to the theoretical Henderson Hasselbalch curve (red line) and apparent pKa's and adjusted R^2 values are given in Table 4.1. The peak centre of the signal at 17-- cm^{-1} was not pH sensitive.

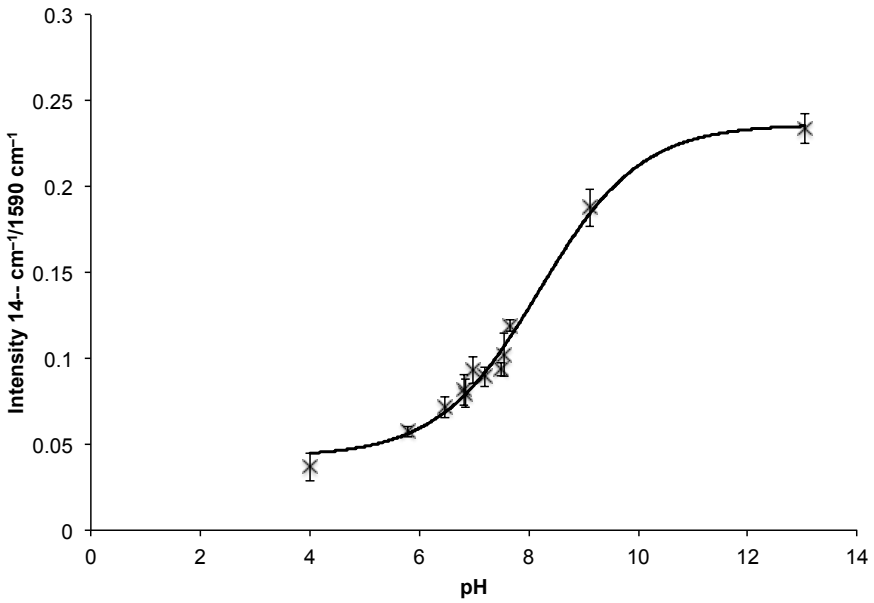

Figure 4.7 illustrates the plot of peak intensity ratio of the peak at 14-- cm^{-1} divided by that at 1590 cm^{-1} for MBA-NPs calibrated on a Renishaw inVia system. The black line is the Boltzmann fit with apparent pKa = 8.2; adjusted R^2 = 0.9652 and rearranged equation to give pH from ratio given in equation 4.5.

$$pH = \left(ln\left(\frac{-0.19349}{ratio - 0.23629}\right) - 1\right)0.92434 + 8.19402 \tag{4.5}$$

4.1.1.2 MBA-NP Calibration: Ocean Optics QE65 Pro

Calibration of MBA-NPs was also carried out on an Ocean Optics QE65 Pro spectrometer. In this case, an extended scan ranging from approximately –80 cm^{-1} to 2800 cm^{-1} was recorded in a single spectrum, and therefore the reference peak at approximately 1077 cm^{-1} could also be observed and used in calibration plots. Again, using the maximum intensity in the region from 1390 cm^{-1} and 1430 cm^{-1} as well as the intensity at a set value of 1426 cm^{-1} was compared. As the peak centre at approximately 1700 cm^{-1} did not correlate with pH and the resolution of the Ocean Optics spectrometer was lower than the Renishaw inVia system, this meant that there was very little variation in the peak centre, so only the maximum intensity in the region of 17-- cm^{-1} was used. All plots showed good fits with adjusted R^2 values as well as apparent pKa values given in Table 4.3. Again, plots where intensity at a set value, (b) and (d), rather than maximum intensity, (a) and (c), showed higher error. Plots (a)-(f) have apparent pKa values ranging from 8.6 to 8.8 while (g) and (h) have apparent pKa values of 6.2

and 6.5 respectively. The final two are plots of the maximum intensity of the 17-- cm^{-1} peak divided by the maximum intensity of the 1077 cm^{-1} reference peak and 1590 cm^{-1} reference peak respectively. These plots deviate most from the Henderson Hasselbalch curves. Other plots are very close or slightly stretched versions of the Henderson Hasselbalch curves. The 14-- cm^{-1} maximum intensity divided by 1590 cm^{-1} maximum intensity was again selected as the plot for calibration.

Following from selection of the desired peak ratio of 14-- cm^{-1} divided by 1590 cm^{-1}, four separate calibrations using this ratio were compared (Figure 4.9). In this case, peak ratios were not normalised and the resultant Boltzmann fit was rearranged to give pH. Equations 4.6, 4.7, 4.8 and 4.9 give the resultant equations for Figure 4.9(a), (b), (c) and (d) respectively and Table 4.3 gives apparent pKa and adjusted R^2 values for each plot. Figure 4.10(a) plots these four calibrations together showing good similarity. Figure 4.10(b) shows the fit of a Boltzmann curve to points from all four calibrations collectively giving apparent pKa 8.4 and adjusted R^2 of 0.89823. The equation of this Boltzmann curve rearranged to give pH is given in equation 4.10 and this was used for pH determination from unknown spectra.

Table 4.3 details the apparent pKa determined from x0 and adjusted R^2 values from the Boltzmann fits for plots of peak intensity ratios against pH given in Figure 4.8.

Plot	Apparent pKa	Adjusted R^2
14-- cm^{-1}/1077 cm^{-1}	8.8	0.99641
1426 cm^{-1}/1077 cm^{-1}	8.7	0.99879
14-- cm^{-1}/1590 cm^{-1}	8.7	0.9975
1426 cm^{-1}/1590 cm^{-1}	8.6	0.99897
1702 cm^{-1}/14-- cm^{-1}	8.6	0.99901
14-- cm^{-1}/1702 cm^{-1}	8.6	0.99264
1702 cm^{-1}/1077 cm^{-1}	6.2	0.98382
1702 cm^{-1}/1590 cm^{-1}	6.5	0.98573

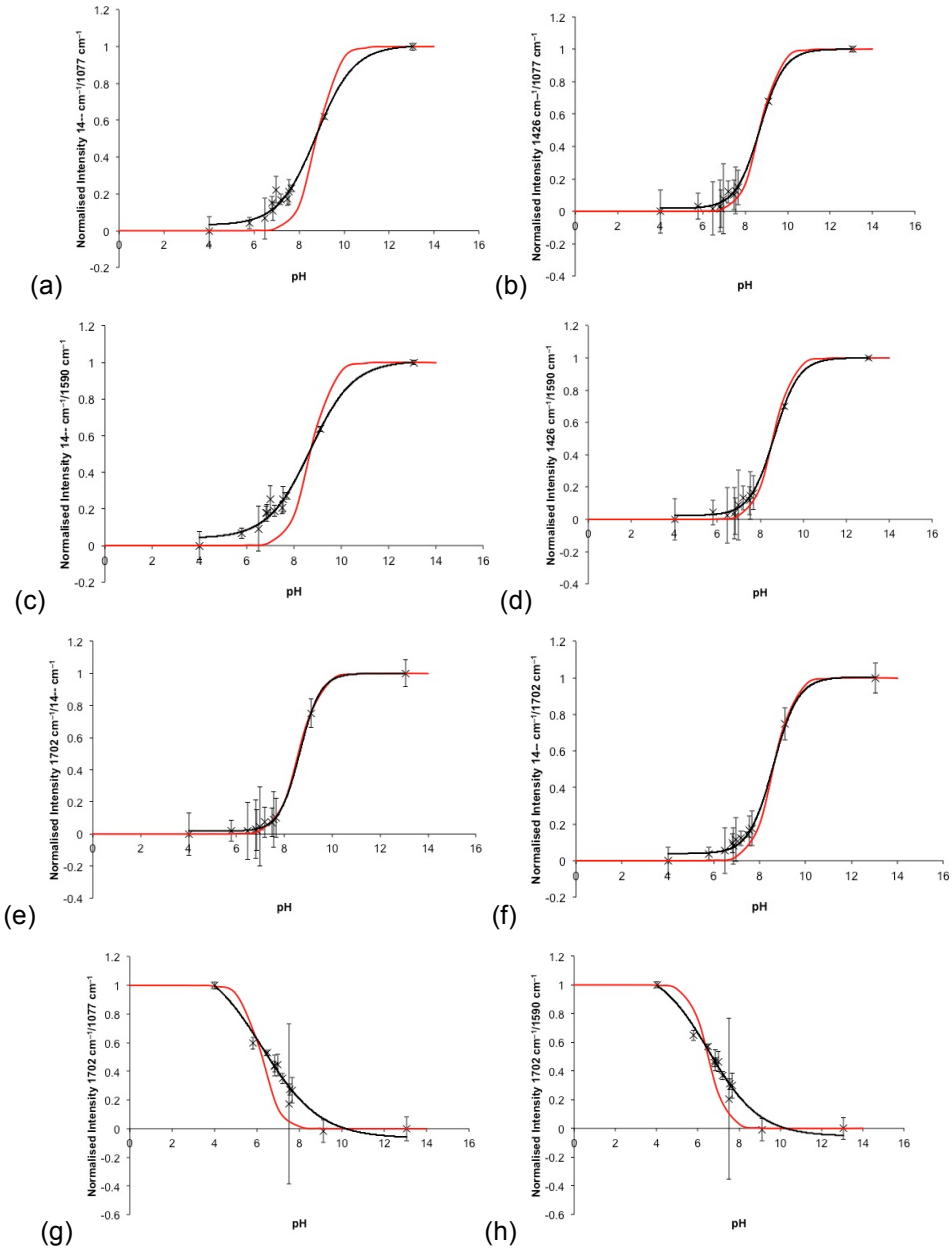

Figure 4.8 illustrates graphs that plot normalised peak intensity ratios against pH for various peak combinations for the calibration of MBA-NPs on an Ocean Optics QE65 spectrometer. Black lines are the Boltzmann fit to plotted points and red lines are the theoretical Henderson Hasselbalch curves with pKa determined from the Boltzmann fit as equal to x0. Maximum intensity for the pH sensitive peak at 14-- cm^{-1} divided by peak intensities for the non pH sensitive peaks at approximately 1077 cm^{-1} and 1590 cm^{-1} against pH are given in (a) and (c) respectively. The same plots using the peak intensity at a set wavenumber of 1426 cm^{-1} are given in (b) and (d) respectively. Maximum intensity for the peak at 17-- cm^{-1} divided by that for the peak at 14-- cm^{-1} and the inverse are given in (e) and (f) respectively. Maximum intensity for the pH sensitive peak at 17-- cm^{-1} divided by peak intensities for the non pH sensitive peaks at 1077 cm^{-1} and 1590 cm^{-1} against pH are given in (g) and (h) respectively.

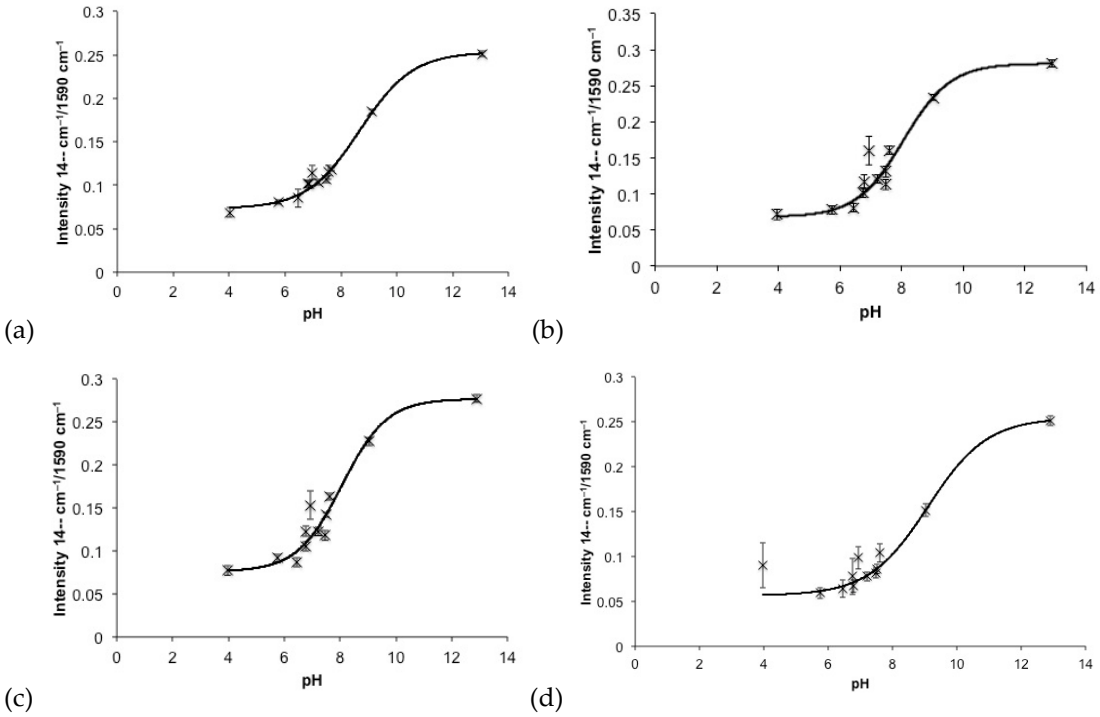

Figure 4.9 compares graphs from four separate calibrations that plot the peak intensity of the peak at 14--cm^{-1} divided by that at 1590 cm^{-1} against pH for calibration of MBA-NPs on an Ocean Optics QE65 spectrometer. Black lines are Boltzmann fits. Corresponding adjusted R^2 values for Boltzmann fits and apparent pKa's from x0 in Boltzmann fits are given in Table 4.4.

Table 4.4 details the apparent pKa determined from x0 and adjusted R^2 values from the Boltzmann fits for plots in Figure 4.9 for peak intensity of the peak at 14--cm^{-1} divided by that at 1590 cm^{-1} against pH for four separate calibations on an Ocean Optics QE65 spectrometer.

Plot	Apparent pKa	Adjusted R^2
Figure 4.9(a)	8.7	0.99312
Figure 4.9(b)	8.1	0.97428
Figure 4.9(c)	8.1	0.96216
Figure 4.9(d)	9.1	0.98687

$$pH = \left(ln\left(\frac{-0.18024}{ratio - 0.25335}\right) - 1\right)0.94333 + 8.67706 \tag{4.6}$$

$$pH = \left(ln\left(\frac{-0.2129}{ratio - 0.2809}\right) - 1\right)0.76238 + 8.06058 \tag{4.7}$$

$$pH = \left(ln\left(\frac{-0.20111}{ratio - 0.27713}\right) - 1\right)0.80234 + 8.06369 \tag{4.8}$$

$$pH = \left(ln\left(\frac{-0.198}{ratio - 0.25456}\right) - 1\right)0.92004 + 9.0965 \tag{4.9}$$

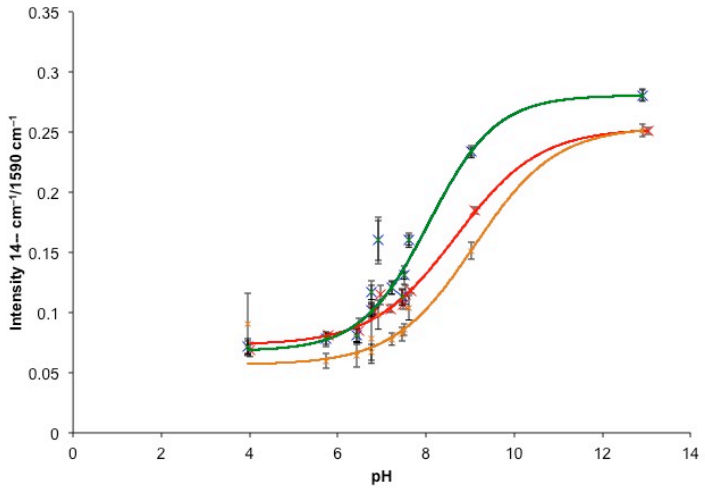

(a)

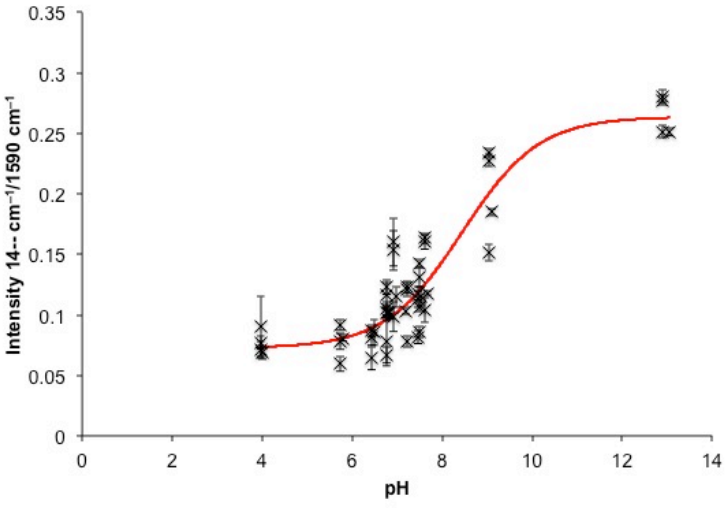

(b)

Figure 4.10 compares graphs from four separate calibrations that plot the peak intensity of the peak at 14--cm^{-1} divided by that at 1590 cm^{-1} against pH for calibration of MBA-NPs on an Ocean Optics QE65 spectrometer. The plots are fitted separately for comparison in (a), with red corresponding to Figure 4.9(a), blue (masked by green) to 4.9(b), green to 4.9(c) and orange to 4.9(d). A Boltzmann fit (red line) is made to all data points from the four separate calibrations in (b) with an adjusted R^2 value of 0.89823 and apparent pKa 8.4.

$$pH = \left(ln\left(\frac{-0.19122}{ratio - 0.26374}\right) - 1\right)0.85304 + 8.44253 \tag{4.10}$$

4.1.1.3 MBA-NPs Calibration: WITec

Finally, the calibration of MBA-NPs was carried out on a WITec spectrometer. These spectra were collected by Aleksandra Jaworska, of Jagiellonian University. In this case, MBA-NP solutions were mixed with buffers of different pH as detailed in Chapter 2, before recording spectra from the solutions in a 96-well plate. Figure 4.11 shows the peak intensity ratio for the peaks at 14-- cm^{-1} and 1590 cm^{-1} against pH with a Boltzmann curve fitted giving an apparent pKa of 7.2 and adjusted R^2 0.98687. Equation 4.11 gives the rearranged Boltzmann equation for unknown pH determination from a known peak ratio.

$$pH = \left(ln\left(\frac{-0.2224}{ratio - 0.243}\right) - 1\right)0.6602 + 7.22104 \tag{4.11}$$

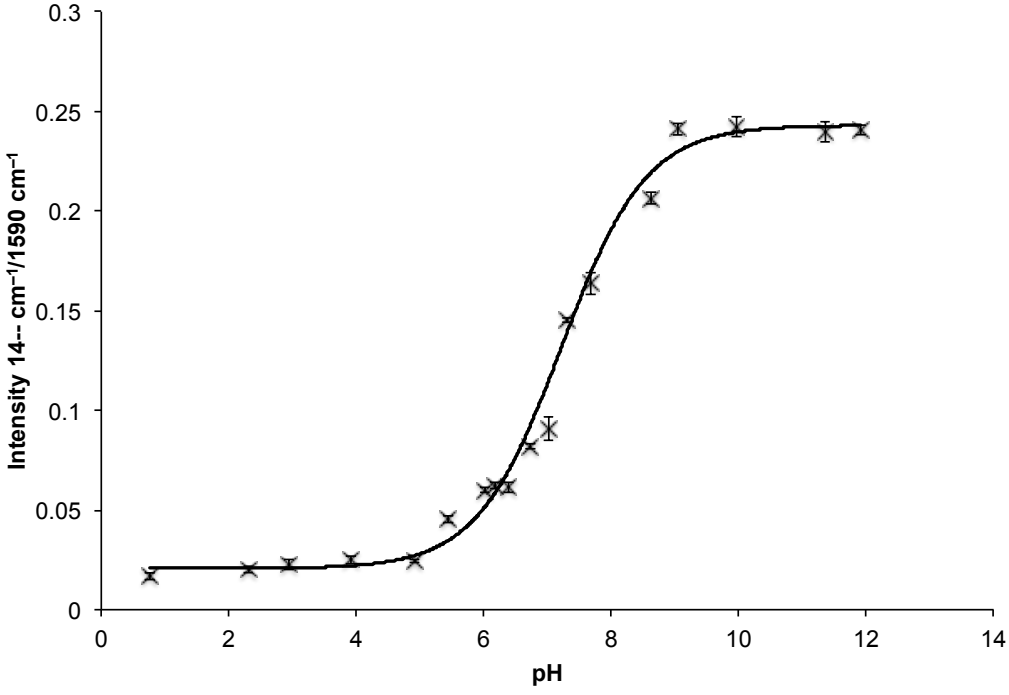

Figure 4.11 illustrates the plot of peak intensity ratio of the peak at 14-- cm^{-1} divided by that at 1590 cm^{-1} for MBA-NPs calibrated on a WITec system. The black line is the Boltzmann fit with apparent pKa = 7.2; adjusted R^2 = 0.98687 rearranged equation to give pH from ratio given in equation 4.11.

4.1.1.4 MBA-NPs Calibration Comparison

Figure 4.12 compares the selected calibration plots from the three different instruments. While plots are not identical, they show good similarity between instruments. Therefore, it could be concluded that inter instrument variation was minimal and, if necessary, measurements taken on one instrument could be used in conjunction with any calibration plot to determine unknown pH values from peak intensity ratios. Where possible, however, the calibration plot corresponding to a particular instrument would be used. While there is variation in apparent pKa between instruments, tabulated in Table 4.5, all plots reveal

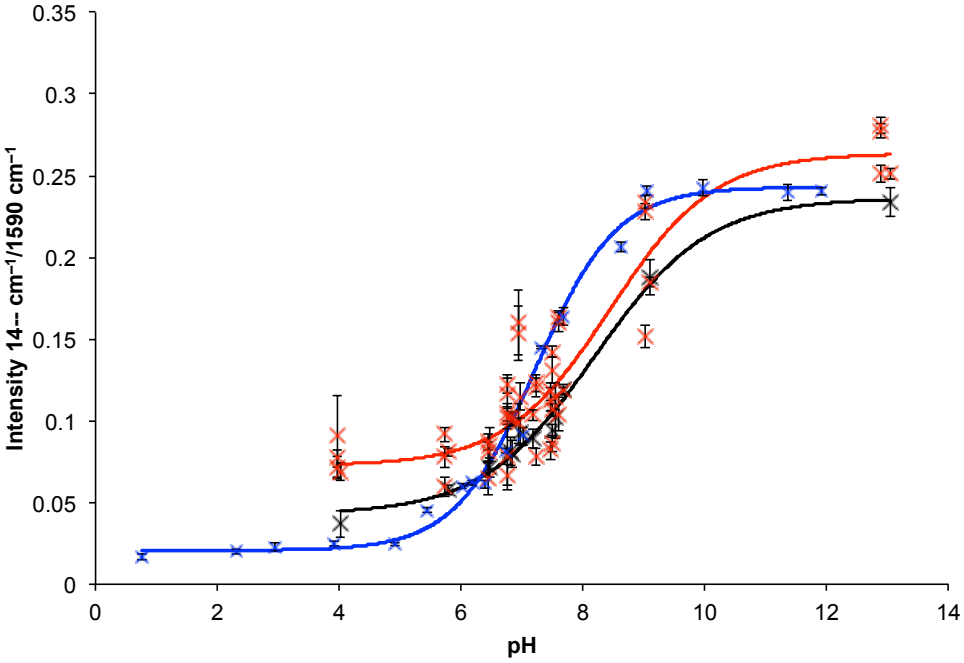

Figure 4.12 compares Boltzmann fitted calibration plots for MBA-NPs generated from three different spectrometers – a Renishaw inVia system (black), an Ocean Optics QE65 Pro system (red) and a Witec system (blue). The ratio of peak intensity from the pH responsive peak at 14-- cm^{-1} and at 1590 cm^{-1} were selected for calibration and apparent pKa and adjusted R^2 values are given in Table 4.5.

Table 4.5 summarises apparent pKa and adjusted R^2 values determined from the Boltzmann fitted curves in Figure 4.12 for MBA-NPs from three different spectrometers.

Spectrometer	Apparent pKa	Adjusted R^2
Renishaw inVia	8.2	**0.**9652
Ocean Optics QE65 Pro	8.4	0.89823
WITec	7.2	**0.**98687

greatest sensitivity to pH changes between approximately pH 6 and 9. The pH range offered by the MBA-NPs is well suited to the measurement of intracellular pH. It is interesting to note, the difference in adjusted R^2 values between instruments, the Renishaw inVia and WITec systems having higher values at 0.97 and 0.99 respectively compared to the Ocean Optics system at 0.90. The most likely cause of this, suggesting increased error and less precision for Ocean Optics measurements, was differences in the CCD camera sensitivity between instruments. It is worth considering that while the Renishaw inVia and WITec systems had CCD cameras cooled to between –60 °C and – 70 °C, the Ocean Optics system CCD was only cooled to approximately –20 °C. This in itself would lead to an increase in noise of spectra collected and therefore decreased precision with the Ocean Optics system, accounting for the decreased adjusted R^2 value.

In the future, it would be desirable for data processing to be automated. This provides many advantages over manual processing. Firstly the time required for manual processing becomes unmanageable. Each spectrum generated takes approximately 3 minutes to process manually. A single cell map, generated in just over 3 minutes, contains 147 spectra. Therefore, if all spectra contained signals, this would take approximately 441 minutes (7.4 hr) to process manually a set of results generated in just over 3 minutes of spectrometer time. Automated data processing should also reduce error. Manual processing is subject to human error including bias as well as inter- and intra- person variations. For example, it is likely that manual baseline subtraction will be subject to inter- person variations in exact positioning as well as intra- person variations depending on the time of day, how much processing has already been done and tiredness. Due to the highly quantitative nature of this technique, however, an automated data processing must be very specifically generated with high accuracy and minimal error. An automated data processing program has recently been developed by Kate Fisher based on the calibration data used for the previous manual calibrations.[187] Figure 4.13 and Table 4.6 compare the average pH determined from 10 consecutive MBA-NP signals processed manually and by the automated method. It can be observed that average pH gives a slightly different value using the automated approach and a much smaller standard deviation. Automated data processing also allowed multiple parameters to be taken into account. For example, peak centre of one or more signals, intensity of one or more peaks and area of one or more peaks. Figure 4.13 shows how this was able to further reduce error in measurement. Even using one parameter gave a reduced error, however.

Table 4.6 compares mean pH, standard deviation and mean error determined from manual and automated data processing of 10 consecutive spectra from MBA-NPs dried onto a glass bottomed imaging dish (data acquired by Kate Fisher).[187]

	Manual processing	Automated processing
Mean estimated pH	6.56	7.14
Standard deviation	0.29	0.09
Mean error	-	0.28

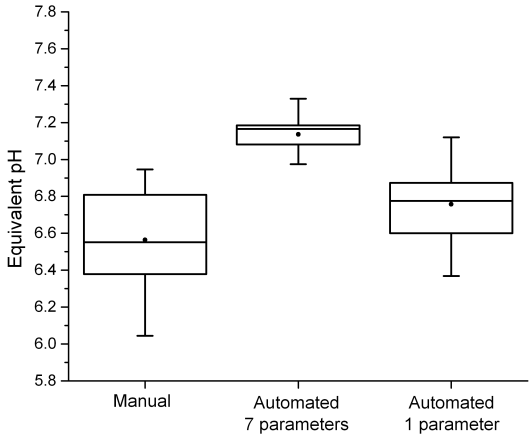

Figure 4.13 compares pH determined from manual and automated data processing of 10 consecutive spectra from MBA-NPs dried onto a glass bottomed imaging dish. Black circles show mean values. Manual processing uses a single parameter to determine pH from relative peak intensity of 14--cm^{-1} and 1590 cm^{-1} signals while automated processing can incorporate more parameters with 7 being used to determine pH. Both this method and an analogous automated method to the manual method based on one parameter are shown. Tabl4 4.6 compares mean pH values along with standard deviation and mean error for manual and automated methods (data and figure produced by Kate Fisher).[187]

4.1.2 Other SERS pH Sensors

MBA-NPs were successfully calibrated for use in intracellular measurements and were taken forward to monitor intracellular pH changes. At the same time, MBA-NPs still had the drawback that the pH responsive peaks were of low intensity therefore increasing error and decreasing sensitivity with measurements. Therefore, new molecules capable of SERS pH sensing were investigated to attempt to overcome this problem.

4.1.2.1 4-Mercaptopyridine as a SERS pH Sensor

4MP has been documented in literature as a SERS pH sensor.[198–200] Figure 4.14(a) illustrates the equilibrium between protonated and non-protonated 4MP-NPs and Figure 4.13(b) illustrates spectra of 4MP-NPs at high and low pH. The major changes observed in the spectra, documented in literature, are the relative intensities of the peaks at approximately 1000 cm^{-1} and 1100 cm^{-1}, splitting of the peak at approximately 1600 cm^{-1} and variations in the signal at approximately 1200 cm^{-1}. The peak at approximately 1000 cm^{-1} is attributed to ring breathing present in both forms of the molecule. The peak at 1100 cm^{-1} is attributed to another ring breathing mode coupled to C-S stretching. Peaks around 1600 cm^{-1} are assigned to C=C stretching in the pyridine ring and at 1200 cm^{-1} to C-H in plane bending in the pyridine ring. Additional changes of the peak at approximately 1060 cm^{-1} were also investigated, with this peak also attributed to C-H in plane bending in the pyridine ring. These assignments are summarised in Table 4.6.

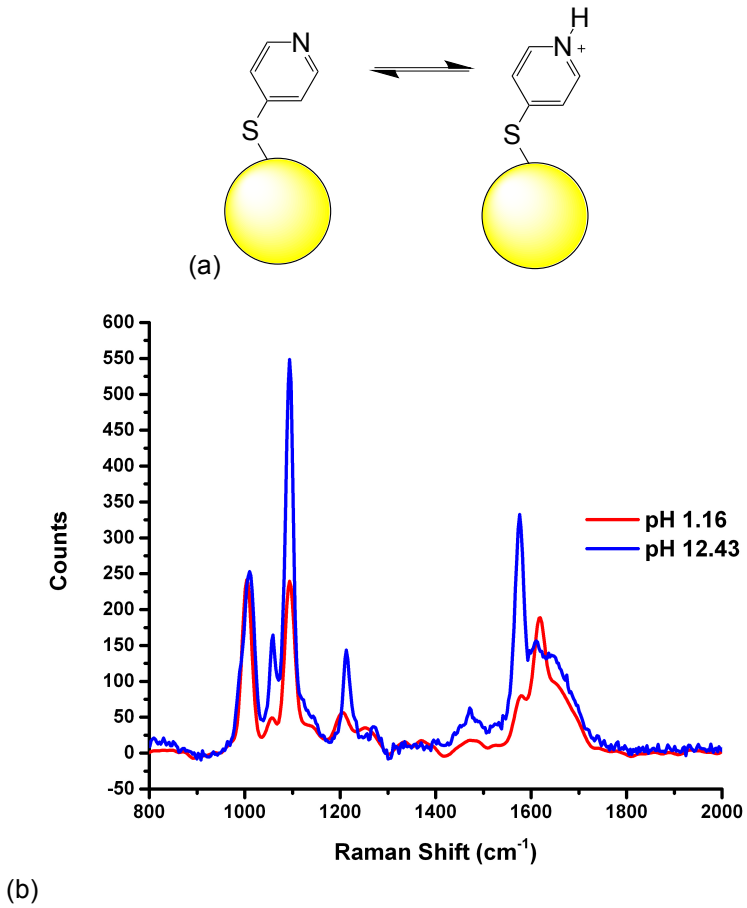

Figure 4.14 (a) illustrates the equilibrium between protonated and deprotonated 4MP-NPs where the yellow spheres represent NPs and (b) illustrates representative 4MP-NP spectra at high and low pH.

Table 4.7 summarises the main SERS peaks found in 4MP-NP spectra.[198,200]

Wavenumber (cm^{-1})	Assignment	pH sensitive?
1000	ring breathing	yes
1059	C-H in plane bending ring	yes
1100	ring breathing coupled with C-S stretch	yes
1200	C-H in plane bending ring	yes
1600	C=C stretching ring	yes

When plotting the peak intensity ratio of different combinations of these pH sensitive peaks against pH, as illustrated in Figure 4.15, a correlation was observed. However, the apparent pKa value determined ranged from 2.1 to 4.5 and therefore the measurement range of this sensor was outside the desired range for the measurement of physiological conditions. Fits were also generally poorer than with MBA-NPs with further investigation required to optimise this. It was proposed that adding an electron donating group, particularly to the 2 position, of the pyridine would make it easier to protonate and therefore increase the pKa. This could be a subject of further investigation in the future.

Calibration of 4MP-NPs was also attempted on the Renishaw inVia system and Figure 4.16 illustrates a plot of the peak intensity ratio of the 1000 cm^{-1} and 1100 cm^{-1} peaks against pH. Again a trend was observed but with poorer fit and an apparent pKa of 1.2 therefore not covering the relevant physiological range of pH values being investigated.

Table 4.8 details the apparent pKa determined from x0 and adjusted R^2 values from the Boltzmann fits for plots of peak intensity ratios against pH given in Figure 4.15.

Plot	Apparent pKa	Adjusted R^2
1100 cm^{-1}/1000 cm^{-1}	2.8	0.91625
1000 cm^{-1}/1100 cm^{-1}	2.1	0.93861
1200 cm^{-1}/1000 cm^{-1}	3.2	0.97532
1200 cm^{-1}/1100 cm^{-1}	4.5	0.88122
1059 cm^{-1}/1000 cm^{-1}	2.6	0.93752
1059 cm^{-1}/1100 cm^{-1}	2.6	0.92818
1580 cm^{-1}/1620 cm^{-1}	3.9	0.63078
1620 cm^{-1}/1580 cm^{-1}	3.1	0.91509

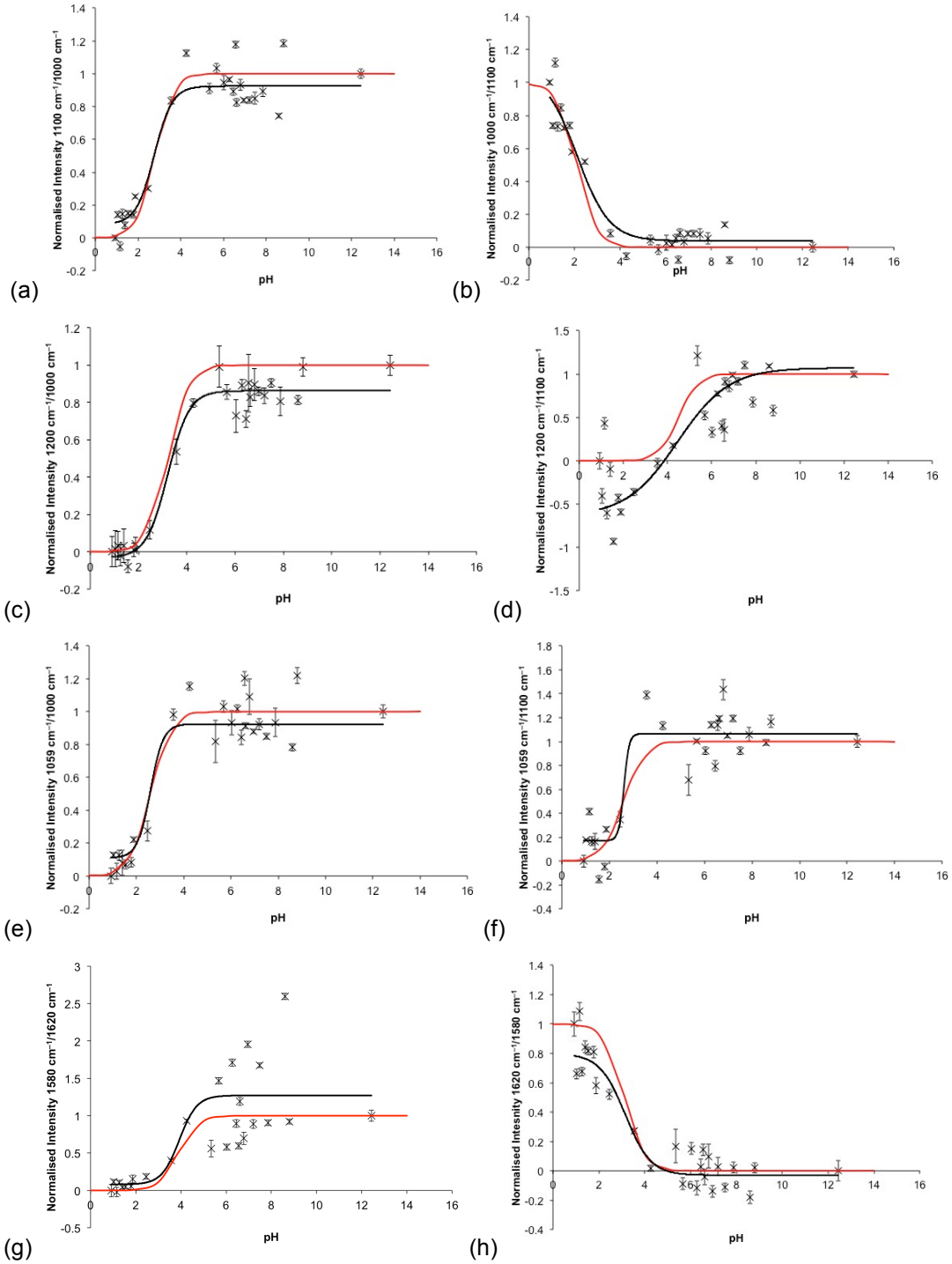

Figure 4.15 illustrates graphs that plot normalised peak intensity ratios against pH for various peak combinations for the calibration of 4MP-NPs on an Ocean Optics QE65 spectrometer. Black lines are the Boltzmann fit to plotted points and red lines are the theoretical Henderson Hasselbalch curves with pKa determined from the Boltzmann fit as equal to x0. Various combinations of peak intensity ratios were investigated using peaks at approximately 1000 cm^{-1}, 1059 cm^{-1}, 1100 cm^{-1}, 1200 cm^{-1}, 1580 cm^{-1} and 1620 cm^{-1}.

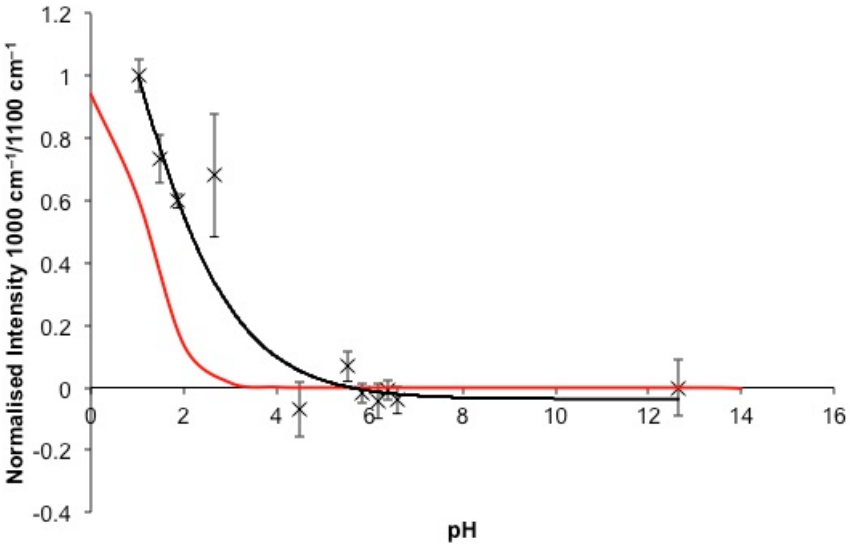

Figure 4.16 illustrates a graph plotting the normalised peak intensity ratio of the 1000 cm^{-1} and 1100 cm^{-1} peaks against pH for calibration of 4MP-NPs on a Renishaw inVia spectrometer. The black line is the Boltzmann fit to plotted points and the red line is the theoretical Henderson Hasselbalch curves with apparent pKa determined from the Boltzmann fit (x0) as 1.2 and adjusted R^2 of 0.98443.

4.1.2.2 4-Aminobenzenethiol as a SERS pH Sensor

Another molecule reported in literature to have pH dependent SERS peaks was 4ABT.[201] Figure 4.17(a) shows the equilibrium between protonated and deprotonated 4ABT-NPs and Figure 4.17(b) shows representative spectra of 4ABT-NPs at high and low pH. Initially, calibration of 4ABT-NPs was attempted using the same procedure as previously. However, results showed a random correlation of peak intensity ratios with pH. One suggestion is that 'hotspots'[206] could be greatly enhancing the intensity from one or a few individual molecules and therefore skewing the overall average depending on the protonation state of the molecules in these 'hotspots'. Therefore, it was suggested that a better setup would be to perform calibration in solution. This is also more representative of the environment that NPs would be in during application for intracellular measurements. For this experiment, equal volumes of 4ABT-NPs and buffer were mixed on a gold coated slide before recording the pH using a micro pH meter and collecting spectra of the solution as described in Chapter 2. Five peaks were selected for calibration purposes as detailed in Table 4.9 and shown in Figure 4.18. The peaks between 1100 cm^{-1} and 1500 cm^{-1} appear to be pH sensitive and are assigned to b_2-type bands only present in SER spectra and not in normal Raman spectra. The peak at approximately 1080 cm^{-1} is assigned to ring deformation and those at 1580 cm^{-1} and 1640 cm^{-1}

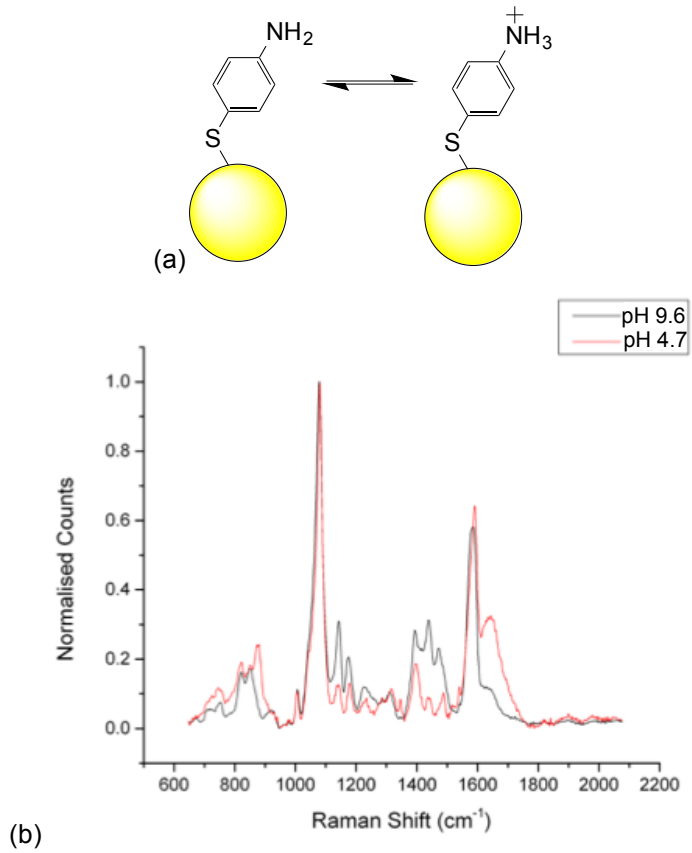

Figure 4.17 (a) illustrates the equilibrium between protonated and deprotonated 4ABT-NPs where the yellow spheres represent NPs and (b) illustrates representative 4ABT-NP spectra at high and low pH.

to ring breathing. The 1640 cm^{-1} peak appears to be pH sensitive while the other two are not. A variety of plots were made using different peak intensity ratios against pH showing a correlation. However adjusted R^2 values were poor and further work would be required to optimise this as a SERS pH probe. The apparent pKa values determined ranged from 6.1 to 6.8 meaning that with further optimisation 4ABT-NPs could potentially monitor intracellular pH within the physiologically relevant range.

Table 4.9 summarises the main SERS peaks found in 4ABT-NP spectra.[201]

Wavenumber (cm^{-1})	Assignment	pH sensitive?
1080	ring deformation	no
1400	b_2-type band	yes
1440	b_2-type band	yes
1580	ring breathing	no
1640	ring breathing	yes

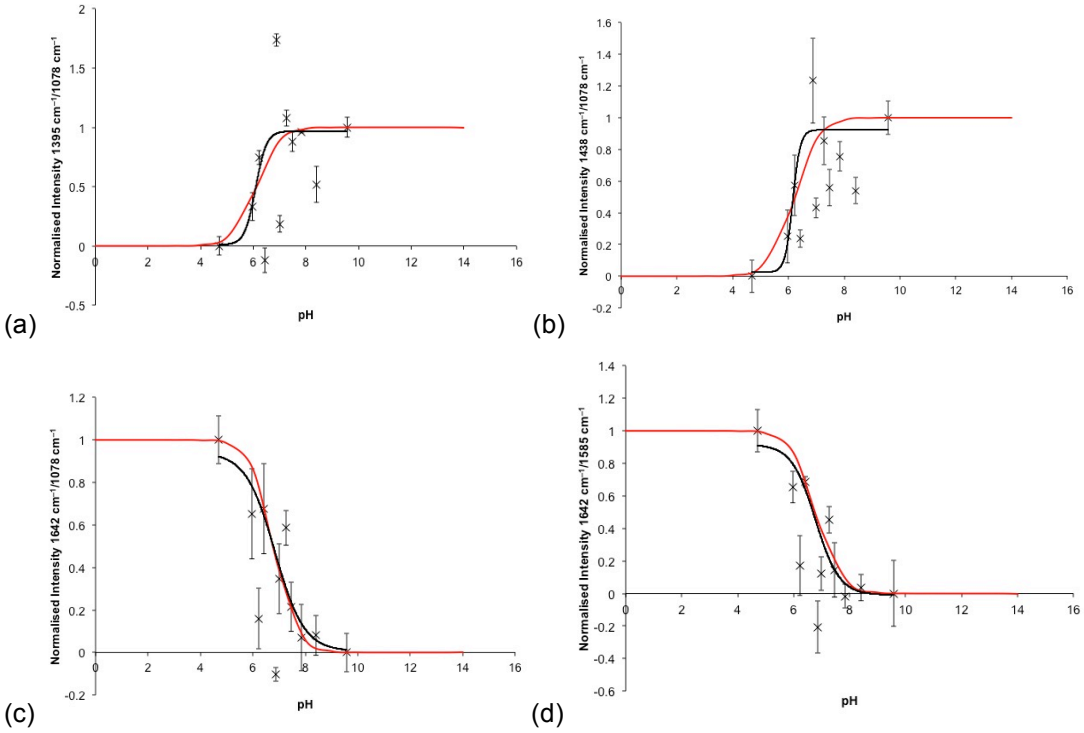

Figure 4.18 illustrates graphs that plot normalised peak intensity ratios against pH for various peak combinations for the calibration of 4ABT-NPs on an Ocean Optics QE65 spectrometer. Black lines are the Boltzmann fit to plotted points and red lines are the theoretical Henderson Hasselbalch curves determined from the Boltzmann fit as equal to x0. Various combinations of intensity ratios were investigated using peaks at approximately 1080 cm^{-1}, 1400 cm^{-1}, 1440 cm^{-1}, 1580 cm^{-1}, and 1640 cm^{-1}.

Table 4.10 details the apparent pKa determined from x0 and adjusted R^2 values from the Boltzmann fits for plots of peak intensity ratios against pH given in Figure 4.18.

Plot	Apparent pKa	Adjusted R^2
1395 cm^{-1}/1078 cm^{-1}	6.1	0.03104
1438 cm^{-1}/1078 cm^{-1}	6.2	0.2451
1642 cm^{-1}/1078 cm^{-1}	6.8	0.61816
1642 cm^{-1}/1585 cm^{-1}	6.8	0.64892

4.1.2.3 Mercaptonitrobenzoic Acid (NBA) as a SERS pH Sensor

As already suggested, it was proposed that the pKa of a particular SERS pH sensor could be altered by adding electron donating or electron withdrawing groups to different positions on the benzene ring. Therefore, a substituted mercaptobenzoic acid was investigated as a SERS

pH sensor. Due to commercial availability, a substituted 2-mercaptobenzoic acid, rather than *para*mercaptobenzoic acid, was used, with a nitro group in the *para* position. A nitro group is electron withdrawing and therefore would stabilise the deprotonated form of NBA, and, in theory, decrease the pKa.[206,207] Figure 4.19 shows the equilibrium between protonated and deprotonated NBA-NPs and an example of SERS spectra collected at high and low pH. Again calibration of this sensor was carried out in solution, but no major correlation between peak intensity ratio and pH was observed. Peaks at 1070 cm^{-1}, 1330 cm^{-1} and 1560 cm^{-1} were investigated and results are shown in Figure 4.20 where no significant correlation is observed.

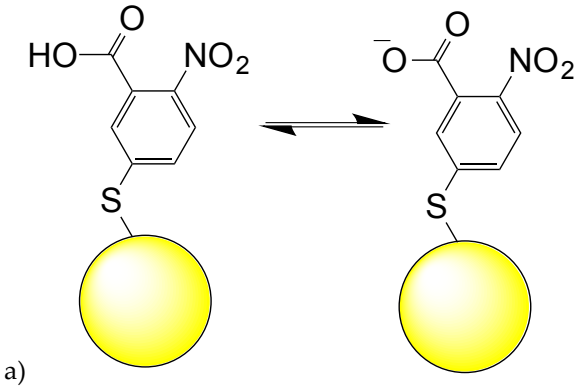

a)

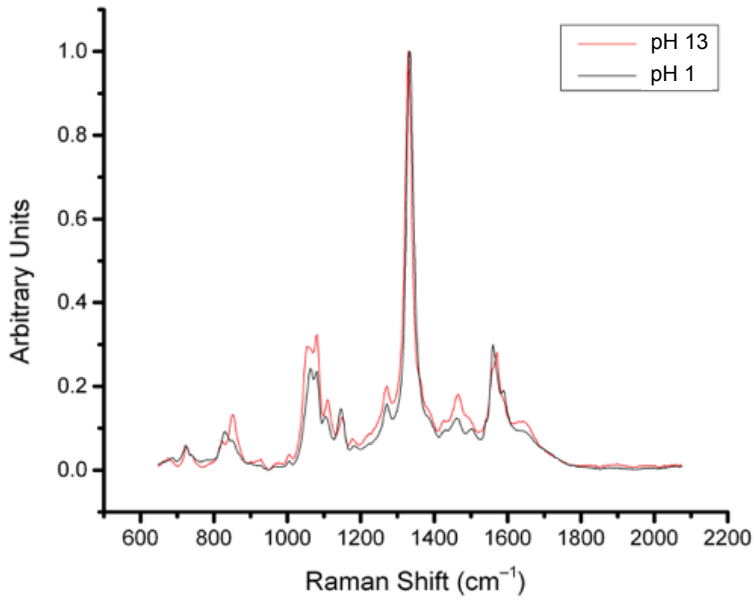

(b)

Figure 4.19 (a) illustrates the equilibrium between protonated and deprotonated NBA-NPs where the yellow spheres represent NPs and (b) illustrates representative NBA-NP spectra at high and low pH.

Table 4.11 summarises the main SERS peaks found in NBA-NP spectra.[208]

Wavenumber (cm^{-1})	Assignment	pH sensitive?
1070	aromatic ring	no
1330	nitro symmetric stretch	no
1560	aromatic ring stretch	no

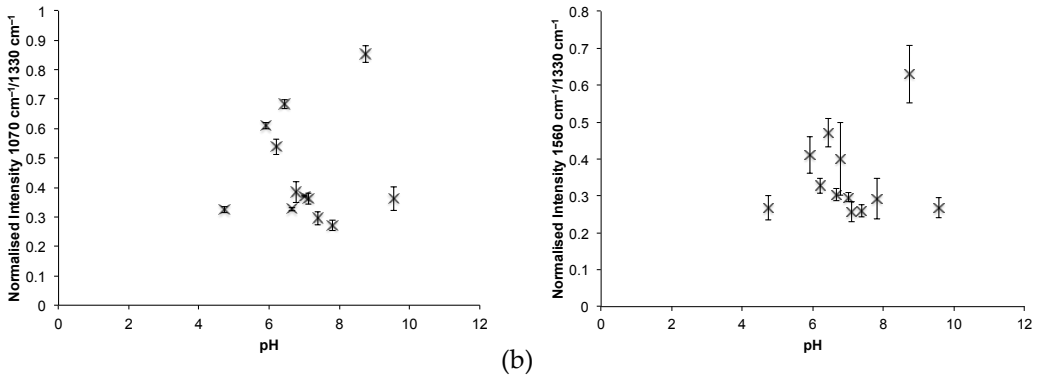

(a) (b)

Figure 4.20 illustrates graphs that plot normalised peak intensity ratios against pH for for the calibration of NBA-NPs on an Ocean Optics QE65 spectrometer. Intensity ratios of the signals at 1070 cm^{-1} and 1330 cm^{-1} (a) and 1560 cm^{-1} and 1330 cm^{-1} (b) were investigated and showed no significant correlation with pH.

4.2 Intracellular pH Measurements in Monolayer Culture Using MBA-NPs

While some other sensors showed potential for future development after further modifications, MBA-NPs were the most successfully calibrated SERS nanosensor to take forward for intracellular measurement. This sensor was firstly delivered to MCF7 breast cancer cells (being used in most of this research) and pH was detected during the progression of apoptosis stimulated chemically by treatment with staurosporine (STS). In a collaborative project, MBA-NPs were delivered to endothelial cells and pH monitored under normoxic conditions and in response to changing pH in the extracellular environment and treatment with tumour necrosis factor-α.

4.2.1 pH Changes During Apoptosis

MBA-NPs were delivered to MCF7 cells in monolayer culture by overnight incubation as described in Chapter 2. Cells were mapped using a Renishaw inVia spectrometer, as described in Chapter 2 Section 2.2.7.1, and spectra were processed, yielding a mean pH of 8.6 ± 1.2. This was significantly higher than the expected intracellular pH in cells. However, it could be attributed to exposure to air when the cells were taken from the incubator for measurement.

As it is common to find regions of apoptosis and necrosis in MTS, MCF7 cells in monolayer culture incubated overnight with MBA-NPs were treated with staurosporine (STS) to induce apoptosis and allow pH to be monitored during this process. This could provide an indication of the changes in pH during apoptosis and perhaps a point of comparison when monitoring changes in MTS, to indicate the life cycle stage the cells were in. STS is a protein kinase inhibitor and it has been shown to primarily induce apoptosis via caspase-3 (CASP3), one of the primary caspases involved in apoptosis. While MCF7 cells do not express CASP3, STS has still been shown to successfully induce apoptosis and necrosis in MCF7 cells through other mechanisms.[209–211]

Figure 4.21 shows typical white light images of the appearance of cells at different times after treatment with STS. The primary difference in morphology observed was a rounding of cells into spherical shapes and the observation of the start of detachment of cells from the substrate, as they become raised from the surface. Figure 4.22 and Table 4.12 summarise changes in pH observed under treatment of MCF7 cells with STS over various time periods. All cells were treated at the same time and measurements were made on different plates for each time point. Therefore, cells were exposed to the atmosphere for approximately the same time in each condition. After treatment, a large volume of the spectra recorded and processed gave a ratio that was outside the range of pH values possible to detect using MBA-NPs. In all cases, the ratio was above the basic limit of the sensor, meaning that the ratio was above 0.24. Therefore, as well as average pH and standard deviation for all measurable pH values under each condition, the percentage of spectra that gave measurable pH values was determined. Both of these values were recorded in Figure 4.22 and Table 4.12.

A one-way ANOVA was used to compare the means of each condition and significantly different results at the 0.05 level are marked in Figure 4.22. A significant change in pH was

observed immediately after treatment with STS, increasing from 8.6 ± 1.2 to 10.9 ± 1.0, the majority of the spectra being above the basic limit. The pH remained approximately constant after 1 hr, with no significant change from immediately after treatment (0-1 hr) with an average pH of 10.7 ± 1.6. After this, the average pH decreased again to 9.4 ± 1.1 after 2-3 hr treatment, a significant difference from the 1-2 hr time point. There was no significant difference going to the 4 hr timepoint, with a slight increase to 10.1 ± 1.4 followed by a significant change to 9.1 ± 1.1 after 5-6 hr and 9.4 ± 0.8 after 6-7 hr. The percentage of spectra with values within the limit of MBA-NP measurement reflected the same trend as average pH values. The most significant trend was the initial dramatic increase in pH, followed by a slight decrease, but still an increase from the untreated sample, from 2 hr onward. All pH values recorded were much more basic than expected under physiological conditions, but could be attributed to exposure of cells to the atmosphere, and therefore a decrease in CO_2 level, prior to measurement.[212] There was, however, a definite change in pH measured after STS treatment, with differences observed during the time course of treatment, showing the applicability of the SERS technique for this purpose. One possible explanation for the pH trend observed would be that the initial stages of apoptosis involve mitochondrial membrane depolarisation and permeabilisation[213], leading to release of their contents into the cytosol. Mitochondria have a more basic pH than the cytosol[214] and therefore this could account for an increase in pH during apoptosis. Following from this, later stages of apoptosis involving the lysing of acidic lysosomes could reduce the pH from this initial increase.[215] It is possible that the initial dramatic response upon treatment could be a stress response from cells, which then fight to adapt and therefore regulate the increase slightly.

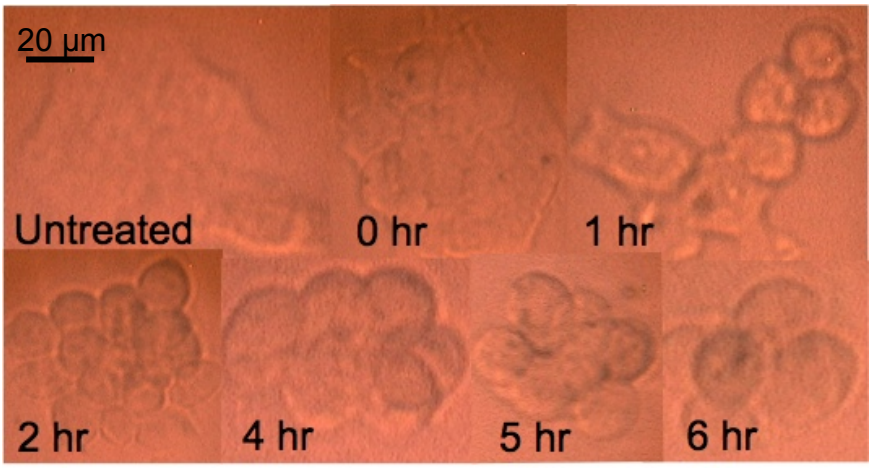

Figure 4.21 shows white light images of MCF7 cells under the Raman microscope before and after treatment with STS at a variety of time points.

Table 4.12 tabulates results for the variation in pH of MCF7 cells before and after treatment with STS at a variety of time points determined using the SERS pH sensor MBA-NP.

Time after STS treatement	n	% spectra within measurable limit	Average pH	Standard Deviation
Untreated	17	100	8.6	1.2
0-1 hr	46	13	10.9	1.0
1-2 hr	210	29	10.7	1.6
2-3 hr	160	76	9.4	1.1
4-5 hr	19	47	10.1	1.4
5-6 hr	261	83	9.1	1.1
6-7 hr	44	95	9.4	0.8

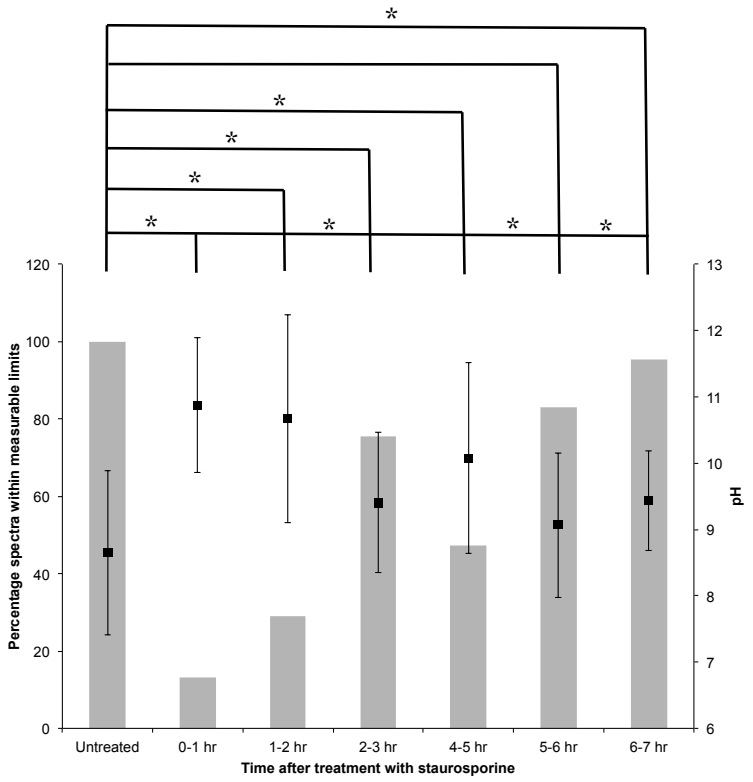

Figure 4.22 shows graphically the variation in pH of MCF7 cells before and after treatment with STS at a variety of time points determined using the SERS pH sensor MBA-NP. Bars show the percentage of spectra collected under each condition that were within the limits of detection of the sensor used (others were above the basic limit) and points show the pH determined from those within the limits. One-way ANOVA was used to determine if mean pH were significantly different and those marked * were significantly different at the 0.05 level.

4.2.2 Monitoring Intracellular pH in Endothelial Cells using MBA-NPs and Response to Changing pH of Extracellular Environment and Tumour Necrosis Factor-α

In collaboration with the Baranska group at Jagiellonian University in Poland, MBA-NPs were used to monitor intracellular pH in EA.hy926 endothelial cells. Endothelial cells line the inside of blood and lymphatic vessels and have many important roles in the body including involvement in inflammation, vasoregulation and coagulation.[216] It has been demonstrated that intracellular pH plays an important role in many of these processes and, for example, acidification of intracellular pH in endothelial cells has been linked to many severe pathologies in humans.[217] It is worth noting that intracellular pH plays an important role in numerous processes in all cell types and not just endothelial cells and therefore quantitative measurement of intracellular pH by SERS could provide vital information in the study of many cells and the development of new therapies for the treatment of disease where dysregulation of intracellular pH may play an important factor. Processes highly dependent on intracellular pH include regulation of cell volume, metabolism and trafficking via vesicles.[218] For these reasons it was important to demonstrate the applicability of SERS as a tool for intracellular pH monitoring quantitatively using MBA-NPs. This is an improvement on fluorescence based techniques as already discussed.

For this particular study 40 nm gold NPs were synthesised and functionalised with MBA as described in Chapter 2 Section 2.2.2 and Section 2.2.2.3 respectively. Uptake of functionalised NPs was studied over different time points for optimisation, as previous studies carried out in the Baranska group had observed that rhodamine 6G (R6G) functionalised NPs were taken up by EA.hy926 cells within 0.5 h and after 2 h where maximum signal was observed, R6G started detaching from the NPs.[184] It was expected that that MBA-NPs would behave differently and MBA would remain attached to the NP surface as the nature of the interaction is different – MBA is attached by a covalent Au-S bond, while R6G is attached electrostatically.[219] In order to investigate uptake, maps of intensity of the 1070 cm^{-1} peak in EA.hy926 cells were created for the different time points. Cells were treated with MBA-NPs as described in Chapter 2 Section 2.2.7.2.1, and washed before SERS maps were obtained. Figure 4.23 displays these maps along with a representative spectrum for each time point. It could be observed that peak intensity increased with increasing incubation time, with the less

intense pH sensitive peaks only visible above the noise after 4 hr incubation. Therefore, a 12 hr incubation was selected for measurements.

Following from selection of incubation time, cells were mapped under various conditions to investigate the effect of change in extracellular pH on the resulting intracellular pH. Hierarchical k-means cluster analysis was used to analyse SERS maps under each condition, as described in Chapter 2 Section 2.2.4. Figure 4.24 shows the results from cluster analysis giving a variety of pH values under each condition. For control cells (pH 7.2), cells were incubated with PBS, and other conditions involved incubation with buffers of pH 3.9, 6.2, 8.6 and 11.3. In this case, calibration data for determination of pH values for each cluster were taken from plots using the 1070 cm^{-1} peak intensity shown in Figure 4.25. Cells responded to changes in extracellular environment pH as expected with average cluster pH moving to more acidic and basic values on application of more acidic and basic buffers in the extracellular environment respectively. Clusters that gave pH values at the more extreme ends of the scale under each condition could be attributed to NPs present inside internal cellular structures, particularly in the endocytic cycle. As described in Chapter 3 Section 3.3, it is thought that NPs are taken up by endocytosis followed by potential release into the cytosol. However, some NPs remain in vesicles (with Salvati *et al.*[193] demonstrating that NPs tend to accumulate in lysosomes) and this could be the environment being measured by these particular clusters.

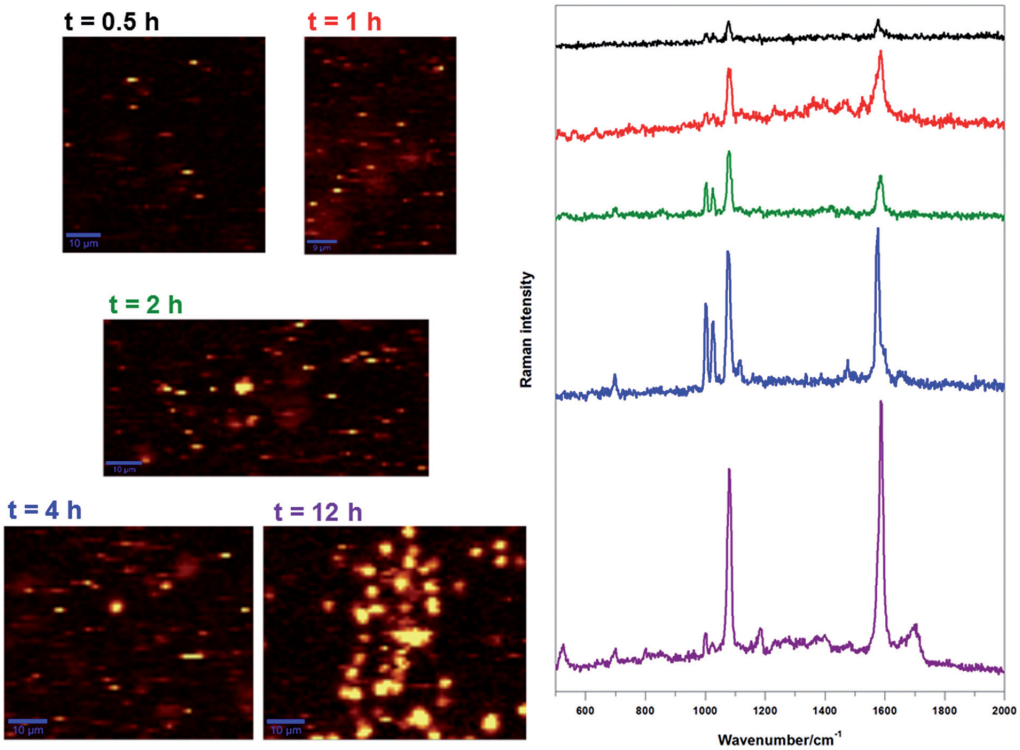

Figure 4.23 illustrates SERS intensity maps of 1070 cm^{-1} peak intensity in EA.hy926 cells treated with MBA-NPs for various time periods indicated and corresponding representative SER spectra from a region of high intensity under each condition. Black corresponds to 0.5 h incubation, red to 1 h incubation, green to 2 h incubation, blue to 4 h incubation and purple to 12 h incubation. Peak intensity increased with increasing incubation and 12 h incubation was used for further measurements. In each case cells were washed before recoding SERS spectra.

TNF-α is another apoptotic agent, known to induce depolarisation of mitochondrial membranes, increase concentration of intracellular Ca^{2+} and cause the release of cytochrome c and changes of pH in the cytosol.[220,221] EA.hy926 cells incubated with MBA-NPs were treated with TNF-α as described in Chapter 2 Section 2.1.7.2, and cells were mapped for SERS pH measurements as previously (experiments carried out by Aleksandra Jaworska). Figure 4.26 shows the results of cluster analysis on the cells. The bright field image also highlights the cell rounding and cell blebbing expected upon induction of apoptosis. It is worth noting that cluster analysis revealed a more uniform distribution of SERS signals over the cells compared to untreated cells and this is likely to be a result of loss of internal cell structure integrity allowing MBA-NPs to be distributed throughout the whole cell volume.

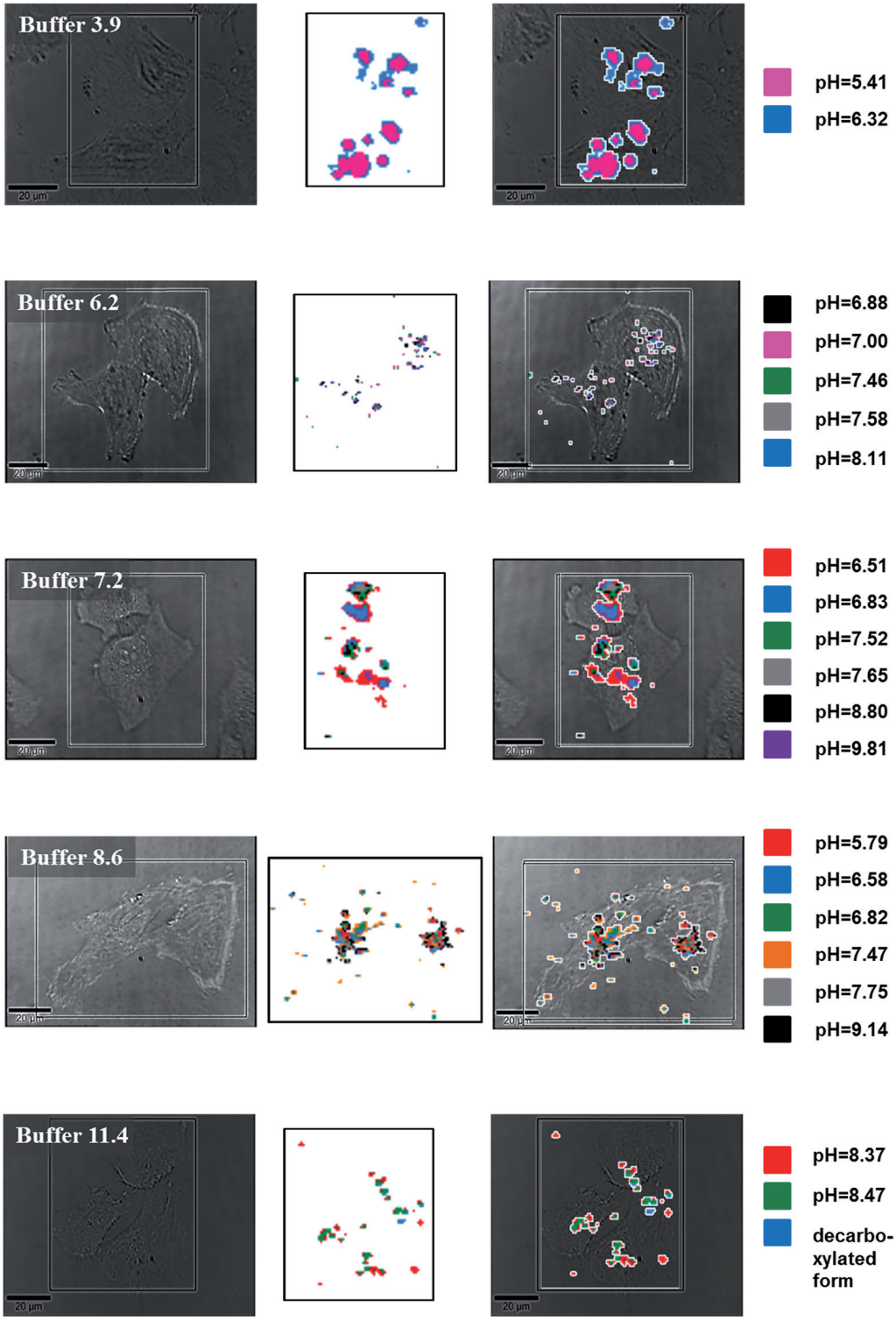

Figure 4.24 shows bright field (left) images of EA.hy926 cells incubated with MBA-NPs for 12 hr and mapped using a Raman spectrometer for SERS signals from MBA-NPs. K-means cluster analysis was used to analyse the distribution of pH within each cell (middle) with an overlay on the bright field image on the right. Cells were measured under normal conditions (PBS – Buffer 7.2) as well as using different extracellular buffers.

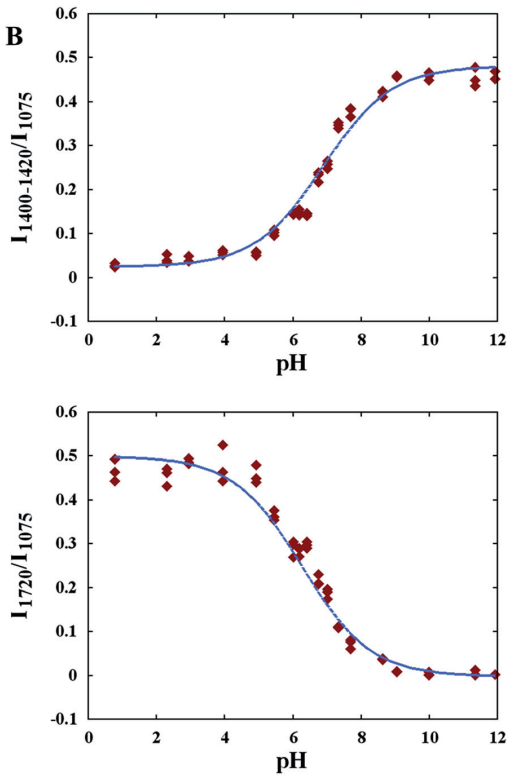

Figure 4.25 shows the calibration curves used to generate the pH measurements for EA.hy926 cells incubated with MBA-NPs and under different extracellular buffer conditions. Plots examine the ratio of intensity of peaks at 14—cm^{-1} and 1075 cm^{-1} (top) and 17—cm^{-1} and 1075 cm^{-1} (bottom).

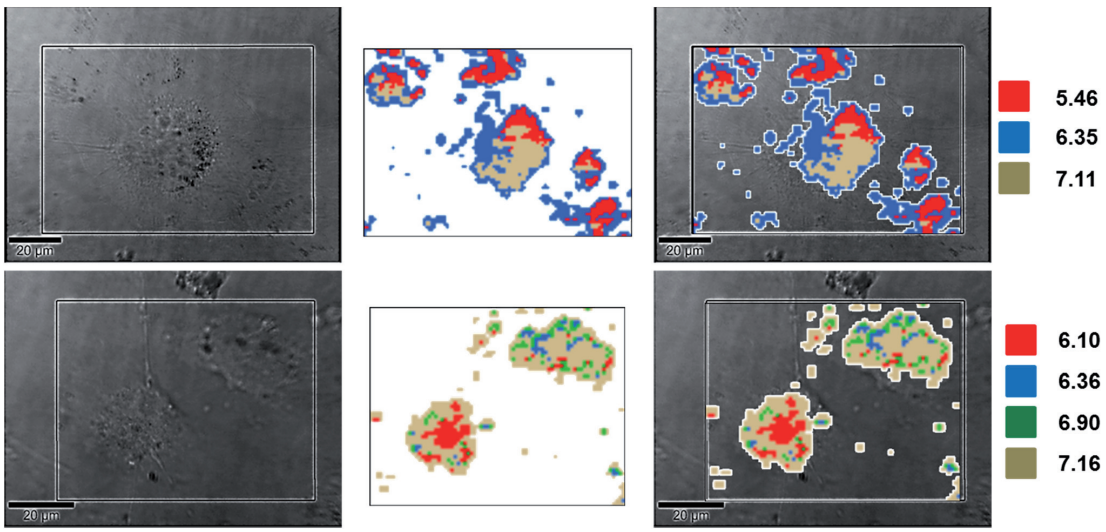

Figure 4.26 shows bright field images (left) of EA.hy926 cells incubated with MBA-NPs for 13 hr and treated with TNF-α before performing a Raman map of the cells and k-means cluster analysis of the resultant spectra (middle), overlaid with the bright field image (right).

4.3 Conclusions

This chapter has demonstrated the development of MBA-NPs as a SERS pH sensor. Attempts were also made to develop further SERS pH sensors to improve on the drawback of MBA that the pH responsive peaks are weak in comparison to the other peaks in the spectrum. 4MP-NPs showed pH responsive trends but the pKa and range covered was too low for physiological conditions. It was proposed that adding substituents could modify this in the future. ABT-NPs showed potential as a SERS pH sensor but further work was required to reduce error in calibration. NBA-NPs were investigated as a substituted version of MBA but no correlation between peak intensity ratio and pH was observed.

After establishing MBA-NPs as a suitable SERS pH sensor, intracellular SERS measurements using this sensor were performed. Intracellular pH is an important characteristic involved in many cellular processes and dysregulation of this could also lead to disease development. Therefore, monitoring intracellular pH and response to stimuli such as drugs is important. Changes in intracellular pH of MCF7 cells during apoptosis progression induced by STS and in EA.hy926 cells treated with buffers of different pH and TNF-α were investigated. Both experiments demonstrated successful use of MBA-NPs as a SERS pH sensor to allow quantitative measurement of intracellular pH and response to treatment.

Chapter 5

Simultaneous Intracellular Redox Potential and pH Measurements in Monolayer Culture and MTS

"I don't run away from a challenge because I am afraid. Instead, I run toward it because the only way to escape fear is to trample it beneath your feet." – **Nadia Comaneci**

Following from development of MBA-NPs as a suitable SERS pH sensor for intracellular pH measurements, attempts were made to combine this with intracellular redox potential measurements in monolayer culture and MTS. As discussed, further development of SERS pH sensors could provide a more accurate sensor with pH responsive peak intensities more similar in intensity to reference peak intensities. However, within the time period MBA-NPs were the most optimal sensor to take forward for further investigation. Initially, measurements were performed in monolayer culture using MBA-NPs for pH detection along with AQ-NPs for redox potential detection. Following from this, measurements were performed in MTS using MBA-NPs for pH detection along with AQ-NPs and NQ-NPs for redox potential detection. Detection of pH and redox potential simultaneously allowed suitable correction to be made to redox potential values to provide accurate measurements.

5.1 Simultaneous Intracellular Redox Potential and pH Measurements in Live Cells in Monolayer Culture Using SERS Nanosensors

Initial work towards simultaneous intracellular measurement of redox potential and pH was carried out in monolayer culture. It was proposed that NPs functionalised with MBA and NPs functionalised with a redox probe (either NQ or AQ) would be delivered simultaneously to cells growing in monolayer culture before performing Raman mapping of cells on a WITec spectrometer. Initially, it was proposed that MBA could be functionalised onto NPs resonant at one wavelength and NQ/AQ could be functionalised onto different NPs resonant at a different wavelength. By mapping the same cell with different lasers, corresponding to the resonant wavelengths of each of the NPs, the same cell could then be mapped separately for

pH and redox potential, giving distinct spectra in each case. For this purpose, it was initially proposed that 40 nm NPs, resonant at 530 nm, and 150 nm NPs, resonant at 780 nm, could be used. These were chosen as this work was carried out in collaboration with the Baranska group, in which they used 40 nm NPs with a 633 nm laser, while our group uses 150 nm NPs with a 785 nm laser. Measurements were unsuccessful, however, as MBA-NP signals (see Chapter 4 Section 4.1.1 Figure 4.2 for example of MBA-NP spectra) were observed in all cases – 40 nm MBA-NPs still gave a signal using the 785 nm laser. This was most likely a result of MBA having such a high cross section for Raman scattering, meaning that, while 785 nm is not an optimal resonance for the 40 nm NPs, they still gave enough resonance for MBA signals to be observed. It could also be a result of broad absorbance of the NPs, meaning that, while 40 nm NPs have their maximum resonance at 530 nm, there remains some surface plasmon resonance at 785 nm. Aggregation of NPs could also be contributing, as aggregation has been shown to broaden and red shift plasmon resonances.[222]

Following from this, different combinations of NPs were investigated. 2.2 nm and 10 nm NPs (both resonant at 530 nm) and silver NPs (resonant at 409 nm) were introduced. NPs dried outside the cell were probed using 532 nm, 633 nm and 785 nm lasers. The problem remained that all NPs functionalised with MBA gave spectra using all lasers, despite maximum surface plasmon resonance at 633 nm, and therefore NQ/AQ-NP spectra could not be obtained independently of MBA. Again this could be explained by the broad absorbance of the 40 nm NPs, possibly further broadened by aggregation, and combined with MBA having a large cross section for Raman scattering. Therefore, as spectra could not be obtained independently, it was decided that a different approach would be taken, whereby 40 nm NPs would be used for both the pH and redox probes and cells would be mapped with a 633 nm laser. Resultant spectra should potentially display distinct MBA and AQ/NQ spectra and spectra with a combination of MBA and AQ/NQ signals. For this purpose, AQ was chosen as the redox probe, as signals in the AQ spectra were less similar to those from MBA. Figure 5.1(a) shows the equilibrium between oxidised and reduced AQ and Figure 5.1(b) shows representative spectra at highly oxidising and highly reducing conditions for this particular probe. The peak at 1666 cm^{-1}, corresponding to C=O stretching, reports on the oxidation state of the reporter and can be plotted relative to the non redox sensitive peak at 1606 cm^{-1}, corresponding to C=C stretching. For NQ the ring breathing peak at approximately 1580 cm^{-1} is too close to the ring breathing peak of MBA at approximately 1590 cm^{-1} for these signals to be resolved.

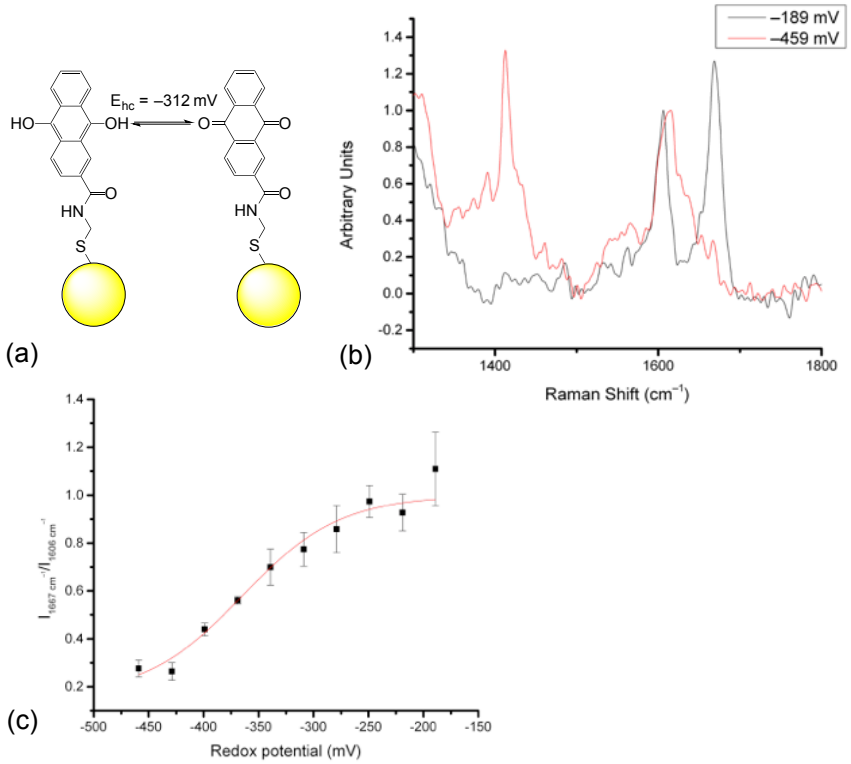

Figure 5.1 shows the equilibrium between oxidised and reduced AQ attached to a gold NP (yellow sphere, not to scale) (a); Representative spectra of fully oxidised (–189 mV) and fully reduced (–459 mV) AQ-NPs (b); and the calibration curve for AQ-NP nanosensors (Adj. R^2 0.96855) (c).

Calibration of AQ-NPs is described in Chapter 2 Section 2.2.5 and Section 2.4.2, and the resultant calibration plot is given in Figure 5.1(c). The resultant calibration is a stretched sigmoid centered around the $E_{1/2}$ of AQ. The stretched nature of the plot has been seen before[223] and is probably the result of hindered electron or proton transfer between the solution and the nanosensor. The Campbell group, University of Edinburgh, have demonstrated that AQ can be used to report on redox potentials that span from normoxia to hypoxia.[95,97] For previous calibration of AQ-NPs, spectra were processed by smoothing and baseline subtraction before extracting maximum intensities of the peaks of interest using the peak finding function on Origin 9. As AQ-NP signals were multiplexed with MBA-NP signals in this case, peak fitting was carried out on calibration spectra using the GaussAmp function as described in Chapter 2 Section 2.4.2. Figure 5.2 shows peak fits for an example spectrum for each redox potential.

Cells were incubated with MBA-NPs and AQ-NPs as described in Chapter 2. Cells were located and imaged and then Raman mapping was performed with acquisitions in 1 μm steps in x and y. Hierarchical k-means cluster analysis was performed on the resultant maps

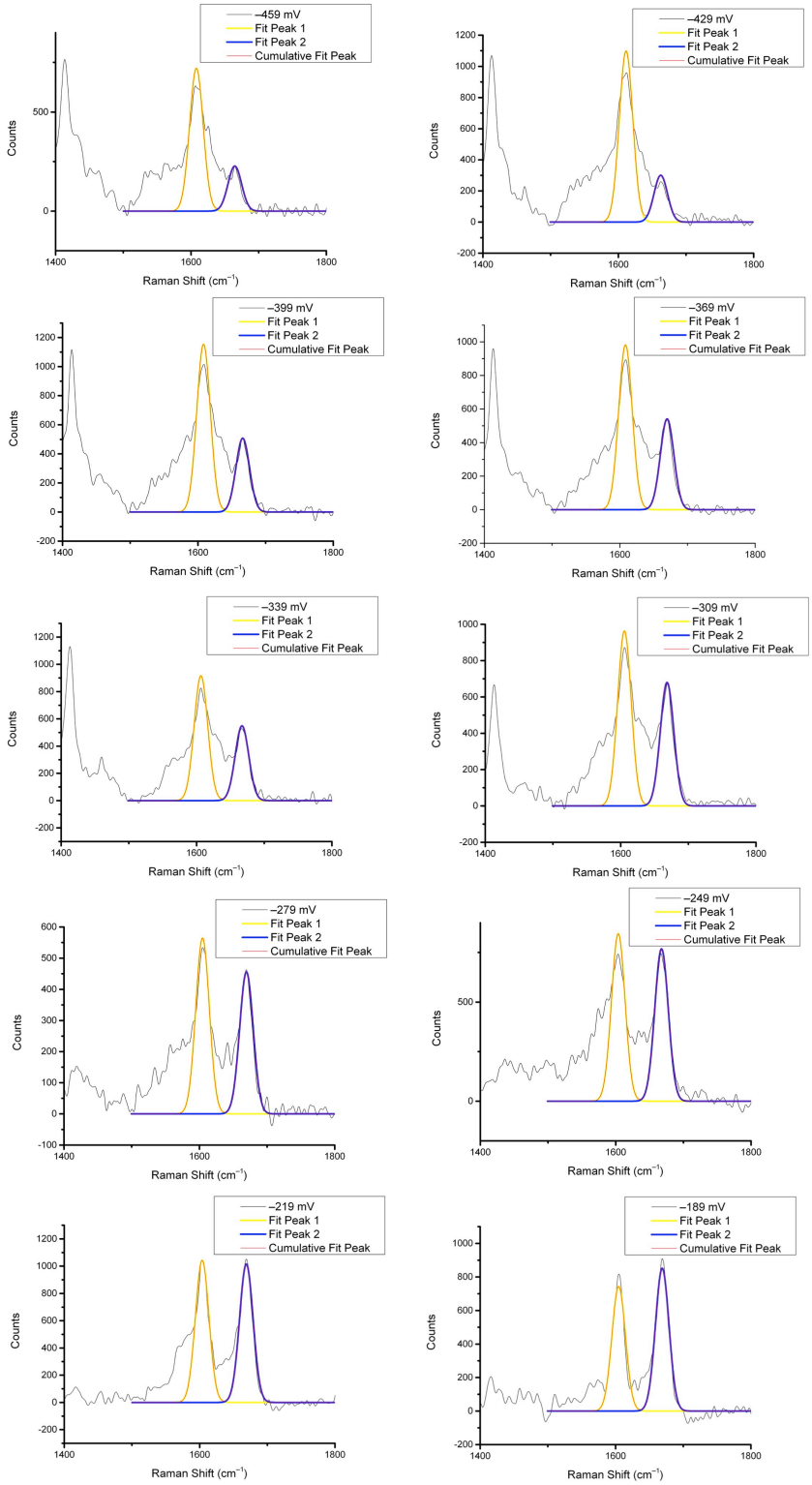

Figure 5.2 shows representative AQ-NP calibration spectra obtained from AQ-NPs in buffer and at a potential set by a potentiostat, with GaussAmp peak fitting at a range of redox potentials. The legend indicates the redox potential that each spectrum was acquired at; the yellow curve shows the peak fitted at *ca.* 1600 cm^{-1} in each case; the blue curve shows the peak fitted at *ca.* 1660 cm^{-1} in each case; and the red curve (largely overlapping with individual peaks) shows the cumulative peak fitting curve for both peaks.

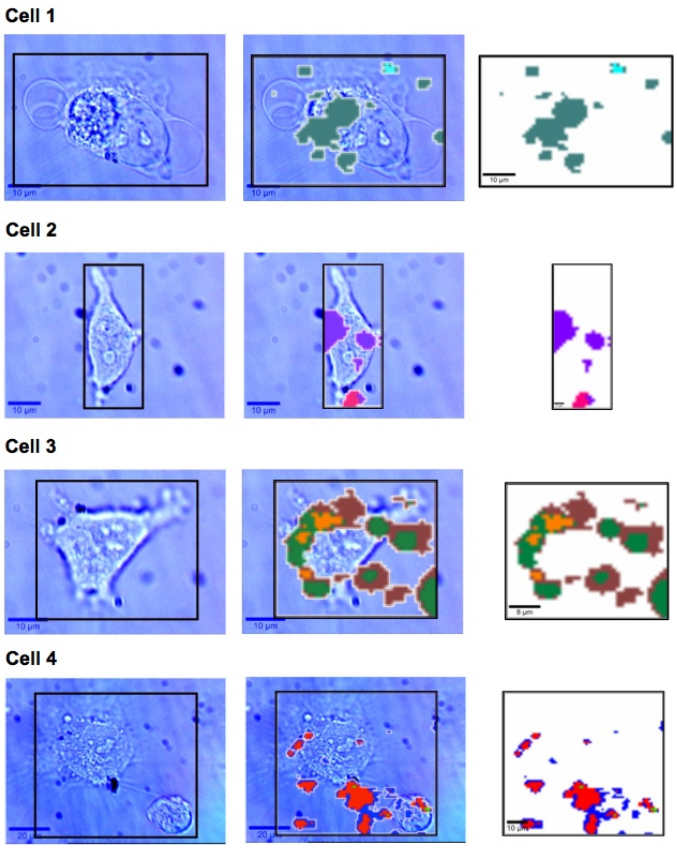

Figure 5.3 White light images of SERS mapped cells (left column) where area highlighted with black box corresponds to the Raman mapped area represented by the corresponding k-means cluster map (right hand column). Photographs and cluster maps are overlaid in the middle column. Each cluster from k-means cluster analysis is represented by a different colour. For cell 1 the turquoise cluster corresponds to a singleplex spectrum of MBA-NPs giving pH 7.1 and the cyan cluster corresponds to a multiplex spectrum of MBA-NPs and AQ-NPs from which redox potential –304 mV was extracted by peak fitting (pH adjusted to –297 mV). For cell 2 the purple cluster corresponds to a singlex spectrum of MBA-NPs giving pH 6.9 and the pink cluster corresponds to a multiplex spectrum of MBA-NPs and AQ-NPs from which redox potential –258 mV was extracted by peak fitting (pH adjusted to –241 mV). For cell 3 the green cluster corresponds to a singleplex spectrum of MBA-NPs giving pH 7.0 and the yellow and brown clusters correspond to multiplex spectra of MBA-NPs and AQ-NPs from which redox potentials of –276 mV and –345 mV were extracted respectively by peak fitting (pH adjusted to –272 mV and –332 mV respectively). For cell 4 the light green cluster corresponds to a singleplex spectrum of MBA-NPs giving pH 7.1 and the blue and red clusters correspond to multiplex spectra of MBA-NPs and AQ-NPs from which redox potentials of –337 mV and –306 mV were extracted respectively by peak fitting (pH adjusted to –320 mV and –300 mV respectively).

(Figure 5.3). This grouped similar spectra together into a single cluster represented by a colour on the false colour images and identified regions that contained NPs. An average spectrum representative of the cluster was generated for each colour. Cluster spectra were processed manually by subtracting a baseline (8 points) in order to give an average spectrum for the cell. Of all spectra collected, signals from MBA-NPs were predominant, with significantly fewer AQ-NP signals in comparison. All cluster spectra with AQ-NP signals were multiplexed with MBA-NP signals while other clusters gave singleplex MBA-NP signals. For this reason data analysis for multiplex spectra was simplified by determining only redox potential by peak fitting. From the 4 mapped cells, cluster analysis for Cell 1 and 2 gave 2 clusters. Analysis of the spectra revealed that one cluster gave a singleplex spectrum with only MBA-NP signals and the other gave a multiplex spectrum with evidence of both MBA-NP and AQ-NP signals. The remaining cells – 3 and 4 – revealed 3 clusters. In each case one cluster contained a singleplex spectrum with MBA-NP signals in isolation and the other 2 contained multiplexed signals at different ratios.

For spectra with only MBA-NP signals, peak finding was performed to determine the intensity of the peak at approximately 1400 cm^{-1} relative to the peak at approximately 1590 cm^{-1} and subsequently determine pH from the calibration data. For spectra with multiplexed signals, peak fitting, as described in the Chapter 2, was performed to extract the intensity of

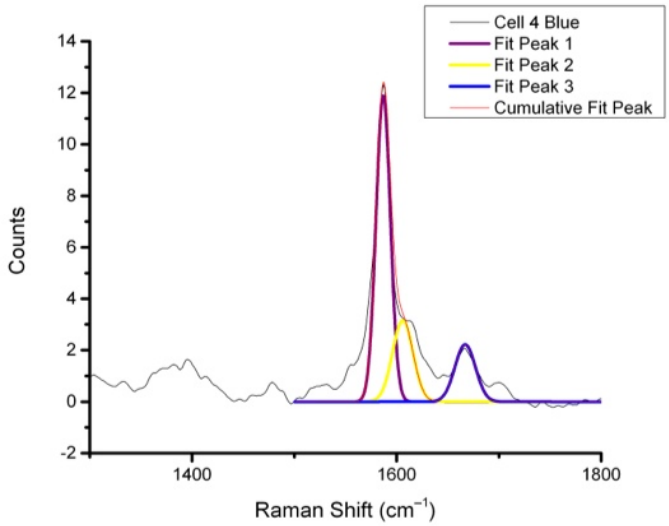

Figure 5.4 Representative example of peak fitting for a multiplex spectrum generated from k-means cluster analysis (cell 4 blue cluster). Peaks were fitted using a GaussAmp function with constrained parameters resulting in the 3 individual peak fits, Fit 1, 2 and 3 and the overall resultant Cumulative Fit Peak shown overlayed on the original spectrum (black line).

the peak at 1667 cm^{-1} relative to that at 1606 cm^{-1} and subsequently determine redox potential from the calibration data. Figure 5.4 illustrates one example of peak fitting for the blue cluster in cell 4. A GaussAmp function was used with fixed y0, peak widths and peak centers and peak intensities of the fitted peaks from AQ-NPs were obtained. All singleplex cluster spectra analysed for pH measurements are overlaid in Figure 5.5(a) and all multiplex cluster spectra analysed for redox measurements are overlaid in Figure 5.5(b).

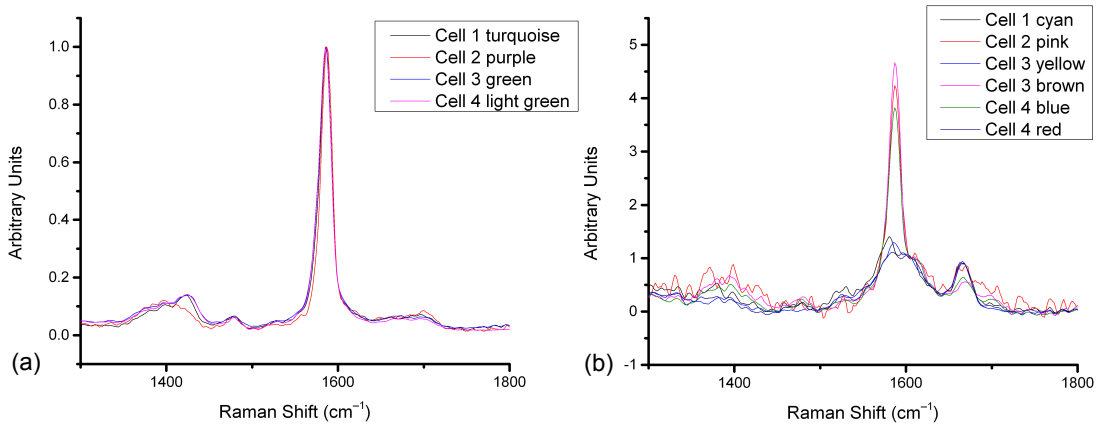

Figure 5.5 (a) Overlay of all singleplex spectra from cells 1-4 corresponding to the clusters indicated. Spectra show MBA-NP signals corresponding to the pH values given in Table 5.1, calculated by taking the intensity ratio of the peaks around 1400 cm^{-1} and 1590 cm^{-1}. (b) Overlay of all multiplex spectra from cells 1-4 corresponding to the clusters indicated. Spectra show both MBA-NP and AQ-NP signals overlapping. Peaks were fitted to extract the intensity ratio of peaks around 1670 cm^{-1} and 1600 cm^{-1} to give redox potential values given in Table 5.1.

Table 5.1 Calculated pH, redox potential and adjusted redox potential values for clusters from cells 1-4.

Cell	pH (Colour)	Redox Potential (mV) (Colour)	Adjusted Redox Potential (mV) (Colour)
1	7.1 (turquoise)	–304 (cyan)	–297 (cyan)
2	6.9 (purple)	–258 (pink)	–241 (pink)
3	7.0 (green)	–276 (yellow)	–272 (yellow)
		–345 (brown)	–332 (brown)
4	7.1 (light green)	–337 (blue)	–320 (blue)
		–306 (red)	–300 (red)

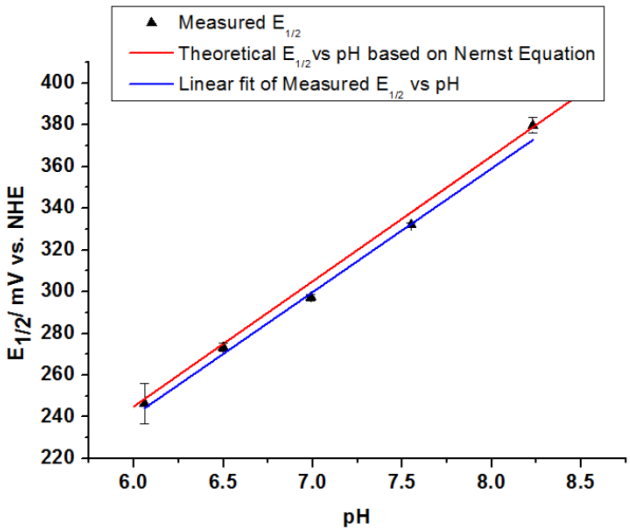

Figure 5.6 Half-cell potential of AQ at different pH measured by cyclic voltammetry, which correlates with the theoretical dependence of half-cell potential with pH according to the Nernst Equation (data collected and presented by J. Jiang).

Table 5.1 documents pH and redox potential values determined from each cluster from each cell in Figure 5.3. The significance of multiplexing pH and redox potential measurements is to allow for redox potential values to be corrected relative to pH. Jiang *et al.*[97] demonstrated that the half-cell potential of AQ relative to pH changed as expected from theory, by 60 mV per pH unit (Figure 5.6). Therefore, the redox potential values determined from each cell could be corrected based on the pH determined from the same cell.

A more detailed analysis of Figure 5.3 reveals that, in some cases, the colours representing clusters from NPs do not always overlay with cell location. It is likely that this is a result of drift during measurements and not signals from outside cells as the cells were washed multiple times before map acquisition. Various studies have supported NP uptake by cells[224–226] by fluorescence and transmission electron microscopy (TEM) and previous work in the Campbell group, University of Edinburgh, have supported this also.[92,95,157,184] Interestingly, the location of clusters corresponding to NPs varies between cells. For example, comparing cell 1 and cell 3, signals appear predominantly in a ring shape around the plasma membrane of cell 3 but in a more circular and centrally located area in cell 1. Location could be one factor influencing pH and redox potential. Both pH and redox potential differences between cells are apparent. In the case of cell 3 and cell 4, intracellular redox potential differences are also apparent. Intercellular pH variations were minimal, as expected for healthy cells, which maintain a pH around 7.2. Calculated pH varied by 0.2 pH units between 6.9 and 7.1. This is

in agreement with measurements assigned to cytosolic pH when the same MBA-NP reporter was used independently.[157] Redox variations were more substantial, with adjusted potential varying by 91 mV from –241 mV to –332 mV. This is in line with the normoxic range in A549 cells determined using AQ-NP[97] and the larger range could be attributed to varying stages of cell life cycle. In the future, this technique could be used to investigate more significant changes in response to, for example, disease and drug treatments.

These results are the first demonstration of simultaneous measurement of redox potential and pH and this greatly improves our ability to analyse intracellular microenvironments. Cluster analysis provided a simple way of condensing large volumes of information for analysis of average redox potential and pH on a cell by cell basis, providing a platform for detailed analysis of whole cell differences and response to treatment. Continued improvements in reporter design will allow for improved multiplexing of spectra with potential to include markers for other biochemical parameters. Importantly for this project, having established a technique for simultaneous measurement of redox potential and pH in monolayer culture as a simpler model system, the approach was then extended into the complex 3D model of MTS.

5.2 Simultaneous Intracellular Redox Potential and pH Measurements in Live Cells in MTS Using SERS Nanosensors – Ocean Optics and Photothermal OCT

Having established a successful technique for simultaneous measurement of intracellular redox potential and pH in cells in monolayer culture, this was extended into the MTS models. By delivering MBA-NPs and AQ-NPs to MTS, pH and redox potential could in theory be mapped in a similar way to previous experiments, but in a 3D manner. However, as discussed in Chapter 1, gaining suitable penetration depth using a confocal Raman system is difficult. It was also necessary to investigate the 3D distribution of NPs delivered to MTS. The Ocean Optics QE65 Pro system uses a fibre optic probe with a large laser focus spot, which allows spectra to be collected as an 'average' from a whole intact MTS. Therefore, it was proposed that an alternative method for measurement of variations in pH and redox potential in MTS would be to control the distribution of NPs to different areas in a MTS and subsequently record average spectra from the MTS for each condition.

5.2.1 Photothermal OCT – Visualising and Controlling 3D NP Distribution in MTS

It was proposed that by controlling NP delivery to different areas of MTS and recording a full MTS average SERS spectrum under each condition, radial differences in pH and redox potential could be investigated. To further investigate this, a method for determining 3D distribution of NPs in MTS was required. Photothermal OCT was used for this purpose. As discussed in Chapter 1, OCT allows greater depth penetration meaning that a full intact MTS could be imaged.[122] Other techniques are often limited by imaging depth and would require MTS to be fixed and sectioned. Therefore, using OCT, a cross section through the centre of an intact MTS could be imaged. In addition to this, the distribution of NPs within a section could be imaged using a photothermal signal. Photothermal OCT has been used previously for detection of gold nanostructures in cells and tissue.[186,227,228] Photothermal OCT work was carried out by Pierre Bagnaninchi. Figure 5.7 shows the experimental setup for this system. Gold NPs (GNPs) in the sample (MTS) are heated on and off by a modulated 785 nm laser, which creates a modulation in the OCT signal phase over time that is subsequently converted by Fourier transform to assign a colour for each pixel by the presence or absence of phase modulation. Figure 5.8 shows one example of a fixed MTS on a coverslip imaged using OCT (a) and an overlay of photothermal signal (red) on OCT intensity (green) (b). Figure 5.8(c) and (d) show examples of phase modulation signals from areas of the MTS without NPs and with NPs respectively and Figure 5.8(e) shows how phase modulation changed in response to a change in laser modulation frequency.

Initial experiments involved delivering NPs to MTS by incubation overnight in monolayer culture before forming hanging drops from the resultant cell suspension. It was hypothesised that this would result in NPs being present mainly in the centre of the MTS, due to NPs being present in the initial cell suspension that would cluster together to form the core of the MTS and cells would grow radially from that. However, upon investigation using photothermal OCT, MTS grown in this way displayed a uniform distribution of NPs throughout the MTS (Figure 5.9(a)). This confirmed the uniform distribution already suggested from IHC staining of MTS in Chapter 3. Figure 5.9(b) shows control cells with no NPs under the same condition, displaying no photothermal signal and therefore confirming the validity of this technique.

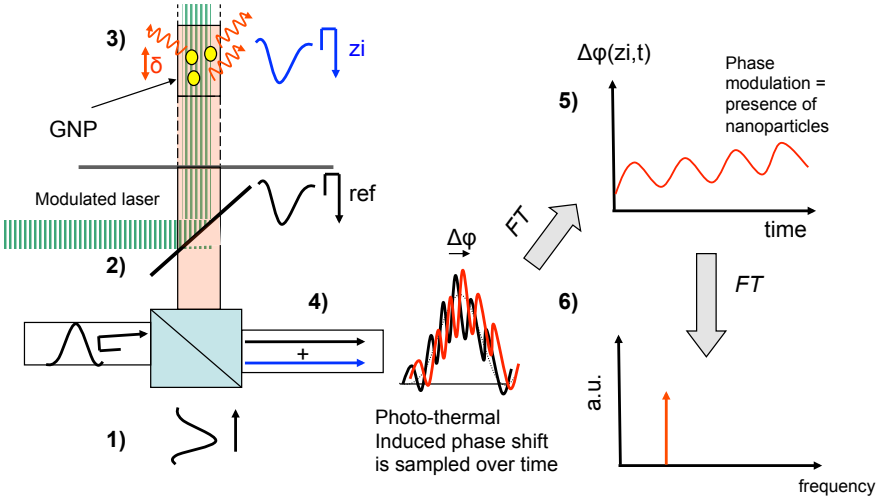

Figure 5.7 shows schematically the setup for obtaining photothermal signals from GNPs in MTS where a modulated laser is pulsed on the sample and a photothermal induced phase shift is detected due to the presence of GNPs (figure produced by Pierre Bagnaninchi).

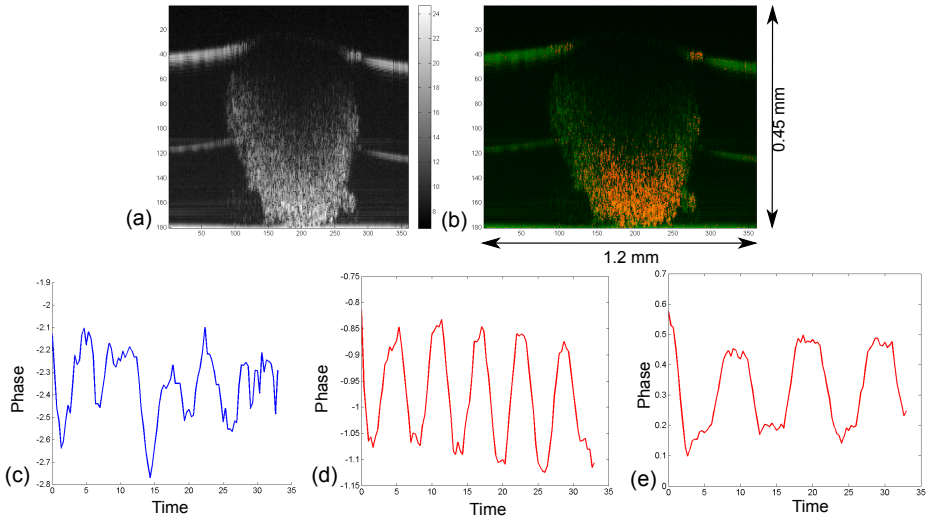

Figure 5.8 shows an OCT image of a fixed MTS (a) and an overlaid photothermal (red) on OCT (green) image of the same MTS. Examples are given of phase modulation signals from areas without (c) and with (d) NPs and with NPs after a change in laser modulation frequency (e)

Following from this, attempts were made to control the distribution of NPs to distinct regions of the MTS. It was proposed that delivery to the outer layers of MTS could be achieved by forming MTS without initial incubation with NPs and adding NPs to the culture medium of the hanging drop in the final stages of growth. Figure 5.9(c) shows distribution of NPs after 24 hr incubation and Figure 5.9(d) after 1 hr incubation. 24 hr incubation again revealed a

uniform distribution of NPs through the MTS while 1 hr incubation showed little uptake with only slight evidence of signal on the outer edges of the MTS. It was therefore proposed that an incubation time in between these would give the desired distribution of NPs on the outer region on the MTS.

In order to control distribution to the central regions of MTS it was proposed that MTS would be grown from cells treated overnight with NPs but subsequently media would be removed from the hanging drop and replaced by cells in suspension that had not been treated with NPs. Details of the exact procedures are given in Chapter 2 Section 2.3.5 and this gave the desired results, showing photothermal signal predominantly in the central regions of MTS as shown in Figure 5.10(b). After carrying out this experiment, a similar technique was proposed to deliver NPs predominantly to the outer region (proliferating ring) of the MTS and predominantly to the intermediate region (quiescent zone). In each case MTS were grown from cells not treated with NPs. For delivery to the intermediate region cells in suspension

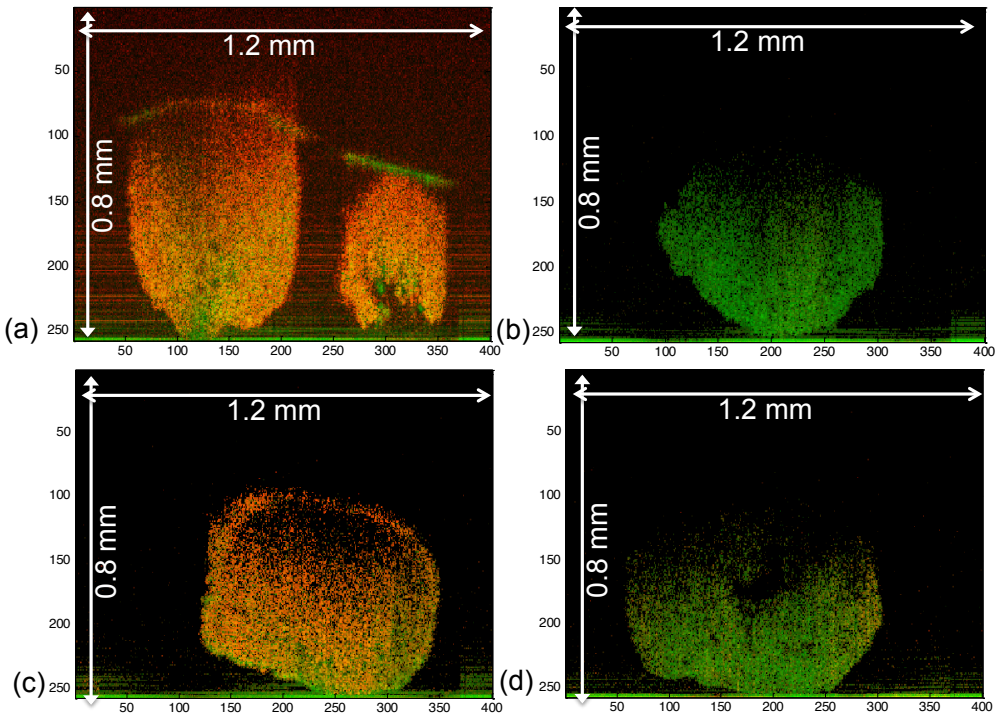

Figure 5.9 shows an overlay of photothermal (red) signal on OCT (green) signal from a series of fixed MTS: MTS grown from cells treated initially with NPs (a); MTS grown from cells untreated with NPs (b); MTS grown from cells untreated with NPs but subsequently treated with NPs 24 hrs before fixing; and MTS grown from cells untreated with NPs but subsequently treated with NPs 1 hr before fixing.

that had been treated overnight with NPs were added on the second day of MTS growth and for delivery to the outer region on the fifth day of MTS growth. As detailed in Chapter 2 Section 2.2.7.3, measurements were made on the sixth day. Figure 5.10(c) shows results for the intermediate region and Figure 5.10(d) for the outer region. Photothermal OCT confirmed that delivery to the desired areas had been successful. Figure 5.10 also shows schematically the different distributions of NPs achieved in this experiment and confirmed by photothermal OCT.

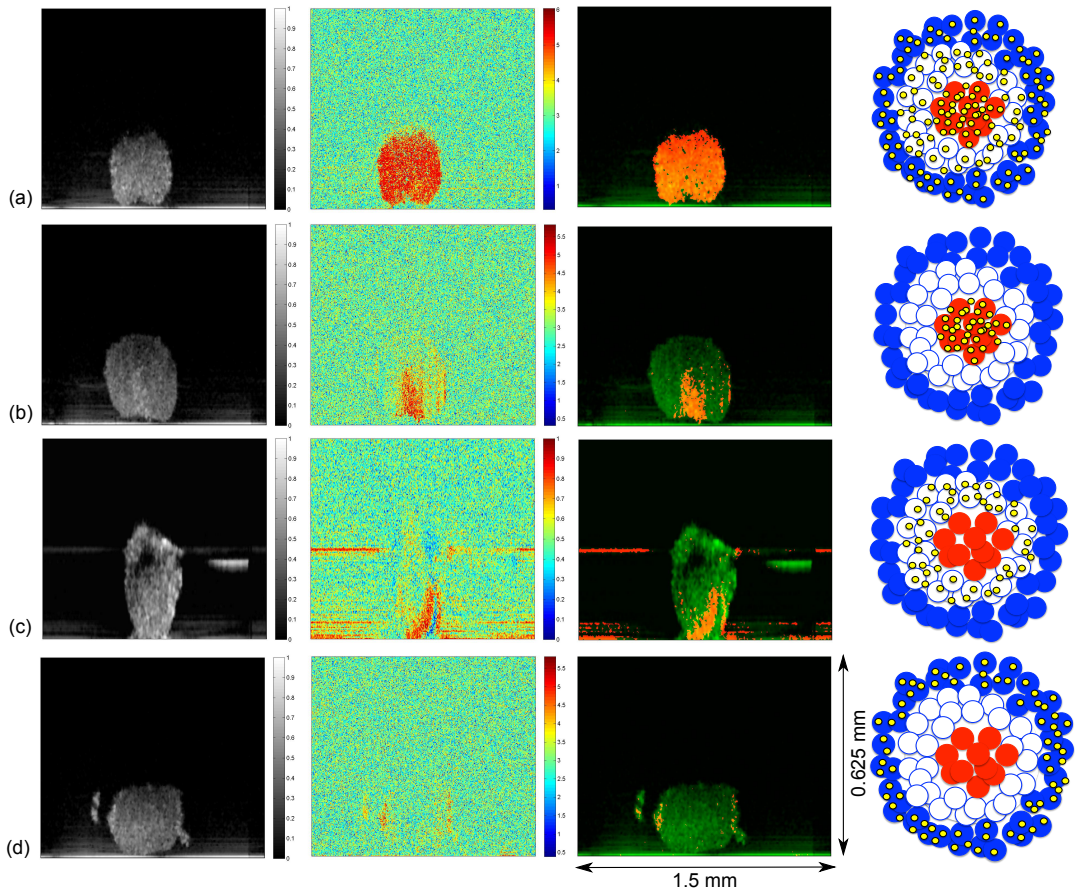

Figure 5.10 shows OCT signals (far left column), photothermal signals (central left column), an overlay of photothermal on OCT signal (central right column) and a schematic of the NP distribution that each condition represents (far right column) for MTS grown from cells initially incubated with NPs (a) (everywhere); cells initially incubated with NPs before replacing with cells untreated with NPs (b) (centre); cells initially untreated where cells treated with NPs were added on the second day of growth (c) (intermediate); and cells initially untreated where cells treated with NPs were added on the final day of growth (d) (outside). Dimensions apply to all photothermal and OCT images.

5.2.2 Raman Fibre Optic Probe – Determining pH and Redox Potential in Different MTS Regions

Following on from being able to control NP distribution to the desired areas of MTS and confirmation via photothermal OCT, Raman measurements were carried out with the Ocean Optics QE65 spectrometer. MTS were transferred in media onto a gold coated glass 'chip' (Figure 5.11 (a)) and immediately taken for measurements using the fibre optic probe (Figure 5.11(b)). Generally, for each MTS, five consecutive spectra were collected with a 30 s acquisition time, as detailed in Chapter 2 Section 2.2.7.3. Three MTS were measured for each condition. Where signals were outside the measurement limits of the probe values were eliminated when determining statistics. Initially, it was proposed that a combination of MBA-NPs for pH sensing and AQ-NPs or NQ-NPs for redox sensing would be used to treat each MTS as required. However, the spectral resolution of this spectrometer did not allow for adequate resolution of signals from each probe and MBA-NP signals tended to 'drown out' any redox signals. Figure 5.12 shows an example of a spectrum obtained from a single MTS with uniform distribution of MBA-NPs and AQ-NPs. There is potentially evidence of an AQ-NP signal at 1669 cm^{-1}, indicated with the red arrow in Figure 5.11. However, this is massively overshadowed by MBA-NP signal and the other AQ-NP signal at 1600 cm^{-1} could not be resolved from the MBA-NP signal at 1590 cm^{-1}.

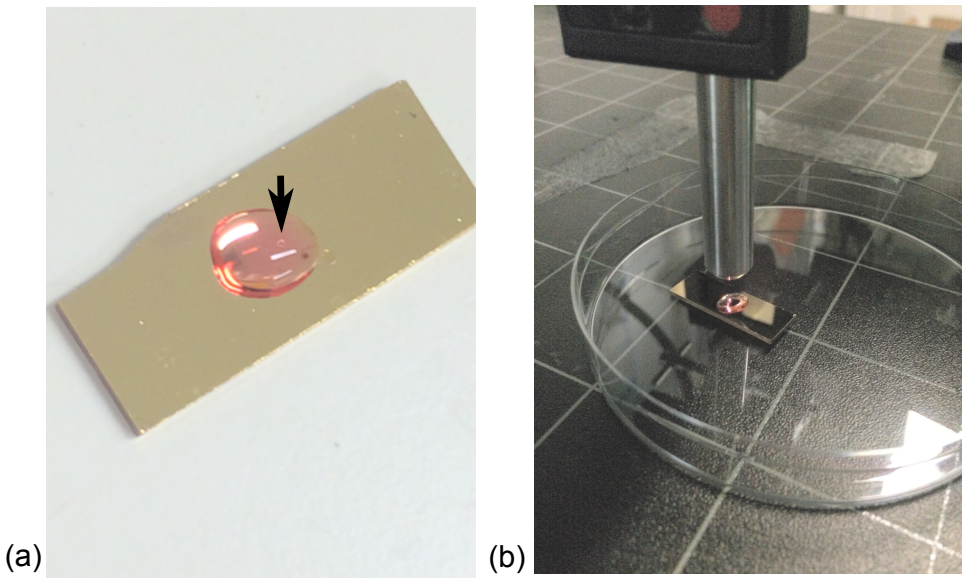

Figure 5.11 shows the experimental setup for taking measurements from MTS on the Ocean Optics QE65 system where MTS were transferred in media onto a gold coated glass 'chip' (a) (MTS indicated by arrow) and spectra were obtained under the fibre optic probe (b).

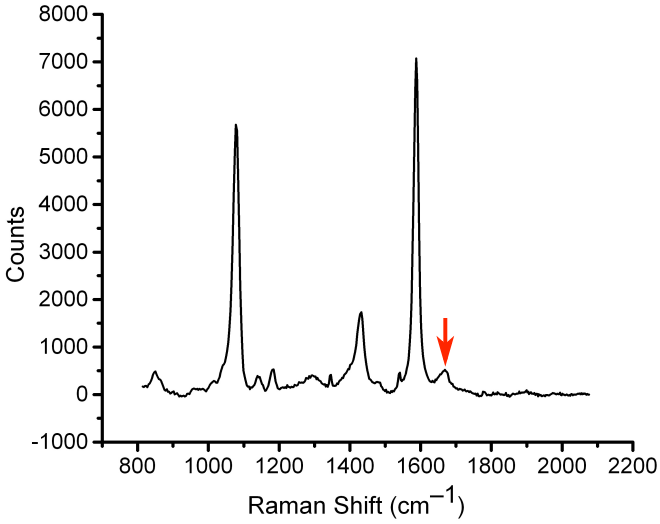

Figure 5.12 shows a representative spectrum obtained from a single MTS containing uniform distribution of MBA-NPs and AQ-NPs where the AQ-NP signal was massively 'overshadowed' by MBA-NP signal. The red arrow indicates a possible AQ-NP peak at 1669 cm^{-1}, however the other peak of interest at approximately 1600 cm^{-1} could not be resolved from the MBA-NP peak at approximately 1590 cm^{-1}.

For this reason it was then proposed that, for each condition, MTS would be grown with only MBA-NPs or only NQ/AQ-NPs. As MTS would be growing under the same conditions in each case, the only difference being NPs applied, it was assumed that the average pH for each condition could be used to correct for the average redox from results. Figure 5.13(a) shows how pH varied under the different conditions, using MBA-NPs for five independent sets of MTS grown on different days. Figure 5.13(b) shows the average for each condition over all MTS analysed.

Figure 5.14(a) shows how pH adjusted redox potential varied under the different conditions, using NQ-NPs for three independent sets of MTS grown on different days. Figure 5.14(b) shows the average for each condition over all MTS analysed. Table 5.2 gives all pH values and standard deviation for measurements in Figure 5.13 and Table 5.3 gives all non-adjusted redox potential, adjusted redox potential and standard deviation for measurements in Figure 5.14.

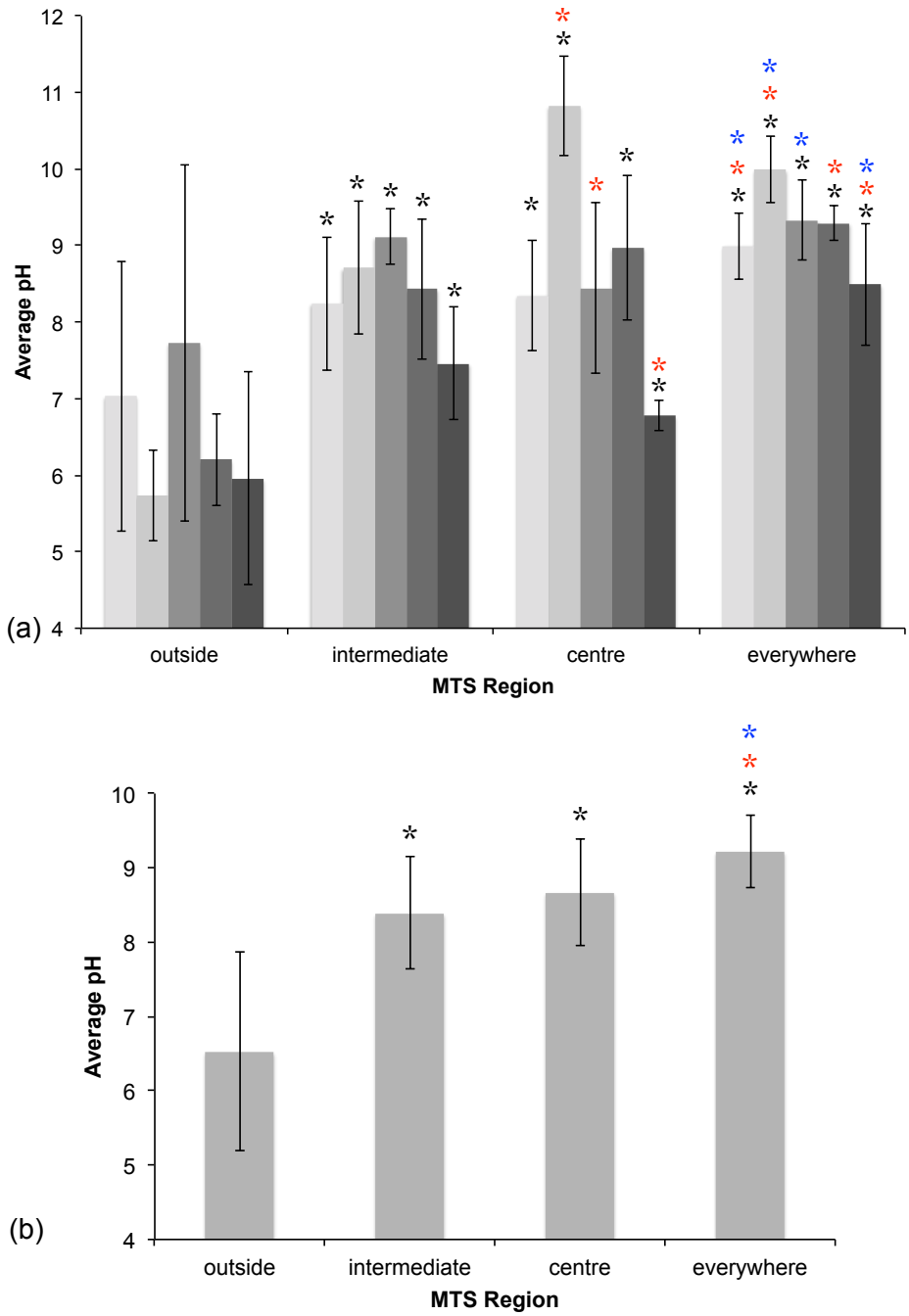

Figure 5.13 shows pH measured from MTS using an Ocean Optics QE65 Pro fibre optic probe and MBA-NPs delivered to MTS to give varying distributions – delivery to the outside region, intermediate region, centre and uniform (everywhere) in the MTS as labeled. Five independent sets of MTS were analysed (a) (each set shaded differently) and average over all sets is given in (b). One-way ANOVA was used to assess significance at the 0.05 level. *(black) indicates significant difference from the outside condition; *(red) indicates significant difference from the intermediate region; and *(blue) indicates significant difference from the centre region. Error bars represent standard deviation.

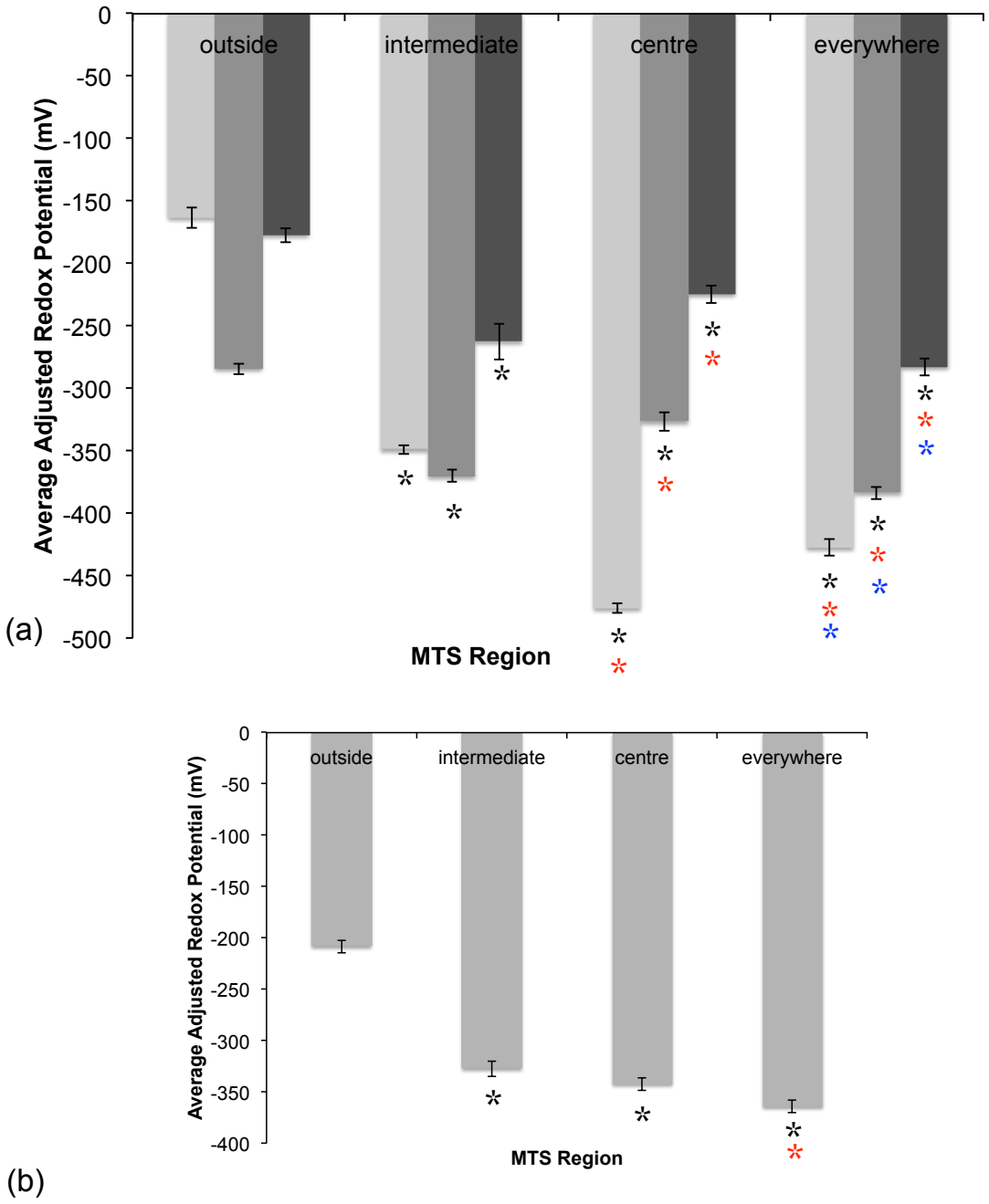

Figure 5.14 shows redox potential measured from MTS using an Ocean Optics QE65 Pro fibre optic probe and NQ-NPs delivered to MTS to give varying distributions – delivery to the outside region, intermediate region, centre and uniform (everywhere) in the MTS as labeled. Three independent sets of MTS were analysed (a) (each set shaded differently) and average over all sets is given in (b). pH measurements for each independent set of MTS were used to adjust redox potential in each case. One-way ANOVA was used to assess significance at the 0.05 level. *(black) indicates significant difference from the outside condition; *(red) indicates significant difference from the intermediate region; and *(blue) indicates significant difference from the centre region. Error bars represent standard deviation.

Table 5.2 gives average pH values obtained from MBA-NPs in different regions of MTS for five independent sets of MTS and the average over all corresponding to Figure 5.13.

MTS Region	pH	Standard Deviation
Outer	7.0, 5.7, 7.7, 6.2, 6.0	1.8, 0.6, 2.3, 0.6, 1.4
Average	6.5	1.3
Intermediate	8.2, 8.7, 9.1, 8.4, 7.5	0.9, 0.9, 0.4, 0.9, 0.7
Average	8.4	0.8
Centre	8.3, 10.8, 8.4, 9.0, 6.8	0.7, 0.6, 1.1, 0.9, 0.2
Average	8.7	0.7
Everywhere	9.0, 10.0, 9.3, 9.3, 8.5	0.4, 0.4, 0.5, 0.2, 0.8
Average	9.2	0.5

Table 5.3 gives average non-adjusted redox potential and adjusted redox potential values obtained from NQ-NPs in different regions of MTS for three independent sets of MTS and the average over all corresponding to Figure 5.14.

Position	Redox Potential (mV) Not adjusted	Redox Potential (mV) Adjusted	Standard Deviation (mV)
Outer	–254	–164	8
	–254	–284	4
	–249	–177	6
Average	-	–208	6
Intermediate	–259	–349	4
	–256	–370	5
	–244	–262	14
Average	-	–327	8
Centre	–260	–476	4
	–255	–327	7
	–249	–225	8
Average	-	–342	6
Everywhere	–259	–427	7
	–257	–383	5
	–235	–283	7
Average	-	–364	6

The overriding observation was that, in general, pH was higher in the centre compared to the outside of MTS and the redox potential, when adjusted for pH, was more reducing in the centre compared to the outside of MTS. This redox potential gradient was as expected from the hypothesis that, on going towards the centre of an MTS, cells become hypoxic (more reduced). The pH trend is possibly counter intuitive to that expected from the hypothesised increase in lactate production from increased anaerobic respiration going towards the centre of MTS, which would suggest a more acidic rather than more basic pH on going towards the central regions of MTS. However, as previously highlighted in Chapter 1 Section 1.4.3.3, there is evidence that that there is a switch from lower intracellular compared to extracellular pH in normoxic cells to higher intracellular compared to extracellular pH in hypoxic cells, attributed to Na^+/H^+ exchanger activation. It is interesting to consider the importance of making pH adjustments to redox potential measurements. Before pH adjustment, trends were generally difficult to observe in redox potential. This is illustrated graphically in Figure 5.15, where a clear emergence of a more significant redox potential is observed when pH adjustments are made. While significant differences were still observed in the non-adjusted case, not all conditions were determined to be significantly different. However, when pH adjustments were made, these emerged.

Significantly, not all data sets showed the exact same gradient, two sets of pH data showing higher pH in the intermediate region than centre region, contrary to other sets. Similarly, two sets of redox potential data showed a more reducing potential in the intermediate region than centre region, contrary to the one other set. This was likely a result of each independent set of MTS being slightly different in size and therefore gradient development stage. This also explains independent variations in values obtained across MTS over each data set. Also, interestingly, particularly in the case of pH, standard deviation tended to be consistently particularly high for the outer regions, suggesting this is the region with most variance. Where NPs were uniformly present, pH and redox potential tended to reflect the more extreme end of pH (basic) and redox potential (hypoxic). This condition is not particularly useful as it provides no spatial information. However, it was interesting to observe the data obtained in this case.

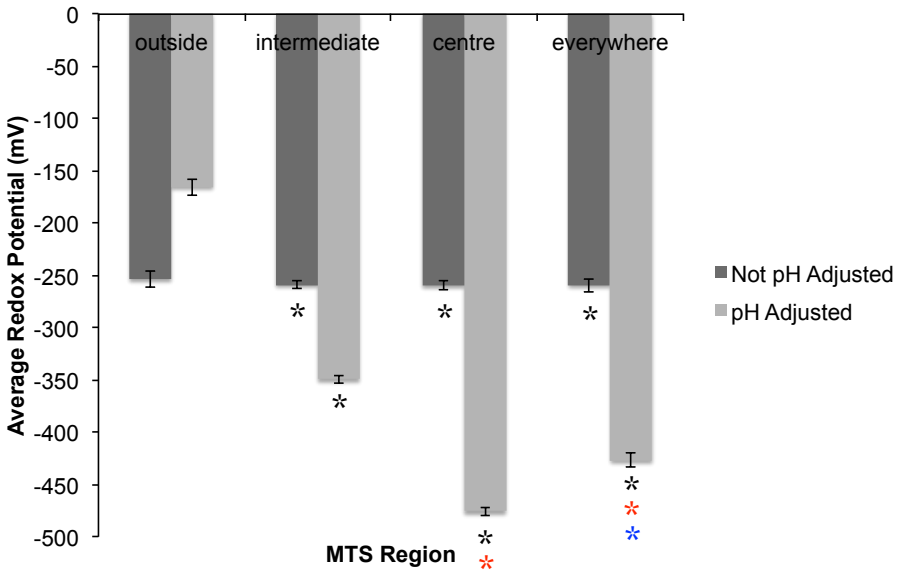

Figure 5.15 shows redox potential measured from MTS using an Ocean Optics QE65 Pro fibre optic probe and NQ-NPs delivered to MTS to give varying distributions – delivery to the outside region, intermediate region, centre and uniform (everywhere) in the MTS as labeled. Comparison between non-pH adjusted and pH adjusted measurements is made for one set of MTS. One-way ANOVA was used to assess significance at the 0.05 level. *(black) indicates significant difference from the outside condition; *(red) indicates significant difference from the intermediate region; and *(blue) indicates significant difference from the centre region. Error bars represent standard deviation.

For redox potential measurements, both AQ-NPs and NQ-NPs were used initially. However, in the case of AQ-NPs, all SER spectra displayed a fully oxidised potential. This made sense, as redox potentials before pH correction using NQ-NPs gave values in the region –250 mV, which corresponds with the oxidised end of the AQ-NP range. Figure 5.16 shows how both the non-adjusted and adjusted redox potential varied for AQ-NPs in MTS. While these values are outside the range over which AQ-NPs can monitor accurately, the trend observed reflected that expected and that observed using NQ-NPs. Table 5.4 gives values including peak intensity ratios.

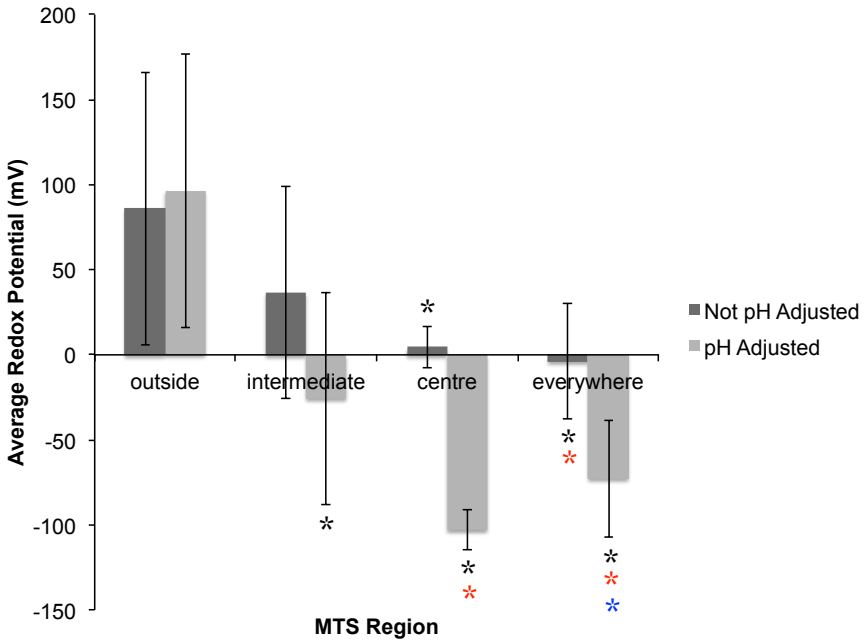

Figure 5.16 shows redox potential measured from MTS using an Ocean Optics QE65 Pro fibre optic probe and AQ-NPs delivered to MTS to give varying distributions – delivery to the outside region, intermediate region, centre and uniform (everywhere) in the MTS as labeled. Comparison between non-pH adjusted and pH adjusted measurements is made for one set of MTS. One-way ANOVA was used to assess significance at the 0.05 level. *(black) indicates significant difference from the outside condition; *(red) indicates significant difference from the intermediate region; and *(blue) indicates significant difference from the centre region. Error bars represent standard deviation.

Table 5.4 gives average intensity ratio, non-adjusted redox potential and adjusted redox potential values obtained from AQ-NPs in different regions of MTS corresponding to Figure 5.16.

Position	**Intensity Ratio 1670 cm^{-1}/1600 cm^{-1}**	**Redox Potential (mV) Not adjusted**	**Redox Potential (mV) Adjusted**	**St Deviation Redox Potential (mV)**
Outer	3.03 ± 0.61	–86	–96	80
Intermediate	2.67 ± 0.42	–37	–26	62
Centre	2.44 ± 0.24	5	–103	34
Everywhere	2.38 ± 0.08	–4	–73	12

5.2.3 Raman Fibre Optic Probe – Response of pH and Redox Potential Gradients to Drug Treatment

This newly established method for quick detection of radial gradients in pH and redox potential in MTS using a simple, and potentially portable, fibre optic probe, provides a potential new platform for monitoring response to drugs and therapy. Increasing movement is being made towards the use of 3D cell culture models for drug screening due to its increased physiological relevance and therefore this method could prove to be a vital tool in monitoring response to drugs and therapy in a 3D culture model.

In order to investigate the applicability of this technique to monitor response of MTS to application of an external chemical/drug, MTS were subsequently treated with 10 μM STS before repeating SERS measurements. This allowed the technique to be explored as a potential platform for drug discovery and monitoring response to drugs/therapy as well as the already established analytical technique for establishing the nature of the pH and redox potential gradients. Establishing the nature of the gradients provides important information for guiding future drug and therapy development, while also providing an analytical platform for easily monitoring the response of MTS to drugs and therapy. STS treatment was performed over various time points to monitor the response of the gradients over time. Figure 5.17 shows pH response to STS treatment in different regions of MTS for four different time course experiments. Figure 5.18 shows adjusted redox potential response to STS treatment in different regions of MTS for three different time course experiments. Table 5.5 and Table 5.6 give corresponding numerical values.

The general overriding observation in this case was that MTS respond almost immediately to treatment with STS, generally showing significant changes within 0-1 hrs after treatment. As expected, gradients tended to become less pronounced after STS treatment, as MTS moved from distinct radial differences in pH and redox potential to more uniform pH and redox potential measurements. Therefore, drugs could be monitored by quantitative diminishment of physiologically relevant gradients. Figure 5.19 shows one example of how average MBA-NP spectra changed from untreated (a) to overnight STS treatment (b) and how average NQ-NP spectra changed from untreated (c) to overnight STS treatment (d). Schematic representations of radial pH gradients are also given in each case. For MBA-NP spectra, a clear change can be observed visually in the 14-- cm^{-1} peak intensity from distinct intensity

differences in the untreated case to very similar intensity after overnight treatment, all progressing towards severely basic pH. For NQ-NP spectra, the opposite was observed, going from very similar intensity of the peak at approximately 1630 cm^{-1} in untreated MTS to distinct difference after overnight treatment. This again highlights the importance of pH correction to establish accurate results, which, when pH corrected, shows the diminishment of these gradients (Figure 5.18(a)).

Figure 5.20 shows how MBA-NP spectra from different regions of MTS changed over time course treatment with STS corresponding to Figure 5.17(d). Generally, an increase in pH (corresponding to an increase in the 14-- cm^{-1} peak intensity) was observed over increasing time course treatment with STS. In this case, the initial increase (0-1 hr) was most dramatic, before a drop after 4-5 hr and then a further slight drop after 11-12 hr for the outer and intermediate regions and slight increase for the centre. This was followed by a slight increase in all three regions after overnight treatment. Significantly, the initial increase was most pronounced in the outer region, probably as this region was in immediate contact with STS on treatment, while it may have taken slightly longer to penetrate to the internal regions. It is possible that, after the initial dramatic change on STS treatment, cells then fought to adapt and regulate pH, leading to the return to slightly lower pH after further time. It is also possible that this mimics the response observed in monolayer culture (Chapter 4 Section 4.2.1), where the initial dramatic increase in pH upon STS was attributed to mitochondrial depolarisation and permeabilisation while the later decrease was attributed to the later stages of apoptosis causing release of acidic lysosomal contents. Significantly in this example, no significant change in pH of MTS with a uniform distribution of MBA-NPs (everywhere) was observed. This highlights the need for radial differences to be monitored as opposed to whole MTS measurements.

Again, exact responses varied between measurement sets as expected, due particularly to differences in MTS size and development stage. For example, in Figure 5.17(c) the same initial increase in pH was observed, but further changes varied slightly. The general trend of increase in pH and diminishment of gradient was consistent, however. Redox potential generally decreased (more reductive) and gradients diminished.

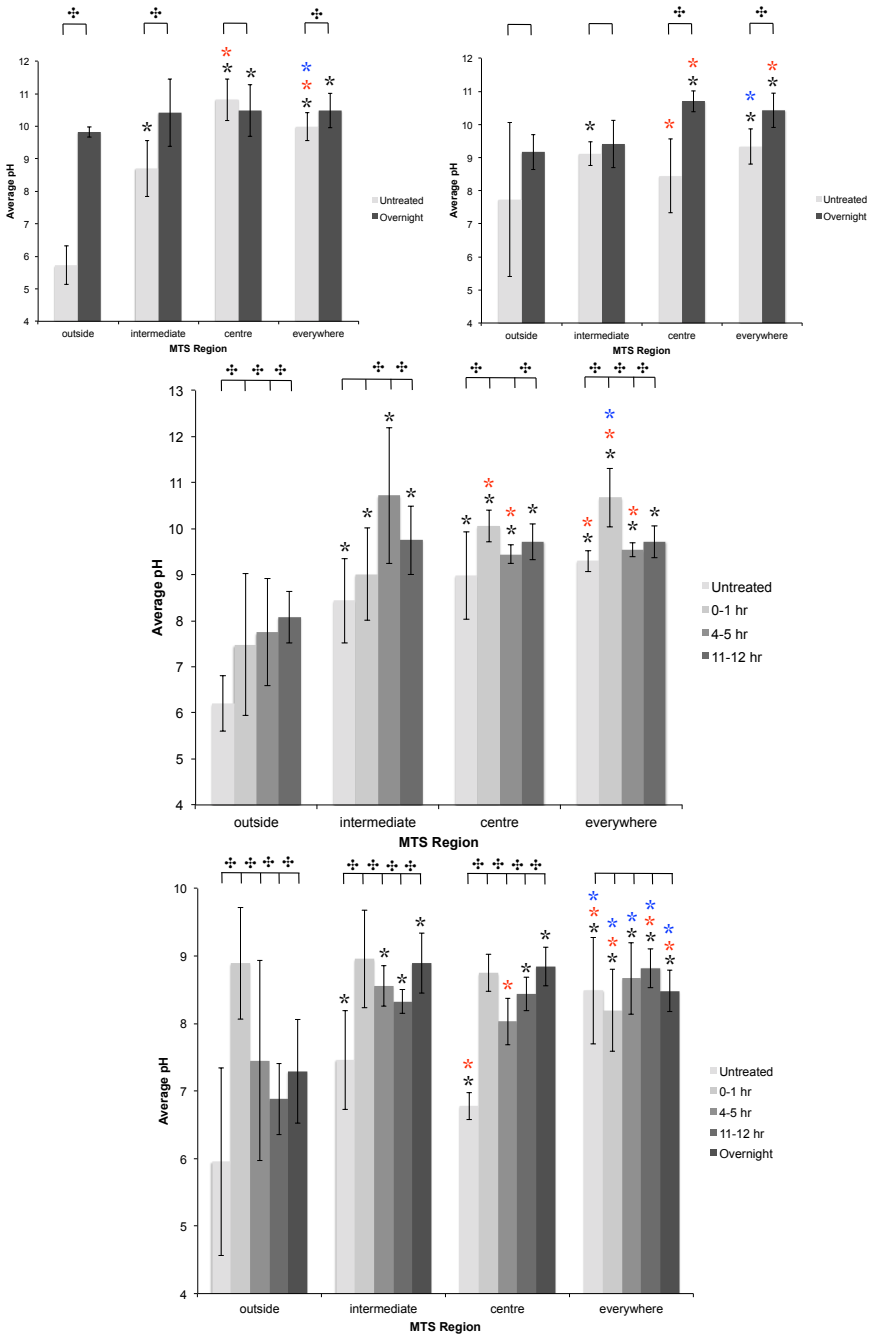

Figure 5.17 shows pH measured from MTS using an Ocean Optics QE65 Pro fibre optic probe and MBA-NPs delivered to MTS to give varying distributions – delivery to the outside region, intermediate region, centre and uniform (everywhere) in the MTS as labeled. MTS were treated with STS and pH changes in each region monitored for four different sets of MTS (a-d). One-way ANOVA was used to assess significance at the 0.05 level. *(black) indicates significant difference from the outside condition; *(red) indicates significant difference from the intermediate region; and *(blue) indicates significant difference from the centre region. ✣ indicates significance at the 0.05 level compared to the untreated condition. Error bars represent standard deviation.

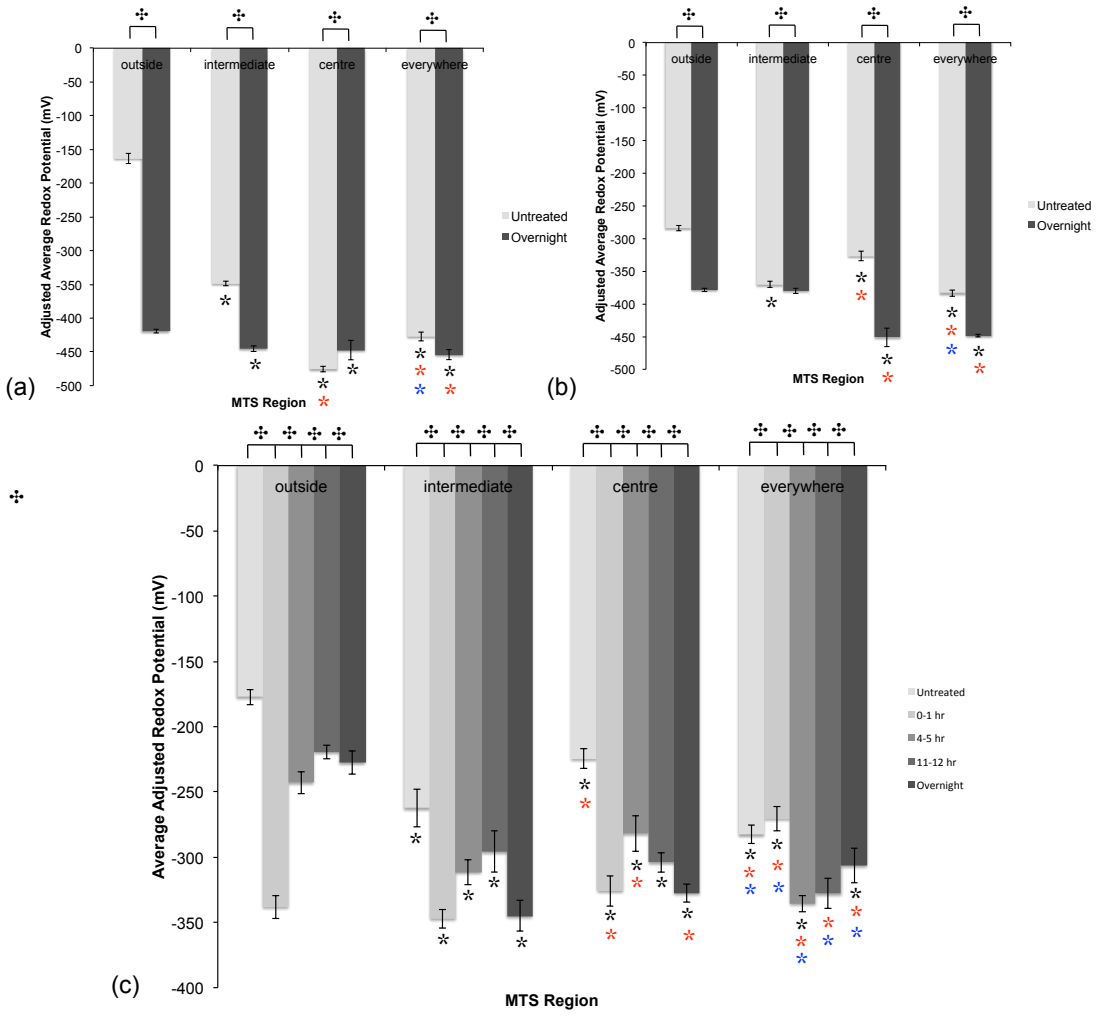

Figure 5.18 shows redox potential measured from MTS using an Ocean Optics QE65 Pro fibre optic probe and NQ-NPs delivered to MTS to give varying distributions – delivery to the outside region, intermediate region, centre and uniform (everywhere) in the MTS as labeled. MTS were treated with STS and redox potential changes in each region monitored for three different sets of MTS (a-c). pH measurements for each set of MTS were used to adjust redox potential in each case. One-way ANOVA was used to assess significance at the 0.05 level. *(black) indicates significant difference from the outside condition; *(red) indicates significant difference from the intermediate region; and *(blue) indicates significant difference from the centre region. ✣ indicates significance at the 0.05 level compared to the untreated condition. Error bars represent standard deviation.

Table 5.5 gives average pH values obtained from MBA-NPs in different regions of MTS over time course treatment with STS corresponding to data in Figure 5.17.

Position	Untreated	0-1 hr STS	4-5 hr STS	11-12 hr STS	Overnight STS
Outer	5.7 ± 0.6				9.8 ± 0.2
	7.7 ± 2.3				9.2 ± 0.5
	6.2 ± 0.6	7.5 ± 1.5	7.7 ± 1.2	8.1 ± 0.6	
	6.0 ± 1.4	8.9 ± 0.8	7.5 ± 1.5	6.9 ± 0.5	7.3 ± 0.8
Intermediate	8.7 ± 0.9				10.4 ± 1.0
	9.1 ± 0.4				9.4 ± 0.7
	8.4 ± 0.9	9.0 ± 1.0	10.7 ± 1.5	9.8 ± 0.7	
	7.5 ± 0.7	9.0 ± 0.7	8.6 ± 0.3	8.3 ± 0.2	8.9 ± 0.4
Centre	10.8 ± 0.6				10.5 ± 0.8
	8.4 ± 1.1				10.7 ± 0.3
	9.0 ± 0.9	10.1 ± 0.4	9.4 ± 0.2	9.7 ± 0.4	
	6.8 ± 0.2	8.7 ± 0.3	8.0 ± 0.3	8.4 ± 0.2	8.8 ± 0.3
Everywhere	10.0 ± 0.4				10.5 ± 0.5
	9.3 ± 0.5				10.4 ± 0.5
	9.3 ± 0.2	10.7 ± 0.6	9.5 ± 0.1	9.7 ± 0.3	
	8.5 ± 0.8	8.2 ± 0.6	8.7 ± 0.5	8.8 ± 0.3	8.5 ± 0.3

Table 5.6 gives average adjusted redox potential values obtained from NQ-NPs in different regions of MTS over time course treatment with STS corresponding to data Figure 5.18.

Position	Untreated	0-1 hr STS	4-5 hr STS	11-12 hr STS	Overnight STS
Outer	–164 ± 8				–420 ± 2
	–284 ± 4				–378 ± 3
	–177 ± 6	–338 ± 9	–243 ± 8	–219 ± 5	–228 ± 9
Intermediate	–349 ± 4				–445 ± 4
	–370 ± 5				–380 ± 4
	–262 ± 14	–347 ± 7	–311± 10	–296 ± 16	–345 ± 12
Centre	–476 ± 4				–447 ± 15
	–327 ± 7				–451 ± 14
	–225 ± 8	–326 ± 12	–282± 13	–304 ± 8	–327 ± 7
Everywhere	–427 ± 7				–454 ± 7
	–383 ± 5				–449 ± 3
	–283 ± 7	–271 ± 10	–336 ± 6	–328 ± 12	–306 ± 13

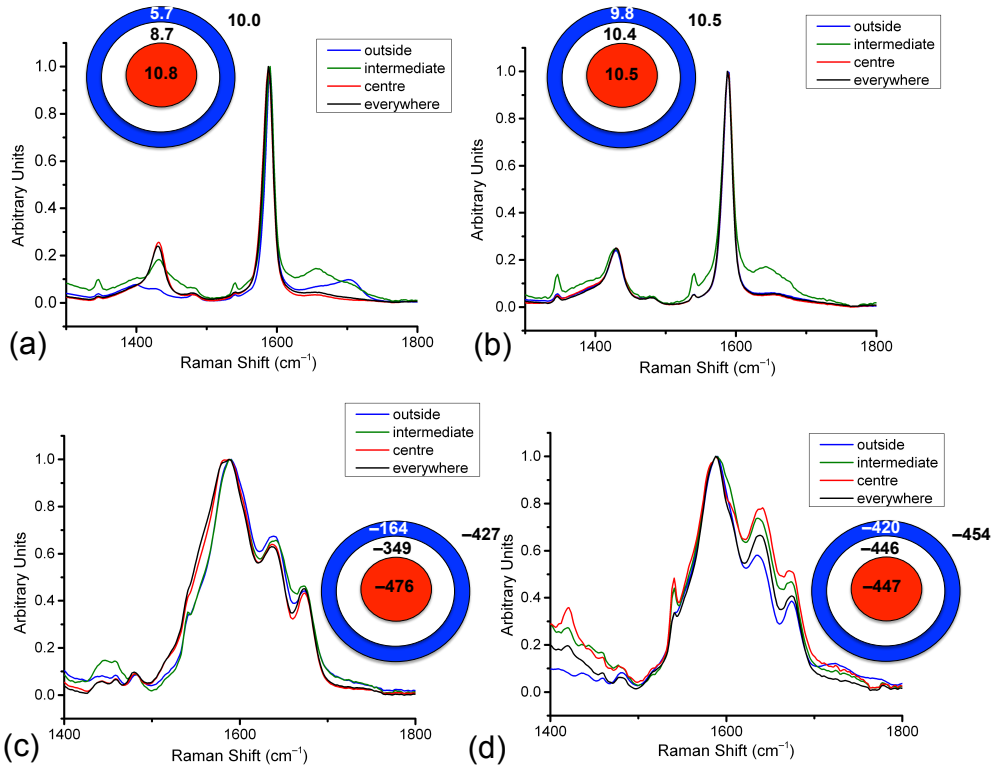

Figure 5.19 shows how average MBA-NP spectra varied over different regions of untreated MTS (a) and MTS treated overnight with 10 μM STS (b) along with schematic representations of the pH gradients observed where the number outside the sphere is attributed to the 'everywhere' condition (corresponding to Figure 5.17(a)). Changes in average NQ-NP spectra over different regions of untreated MTS (c) and MTS treated overnight with 10 μM STS (d) along with schematic representations of the pH adjusted redox potential gradients where the number outside the sphere is attributed to the 'everywhere' condition (corresponding to Figure 5.18(a)) are also shown.

A simple method for determination of quantitative radial differences in the physiologically relevant pH and redox potential measurements has been established using a fibre optic Raman probe for quick and easy measurement of 'average' whole MTS spectra, corresponding to a particular MTS region controlled by targeted NP delivery. Photothermal OCT was used to investigate and confirm NP distribution in MTS allowing a method to be established for controlled delivery of NPs to different regions of MTS. A fibre optic Raman probe could then be used to measure 'average' SERS spectra under different conditions to establish informative quantitative information about pH and redox potential gradients. As well as providing previously unknown quantitative information on these gradients and thus providing

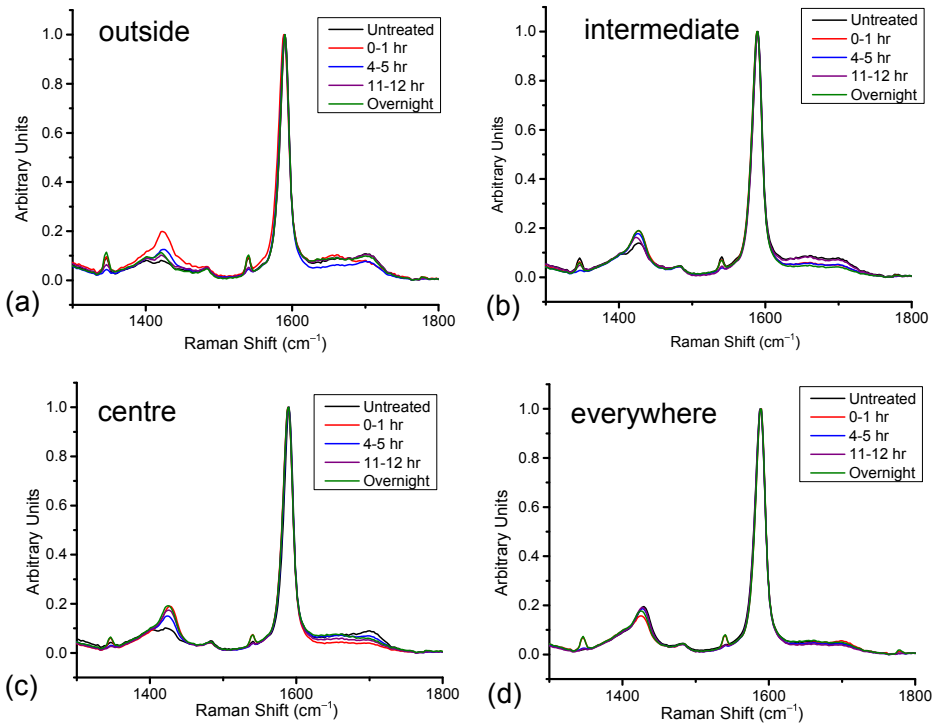

Figure 5.20 shows how average MBA-NP spectra corresponding to different regions of MTS varied over time course treatment with 10 μM STS corresponding to Figure 5.17(d). Changes in the outer region of MTS (a), intermediate region of MTS (b), centre of MTS (c) and everywhere (d) are shown.

potentially vital information for drug and therapy development, this platform has been demonstrated as a potential assay for monitoring response to drug treatment. Response of gradients to treatment with the apoptosis inducer STS were monitored and generally showed a loss of radial gradients and increase in pH and decrease in redox potential after treatment. This could potentially be translated for use in drug screening on the more physiologically relevant 3D cell culture model.

5.3 Simultaneous Intracellular Redox Potential and pH Measurements in Live Cells in MTS Using SERS Nanosensors – Renishaw inVia

Attempts were made to determine spatial variations in pH and redox potential in MTS using a new Renishaw inVia system (see Chapter 2 Section 2.2.1 for details). Due to time constraints after instrument delivery, only preliminary measurements were possible as an investigation into the possibilities and limitations of the system; in this case, if a suitable method could be

established, MTS treated for uniform NP distribution could be used and highly spatially resolved pH and redox potential measurements could potentially be acquired over the full MTS volume at, for example, 1 μm × 1 μm step size in x,y and z. As MTS are imaged live and currently the setup does not allow for physiological conditions to be maintained after the cells are removed from the incubator, there is a trade off element between acquisition time at these highly spatially resolved measurement acquisitions and time the MTS can remain in a physiologically representative state outside the incubator. Laser exposure time for a single sample must also be considered, as under long exposure times samples may be burned. For measurements in this system, MTS were transferred into a collagen matrix, as described in Chapter 2 Section 2.1.4 (Figure 5.21(a)) and then imaged usimg a ×5 objective on the Renishaw inVia system (Figure 5.21(b)). The system was also fitted with a ×20 and a ×50 objective, but the working range of these was too short to allow MTS imaging.

The Renishaw system had volume mapping capabilities. However, due to the lengthy time requirements in this case other approaches were considered. It was proposed that a depth scan through the centre of a single MTS would allow detection of any gradients of interest present. It was also proposed that a 2D map of the MTS area in the xy plane near the centre of the MTS would allow detection of spatially relevant gradients. In both these cases, data acquisition time would be minimised and major gradients should be observed.

(a) 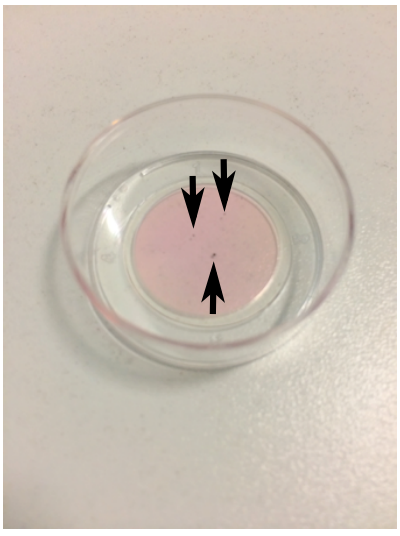 (b) 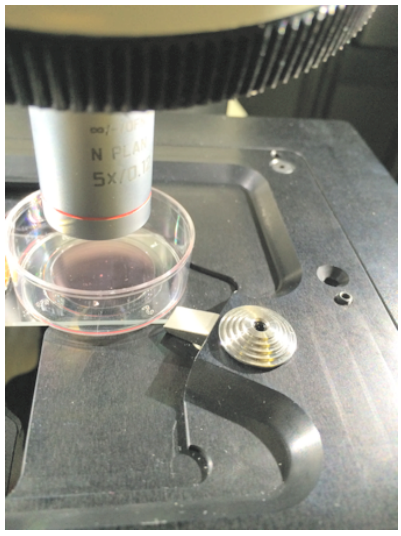

Figure 5.21 shows the experimental setup for taking measurements from MTS on the Renishaw inVia system where MTS were transferred to a collagen matrix (a) (MTS indicated by arrow) and spectra were obtained using a ×5 objective (b).

MTS were prepared with a uniform distribution of MBA-NPs and AQ-NPs and set in collagen. Again, AQ-NP signals were massively overshadowed by MBA-NP signals and therefore another approach would be required for multiplex measurements. This could involve probes with closer cross sections for Raman scattering and more distinct signals. The ratio of MBA-NP to AQ-NP applied could also be explored. Depth scans were performed through the centre of a single MTS. Initially, cycled scanning was used while manually focusing in the z direction to attempt to find the MTS limits by diminishment in SERS signal. However, SERS signals were observed over a large z range, larger than the MTS size. This suggested that a large volume of out of focus signal was also being detected at each z position and that confocality of the system was not sufficient for the required z resolution. A z position where slightly higher signal intensity was observed was therefore selected and depth scans carried out both using high confocality and normal confocality. The depth resolution of the system was *ca.* 2 μm, and the step size used for depth scans was much larger than this in all cases (20 μm was the smallest). Therefore, step size was the limiting factor for depth resolution. Resultant spectra were processed in the Wire 4.1 software by cosmic ray removal, smoothing, baseline subtraction and normalisation as described in Chapter 2. Normalisation was from 0-1 relative to the highest intensity of the peak at 1590 cm^{-1} and then peak intensity at 1425 cm^{-1} (therefore equivalent to 1425 cm^{-1} signal intensity divided by 1590 cm^{-1} signal intensity) was plotted against z position.

Figure 5.22 (a) shows results for high confocality where a 20 μm step size was used over 25 points with an exposure time of 60 s and 10% laser power. Figure 5.22 (b) shows results for normal confocality where 20 μm step size was used over 50 points with an exposure time of 30 s and 10% laser power. This covered a 500 μm and 1000 μm distance in the z direction, respectively, with more negative values further into the MTS sample. No significant gradient was observed, but, as already mentioned, this is likely a result of detection of out of focus signal and poor confocality. For the high confocality measurements, the ratio was approximately constant at 0.16, which corresponds to a pH of 8.6 and for standard confocality the ratio was approximately constant at 0.14 corresponding to a pH of 8.2. The exact pH is not completely accurate, however, due to differences in spectral processing between calibration data (manual) and measurements (using Wire 4.1).

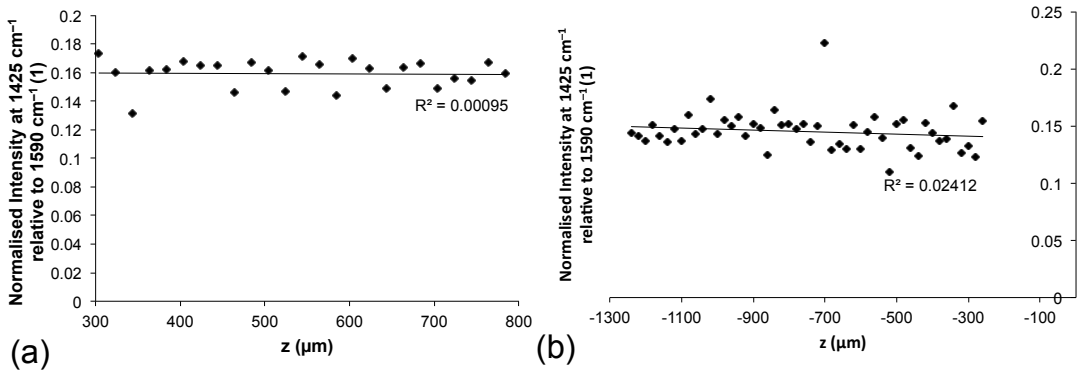

Figure 5.22 shows normalised signal intensity at 1425 cm^{-1} plotted against z position for depth scans through MTS with a uniform distribution of MBA-NPs and AQ-NPs. Signals were normalised from 0-1 relative to the highest signal at 1590 cm^{-1}. Scans were carried out at high confocality with 20 μm step size, 60 s acquisition time and 10% laser power (a) and normal confocality with 20 μm step size, 30 s acquisition time and 10% laser power (b). No significant trend was observed (R^2 values of best fit line shown). The location of signals relative to MTS is unknown as, in theory, SERS signals from NPs should only be observed in MTS regions, and drop off when MTS was no longer being probed, or when probing too far into the z direction for signals to be obtained. This was not observed, illustrating that SERS signal was being collected out with the MTS, and therefore must have come from out of focus signal collection.

These measurements were plotted using the mapping feature in Wire 4.1 and intensity at a particular defined wavenumber (1425 cm^{-1}). Maximum normalised peak intensities of the 14-- cm^{-1} signal were then plotted manually against z position for the high confocality case as well as peak width and area, shown in Figure 5.23. There is a slight gradient observed in the peak intensity case, ranging from around 0.12 (pH 7.8) to 0.15 (pH 8.4) with an R^2 value of 0.23559. Peak width and area showed less significant changes. This gradient suggests the pH is lower going towards the centre of the MTS. However, as it was difficult to determine exact location in MTS, this is not conclusive. For example, the highest z position could correspond to the centre of MTS with lower values going towards the distant edge; or the highest z position could correspond to the nearest edge of the MTS with lower values going towards the centre. Again out of focus signals confound measurements.

Attempts were also made to perform a 2D map in the xy direction at a depth where the outer edge of the MTS was in focus. MTS areas were mapped with 20 μm step size in the x and y directions over an area covering 30 steps in the x direction and 23 in the y direction, using an

exposure time of 1 s and 50% laser power. Again, as spatial resolution in the xy plane was *ca.* 1 μm, it was step size that limited spatial resolution. Spectra were processed using Wire 4.1 as previously. Figure 5.24(a) shows the white light image of the MTS. A map of peak intensity at 1588 cm^{-1} (MBA signal) was created (Figure 5.24(b)) with a representative high intensity spectrum shown in Figure 5.24(b). This shows an MBA-NP spectrum, potentially with evidence of AQ-NP from the small peak around 1670 cm^{-1}, but, no obvious distinguishable peak at 1600 cm^{-1}. This map correlated well with MTS area, showing uniform MBA-NP signals as expected. As the MTS was set in collagen in an imaging dish with a glass bottom, in areas with no MTS and on some of the outer edges of the MTS, strong glass signals were present, with a broad peak around 1400 cm^{-1}. Figure 5.24(d) maps peak intensity at 1373 cm^{-1} and Figure 5.24(e) shows a representative high intensity spectrum, characteristic of glass. Again, this correlates well spatially with the white light image. A map of signal intensity at 1425 cm^{-1} was then created (Figure 5.24(f)). However, due to the presence of strong glass signals in the same region as this pH sensitive MBA peak, this did not provide any useful information, primarily highlighting regions of glass signal again. Due to time constraints, further investigation was not possible. However, in the future a substrate such as CaF_2 windows could be used and potentially a gradient in 1425 cm^{-1} peak intensity would be observed through the MTS. Despite collection of much out of focus signal, a gradient may be observed as, for example, an average over a z depth on the edge should vary from an average over a z depth in the centre. This could provide another platform for drug testing.

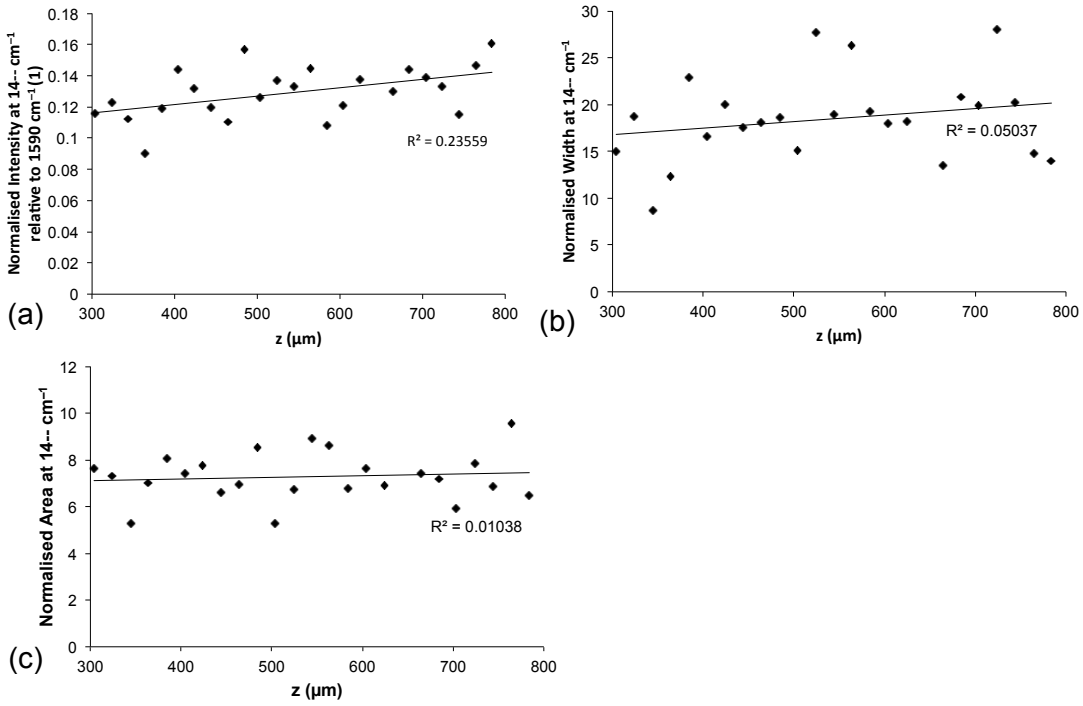

Figure 5.23 shows normalised maximum peak intensity at 14-- cm^{-1} plotted against z position (a); normalised width of peak at 14-- cm^{-1}; and normalised area of peak at 14-- cm^{-1} for depth scans through MTS with a uniform distribution of MBA-NPs and AQ-NPs. Signals were normalised from 0-1 relative to the highest signal intensity at 1590 cm^{-1}. Scans were carried out at high confocality with 20 μm step size, 60 s acquisition time and 10% laser power. The location of signals relative to MTS is unknown as, in theory, SERS signals from NPs should only be observed in MTS regions, and drop off when MTS was no longer being probed, or when probing too far into the z direction for signals to be obtained. This was not observed, illustrating that SERS signal was being collected out with the MTS, and therefore must have come from out of focus signal collection.

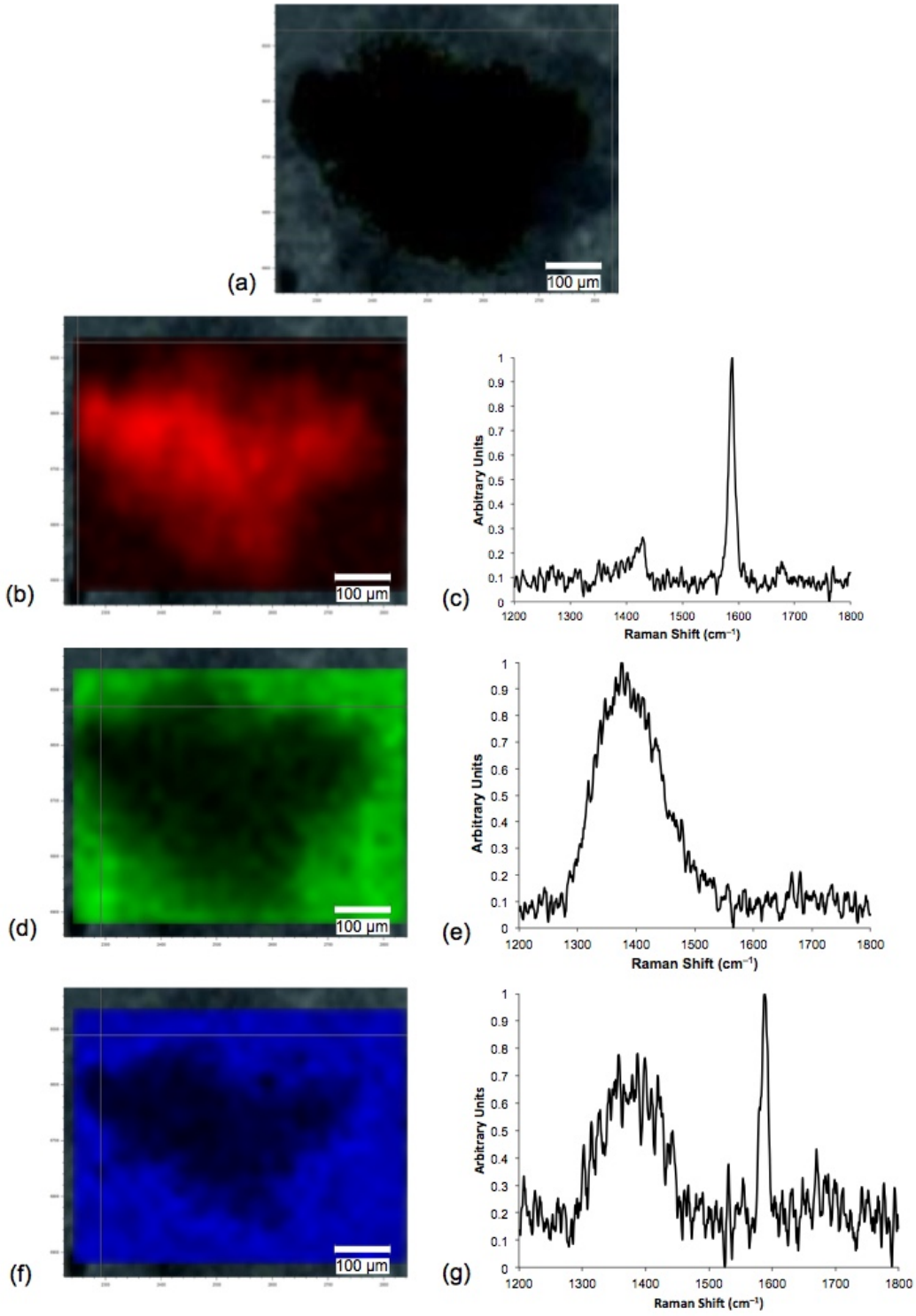

Figure 5.24 shows a bright field image of a single MTS with a uniform distribution of MBA-NPs and AQ-NPs under the Renishaw inVia microscope (×5 objective) (a) and intensity maps for 1588 cm^{-1} (b), 1373 cm^{-1} (d) and 1425 cm^{-1} (f). Representative high intensity spectra for the 1588 cm^{-1} map (c) and 1373 cm^{-1} map (e) are given along with a confounded signal typical around the edge of the MTS where glass signal masks the 1425 cm^{-1} MBA peak (g). Scans were carried out with 20 µm step size in x and y, 1 s acquisition time and 50 % laser power.

In order to investigate redox potential, MTS treated only with NQ-NPs for uniform distribution were used. Again, depth scans were carried out and results are shown in Figure 5.25. Here, scans were performed with no pinhole. In this case, normalisation was not carried out, as the reference peak at 1580 cm^{-1} was not always the maximum intensity. Therefore, intensities at 1635 cm^{-1} and 1582 cm^{-1} were extracted, followed by a ratio intensity map for 1635 cm^{-1}/1582 cm^{-1}. Gradients were more apparent in this case, Figure 5.25(a) having a line of best fit R^2 of 0.45987 and Figure 5.25(c) R^2 of 0.40723. Figure 5.25(b) did not however show this gradient with R^2 of 0.00546. Again, the detection of out of focus signal is apparent – Figure 5.25(b) and (c) cover a z distance of 2500 μm, much larger than the MTS diameter with SERS signals acquired over the full distance. Gradients suggest more reducing conditions going to more negative z direction, which is expected going towards the centre of the MTS. However, it cannot be absolutely confirmed that this is going towards the centre due to lack of z spatial information. There is also no pH correction, which, as discovered in the previous section, is vitally important. Therefore, values without pH correction cannot give us any useful information.

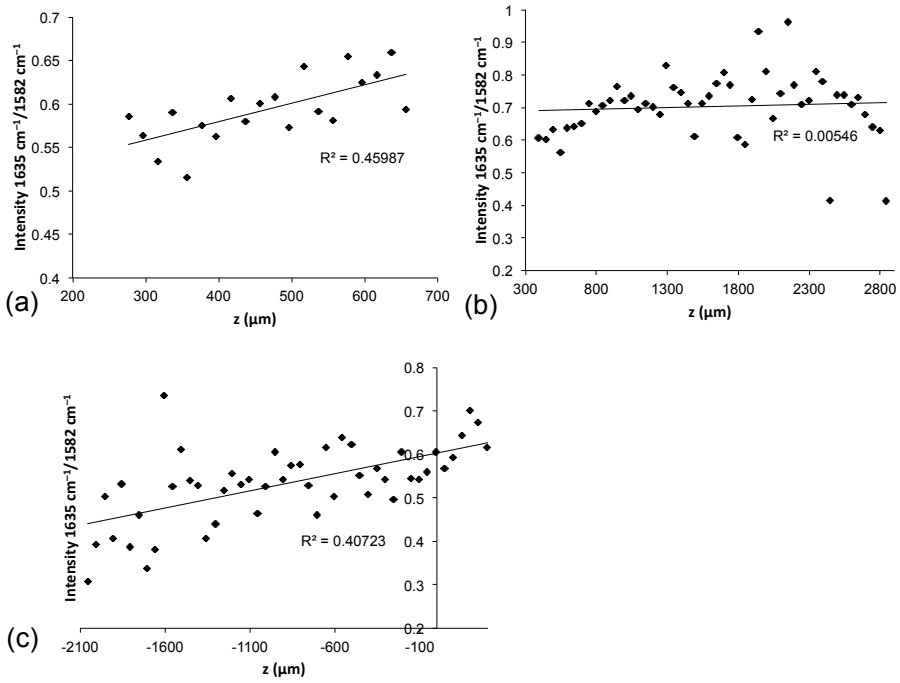

Figure 5.25 shows intensity at 1635 cm^{-1} relative to intensity at 1582 cm^{-1} plotted against z position for depth scans through MTS with a uniform distribution of NQ-NPs. Scans were carried out without the pinhole with 20 μm step size, 1 s acquisition time and 50% laser power (a), with 50 μm step size, 0.5 s acquisition time and 50% laser power (b), and with 50 μm step size, 0.5 s acquisition time and 50% laser power (c). (R^2 values of best fit line shown).

Due to limited time constraints, a full investigation on the Renishaw inVia system was not possible. However, initial measurements reveal important information about the potential and limitations of this system for making highly spatially resolved pH and redox potential measurements through MTS using SERS. Depth scanning using no pinhole, standard confocality and high confocality all revealed that out of focus signal was detected, and therefore z resolution for making these measurements was limited. There was evidence of some gradients emerging. However, this may have limited applicability as the confocality problem in the z direction is a limiting factor. Multiplexing pH and redox measurements was also limited by the high cross section of MBA-NPs for Raman scattering, masking any redox signals. To surmount this problem, investigation into varying ratios of the two probes or development of a different complementary set of probes could be made – selecting a pH and redox probe with a similar Raman cross section and spectrally distinct peaks of interest.

There is potential for development using a 2D mapping technique over the MTS area if the substrate used was changed from glass to, for example CaF_2, as 2D maps picked up MBA-NP signals in good agreement with MTS location from the bright field image. However, glass signals masked the 1425 cm^{-1} peak in many of the MBA-NP spectra. Future work could investigate this technique for determination of physiologically relevant gradients and a potential platform for drug testing. High xy resolution may not be required to pick up basic gradients meaning acquisition time could be limited dependent on application. This technique may be applicable, despite the difficulty in determining exact z location within an MTS. For example, z focus could be used to either focus the laser on the surface of the MTS or find the area with largest MTS diameter before performing measurements. This would make the technique consistent and, as a result of lack of confocality picking up many out of focus signals this would possibly become average signal in the z direction at that point. As the confocality problem is limited by the instrument, another possible extension would be to perform Raman measurements on MTS sections. While this would not allow detection of pH and redox gradients as these are lost on fixation of cells, Raman rather than SERS could be carried out on cells to investigate biochemical spatial differences through MTS. This could also potentially detect changes in concentration of particular redox species through MTS such as glutathione, $NAD(P)^+$/NAD(P)H and thioredoxin.

Chapter 6

Tracking and Controlling Nanoparticle Uptake Into Cellular Compartments

"And – They wondered at the lavish spectacle." – **Circus, London**

As mentioned in Chapter 3 Section 3.3, TEM images of NPs in cells in both monolayer culture and MTS revealed the presence of a large proportion of the NPs inside vesicle structures. It was desirable to deliver NPs predominantly to the cytosol for analysis. Therefore, attempts were made to increase the proportion of NPs delivered to the cytosol relative to vesicles. This was predominantly done by functionalising NPs with different molecules shown to increase release of NPs into the cytosol. TEM was used to investigate results subjectively by counting the proportion of NPs inside and outside vesicle structures. TEM requires cells to be fixed and sectioned and is also a labour intensive and expensive process. Therefore, a new technique for investigation of NP uptake in live cells was also investigated. Confocal fluorescence microscopy (CFM) was used, detecting NPs by imaging in the reflection mode and allowing imaging in live cells and in parallel with fluorescent staining of cells for various organelles allowing colocalisation of NPs with endosomes, lysosomes *etc.* to be investigated. Targetting NPs to different organelles, in particular the nucleus and mitochondria, was then investigated using this technique.

6.1 Increasing Nanoparticle Uptake Into Cytosol vs Endosomes and Analysis by TEM

In order to address the problem of NP uptake into endosomes, TEM was initially used to analyse uptake under various conditions, including differently functionalised NPs, presence or absence of serum during incubation, treatment with drugs during incubation (chloroquine) and cell type. Bare NPs along with NPs functionalised with various molecules being used throughout the project were investigated – NQ-NPs, AQ-NPs, aminoNQ-NPs and CANLS1-NQ-NPs (Figure 6.1). NQ (Figure 6.1(a)) and aminoNQ (Figure 6.1(c)) are naphthoquinone derivatives and AQ (Figure 6.1(b)) is a more hydrophobic anthraquinone derivative. CANLS1 is a nuclear localisation sequence (NLS) peptide, prepared previously in the group by solid phase peptide synthesis. It has the amino acid sequence PKKKRKV (P, Proline; K, Lysine; R,

Arginine; V, Valine) with a cysteine (C) residue at the C-terminal end (V), to allow NP functionalization, and a spacer group and fluorescein moiety at the N-terminal end (P) (Figure 6.1(d)). Typically, cells were incubated overnight with NPs in medium without serum, as previous work demonstrated increased uptake compared to incubation in medium with serum and also serum proteins tended to coat NPs.[92] Chloroquine is known to cause endosome disruption[229] and was applied to cells along with NPs, as described in Chapter 2 Section 2.3.1, to investigate whether it caused increased escape of NPs from endosomes. Work by other group members using different cell types showed better cytosolic uptake of NPs and therefore different cell lines that could also form MTS were investigated. A human colorectal cancer cell line, HCT116, was used along with a double knockout variant HCT116p53–/– (p53-RNAi negative and p53 knockout negative), both of which form MTS.

TEM images were acquired for each condition as described in Chapter 2 Section 2.3.1, and analysis was performed subjectively by manually counting NPs present in endosomes and cytosol. NPs were also present outside cells and in dead cells/cell material. % NPs in cytosol, relative to total number of NPs in cytosol+endosomes, was calculated under each condition and results are represented graphically in Figure 6.2 and tabulated in Table 6.1. The most significant observation was that AQ-NPs showed a greater % of NPs in cytosol and HCT116p53–/– cells displayed a greater % of NPs in cytosol for both 2D and 3D culture. This could possibly be attributed to the greater hydrophobicity of AQ and shows that some cell lines may be more susceptible to release of NPs from endosomes. Studies have shown that the p53 pathway is involved in upregulating activity of endosomal compartments and

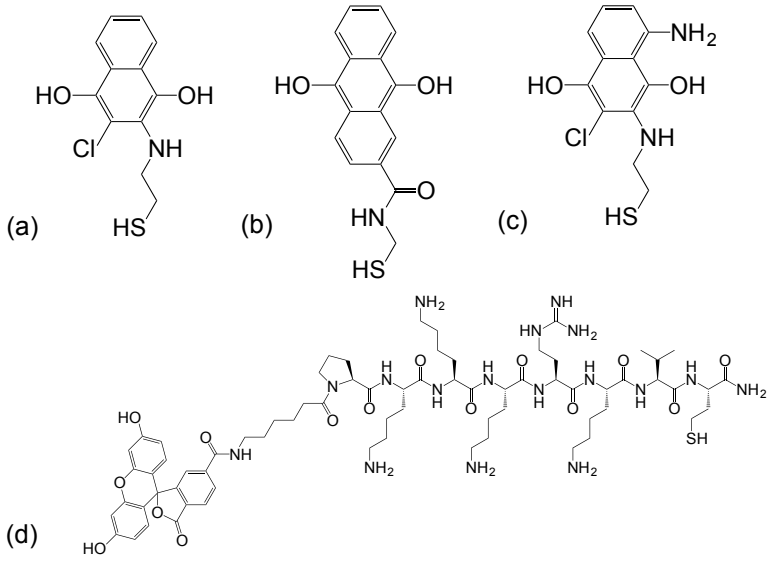

Figure 6.1 shows the structure of reduced NQ (a), AQ (b) and aminoNQ (c) and CANLS1 (d).

suggesting that this observation of decreased percentage NPs in endosomes for the double knockout cell line could be linked to this.[230] Interestingly, some TEM images showed good evidence of uptake via endocytosis, showing NPs in the process of being engulfed by cells (Figure 6.3). Overall, it remained difficult to control NP uptake and there was no definitive result to increase uptake to cytosol with no conditions allowing 100% cytosolic uptake or close to this. There was also a significant number of NPs present on the outside of cells despite washing steps.

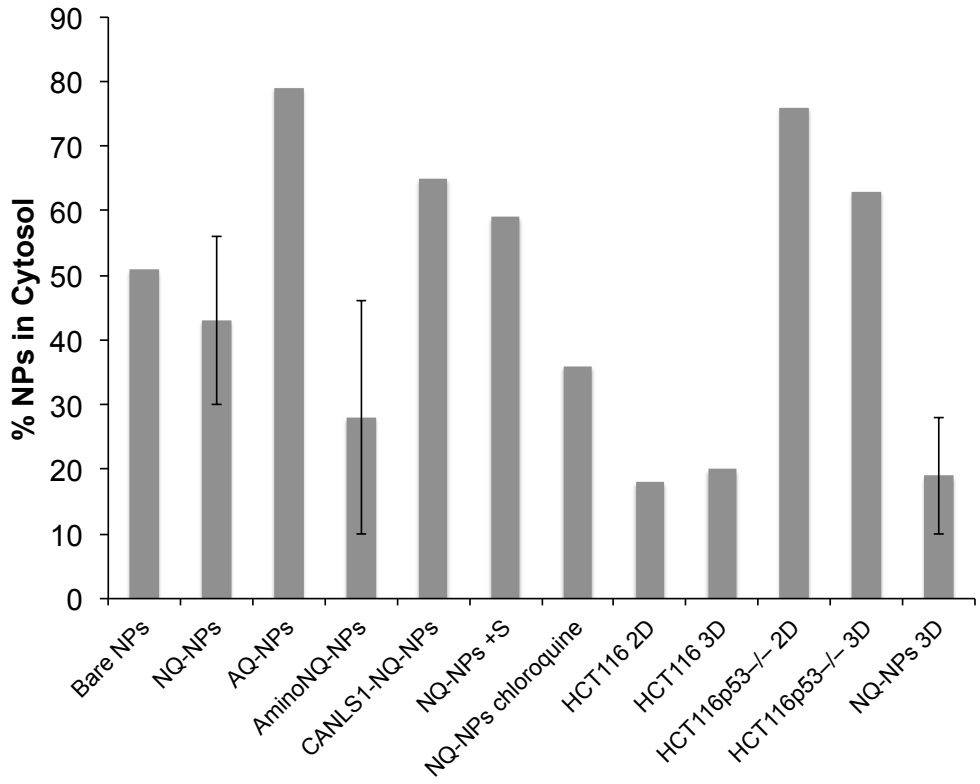

Figure 6.2 graphically represents % of NPs into cytosol relative to endosomes under various conditions as described in Chapter 2 Section 2.3.1. This was measured subjectively by counting NPs present in different locations in cells from TEM images. Where not stated the cell line used was MCF7. Functionalised NPs (bare, NQ, AQ, aminoNQ and CANLS1-NQ); incubation in media with serum (+S) as opposed to without in all other cases; incubation with chloroquine and uptake by different cell lines (HCT116 and HCT116p53–/–) in monolayer culture (2D) and MTS (3D) were investigated. Where experiments were carried out more than once error bars are given (NQ-NPs average of three repeats; AminoNQ-NPs and NQ-NPs 3D average of two repeats), otherwise experiments were only carried out once.

Table 6.1 tabulates results for NP uptake into cells analysed by TEM where NPs were counted subjectively in different cell regions under various conditions. Where not stated the cell line used was MCF7. Functionalised NPs (bare, NQ, AQ, aminoNQ and CANLS1-NQ); incubation in media with serum (+S) as opposed to without in all other cases; incubation with chloroquine and uptake by different cell lines (HCT116 and HCT116p53–/–) in monolayer culture (2D) and MTS (3D) were investigated. Where experiments were carried out more than once the values for each repeat are given with an average and standard deviation for the final % NPs in cytosol.

Condition	**Number NPs inside vesicles**	**Number NPs in cytosol**	**Number NPs outside cell**	**Number NPs dead cells**	**% NPs in cytosol**
Bare NPs	33	35		139	51
NQ-NPs	7/40/17	3/29/22	130/0/68	0/lots/0	43 ± 13
AQ-NPs	3	11	34	11	79
AminoNQ-NPs	3/33	2/6	-/30	89/120	28 ± 18
CANLS1-NQ-NPs	28	51		4	65
NQ-NPs + S	55	80	13		59
NQ-NPs chloroquine	7	4	74		36
HCT116 2D	23	5	13		18
HCT116 3D	47	12		19	20
HCT116p53–/– 2D	4	13	14		76
HCT116p53–/– 3D	17	29	4		63

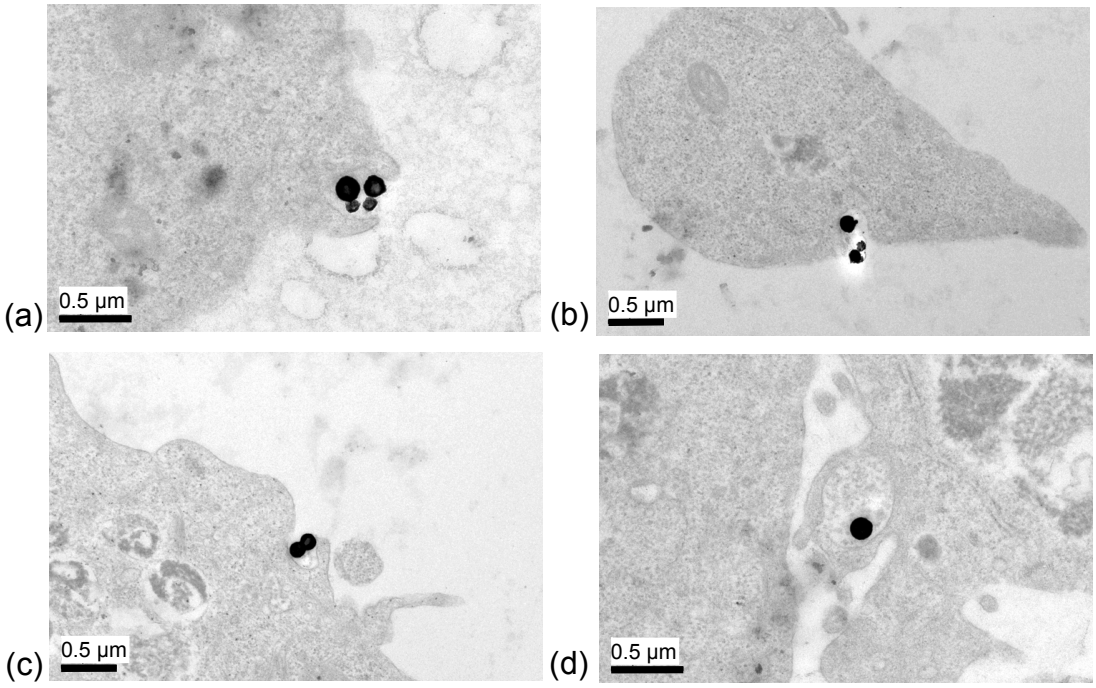

Figure 6.3 shows TEM images of NPs being engulfed by cells. Cells are HCT116 colorectal cancer cells growing in monolayer culture (a-c) and as MTS (d).

Following this initial investigation, further options for functionalisation of NPs with various molecules reported in literature to increase endosomal release of NPs was carried out.[231–235] 1-Thioglucose (TG) was prepared by hydrolysis of 1-Thioglucose tetraacetate (Figure 6.4(a)) and all other molecules were purchased: polyarginine (PLA), cysteamine (2AET), poly(ethylene glycol) methyl ether thiol (PEG800) and O-(2-Mercaptoethyl)-O′-methyl-hexa(ethylene glycol) (PEG6). NPs were functionalised with 1 mM of each molecule as described in Chapter 2 Section 2.2.3.1, and for TG both 0.1 mM and 1 mM solutions were used. Results for NP uptake to MCF7 cells were analysed subjectively, as previously, and are shown graphically in Figure 6.5 and tabulated in Table 6.2. Generally, a slight increase in % of NPs to cytosol was observed for all molecules, PEG6-NPs showing the most success with 80% NPs in cytosol compared to 43 ± 13% for NQ-NPs in monolayer culture. Therefore, PEG6-NP uptake was investigated in MTS and again showed an increase in % NPs in cytosol from 19 ± 9 % for NQ-NPs to 49% for PEG6-NPs. NPs were then functionalised with both NQ and PEG6 by overnight incubation with equal concentrations, as described in Chapter 2 Section 2.2.3.1. In monolayer culture, there was a decrease to 56% in cytosol compared to PEG6-NP, but still higher than NQ-NPs. In MTS, % NPs in cytosol remained similar to that for PEG6-NPs at 51%. Again, none of these modifications were conclusive and a method that could give close to 100% presence of NPs in cytosol in comparison to endosomes would be ideal.

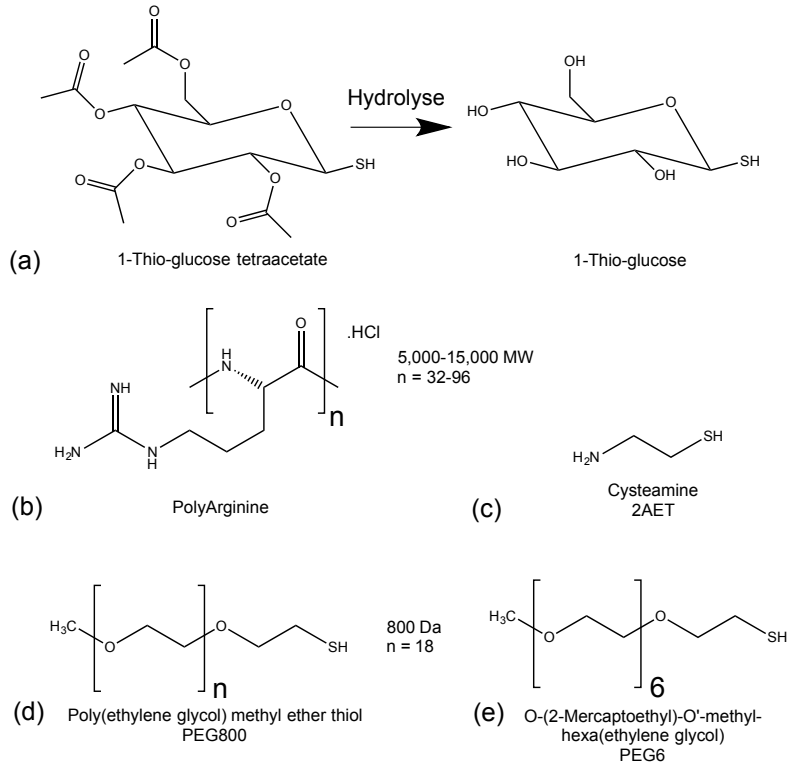

Figure 6.4 shows the structures of various molecules used to functionalise NPs in an attempt to increase release of NPs from endosomes.

These experiments have demonstrated the difficulty in controlling NP uptake into different cellular compartments. It is an important area of research and greater control could allow intracellular variations in pH and redox potential to be observed. This could extend to targeting specific organelles such as nuclei and mitochondria, as will be discussed in the following section.

Table 6.2 tabulates results for % uptake of NPs into cytosol relative to endosomes analysed by TEM where NPs were counted subjectively in different cell regions under various conditions. NPs were functionalised with different molecules and delivered to MCF7 cells in monolayer culture (2D) and MTS (3D).

Condition	Number NPs inside vesicles	Number NPs in cytosol	Number NPs outside cell	Number NPs dead cells	% NPs in cytosol
NQ-NPs 2D	7/40/17	3/29/22	130/0/68	0/lots/0	43 ± 13
TG-NPs 1 mM 2D	18	21	44	0	54

TG-NPs 0.1 mM	9	10	164	0	53
PLA-NPs 2D	12	16	18	0	57
PEG800-NPs 2S	35	29	26	0	45
2AET-NPs 2D	34	82	76	0	71
PEG6-NPs 2D	19	78	158	0	80
PEG6-NQ-NPs 2D	30	38	61	0	56
NQ-NPs 3D	599/15	78/5	0/0	0/11	19 ± 9
PEG6-NPs 3D	22	21	0	0	49
PEG6-NQ-NPs 3D	21	22	9	9	51

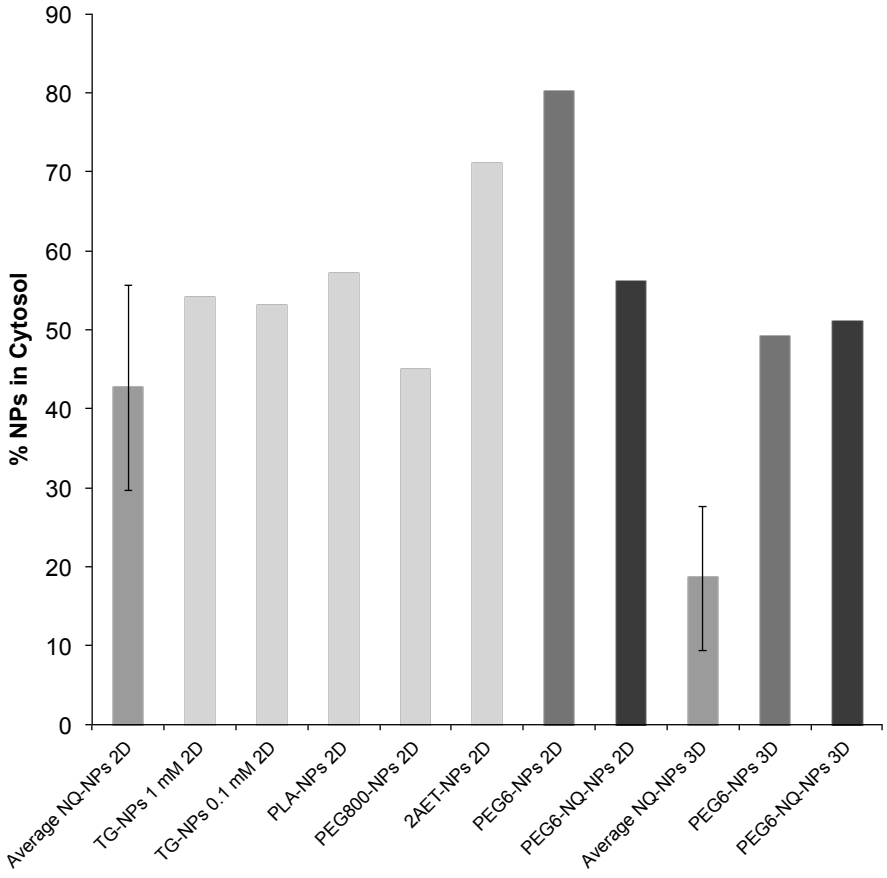

Figure 6.5 graphically represents % uptake of NPs into cytosol relative to endosomes analysed by TEM for NPs functionalised with different molecules and delivered to MCF7 cells in both monolayer culture (2D) and MTS (3D).

6.2 Confocal Fluorescence Microscopy in Reflection Mode as a New Method for Tracking Intracellular Nanoshell Location in Live Cells

Using TEM to analyse NP uptake by cells has some drawbacks, including that it is not possible to analyse live cells and the procedure for preparing cells is labour and cost intensive. Therefore, a new technique for monitoring NP uptake in live cells was investigated using CFM. As the NPs are gold they could be detected by imaging in reflection mode.

6.2.1 Technique Development

It was proposed that NPs could be visualised using CFM in reflection mode. This could then be combined with fluorescence imaging of dyes to stain various cell compartments in order to investigate intracellular NP localisation by colocalisation of reflection and fluorescence images. Excitation wavelengths and emission filters for all experiments are given in Chapter 2 Section 2.3.4. For proof of principle, NPs in agarose on a glass slide with coverslip were imaged using reflection from a 488 nm laser (Figure 6.6).

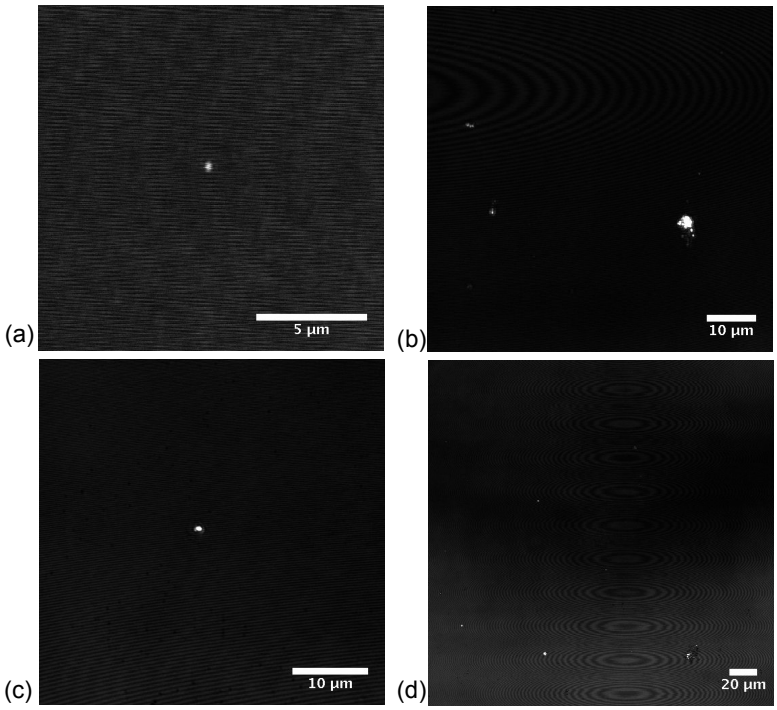

Figure 6.6 shows images of NPs in agarose on glass slides with coverslips. Images were acquired using reflection from a 488 nm laser and a ×63 objective and show bright 'speckles' attributed to the presence of NPs.

Following from this, MCF7 cells were incubated overnight with bare NPs and cells were imaged in 3D the following day after washing steps as detailed in Chapter 2 Section 2.3.4. Cells were mapped in 3D using CFM to generate both a bright field image and reflection image, in this case from a 594 nm laser. Control cells, untreated with NPs, were also imaged. Image J software was used to create volume images of control cells (Figure 6.7(a) and (b)) and cells treated with NPs (Figure 6.7(c) and (d)). Results clearly indicated the presence of 'speckles' detected by reflection due to the presence of NPs in the treated sample compared to control cells where only background cell reflection was observed.

It was then proposed that this technique could be used as a replacement for TEM to analyse endosomal vs cytosolic uptake of NPs, if cells were treated with a fluorescent dye to stain endosomes to allow detection of endosomes as well as NPs using CFM. As this was possible in live cells, it would also allow NP uptake to be monitored over a time course. LysoSensor™ Green DND-153 and DiD were used as fluorescent stains. Lysosensor is an amine that is a weak base and accumulates in acidic cellular compartments, therefore labeling acidic

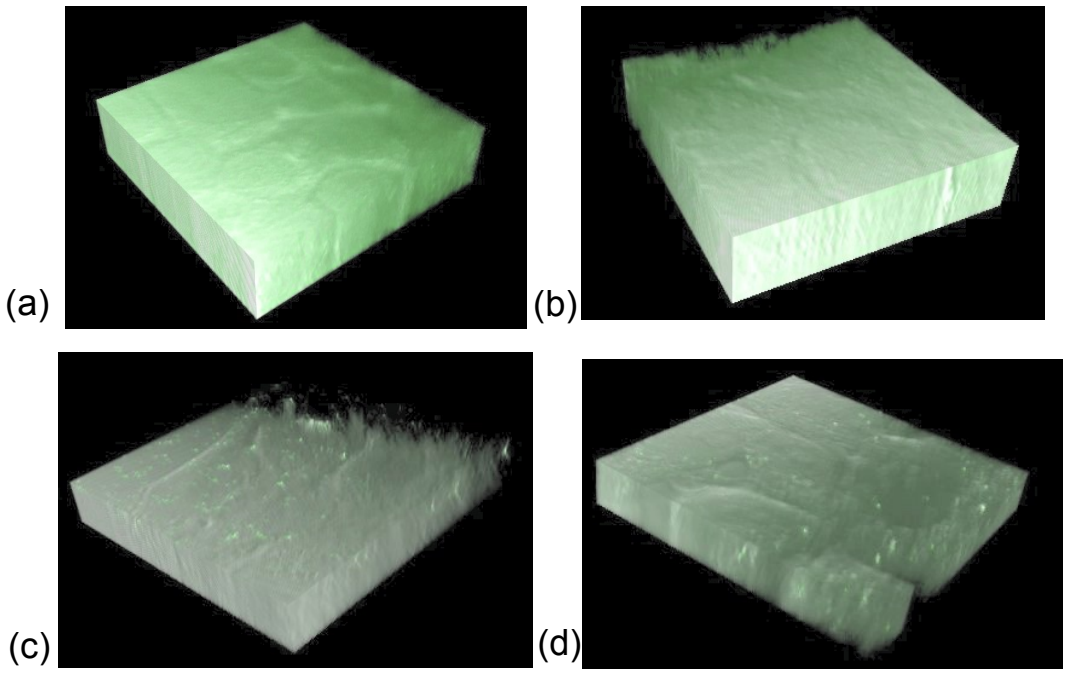

Figure 6.7 shows volume images created using Image J of areas of MCF7 cells untreated (a-b) and incubated overnight with bare NPs (c-d) and imaged using CFM to create both a bright field image and image of reflection from 594 nm laser using a ×40 objective.

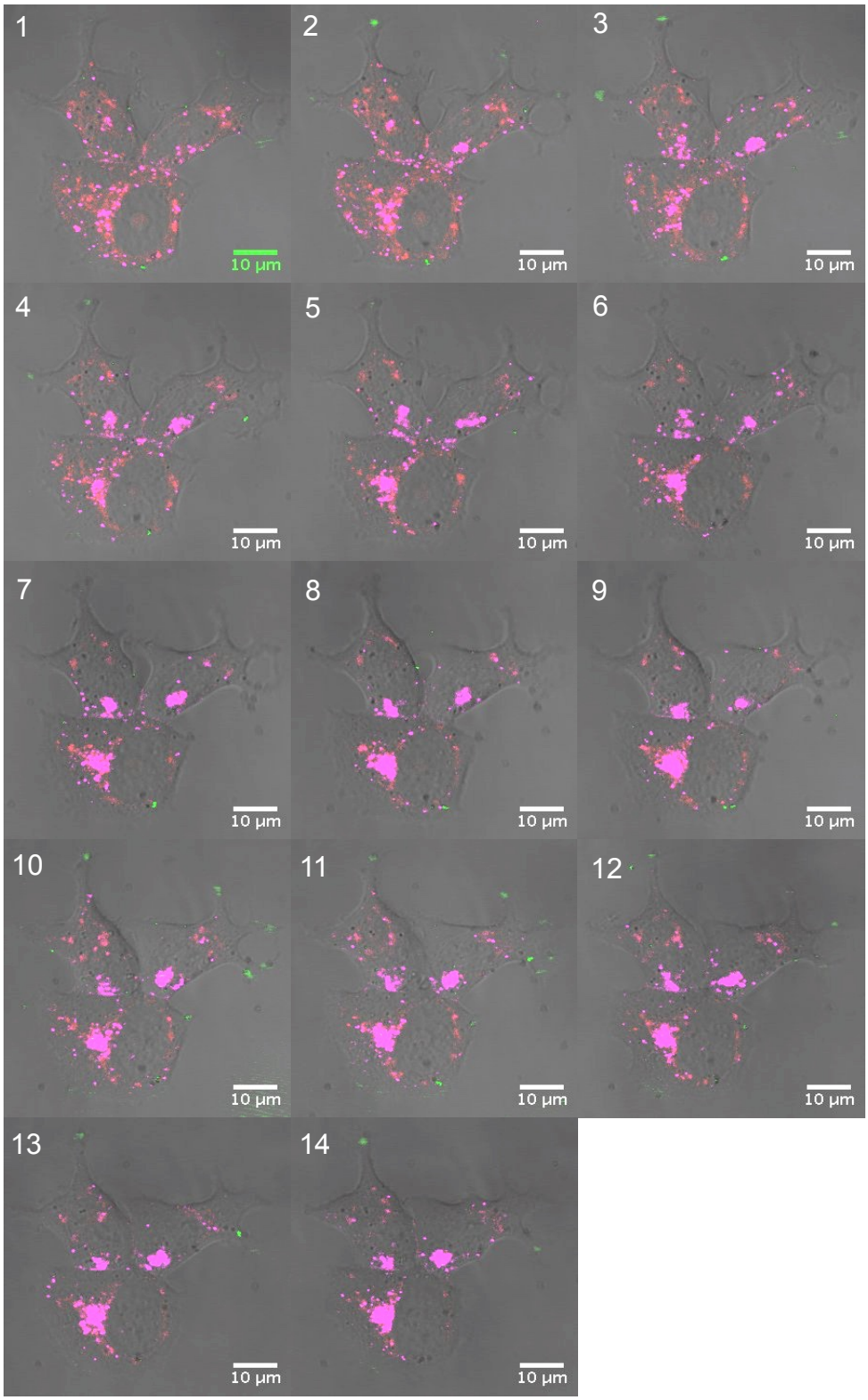

Figure 6.8 shows time course images of MCF7 cells stained with Lysosensor (pink) and DiD (red) and treated with NPs at the start of the experiment. NPs were imaged by laser reflection (green) and images were acquired at 504 s intervals over 14 time points (labeled) using a ×63 objective.

organelles such as lysosomes. It absorbs at 442 nm and emits at 505 nm. It is likely that Lysosensor will stain endosomes as well as lysosomes, as they are also acidic. However, early endosomes are do not exhibit as low a pH as late endosomes and lysosomes[13], and therefore may not be stained as successfully. DiD is a carbocyanine membrane stain that accumulates in membranes due to high lipophilicity. It absorbs at 644 nm and emits at 665 nm. Lysosensor should allow detection of acidic vescicles and DiD should allow detection of all vesicles by membrane staining. MCF7 cells were stained with both Lysosensor and DiD as described in Chapter 2 Section 2.1.8. A time course experiment was then carried out, following addition of NPs to cells. Images were acquired at time intervals of 540 s and the results are shown in Figure 6.8 over 14 time points. Lysosensor (pink) was more effective as a fluorescence stain. The presence of NPs (green) could be imaged alongside fluorescent probes over a time course. Overlaid images over time points were again created using Image J. Generally NPs and fluorescent stains did not appear to colocalise over this time frame but a quantitative method was required to confirm this.

To quantify NP uptake, the software Image-Pro Premier was used. This allowed isosurface plots to be created for each channel from CFM images, in addition to isosurface plots of overlaid channels. A series of MCF7 cells treated overnight with AQ-NPs were analysed using this method. Cells were stained with Lysosensor prior to imaging in 3D for both lysosensor fluorescence and reflection from NPs. Isosurfaces were created using Image-Pro Premier 3D as described in Chapter 2 Section 2.4.9 and shown in Figure 6.9, overlaid on the bright field cell image. Isosurfaces of Lysosensor fluorescence (red), reflection (green) and overlaid Lysosensor and reflection (yellow) were created. By extracting volumes from each surface, the percentage overlaid vs total NPs could be calculated i.e. the percentage of NPs present in vesicles labeled with Lysosensor vs free in the cytosol (assuming they were present in no other organelles). The average percentage over the four cells analysed was 20 ± 13%, which agreed well with previous results for AQ-NPs from TEM in the previous section where 79% were found in the cytosol relative to vesicles. In one outlier case, only 1% was overlaid. This, along with the large standard deviation, highlights how much cell-cell variation there can be in NP uptake. This technique has been established as a cheaper and less labour intensive technique than TEM for analysis of NP uptake in live cells using CFM and allows colocalisation of NPs with fluorescently labeled organelles to be studied.

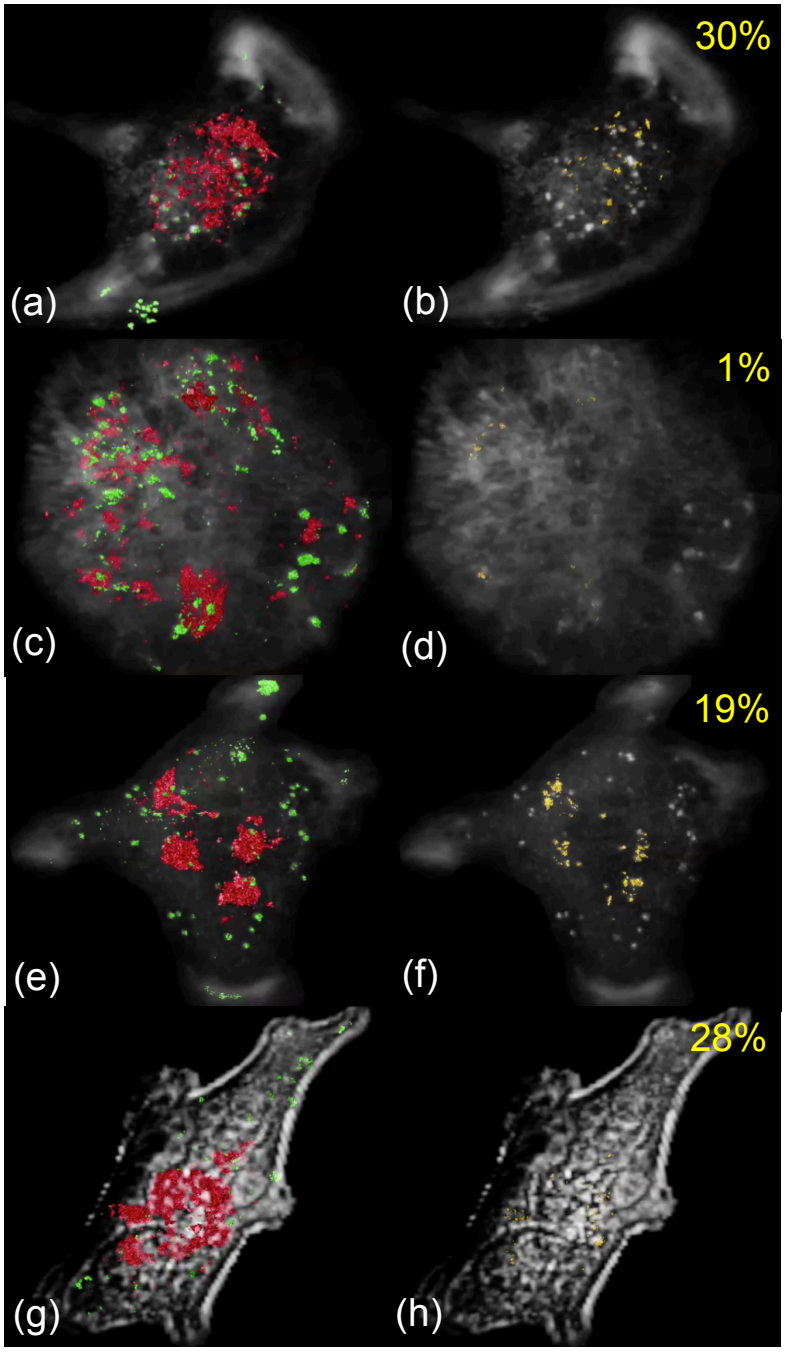

Figure 6.9 shows processed images of MCF7 cells treated overnight with AQ-NPs and stained with Lysosensor. Cells were imaged using CFM with bright field images, fluorescence from Lysosensor and reflection from NPs imaged using a ×63 objective. Images were processed to create isosurfaces for Lysosensor fluorescence, reflection and overlay of both using Image-Pro Premier 3D and percentage area of overlaid vs total reflection signal was determined and is indicated on images where the left hand column shows fluorescence (red) and reflection (green) signals and the right hand column shows overlaid signals. Snapshots were taken from the 3D images generated.

6.2.2 Targeting Nuclei and Mitochondria and Analysis using CFM

After establishing this technique, attempts were made to target NPs to both nuclei and mitochondria and analyse results by colocalisation of reflection with fluorescence from nuclei and mitochondria, analysed in the same manner as previously. For nuclear staining NucBlue® Live ReadyProbes® Reagent was used, and for mitochondrial staining, TMRM was used. NucBlue is a Hoechst 33342 stain, which fluoresces when it binds to DNA and has an excitation at 360 nm and emission at 460 nm. TMRM accumulates in mitochondria and has an excitation at 535 nm and emission at 600 nm.

For NP targeting to nuclei, NPs were functionalised with CANLS1 (Figure 6.10(a)) or NLS2 (Figure 6.10(b)) – two similar nuclear localisation sequences previously synthesised in the Campbell group, University of Edinburgh, and based on the amino acid sequence PKKKRKV (for experimental synthetic details see Auchinvole, C.A.R[94]). For mitochondrial targeting, a modified triphenyl phosphonium (TPP) cation, known to accumulate in mitochondria[236,237], was synthesised by Patrick Thomson, University of Edinburgh, 4-sulfanylbutylphenylphosphanium bromide (SBTPP) (Figure 6.10(c)). NPs with a diameter of 150 nm and 50 nm were investigated with each targeting molecule. NPs were functionalised by overnight incubation with 1 mM solutions of each targeting molecule as described in the Chapter 2 Section 2.2.3.1.

MCF7 cells were incubated overnight with each functionalised NP. Cells were stained with the relevant fluorescent dye the following day and imaged in 3D using CFM, as previously, but with the correct excitation and filters for the fluorescent probe being used. Again images were processed using Image-Pro Premier 3D by creating isosurfaces to analyse colocalisation. Control cells untreated with NPs were also analysed in each case. Figure 6.11 shows results for CANLS1. Control cells confirmed no significant reflection was observed in the absence of NPs (a). No colocalisation was observed with CANLS1-NP(150 nm) or CANLS1-NP(50 nm) (c). For NLS2-NP (Figure 6.12), no colocalisation was again observed for NLS2-NP(150 nm), some was present for NLS2-NP(50 nm). However, colocalisation observed was minimal and therefore further research would be required to optimise delivery, but this suggests, as expected, a smaller NP size was desirable for nuclear delivery as the nuclear pores are thought to be *ca.* 120-140 nm diameter themselves.[222] Figure 5.13 shows results for mitochondrial targeting with control cells (a) showing no reflection as

expected and SBTPP-NP(150 nm) (b) and SBTPP-NP(50 nm) (c) showing no colocalisation. Further work would be required to optimise mitochondrial targeting, perhaps requiring even smaller NPs for the small mitochondrial structures.

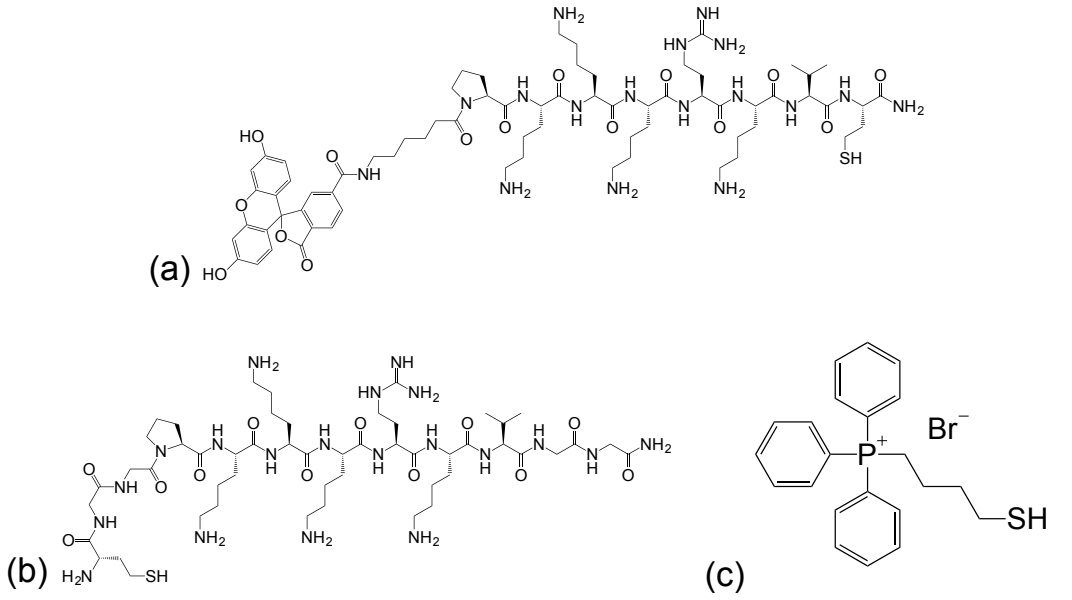

Figure 6.10 shows the structures of CANLS1 (a), NLS2 (b) and SBTPP (c).

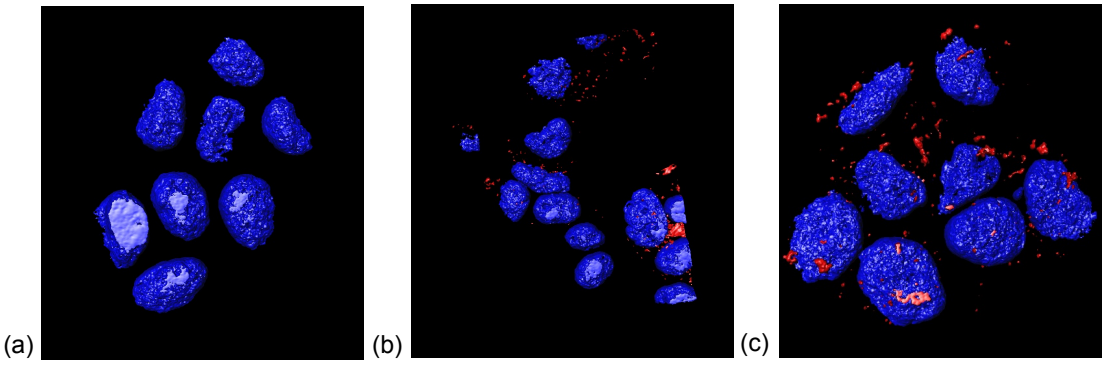

Figure 6.11 shows isosurfaces created using Image-Pro Premier 3D for MCF7 cells stained with NucBlue (blue) and not treated with NPs (a), treated overnight with CANLS1-NPs(150 nm) (b), and treated overnight with CANLS1-NPs(50 nm) (c). NPs were imaged using reflection indicated by the red isosurface and fluorescence from stained nuclei indicated by the blue isosurface using a ×63 objective.

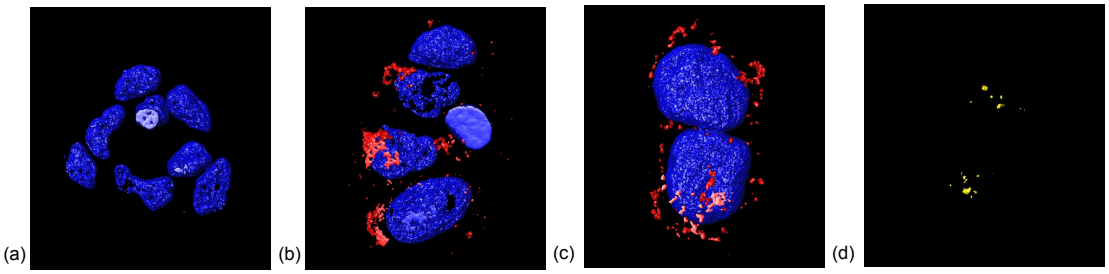

Figure 6.12 shows isosurfaces created using Image-Pro Premier 3D for MCF7 cells stained with NucBlue (blue) and untreated with NPs (a), treated overnight with NLS2-NPs(150 nm) (b), and treated overnight with NLS2-NPs(50 nm) (c). NPs were imaged by reflection indicated by the red isosurface and fluorescence from stained nuclei indicated by the blue isosurface using a ×63 objective. Where there was colocalisation this is represented by the yellow isosurface (d). Cells in (c) and (d) are identical with different isosurfaces highlighted.

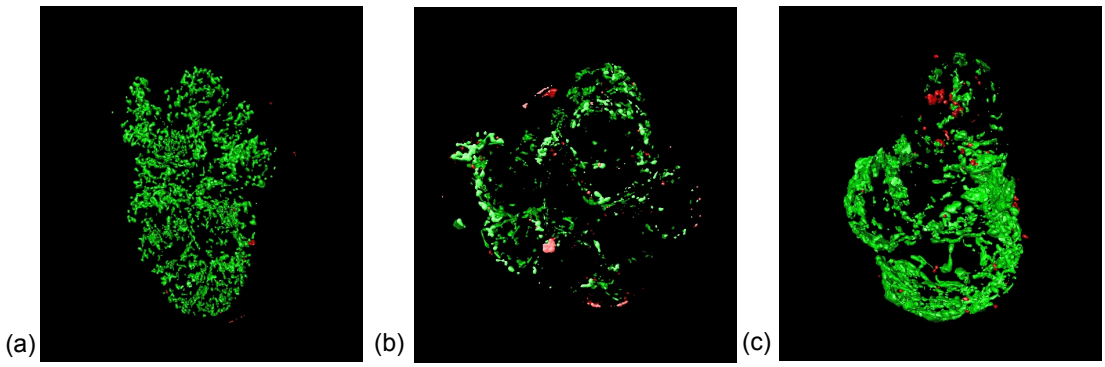

Figure 6.13 shows isosurfaces created using Image-Pro Premier 3D for MCF7 cells stained with TMRM (green) and untreated with NPs (a), treated overnight with SBTPP-NPs(150 nm) (b), and treated overnight with SBTPP-NPs(50 nm) (c). NPs were imaged by reflection indicated by the red isosurface and fluorescence from stained mitochondria indicated by the green isosurface using a ×63 objective.

Successful NP targeting to organelles is difficult, and would require further extensive study, which was not possible due to time constraints. CFM has been shown to be a useful and new technique for analysis or NP uptake and intracellular localisation. More success was observed using smaller NPs, so this along with potentially different nuclear and mitochondrial targeting sequences and molecules could be investigated as well as possibly investigating optimal NP functionalisation with these molecules to ensure efficient mode of action when delivered to cells.

Chapter 7

Conclusions

"Exceptional or Nothing" – **Mags**

Intracellular redox potential is a highly regulated and vitally important cellular characteristic and disruption of the finely balanced redox state in cells has been implicated in disease progression. In this work, particular insight was sought into the development of redox potential gradients in cancer tumours in an *in vitro* tumour model – multicellular tumour spheroids (MTS). While research regarding redox potential is often directed towards oxidative stress as a detrimental factor in maintaining healthy cell functioning, this research is focused towards the other end of the redox balance in cells, where a hypoxic environment develops in cancer tumours as blood supply becomes limited deeper into tumour tissue. The tumour microenvironment is mimicked in the *in vitro* MTS model used in this research. This is a 3D cell culture model, compared to the standard monolayer cell culture used in biological research, and is being increasingly used in biology as a more realistic model of cell physiology in the body.

There are currently limited techniques available for quantitative assessment of the redox environment that develops in cancer tumours, small molecule probes such as Hypoxyprobe™ being the current 'gold standard' technique available. This technique has several limitations, including lack of quantitative information, and in the MCF7 cell MTS used in this project has failed to show any information on hypoxic state. A more quantitative discriminatory technique is required for assessment of potentially more subtle development of gradients in MTS. To address this need, the technique of surface enhanced Raman scattering (SERS) was employed, using nanoscale sensors to probe redox state of cells via ratiometric changes in SER spectra of redox active molecules attached to the surface of gold nanoparticles. SERS is a technique encompassed by the field of vibrational spectroscopy, where vibrations of bonds in molecules are detected through the basic processes of IR absorption/emission and Raman scattering. There has been rapid and exciting expansion of this field into biomedical research in recent years, with IR and Raman techniques used widely for applications in biological material *in vivo*, *ex vivo* and *in vitro* and even being

translated into clinical settings. The reported SERS nanosensor technique aims to increase understanding of complex biological systems as a means of improved knowledge for potential drug and therapy development; and provide a potential platform for drug and therapy testing by measurement of response via cellular redox state.

Initial work presented in Chapter 3 revealed key morphological differences between monolayer cell culture and MTS and went on to confirm successful uptake of our SERS nanosensors to MCF7 cells in monolayer culture and MTS, with no cytotoxic effects. Preliminary SERS measurements were conducted and compared between MCF7 cells in monolayer culture and MTS using NQ-NP and AQ-NP SERS sensors. These measurements revealed a significant difference in redox potential measured between the 2D and 3D models with, on average, a more reducing and varied environment found in MTS as expected. Measurements in MTS, however, revealed a wider range than expected and at this stage the need for simultaneous pH measurement was highlighted and development of a SERS pH sensor for simultaneous SERS measurement of redox potential in pH was established as an aim.

Developments towards a SERS pH sensor are presented in Chapter 4 where MBA-NP was established as the most successful SERS pH probe in calibration experiments. Other potential probes – 4MP-NP, 4ABT-NP and NBA-NP – could also be developed further in the future for application also. After extensive calibration of this pH sensor, it was applied to live cells in monolayer culture to report on intracellular pH, an important characteristic in its own right. pH changes during the course of apoptosis were successfully studied in MCF7 cells as well as intracellular pH in EA.hy926 endothelial cells and in response to application of different extracellular buffers and TNFα.

Moving on from singleplex measurements, Chapter 5 reveals how a combination of AQ-NPs for redox potential measurement, and MBA-NPs for pH measurement, were used to monitor redox potential and pH simultaneously in live EA.hy926 cells in monolayer culture. This allowed pH corrections to be applied for accurate redox potential monitoring and also revealed increased physiological information by providing two measurements of physiological parameters, as opposed to a single measurement. Following successful measurements in monolayer culture, this technique was then extended for use in MTS. Due

to limitations in imaging depth and spatial information established in Chapter 3 a new method was proposed for measurement of spatial changes in redox potential and pH in MTS. Techniques were established to control NP localisation in MTS spatially, which was monitored using photothermal OCT. A fibre optic Raman probe was then used to take an average SER spectrum from a whole MTS with a specific NP distribution revealing physiological characteristics in the specific MTS region. This technique allowed redox potential and pH gradients to be successfully probed in MTS as a platform for increasing quantitative knowledge about physiological characteristics of cancer tumours. The technique was also demonstrated to be applicable for monitoring response to drugs in varying MTS regions, where response in targeted specific regions was significant whereas response over the whole MTS, where NP were distributed in a uniform manner, were not always apparent. The potential and limitations of a Renishaw inVia microscope system for establishing more spatially resolved and subtle redox potential and pH changes were investigated, but lack of confocality and collection of out of focus signal severely limited application.

Finally, initial studies into targeted intracellular NP uptake were explored in Chapter 6. This was initially important as TEM experiments in Chapter 3 revealed that NPs were often present in endosome structures in the intracellular environment in addition to the cytosol. As cytosolic measurements were preferential, attempts were made to increase release of NPs into the cytosol using different NP functionalisations along with varying incubation conditions and cell line. There was some success, particularly using certain NP modifications. However, no technique revealed a sufficiently high release of NPs from endosome structures. Further work was required to optimise and investigate other potential solutions. As TEM is an expensive and labour intensive technique and requires cell fixation and sectioning, a new technique was developed for monitoring intracellular NP uptake in live cells using a confocal fluorescence microscope. NPs could be visualised by imaging in reflection mode and this could be coupled with fluorescence staining for various intracellular compartments and overlay of signals anlaysed to determine NP location. This technique was applied for monitoring uptake into intracellular vesicles, including lysosomes and in attempts to deliver NPs to nuclei and mitochondria using NPs functionalised with specific molecules.

This project has employed SERS nanosensors for quantitative monitoring of important cellular characteristics – namely pH and redox potential. The first example of simultaneous measurement of these characteristics using SERS nanosensors has been shown in monolayer culture and MTS revealing important physiological information. In the future, the fibre optic technique could be developed to monitor gradients in MTS from different cell lines and during MTS growth for comparison and as an assay for drug monitoring. Further work using a Raman microscope system could reveal more detailed spatial information on gradients in MTS. Due to limitations as a result of collection of out of focus signal in MTS, a different approach could be to monitor the Raman signals in MTS sections to reveal important biochemical differences in different MTS regions. Alternative technologies such as CARS and SESORS could be investigated for application to the SERS technique also. It is also proposed that a light sheet Raman setup could be applied to MTS treated with these SERS nanosensors.

References

1 G. Waris and H. Ahsan, *J. Carcinog.*, 2006, **5:14**.

2 L. Sherwood, H. Klandorf and P. Yancey, *Animal Physiology: From Genes to Organisms*, Cengage Learning, 2nd edn., 2012.

3 H. Liu, R. Colavitti, I. I. Rovira and T. Finkel, *Circ. Res.*, 2005, **97**, 967–74.

4 T. Finkel, *J. Cell Biol.*, 2011, **194**, 7–15.

5 G. Filomeni, G. Rotilio and M. R. Ciriolo, *Cell Death Differ.*, 2005, **12**, 1555–63.

6 F. Q. Schafer and G. R. Buettner, 2001, **30**, 1191–212.

7 P. Atkins and J. de Paula, *Elements of Physical Chemistry*, OUP Oxford, 2012.

8 S. C. Lu, *FASEB J.*, 1999, **13**, 1169–83.

9 M. Kemp, Y.-M. Go and D. P. Jones, *Free Radic. Biol. Med.*, 2008, **44**, 921–37.

10 Y.-M. Go and D. P. Jones, *Free Radic. Biol. Med.*, 2011, **50**, 495–509.

11 Y.-M. Go and D. P. Jones, *Biochim Biophys Acta.*, 2008, **1780**, 1273–90.

12 C. D. Austin, X. Wen, L. Gazzard, C. Nelson, R. H. Scheller and S. J. Scales, *Proc. Natl. Acad. Sci.*, 2005, **102**, 17987–92.

13 J. R. Casey, S. Grinstein and J. Orlowski, *Nat. Rev. Mol. Cell Biol.*, 2010, **11**, 50–61.

14 D. P. Jones, *J. Intern. Med.*, 2010, **268**, 432–48.

15 S. Kuge, M. Arita, A. Murayama, S. Izawa, Y. Inoue and A. Nomoto, 2001, **21**, 6139-50.

16 P. Vaupel, *Semin. Radiat. Oncol.*, 2004, **14**, 198–206.

17 S. Mitra, PhD Thesis, Univeristy of Rochester, 2004.

18 J. L.-S. Au, S. H. Jang, J. Zheng, C.-T. Chen, S. Song, L. Hu and M. G. Wientjes, *J. Control. Release*, 2001, **74**, 31–46.

19 Online Resources for Disorders Caused by Oxidative Stress, http://www.oxidativestressresource.org (accessed 20/06/2013).

20 D. Hanahan and R. A. Weinberg, *Cell*, 2011, **144**, 646–74.

21 M. W. Dewhirst, Y. Cao and B. Moeller, *Nat. Rev. Cancer*, 2008, **8**, 425–37.

22 P. Vaupel, F. Kallinowski and P. Okunieff, *Cancer Res.*,1989, 49, 6449–65.

23 C. Riganti, E. Gazzano, M. Polimeni, E. Aldieri and D. Ghigo, *Free Radic. Biol. Med.*, 2012, **53**, 421–36.

24 W. H. Koppenol, P. L. Bounds and C. V. Dang, *Nat. Rev. Cancer*, 2011, **11**, 325–37.

25 M. K. Danquah, X. A. Zhang and R. I. Mahato, *Adv. Drug Deliv. Rev.*, 2011, **63**, 623–39.

26 I. H. Shaik and R. Mehvar, 2006, **385**, 105–13.

27 D. Giustarini, I. Dalle-Donne, R. Colombo, A. Milzani and R. Rossi, *Free Radic. Biol. Med.*, 2003, **35**, 1365–72.

28 E. W. Miller, S. X. Bian and C. J. Chang, *J. Am. Chem. Soc.*, 2007, **129**, 3458–9.

29 K. Kundu, S. F. Knight, N. Willett, S. Lee, W. R. Taylor and N. Murthy, *Angew. Chem. Int. Ed. Engl.*, 2009, **48**, 299–303.

30 M. A. Keese, R. Saffrich, T. Dandekar, K. Becker and R. H. Schirmer, *FEBS Lett.*, 1999, **447**, 135–8.

31 G. T. Hanson, R. Aggeler, D. Oglesbee, M. Cannon, R. A. Capaldi, R. Y. Tsien and S. J. Remington, *J. Biol. Chem.*, 2004, **279**, 13044–53.

32 C. T. Dooley, T. M. Dore, G. T. Hanson, W. C. Jackson, S. J. Remington and R. Y. Tsien, *J. Biol. Chem.*, 2004, **279**, 22284–93.

33 Protein Data Bank, www.rcsb.org (accessed 09/11/2015).

34 M. B. Cannon and S. J. Remington, *Protein Sci.*, 2006, **15**, 45–57.

35 H. Ostergaard, A. Henriksen, F. G. Hansen and J. R. Winther, *EMBO J.*, 2001, **20**, 5853–62.

36 C. V. Raman and K. S. Krishnan, *Nature*, 1928, 121, 501–2.
37 J. Atkins, P. De Paula, *Atkins' Physical Chemistry*, Oxford University Press, Oxford, 8th Editio., 2006.
38 E. L. Ru and P. Etchegoin, *Principles of Surface-Enhanced Raman Spectroscopy: and related plasmonic effects*, Elsevier, 2008, 29-120.
39 A. Barth and P. I. Haris, *Biological and Biomedical Infrared Spectroscopy*, IOS Press, Volume 2 o., 2009.
40 A. Zoubir, Ed., *Raman Imaging: Techniques and Applications*, Volume 168., 2012.
41 F. Severcan and P. I. Haris, *Vibrational Spectroscopy in Diagnosis and Screening*, IOS Press, Volume 6 o., 2012.
42 H. Czichos, T. Saito and L. E. Smith, Eds., *Springer Handbook of Metrology and Testing*, Spinger Science & Business Media, 2, illustr., 2011.
43 M. B. Fenn, P. Xanthopoulos, G. Pyrgiotakis, S. R. Grobmyer, P. M. Pardalos and L. L. Hench, *Adv. Opt. Technol.*, 2011, **2011**.
44 M. Fleischmann, P. J. Hendra and A. J. McQuillan, *Chem. Phys. Lett.*, 1974, **26**, 163–6.
45 D. L. Jeanmaire and R. P. Van Duyne, *J. Electroanal. Chem. Interfacial Electrochem.*, 1977, **84**, 1–20.
46 A. J. McQuillan, *Notes Rec. R. Soc.*, 2009, **63**, 105–9.
47 E. L. Ru and P. Etchegoin, *Principles of Surface-Enhanced Raman Spectroscopy: and related plasmonic effects*, Elsevier, 2008, 1-27.
48 K. H. Su, Q. H. Wei, X. Zhang, J. J. Mock, D. R. Smith and S. Schultz, *Nano Lett.*, 2003, **3**, 1087–90.
49 D. Ruiz-Molina, F. Novio and C. Roscini, *Bio- and Bioinspired Nanomaterials*, John Wiley & Sons, 2014.
50 L. R. Hirsch, A. M. Gobin, A. R. Lowery, F. Tam, R. A. Drezek, N. J. Halas and J. L. West, *Ann. Biomed. Eng.*, 2006, **34**, 15–22.
51 J. Hammond, N. Bhalla, S. Rafiee and P. Estrela, *Biosensors*, 2014, **4**, 172–188.
52 E. L. Ru and P. Etchegoin, *Principles of Surface-Enhanced Raman Spectroscopy: and related plasmonic effects*, Elsevier, 2008, 185-264.
53 H. J. Byrne, M. Baranska, G. J. Puppels, N. Stone, B. Wood, K. M. Gough, P. Lasch, P. Heraud and J. Sulé-Suso, *Analyst*, 2015, **140**, 2066–73.
54 M. Diem, M. Romeo, S. Boydston-White, M. Miljkovic and C. Matthaus, *Analyst*, 2004, **129**, 880–5.
55 M. J. Baker, J. Trevisan, P. Bassan, R. Bhargava, H. J. Butler, K. M. Dorling, P. R. Fielden, S. W. Fogarty, N. J. Fullwood, K. a Heys, C. Hughes, P. Lasch, P. L. Martin-Hirsch, B. Obinaju, G. D. Sockalingum, J. Sulé-Suso, R. J. Strong, M. J. Walsh, B. R. Wood, P. Gardner and F. L. Martin, *Nat. Protoc.*, 2014, **9**, 1771–91.
56 E. Levenson, P. Lerch and M. C. Martin, *J. Synchrotron Radiat.*, 2008, **15**, 323–8.
57 C. Hughes, A. Henderson, M. Kansiz, K. Dorling, M. Jimenez-Hernandez, M. D. Brown, N. W. Clarke and P. Gardner, *Analyst*, 2015, **140**, 2080–5.
58 P. Lasch, W. Haensch, D. Naumann and M. Diem, *Biochim. Biophys. Acta - Mol. Basis Dis.*, 2004, **1688**, 176–86.
59 D. C. Fernandez, R. Bhargava, S. M. Hewitt and I. W. Levin, *Nat. Biotechnol.*, 2005, **23**, 469–74.
60 D. Townsend, M. Miljković, B. Bird, K. Lenau, O. Old, M. Almond, C. Kendall, G. Lloyd, N. Shepherd, H. Barr, N. Stone and M. Diem, *Analyst*, 2015, **140**, 2215–23.
61 A. Derenne, V. Van Hemelryck, D. Lamoral-Theys, R. Kiss and E. Goormaghtigh, *Biochim. Biophys. Acta - Mol. Basis Dis.*, 2013, **1832**, 46–56.
62 C. Hughes, M. Brown, G. Clemens, A. Henderson, G. Monjardez, N. W. Clarke and P.

Gardner, *J. Biophotonics*, 2014, **7**, 180–8.
63 L. Lovergne, G. Clemens, V. Untereiner, R. A. Lukaszweski, G. D. Sockalingum and M. J. Baker, *Anal. Methods*, 2015, **7**, 7140-9.
64 Infrared light puts malaria to the test, http://monash.edu/news/show/infrared-light-puts-malaria-to-the-test (accessed 06/09/2015).
65 A. Khoshmanesh, M. W. A. Dixon, S. Kenny, L. Tilley, D. McNaughton and B. R. Wood, *Anal. Chem.*, 2014, **86**, 4379-86.
66 K. Kong, C. Kendall, N. Stone and I. Notingher, *Adv. Drug Deliv. Rev.*, 2015, **89**, 121–34.
67 D. I. Ellis and R. Goodacre, *Analyst*, 2006, **131**, 875–85.
68 C. Kallaway, L. M. Almond, H. Barr, J. Wood, J. Hutchings, C. Kendall and N. Stone, *Photodiagnosis Photodyn. Ther.*, 2013, **10**, 207–19.
69 L. M. Almond, J. Hutchings, G. Lloyd, H. Barr, N. Shepherd, J. Day, O. Stevens, S. Sanders, M. Wadley, N. Stone and C. Kendall, *Gastrointest. Endosc.*, 2014, **79**, 37–45.
70 Laser detects brain tumour cells during surgery, http://www.bbc.co.uk/news/health-34041863 (accessed 06/09/2015).
71 L. T. Kerr, H. Byrne and B. M. Hennelly, *Anal. Methods*, 2015, **7**, 5041–52.
72 G. R. Lloyd, L. E. Orr, J. Christie-Brown, K. McCarthy, S. Rose, M. Thomas and N. Stone, *Analyst*, 2013, **138**, 3900–8.
73 F. M. Lyng, D. Traynor, I. R. M. Ramos, F. Bonnier and H. J. Byrne, *Anal. Bioanal. Chem.*, 2015, **407**, 8279-89.
74 Z. Farhane, F. Bonnier, A. Casey and H. Byrne, *Analyst*, 2015, **140**, 4212–23.
75 S. McAughtrie, K. Faulds and D. Graham, *J. Photochem. Photobiol. C Photochem. Rev.*, 2014, **21**, 40–53.
76 D. Graham and R. Goodacre, *Chem. Soc. Rev.*, 2008, **37**, 883–4.
77 R. Stevenson, S. McAughtrie, L. Senior, R. J. Stokes, H. McGachy, L. Tetley, P. Nativo, J. M. Brewer, J. Alexander, K. Faulds and D. Graham, *Analyst*, 2013, **138**, 6331–6.
78 O. Lyandres, N. C. Shah, C. R. Yonzon, T. Walsh, M. R. Glucksberg, R. P. Van Duyne and J. T. W. Jr, 2005, **77**, 6134–9.
79 S. Lee, H. Chon, J. Lee, J. Ko, B. H. Chung, D. W. Lim and J. Choo, *Biosens. Bioelectron.*, 2014, **51**, 238–43.
80 C. L. Zavaleta, B. R. Smith, I. Walton, W. Doering, G. Davis, B. Shojaei, M. J. Natan and S. S. Gambhir, *Proc. Natl. Acad. Sci.*, 2009, **106**, 13511–6.
81 F. Lyng, I. Ramos, O. Ibrahim and H. Byrne, *Appl. Sci.*, 2015, **5**, 23–35.
82 L. L. Ma, M. D. Feldman, J. M. Tam, A. S. Paranjape, K. K. Cheruku, T. A. Larson, J. O. Tam, D. R. Ingram, V. Paramita, J. W. Villard, J. T. Jenkins, T. Wang, G. D. Clarke, R. Asmis, K. Sokolov, B. Chandrasekar, T. E. Milner and K. P. Johnston, *ACS Nano*, 2009, **3**, 2686-96.
83 S. Kumar, N. Harrison, R. Richards-Kortum and K. Sokolov, *Nano Lett.*, 2007, **7**, 1338–43.
84 L. Cognet, C. Tardin, D. Boyer, D. Choquet, P. Tamarat and B. Lounis, *Proc. Natl. Acad. Sci.*, 2003, **100**, 11350–5.
85 H. Ow, D. R. Larson, M. Srivastava, B. A. Baird, W. W. Webb and U. Wiesner, *Nano Lett.*, 2005, **5**, 113–7.
86 L. C. Kennedy, L. R. Bickford, N. A. Lewinski, A. J. Coughlin, Y. Hu, E. S. Day, J. L. West and R. a Drezek, *Small*, 2011, **7**, 169–83.
87 C. Liu, C. C. Mi and B. Q. Li, *IEEE Trans. Nanobioscience*, 2008, **7**, 206–14.
88 C. Loo, A. Lowery, N. Halas, J. West and R. Drezek, *Nano Lett.*, 2005, **5**, 709–11.
89 A. M. Gobin, M. H. Lee, N. J. Halas, W. D. James, R. a Drezek and J. L. West, *Nano*

Lett., 2007, **7**, 1929–34.
90 P. M. Tiwari, K. Vig, V. A. Dennis and S. R. Singh, *Nanomaterials*, 2011, **1**, 31–63.
91 T. A. Erickson and J. W. Tunnell, *Gold Nanoshells in Biomedical Applications*, Wiley-VCH, 2009, Nanomaterials for the Life Science vol. 3., 1-44.
92 M. A. Ochsenku, P. R. T. Jess, H. Stoquert, K. Dholakia, and C. J. Campbell, *ACS Nano*, 2009, **3**, 3613–21.
93 K. M. Fisher and C. J. Campbell, *Biochem. Soc. Trans*, 2014, **42**, 899-904.
94 C. A. R. Auchinvole, PhD Thesis, University of Edinburgh, 2011.
95 C. A. R. Auchinvole, P. Richardson, C. McGuinnes, V. Mallikarjun, K. Donaldson, H. McNab and C. J. Campbell, *ACS Nano*, 2012, **6**, 888–96.
96 J. Jiang, PhD Thesis, University of Edinburgh, 2014.
97 J. Jiang, C. Auchinvole, K. Fisher and C. J. Campbell, *Nanoscale*, 2014, **6**, 12104–10.
98 P. I. T. Thomson, V. L. Camus, Y. Hu and C. J. Campbell, *Anal. Chem.*, 2015, **87**, 4719-25.
99 F. Hirschhaeuser, H. Menne, C. Dittfeld, J. West, W. Mueller-Klieser and L. A. Kunz-Schughart, *J. Biotechnol.*, 2010, **148**, 3–15.
100 H. Page, P. Flood and E. G. Reynaud, *Cell Tissue Res.*, 2013, **352**, 123–31.
101 G. Mehta, A. Y. Hsiao, M. Ingram, G. D. Luker and S. Takayama, *J. Control. Release*, 2012, **164**, 192–204.
102 Y.-C. Tung, A. Y. Hsiao, S. G. Allen, Y. Torisawa, M. Ho and S. Takayama, *Analyst*, 2011, **136**, 473–8.
103 K. Carver, X. Ming and R. L. Juliano, *Mol. Ther. Nucleic Acids*, 2014, **3**, e153.
104 C. R. Thoma, M. Zimmermann, I. Agarkova, J. M. Kelm and W. Krek, *Adv. Drug Deliv. Rev.*, 2014, **69-70**, 29–41.
105 L.-B. Weiswald, D. Bellet and V. Dangles-Marie, *Neoplasia*, 2015, **17**, 1–15.
106 A. S. Mikhail, S. Eetezadi, S. N. Ekdawi, J. Stewart and C. Allen, *Int. J. Pharm.*, 2014, **464**, 168–77.
107 R.-Z. Lin, R.-Z. Lin and H.-Y. Chang, *Biotechnol. J.*, 2008, **3**, 1172–84.
108 F. Pampaloni, N. Ansari and E. H. K. Stelzer, *Cell Tissue Res.*, 2013, **352**, 161–77.
109 H.-G. Kang, J. M. Jenabi, J. Zhang, N. Keshelava, H. Shimada, W. A. May, T. Ng, C. P. Reynolds, T. J. Triche and P. H. B. Sorensen, *Cancer Res.*, 2007, **67**, 3094–105.
110 J. Holtfreter, *J. Exp. Zool.*, 1944, **95**, 171–212.
111 A. Moscona and H. Moscona, *J. Anat.*, 1952, **86**, 287–301.
112 *Using Perfecta3D™ Hanging Drop Plates to Assess Chemosensitivity (White Paper)*, 3D BiomatrixTM, https://3dbiomatrix.com/wp-content/uploads/downloads/2011/11/3D-Biomatrix-White-Paper-Hanging-Drop-Plate.pdf (accessed March 2015).
113 G. Hamilton, *Cancer Lett.*, 1998, **131**, 29–34.
114 A.L. van Wezel, *Nature*, 1967, **216**, 64-65.
115 J. Comley, *Drug Discovery World*, 2010 (summer), 25-41.
116 H. Hardelauf, J.-P. Frimat, J. D. Stewart, W. Schormann, Y.-Y. Chiang, P. Lampen, J. Franzke, J. G. Hengstler, C. Cadenas, L. a Kunz-Schughart and J. West, *Lab Chip*, 2011, **11**, 419–28.
117 L. Le Roux, D. Schellingerhout, A. Volgin, D. Maxwell, K. Ishihara and J. Gelovani, *Microsc. Microanal.*, 2008, **14**, 734–5.
118 R. M. Williams, W. R. Zipfel and W. W. Webb, *Curr. Opin. Chem. Biol.*, 2001, **5**, 603–8.
119 W. R. Zipfel, R. M. Williams and W. W. Webb, *Nat. Biotechnol.*, 2003, **21**, 1369–77.
120 V. E. Centonze and J. G. White, *Biophys. J.*, 1998, **75**, 2015–24.
121 K. König, A. Uchugonova and E. Gorjup, *Microsc. Res. Tech.*, 2011, **74**, 9–17.
122 J. G. Fujimoto, C. Pitris, S. A. Boppart and M. E. Brezinski, *Neoplasia*, 2000, **2**, 9–25.

123 J. Sharpe, *Annu. Rev. Biomed. Eng.*, 2004, **6**, 209–28.
124 J. Sharpe, U. Ahlgren, P. Perry, B. Hill, A. Ross, J. Hecksher-Sørensen, R. Baldock and D. Davidson, *Science*, 2002, **296**, 541–5.
125 M. Sharma, Y. Verma, K. D. Rao, R. Nair and P. K. Gupta, *Biotechnol. Lett.*, 2007, **29**, 273–8.
126 A. Desmaison, C. Lorenzo, J. Rouquette, B. Ducommun and V. Lobjois, *J. Microsc.*, 2013, **251**, 128–32.
127 F. O. Fahrbach, V. Gurchenkov, K. Alessandri, P. Nassoy and A. Rohrbach, 2013, **21**, 1492–1505.
128 O.E. Olarte, J. Andilla, R. Jorand, B. Ducommun, C. Lorenzo and P. Loza-Alvarez, http://www.focusonmicroscopy.org/2013/PDF/392_Olarte.pdf (accessed March 2015).
129 T. Vettenburg, H. I. C. Dalgarno, J. Nylk, C. Coll-Lladó, D. E. K. Ferrier, T. Čižmár, F. J. Gunn-Moore and K. Dholakia, *Nat. Methods*, 2014, **11**, 541–4.
130 R. M. Sutherland, J. A. McCredie and W. R. Inch, *J. Natl. Cancer Inst.*, 1971, **46**, 113–20.
131 T. Nederman, B. Norling, B. Glimelius, J. Carlsson and U. Brunk, *Cancer Res.*, 1984, **44**, 3090–7.
132 W. Y. Ho, S. K. Yeap, C. L. Ho, R. A. Rahim and N. B. Alitheen, *PLoS One*, 2012, **7**, e44640.
133 M. T. Santini, G. Rainaldi and P. L. Indovina, *Crit. Rev. Oncol. Hematol.*, 2000, **36**, 75–87.
134 H. Ma, Q. Jiang, S. Han, Y. Wu, J. C. Tomshine, D. Wang, Y. Gan and G. Zou, *Mol. Imaging*, 2012, **11**, 487–98.
135 G. Hlawacek, V. Veligura, R. van Gastel and B. Poelsema, *J. Vac. Sci. Technol.*, 2014, **32**, 020801.
136 T. Anada, J. Fukuda, Y. Sai and O. Suzuki, *Biomaterials*, 2012, **33**, 8430–41.
137 A. Hunter, A. Hendrikse, M. Renan and R. Abratt, *Apoptosis*, 2006, **11**, 1727–35.
138 H. Harada, *J. Radiat. Res.*, 2011, **52**, 545–56.
139 K. A. Krohn, J. M. Link and R. P. Mason, *J. Nucl. Med.*, 2008, **49**, 129S–48S.
140 G. L. Semenza, *Nat. Rev. Cancer*, 2003, **3**, 721–32.
141 A. J. Varghese, S. Gulyas, J. K. Mohindra and A. Varghese, *Cancer Res.*, 1976, **36**, 3761-5.
142 *HypoxyprobeTM-1 Plus Kit for the Detection of Tissue Hypoxia*, Chemicon International, http://webcache.googleusercontent.com/search?q=cache:8bxU7yy_OUoJ:www.ibrarian.net/navon/paper/HypoxyprobeTM_1_Plus_Kit_for_the_Detection_of_Tis.pdf%3Fpaperid%3D4633961+&cd=5&hl=en&ct=clnk&gl=uk (accessed March 2015).
143 J. A. Raleigh, G. G. Miller, A. J. Franko, C. J. Koch, A. F. Fuciarelli and D. A. Kelly, *Br. J. Cancer*, 1987, **56**, 395–400.
144 J. D. Chapman, A. J. Franko and J. Sharplin, *Br. J. Cancer*, 1981, **43**, 546–50.
145 J. D. Chapman, K. Baer and J. Lee, *Cancer Res.*, 1983, **43**, 1523–8.
146 A. J. Franko and C. J. Koch, *Int. J. Radiation Oncology Biol. Phys.*, 1984, **10**, 1333-6.
147 A. J. Varghese and G. F. Whitmore, *Int. J. Radiation Oncology Biol. Phys.*, 1984, **10**, 1341–5.
148 J. A. Raleigh, A. J. Franko, C. J. Koch and J. L. Born, *Br. J. Cancer*, 1985, **51**, 229–35.
149 R. C. Urtasun, C. J. Koch, a J. Franko, J. a Raleigh and J. D. Chapman, *Br. J. Cancer*, 1986, **54**, 453–7.
150 J. A. Raleigh, D. P. Calkins-adams, L. H. Rinker, C. A. Ballenger, M. C. Weissler, W. C. Fowler, D. B. Novotny and M. A. Varia, *Cancer Res.*, 1998, **58**, 3765–8.
151 W. Fayad, L. Rickardson, C. Haglund, M. H. Olofsson, P. D'Arcy, R. Larsson, S. Linder and M. Fryknäs, *Chem. Biol. Drug Des.*, 2011, **78**, 54771.

152 B. Bourrat-Floeck, K. Groebe and W. Mueller-Klieser, *Int. J. Cancer*, 1991, **47**, 792–99.
153 R. I. Dmitriev, A. V. Kondrashina, K. Koren, I. Klimant, A. V. Zhdanov, J. M. P. Pakan, K. W. McDermott and D. B. Papkovsky, *Biomater. Sci.*, 2014, **2**, 853-66.
154 H. Koo, M. S. Huh, J. H. Ryu, D.-E. Lee, I.-C. Sun, K. Choi, K. Kim and I. C. Kwon, *Nano Today*, 2011, **6**, 204–20.
155 D. Rotin, D. Steele-Norwood, S. Grinstein and I. Tannock, *Cancer Res.*, 1989, **49**, 205–11.
156 S. Walenta, J. Doetsch, W. Mueller-Klieser and L. A. Kunz-Schughart, *J. Histochem. Cytochem.*, 2000, **48**, 509–22.
157 A. Jaworska, L. E. Jamieson, K. Malek, C. J. Campbell, J. Choo, S. Chlopicki and M. Baranska, *Analyst*, 2014, **140-**, 2321-9.
158 S. W. Bishnoi, C. J. Rozell, C. S. Levin, M. K. Gheith, B. R. Johnson, D. H. Johnson and N. J. Halas, *Nano Lett.*, 2006, **6**, 1687–92.
159 J. Kneipp, H. Kneipp, B. Wittig and K. Kneipp, *Nano Lett.*, 2007, **7**, 2819-23.
160 J. Kneipp, H. Kneipp, B. Wittig and K. Kneipp, *J. Phys. Chem. C*, 2010, **114**, 7421–6.
161 M. A. Ochsenkuehn, P. R. T. Jess, H. Stoquert, K. Dholakia and C. J. Campbell, *ACS Nano*, 2009, **3**, 3613–21.
162 L. E. Jamieson, A. Jaworska, J. Jiang, M. Baranska, D. J. Harrison and C. J. Campbell, *Analyst*, 2015, **140**, 2330-5.
163 J. Alvarez-Pérez, P. Ballesteros and S. Cerdán, *MAGMA*, 2005, **18**, 293–301.
164 J. Z. Zhang, N. S. Bryce, R. Siegele, E. A Carter, D. Paterson, M. D. de Jonge, D. L. Howard, C. G. Ryan and T. W. Hambley, *Integr. Biol. (Camb).*, 2012, **4**, 1072–80.
165 K. M. Comerford, T. J. Wallace, J. Karhausen, M. D. R. Gene, N. A. Louis, M. C. Montalto and S. P. Colgan, *Cancer Res.*, 2002, **62**, 3387–94.
166 R. L. Camp, G. G. Chung and D. L. Rimm, *Nat. Med.*, 2002, **8**, 1323–8.
167 N.-C. Cheng, S. Wang and T.-H. Young, *Biomaterials*, 2012, **33**, 1748–58.
168 J. M. Lee, P. Mhawech-Fauceglia, N. Lee, L. C. Parsanian, Y. G. Lin, S. A. Gayther and K. Lawrenson, *Lab. Invest.*, 2013, **93**, 528–42.
169 P. M. Tiwari, K. Vig, V. A. Dennise and S. R. Singh, *Nanomaterials*, 2011, **1**, 31-63.
170 E. Salomonnson, A. C. Stacer, A. Ehrlich, K. E. Luker and G. D. Luker, *PLoS One*, 2013, **8**, e51500.
171 K. McMahon, PhD Thesis, University of Bradford, 2011.
172 R. J. A. Goodwin, S. R. Pennington and A. R. Pitt, *Proteomics*, 2008, **8**, 3785–800.
173 M. Stoeckli, P. Chaurand, D. E. Hallahan and R. M. Caprioli, *Nat. Med.*, 2001, **7**, 493–6.
174 M. C. Djidja, E. Claude, M. F. Snel, P. Scriven, S. Francese, V. Carolan and M. R. Clench, *J. Proteome Res.*, 2009, **8**, 4876–84.
175 R. J. A. Goodwin, A. R. Pitt, D. Harrison, S. K. Weidt, P. R. R. Langridge-Smith, M. P. Barrett and C. Logan MacKay, *Rapid Commun. Mass Spectrom.*, 2011, **25**, 969–72.
176 E. Zuser, PhD Thesis, Northeastern University, 2013.
177 D. R. Ahlf, R. N. Masyuko, A. B. Hummon and P. W. Bohn, *Analyst*, 2014, **139**, 4578–5.
178 B. G. Reid, T. Jerjian, P. Patel, Q. Zhou, B. H. Yoo, P. Kabos, C. A. Sartorius and D. V Labarbera, *Curr. Chem. genomics Transl. Med.*, 2014, **8**, 27–35.
179 R. An, D. Merrill, L. Avramova, J. Sturgis, M. Tsiper, J. P. Robinson, J. Turek and D. D. Nolte, *J. Biomol. Screen.*, 2014, **19**, 526–37.
180 J. S. Basuki, H. T. T. Duong, A. Macmillan, R. B. Erlich, L. Esser, M. C. Akerfeldt, R. M. Whan, M. Kavallaris, C. Boyer and T. P. Davis, *ACS Nano*, 2013, **7**, 10175–89.
181 X. Liu, E. M. Weaver and A. B. Hummon, *Anal. Chem.*, 2013, **85**, 6295-302.
182 A. D. Leeper, J. Farrell, L. J. Williams, J. S. Thomas, J. M. Dixon, S. E. Wedden, D. J. Harrison and E. Katz, *Biomaterials*, 2012, **33**, 907–15.

183 G. Frens, *Nat. Phys. Sci.*, 1973, **241**, 20.
184 A. Jaworska, T. Wojcik, K. Malek, U. Kwolek, M. Kepczynski, A. A. Ansary, S. Chlopicki and M. Baranska, *Microchim. Acta*, 2014, **182**, 119-27.
185 C. A. R. Auchinvole, P. Richardson, C. McGuinnes, V. Mallikarjun, K. Donaldson, H. McNab and C. J. Campbell, *ACS Nano,* 2012, **6**, 888-96.
186 J.-H. Pai, T. Liu, H.-Y. Hsu, A. B. Wedding, B. Thierry and P. O. Bagnaninchi, *RSC Adv.*, 2014, **4**, 27067-73.
187 K. Fisher, PhD Thesis, University of Edinburgh, 2015.
188 J. Notte, B. Ward, N. Economou, R. Hill, R. Percival, L. Farkas and S. McVey, *AIP Conf. Proc.*, 2007, **931**, 489–96.
189 M. S. Joens, C. Huynh, J. M. Kasuboski, D. Ferranti, Y. J. Sigal, F. Zeitvogel, M. Obst, C. J. Burkhardt, K. P. Curran, S. H. Chalasani, L. A. Stern, B. Goetze and J. A. J. Fitzpatrick, *Sci. Rep.*, 2013, **3**, 3514.
190 A. Yaromina, T. Hölscher, W. Eicheler, A. Rosner, M. Krause, F. Hessel, C. Petersen, H. D. Thames, M. Baumann and D. Zips, *Radiother. Oncol.*, 2005, **76**, 206–12.
191 L. Y. T. Chou, K. Ming and W. C. W. Chan, *Chem. Soc. Rev.*, 2011, **40**, 233–45.
192 G. Levkowitz, H. Waterman, E. Zamir, Z. Kam, S. Oved, W. Y. Langdon, L. Beguinot, B. Geiger and Y. Yarden, *Genes Dev.*, 1998, **12**, 3663–74.
193 A. Salvati, C. Åberg, T. dos Santos, J. Varela, P. Pinto, I. Lynch and K. A. Dawson, *Nanomedicine*, 2011, **7**, 818–26.
194 D. Guarnieri, O. Muscetti, A. Falanga, S. Fusco, V. Belli, E. Perillo, E. Battista, V. Panzetta, S. Galdiero and P. A. Netti, *Nanotechnology*, 2015, **26**, 415101.
195 B. S. Murty, P. Shankar, B. Raj, B. B. Rath and J. Murday, *Textbook of Nanoscience and Nanotechnology*, Springer Science & Business Media, 2013, 153.
196 B. D. Ratner, A. S. Hoffman, F. J. Schoen and J. E. Lemons, *Biomaterials Science: An Introduction to Materials in Medicine*, Academic Press, 3rd edn., 2012, 468.
197 A. Bonifacio, S. Dalla Marta, R. Spizzo, S. Cervo, A. Steffan, A. Colombatti and V. Sergo, *Anal. Bioanal. Chem.*, 2014, **406**, 2355–65.
198 H. Z. Yu, N. Xia and Z. F. Liu, *Anal. Chem.*, 1999, **71**, 1354–8.
199 K. L. Nowak-Lovato and K. D. Rector, *Int. J. Anal. Chem.*, 2012, **2012**, 390182-98.
200 K. L. Nowak-Lovato and K. D. Rector, *Microsc. Microanal.*, 2009, **15**, 52–53.
201 K. Kim, K. L. Kim, D. Shin, J. Choi and K. S. Shin, *J. Phys. Chem.*, 2012, **116**, 4774-9.
202 Z. Wang, A. Bonoiu, M. Samoc, Y. Cui and P. N. Prasad, *Biosens. Bioelectron.*, 2008, **23**, 886–91.
203 M. E. Aulton and K. Taylor, *Aulton's Pharmaceuticals: The Design and Manufacture of Medicines*, Elsevier Health Sciences, illustrate., 2013, 41-5.
204 H. Sigel, *Metal Ions in Biological Systems: Volume 37: Manganese and Its Role in Biological Processes*, CRC Press, 2000, 308.
205 Boltzmann, http://www.originlab.com/doc/Origin-Help/Boltzmann-FitFunc (accessed 07/09/2015).
206 A. Cusano, F. J. Arregui, Mi. Giordano and A. Cutolo, Eds., *Optochemical Nanosensors*, CRC Press, 2012, 430.
207 M. A. Hernandez and A. Rathinavelu, *Basic Pharmacology: Understanding Drug Actions and Reactions*, illustrate., 2006, 47-52.
208 C.-C. Lin and C.-W. Chang, *Biosens. Bioelectron.*, 2014, **51**, 297–303.
209 L. Y. Xue, S. M. Chiu and N. L. Oleinick, *Exp. Cell Res.*, 2003, **283**, 135–45.
210 L. M. Mooney, K. A. Al-Sakkaf, B. L. Brown and P. R. M. Dobson, *Br. J. Cancer*, 2002, **87**, 909–17.
211 L. Poliseno, L. Bianchi, L. Citti, S. Liberatori, L. Mariani, A. Salvetti, M. Evangelista,

L. Bini, V. Pallini and G. Rainaldi, *Biochem. J.*, 2004, **379**, 823–32.
212 M. Butler, *Animal Cell Culture and Technology*, Garland Science, 2nd edn., 2003, 34-38.
213 G. Mor and A. Alvero, Eds., *Apoptosis and Cancer: Methods and Protocols*, illustrate., 2007, 95-7.
214 J. J. Lemasters and A.-L. Nieminen, *Mitochondria in Pathogenesis*, Springer Science & Business Media, illustrate., 2007, 29.
215 J. T. Kumpulainen and J. T. Salonen, *Natural Antioxidants and Anticarcinogens in Nutrition, Health and Disease*, Elsevier, 1999, 63-5.
216 P. F. Davies, *Physiol. Rev.*, 1995, **75**, 519–60.
217 E. Crimi, F. S. Taccone, T. Infante, S. Scolletta, V. Crudele and C. Napoli, *J. Crit. Care*, 2012, **27**, 108–18.
218 F. B. Loiselle and J. R. Casey, *Membrane Transporters in Drug Discovery and Development, Methods in Molecular Biology*, Springer Science & Business Media, 2010, vol 637.
219 A. V. Zayats and D. Richards, *Nano-optics and Near-field Optical Microscopy*, Artech House, 2009, 204.
220 J. Cheng, W. Tang, Z. Su, J. Guo, L. Tong and Q. Wei, *Cancer Lett.*, 2011, **321**, 169–78.
221 Z. Jin, L. Pei and D. Wang, *Zhonghua Fu Chan Ke Za Zhi*, 2000, **35**, 657–9.
222 The University of Texas at Austin, *Plasmonic Nanoparticles for Imaging Intracellular Biomarkers*, ProQuest, 2007, 20-5.
223 W. J. Albery, M. G. Boutelle, P. J. Colby, A. R. Hillman, *J. Electroanal. Chem. Interfacial Electrochem.*, 1982, **133**, 135-45.
224 M. Ekkapongpisit, A. Giovia, C. Follo, G. Caputo and C. Isidoro, *Int. J. Nanomedicine*, 2012, **7**, 4147–58.
225 R. R. Sathuluri, H. Yoshikawa, E. Shimizu, M. Saito and E. Tamiya, *PLoS One*, 2011, **6**, e22802.
226 J. Huang, C. Zong, H. Shen, M. Liu, B. Chen, B. Ren and Z. Zhang, *NanoSmallMicro*, 2012, **10**, 2577–84.
227 C. Zhou, T.-H. Tsai, D. C. Adler, H.-C. Lee, D. W. Cohen, A. Mondelblatt, Y. Wang, J. L. Connolly and J. G. Fujimoto, *Opt. Lett.*, 2010, **35**, 700–2.
228 M. C. Skala, M. J. Crow, A. Wax and J. A. Izatt, *Nano Lett.*, 2009, **8**, 73461-7.
229 A. K. Varkouhi, M. Scholte, G. Storm and H. J. Haisma, *J. Control. Release*, 2011, **151**, 220–8.
230 Z. Feng, *Cold Spring Harb. Perspect. Biol.*, 2010, **2**, a001057.
231 S. Febvay, D. M. Marini, A. M. Belcher and D. E. Clapham, *Nano Lett.*, 2010, **10**, 2211–9.
232 P. Nativo, I. A. Prior and M. Brust, *ACS Nano*, 2008, **2**, 1639–44.
233 R. Lévy, U. Shaheen, Y. Cesbron and V. Sée, *Nano Rev.*, 2010, **1**,4889-917.
234 K. Boeneman, J. B. Delehanty, J. B. Blanco-Canosa, K. Susumu, M. H. Stewart, E. Oh, A. L. Huston, G. Dawson, S. Ingale, R. Walters, M. Domowicz, J. R. Deschamps, W. R. Algar, S. Dimaggio, J. Manono, C. M. Spillmann, D. Thompson, T. L. Jennings, P. E. Dawson and I. L. Medintz, *ACS Nano*, 2013, **7**, 3778–96.
235 T. Kong, J. Zeng, J. Yang, Y. Yao, X. Wang, P. Li, A. Yang, W. Roa, J. Xing, J. Chen, "Surface modifications of gold-nanoparticles to enhance radiation cytotoxicity", in *Life Science Systems and Applications Workshop, 2007, LISA 2007, IEEE/NIH*, 2658, 8-9 Nov. 2007.
236 G. F. Kelso, C. M. Porteous, C. V. Coulter, G. Hughes, W. K. Porteous, E. C. Ledgerwood, R. A. J. Smith and M. P. Murphy, *J. Biol. Chem.*, 2001, **276**, 4588–96.
237 R. A. Smith and M. P. Murphy, *Discov. Mediicine*, 2011, **11**, 106–14.

Appendix 1

Redox Calibrations

Figure A1.1 shows spectral changes of NQ-NPs in response to redox potential applied by spectroelectrochemistry (a) and calibration of NQ-NPs by spectroelectrochemistry (b) carried out by Auchinvole.[94]

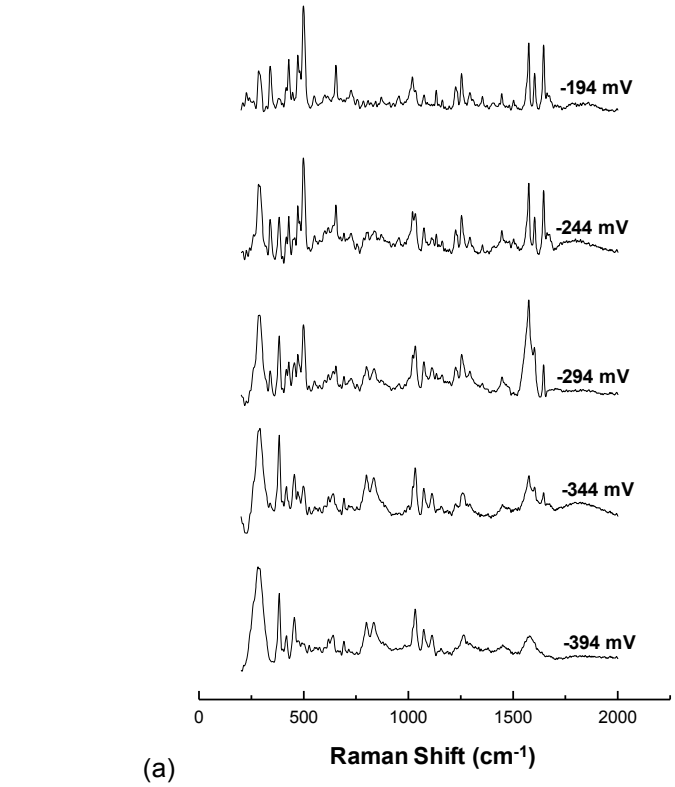

(a)

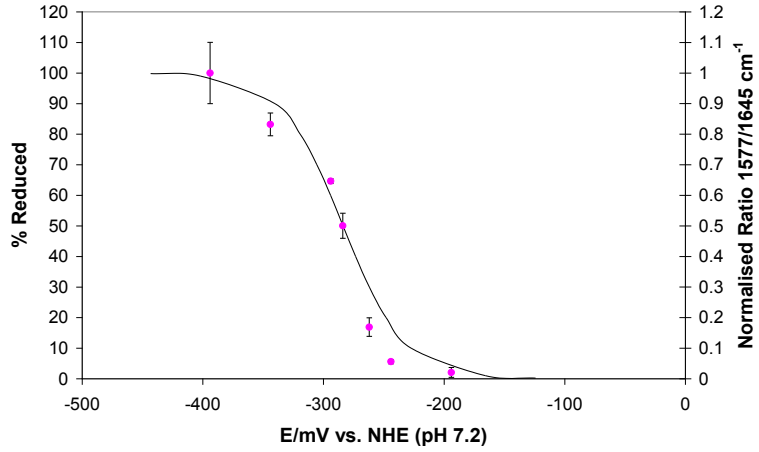

(b)

Figure A1.1 (a) illustrates the change in the SERS spectrum of NQ as measured by spectroelectrochemistry and (b) illustrates the calibration curve for NQ generated using this data (acquired by and sourced from Auchinvole[94]).

Equations A1.1 and A1.2 were determined from calibration experiments for NQ-NPs to allow redox potential determination from an unknown ratio of signal intensity at approximately 1635 cm^{-1} to that at approximately 1580 cm^{-1} (Ratio).[94] Equations A1.3 and A1.4 were determined from calibration experiments for AQ-NPs to allow redox potential determination from an unknown ratio of signal intensity at approximately 1670 cm^{-1} to that at approximately 1600 cm^{-1} (Ratio).[96]

$$\frac{\left[\frac{\text{Ratio}}{5.45}\right] - 0.17}{0.83} = \text{Fraction reduced (between 0 and 1)} \quad \text{(A1.1)}^{94}$$

$$\text{E} = -283 - 29.188\left(\log\frac{\text{Fraction reduced}}{\text{Fraction oxidised}}\right) \text{ (in mV)} \quad \text{(A1.2)}^{94}$$

$$\frac{1.413 - \text{Ratio}}{1.034} = \text{Fraction reduced (R)} \quad \text{(A1.3)}^{96}$$

$$E = -217 + \left((-442)\times R\right) + (1626\times R^2) + \left((-3954)\times R^3\right) + (4143\times R^4) + ((-1584)\times R^5) \text{ (in mV)} \quad \text{(A1.4)}^{96}$$

Appendix 2

Poster

Presented at CLIRSPEC Summer School, Lake District, July 2015

Measuring Redox Potential in 3D Breast Cancer Tumour Models using SERS Nanosensors

L. Jamieson[1], K. Fischer[1], J. Jiang[1], A. Bell[2], P. Bagnaninchi[3], A. Jaworska[4], D. Harrison[4], C. Campbell[1]

[1]School of Chemistry, University of Edinburgh, Joseph Black Building, West Mains Road, Edinburgh, EH9 3JJ
[2]Trinity College Dublin, CRANN
[3]MRC Centre for Regenerative Medicine, Chancellor's Building, 49 Little France Crescent, Edinburgh, EH16 4SB
[4]Faculty of Chemistry, Jagiellonian University, 3 Ingardena Str. 30-060 Krakow, Poland
[5]Medical and Biological Sciences Building, University of St Andrews, North Haugh, St Andrews, Fife, KY16 9TF

Background

Intracellular Redox Potential

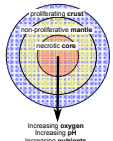

Figure 1 The Tumour Microenvironment' Tumour and multicellular tumour spheroid (MTS) organisation of cells and developing gradients.

- Intracellular redox potential is **highly regulated** by a number of species and redox couples in the cell.
- Intracellular redox potential is important for the regulation of numerous cellular processes and its disregulation is implicated in numerous diseases.
- **The Tumour Microenvironment** refers to the biological environment that exists within a tumour (Figure 1).
  - ➢ The central regions of cancer tumours have poor vasculature and thus poor supply of oxygen and other nutrients.
  - ➢ The **hypoxic** central regions tend to be resistant to therapy.

Surface Enhanced Raman Scattering (SERS) Nanosensors

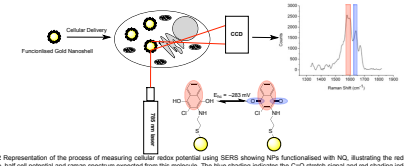

Figure 2 Representation of the process of measuring cellular redox potential using SERS showing NPs functionalised with NQ, illustrating the reduced and oxidised forms of the molecule, half cell potential and raman spectrum expected from this molecule. The blue shading indicates the C=O stretch signal and red shading indicates the ring breathing signal.

- Gold nanoparticles (NPs) are functionalised with redox active molecules and delivered to cells (Figure 2).
- Characteristic raman signals change in ratio as a result of degree of oxidation/reduction in their environment.

Figure 3 Raman Spectrometer

- From this ratio fraction of redox active signalling molecules reduced and oxidised can be determined and translated into a redox potential value.

From Monolayer to MTS - Cell Morphology

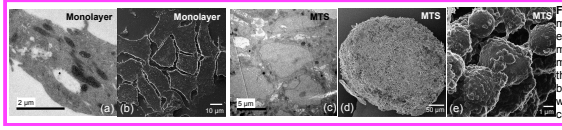

Figure 4 compares MCF7 cell morphology in monolayer culture and MTS using transmission electron microscopy (TEM) and helium ion microscopy (HIM). The flat nature of cells in monolayer culture primarily in contact with the surface they were growing on and the culture media is shown by TEM (a) and HIM (b) and the 3D nature of MTS with cell-cell and cell-extracellular matrix (ECM) contacts is shown by TEM (c) and HIM (d and e).

From Monolayer to MTS - SERS

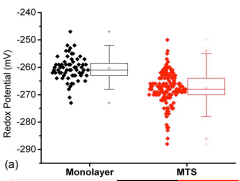

	NQ-NPs monolayer	NQ-NPs MTS
n	6	141
Mean (mV)	−260	−268
Standard Deviation (mV)	4.5	5.9
Maximum (mV)	−247	−250
Q3 (mV)	−259	−264
Median (mV)	−261	−268
Q1 (mV)	−263	−270
Minimum (mV)	−273	−288

(b)

Figure 8 compares mean intracellular redox potential obtained from cells incubated with NQ-NPs in monolayer culture and MTS. A one way ANOVA confirmed that the means were significantly different at the 0.05 level with MTS having a more reductive potential as expected. Standard deviation was also larger for MTS. Results are compared by boxplot in (a) and statistics are displayed in the table in (b).

Delivering Nanosensors to Cells

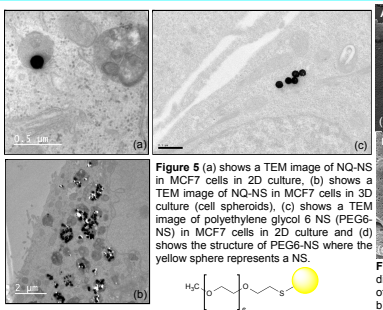

Figure 5 (a) shows a TEM image of NQ-NS in MCF7 cells in 2D culture, (b) shows a TEM image of NQ-NS in MCF7 cells in 3D culture (cell spheroids), (c) shows a TEM image of polyethylene glycol 6 NS (PEG6-NS) in MCF7 cells in 2D culture and (d) shows the structure of PEG6-NS where the yellow sphere represents a NS.

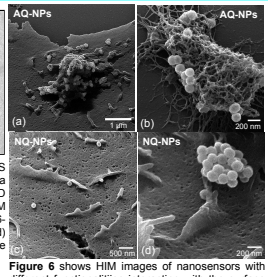

Figure 6 shows HIM images of nanosensors with different functionalitiies interacting with the surface of MCF7 cells in monolayer culture. AQ-NPs (a and b) are more hydrophobic and appear to aggregate more, with some present in what appears to be ECM (b). NQ-NPs (c and d) appear to be more disperse and less aggregated.

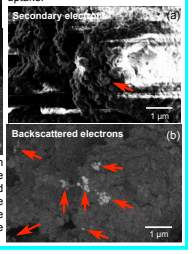

Figure 7 shows scanning electron microscopy (SEM) images of regions of MTS imaged with secondary electrons (a) and backscattered electrons (b). Red arrows point out regions where NPs were detected, confirming uptake.

Measuring Intracellular pH using SERS

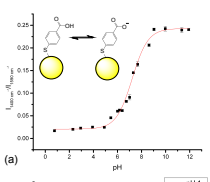

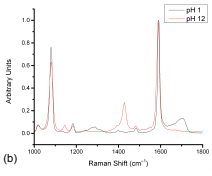

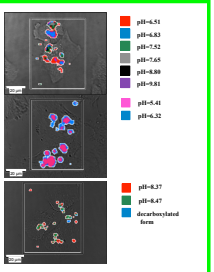

Figure 9 (a) illustrates the equilibrium between protonated and deprotonated paramercaptobenzoic acid (pMBA) functionalised NPs and the calibration curve for this sensor, (b) illustrates the SERS spectra of pMBA-NPs at high and low pH and (c) shows intracellular maps of pH measured by SERS under different extracellular buffers.

Multiplexing Intracellular pH and Redox Measurements

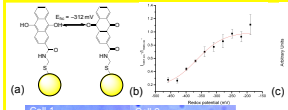

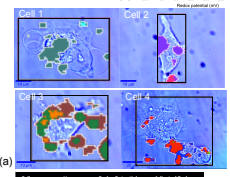

Cell	pH (Colour)	Redox Potential (mV) (Colour)	Adjusted Redox Potential (mV) (Colour)
1	7.1 (turquoise)	−308 (cyan)	−307 (cyan)
2	6.9 (purple)	−258 (pink)	−245 (pink)
3	7.0 (green)	−276 (yellow) −345 (brown)	−272 (yellow) −332 (brown)
4	7.1 (light green)	−337 (blue) −306 (red)	−320 (blue) −300 (red)

(d)

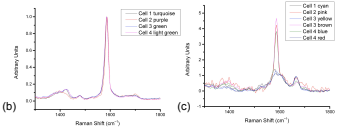

Figure 10 (a) illustrates the equilibrium between oxidised and reduced AQ-NPs, (b) illustrates the calibration curve for this redox sensor and (c) shows the SERS spectra of AQ-NPs at oxidising and reducing redox potentials.

Figure 11 (a) shows intracellular maps of pH and redox measured by SERS using pMBA-NPs and AQ-NPs. Cluster analsis was used to analyse mapped cells and gave one cluster in each case used to determine intracellular pH (spectra for each cell shown in (b)) and an additional one or two clusters used to determine intracellular redox potential (spectra for each cell shown in (c)). Calculated pH, redox potential and adjusted redox potential for each cell are tabulated in (d).

Conclusions and Further Work

- Cell morphology was compared between monolayer culture and MTS using TEM and HIM.
- Nanosensors were successfully delivered to cells in MTS.
- Mean redox potential was significantly difference between monolayer culture and MTS.
- A SERS pH sensor was used to map intracellular pH in live cells.
- Intracellular pH and redox potential were measured simultaneously using SERS.

Future work:

Figure 12 illustrates the next step for the work - to establish a quantitative picture of the changes in redox potential and pH in MTS and use this to guide drug and therapy development as well as monitor response to drugs and therapy.

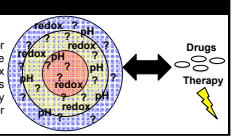

G.A.R. Auchinvole, P. Richardson, C. McGuinness, V. Mallikarjun, K. Donaldson, H. McNab and C. J. Campbell, ACS Nano, 2012, 6, 888-896.
M.A. Ochsner, P.R. Richardson, T. Bosquet, K. Dholakia and C. J. Campbell, ACS Nano, 2009, 3, 3613-3621.
D.W. Bishnoi, C.J. Rosell, C.S. Levin, M.K. Gheith, S.R. Johnson, D.H. Johnson and N.J. Halas, Nano Lett., 2006, 6, 1687-1692.
S.E. Jamieson, D.J. Harrison and C.J. Campbell, Analyst, 2015 (DOI: 10.1039/c5an00224h).
R.-Z. Lin and H.-Y. Chang, Biotechnol. J., 2008, 3, 1172-1184.
A. Jaworska, L.E. Jamieson, K. Malek, C.J. Campbell, J. Choo, S. Chlopicki and M. Baranska, Analyst, 2015, 140, 2321-2329.
L.E. Jamieson, A. Jaworska, J. Jiang, M. Baranska, D.J. Harrison and C.J. Campbell, Analyst, 2015, 140, 2330-2335.
J. Jiang, C. Auchinvole, K. Fisher and C.J. Campbell, Nanoscale, 2014, 6, 12104-12110.
L.E. Jamieson, A.F. Bell, D.J. Harrison and C.J. Campbell, SPIE Biophotonics South America Proceedings, 2015.

Analyst

TUTORIAL REVIEW

View Article Online
View Journal | View Issue

CrossMark click for updates

Cite this: *Analyst*, 2015, **140**, 3910

Chemical analysis of multicellular tumour spheroids

L. E. Jamieson,[a] D. J. Harrison[b] and C. J. Campbell*[a]

Conventional two dimensional (2D) monolayer cell culture has been considered the 'gold standard' technique for *in vitro* cellular experiments. However, the need for a model that better mimics the three dimensional (3D) architecture of tissue *in vivo* has led to the development of Multicellular Tumour Spheroids (MTS) as a 3D tissue culture model. To some extent MTS mimic the environment of *in vivo* tumours where, for example, oxygen and nutrient gradients develop, protein expression changes and cells form a spherical structure with regions of proliferation, senescence and necrosis. This review focuses on the development of techniques for chemical analysis of MTS as a tool for understanding *in vivo* tumours and a platform for more effective drug and therapy discovery. While traditional monolayer techniques can be translated to 3D models, these often fail to provide the desired spatial resolution and *z*-penetration for live cell imaging. More recently developed techniques for overcoming these problems will be discussed with particular reference to advances in instrument technology for achieving the increased spatial resolution and imaging depth required.

Received 16th March 2015,
Accepted 23rd April 2015

DOI: 10.1039/c5an00524h

www.rsc.org/analyst

Open Access Article. Published on 23 April 2015. Downloaded on 04/09/2015 14:19:06.
This article is licensed under a Creative Commons Attribution 3.0 Unported Licence.

Introduction

Cell culture is used to study all aspects of cellular characteristics and function and for *in vitro* testing of drug candidates and therapies. Conventionally cells are cultured on a flat surface in a petri dish or flask where their primary physical contacts are with the substrate on which they are growing and the culture medium surrounding them, with very little cell–cell interaction.[1] This suffers from the major drawback that the cells are not in a realistic physiological environment. *In vivo*, cells are in a 3D environment with the major physical contact being cell–cell interactions with surrounding cells, and cell–matrix interactions with the extracellular matrix (ECM). This 3D environment introduces complexity that is not observed in traditional monolayer cell culture. As a result, drugs and disease therapies that prove effective in the monolayer cell culture models often fail to carry this efficacy forward into *in vivo* trials.[2] While tissue explants grown in culture provide a step between monolayer cell culture and the *in vivo* environ-

[a]*EaStCHEM, School of Chemistry, University of Edinburgh, Edinburgh, EH9 3JJ, UK. E-mail: colin.campbell@ed.ac.uk*
[b]*Medical and Biological Sciences Building, University of St Andrews, North Haugh, St Andrews, Fife KY16 9TF, UK*

L. E. Jamieson

Lauren Jamieson graduated with a BSc (Hons) in Chemistry with Medicinal Chemistry in 2012 from the University of St Andrews. She subsequently started her PhD at the University of Edinburgh under the supervision of Dr Colin Campbell and Prof. David Harrison. Her research focuses on using SERS nanosensors to measure redox potential and pH in multicellular tumour spheroids (MTS).

D. J. Harrison

David Harrison is a clinician with an interest in cellular determinants of response to injury and quantitative systems biology application in pathology. He is Professor of Pathology in University of St Andrews, with an honorary professorship in University of Edinburgh, and he is Director of Laboratory Medicine in Edinburgh overseeing clinical provision in four hospitals. He chairs the steering group of the Framework 7 concerted action CASyM, drawing up the roadmap for implementation of systems medicine in Europe.

This journal is © The Royal Society of Chemistry 2015

Open Access Article. Published on 23 April 2015. Downloaded on 04/09/2015 14:19:06.
This article is licensed under a Creative Commons Attribution 3.0 Unported Licence.

ment, access to such samples is limited. There is therefore a need for an *in vitro* model of tumour biology that mimics better the 3D environment that exists *in vivo* without the added ethics, health, safety, cost and availability limitations encountered when using animal models or explanted tissue.

Multicellular tumour spheroids (MTS) have become increasingly used for the study of cell function and testing of drugs as they satisfy the requirement for a more complex and physiologically relevant cell culture model. Attempts have been made to incorporate cells of different types, for example by mixing cancer cell lines with non-malignant fibroblast or other stromal cells.[2,3] In particular MTS are used as an *ex vivo* model of cancer. Importantly, the blood supply to many cancers *in vivo* is poor due to rapidly proliferating cells producing cellular masses where the centre regions may be far from the well organised vasculature of the body. Cancer cells are capable of signalling for the formation of new blood vessels *via* proteins such as vascular endothelial growth factor (VEGF),[4] however the resulting vasculature is disorganised and leaky so does not effectively deliver oxygen and nutrients to the tumour. As a result, concentration gradients develop in factors including oxygen, nutrients and pH (Fig. 1).[5] The concentration gradients developed *in vivo* are mimicked by MTS where a radial structure develops with a core that is frequently necrotic, surrounding quiescent cells and an outer proliferating layer (Fig. 1).[6]

The microenvironments[4] that develop in cancer give rise to local heterogeneity in aspects including gene expression and regulation; cell differentiation, proliferation, viability and death; drug metabolism; and response to stimuli (Fig. 1).[8] This combination of factors leads to increased complexity when considering drug and therapy treatments *in vivo* compared to simple monolayer cell culture assays. For example, increased resistance to cytotoxic drugs and ionising radiation *in vivo* may be a direct consequence of the microenvironment that develops.[5,9] This makes the use of MTS in drug and therapy development increasingly important as they mimic better the *in vivo* environment in comparison to traditional monolayer culture models. This review brings together the current techniques and enabling technologies for chemical analysis of various characteristics of MTS. It summarises the latest technologies being used to improve analysis of MTS as an important model of tumour biology highlighting where there is room for improvement in chemical, spatial and temporal resolution.

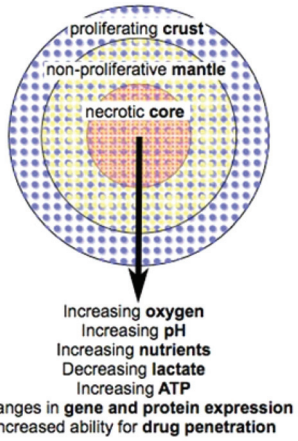

Fig. 1 MTS organisation and radial changes that are established or predicted (adapted from Lin R. *et al.*[7]).

Methods for growing MTS

A variety of techniques have been developed for the formation of MTS. The basic requirement for MTS formation is that adhesions between cells is stronger than that between cells and the substrate they are grown on.[7] The first examples of multicellular spheroid growth were performed by Holtfreter[10] who was studying gastrulation, and Moscona and Moscona[11] who demonstrated the aggregation of isolated chick chondrogenic and myogenic cells.[5] These initial studies formed non-tumour multicellular spheroids with the advantage that they better mimic the *in vivo* 3D environment. While this review focuses on MTS as an *in vitro* cancer tumour model, techniques discussed are equally applicable to non-tumour spheroids and organoids.

Depending on the culture technique and cell type employed, spheroids are formed in varying quantities, over various time periods and with varying degrees of homogeneity and the particular technique used is likely to be guided by the particular application being employed. For example, using spinner flasks allows large quantities of MTS to be formed but these often lack homogeneity while using the hanging drop technique allows much more homogenous and uniform MTS formation but is difficult to perform on a large scale.[1,7]

Fig. 2 illustrates some of the techniques employed for MTS formation.

C. J. Campbell

Colin Campbell is Director of the EPSRC and MRC CDT in Optical Medical Imaging and a Senior Lecturer in the School of Chemistry at the University of Edinburgh. He works exclusively at the interface with biology and medicine. His interest is primarily in understanding the role of redox processes in determining phenotype and his research primarily focuses on developing new biophysical techniques to measure cellular redox states and developing new approaches to analyse, visualize and interpret redox biology in cells and tissues.

Open Access Article. Published on 23 April 2015. Downloaded on 04/09/2015 14:19:06.
This article is licensed under a Creative Commons Attribution 3.0 Unported Licence.

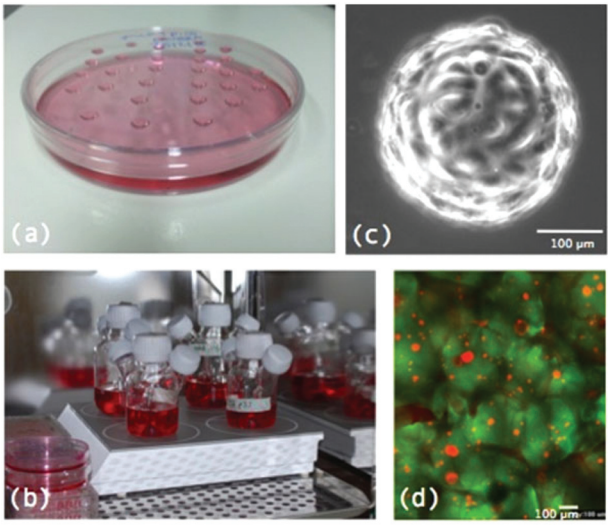

Fig. 2 Examples of methods of MTS formation: (a) MTS being grown using the basic hanging drop technique, (b) MTS growing in spinner flasks, (c) MTS being grown on microcarrier beads and (d) cells (red) growing in a scaffold of alginate gel (green), an example of the start of MTS growth in a scaffold of NovaMatrix-3D™.

Spontaneous aggregation

The simplest method for the formation of MTS is spontaneous aggregation, where the cells spontaneously cluster to form cell aggregates that grow in 3D. Technically these are cell aggregates rather than MTS and only a few cell lines grow in this way – MDA-MB-435 human breast cancer cells being one example.[1] Due to these limitations, a variety of other more complex methods have been developed.

Hanging drop

In its simplest form, the hanging drop methods involves growing MTS from drops of cell suspension in culture media suspended from the lid of a petri dish (Fig. 2a). Cells aggregate in the drops which remain in place by surface tension and then grow into MTS.[7] More recent technologies have developed multiwell plates for the growth of MTS using the hanging drop method including the Perfecta3D™ Hanging Drop Plates[12] where the new design allows for easier treatment, media exchange and handling of the MTS. Growing MTS using this method allows for the formation of MTS of uniform size although it is difficult to culture large numbers of MTS in this way.[13]

Gyratory methods and spinner flasks

A popular method for formation of large numbers of MTS is the spinner flask method (Fig. 2b). This involves putting a suspension of cells in media into a flask which is constantly kept stirring. Due to the constant motion, cells are not given the chance to adhere to surfaces in the flask and therefore aggregate together and grow to form MTS. Similarly gyratory methods involve placing the cell suspension in flasks that are put into incubators where they are rotated by gyratory motions. Both of these techniques allow for larger quantities of MTS to be formed however the drawback is that the MTS formed are heterogeneous in size and shape and the constant rotary motion could mechanically alter the MTS.[1,7]

Non adhesive plates/liquid overlay

Another popular method for MTS formation involves growing cells in plates with substrates that limit cell adhesion. This relies on the cell–cell adhesion being stronger than the cell–substrate adhesion, encouraging cells to aggregate and form MTS rather than adhere to the substrate in the plate. Using substrates such as agarose,[14] polyethylene glycol (PEG) and polydimethylsiloxane (PDMS) to coat the bottom of plates allows for this type of MTS formation.[15]

Microcarrier beads

Microcarrier beads are small 100–400 μM diameter[1] solid beads on which cells are grown in 3D (Fig. 2c). They can be produced from various materials including dextran and cellulose. Microcarrier beads are available at a low cost commercially and tend to allow spheroid formation from primary cells and transformed cell lines as well as cell types which are normally difficult to grow such as endothelial cells. As the beads form the central regions of these cultures there is less likelihood that a necrotic core will develop and therefore these models are more representative of healthy cells growing *in vivo* as opposed to cancer tumour cell lines.[16]

Scaffolds

Scaffolds are extracellular matrix (ECM) mimics that can either be synthetic *e.g.* polyglycolic acid or naturally derived *e.g.* type I collagen and Matrigel® (Fig. 2d). They are highly porous 3D matrices which allow cells to attach, proliferate and differentiate and guide cells to produce 3D MTS structures.[2] 3D Biotek have developed culture kits based on the biodegradable scaffold poly(γ-caprolactone) (PCL).[17]

Microwells and microfluidics

A relatively recent advancement in the growth of uniform MTS on a large scale is the use of microwells and microfluidics, enabled by the development of microprinting techniques including photolithography and soft lithography.[7] Arrays of wells are printed into materials such as polyethylene glycol (PEG), polydimethylsiloxane (PDMS) and agarose which are nonadherent to cells.[18] Thousands of wells can be printed in a single substrate with a defined diameter. When a cell suspension is added to such a printed substrate in a plate, cells settle into the wells such that each well contains an equal number of cells that then form MTS homogenous in size and shape. Size and geometry of MTS formed can be controlled by well shape and size. Recently many systems have been developed on microfluidic chips patterned with microwells and microchannels such that MTS can be formed in arrays and, for example, drugs can be delivered to these systems.[2,15]

This journal is © The Royal Society of Chemistry 2015

Open Access Article. Published on 23 April 2015. Downloaded on 04/09/2015 14:19:06.
This article is licensed under a Creative Commons Attribution 3.0 Unported Licence.

Chemical analysis of MTS – understanding tumour physiology

A variety of techniques have been developed to investigate the physiology of MTS and their changes in response to drugs and therapy. These techniques include advances in instrument technology to allow imaging in real time, in 3D; a variety of techniques to allow observation of variation in oxygen, hypoxia, pH and nutrients; and methods to measure protein expression as well as general growth characteristics and morphology.

Advances in instrument technology to analyse MTS

In the simplest form standard histological methods are used to visualise MTS but this involves fixing and sectioning the samples, which introduces artefacts and does not allow the observation of dynamic processes. Conventional histological dyes also have low spatial resolution.[8] New instrumentation has allowed MTS to be analysed *in situ*.

Confocal microscopy can be used to view MTS with *z* resolution but penetration depths are limited and may not allow full *z* penetration through MTS. Efforts have been made to improve resolution and penetration depth of confocal microscopy to achieve the best images including the use of borosilicate glass bottoms on dishes as opposed to polystyrene, a water immersion microscope objective instead of a dry objective and increased laser power/light output at deeper image depths.[19] While better resolution and increased *z* penetration was observed, the *z* penetration was still limited to 350 μM with this technique meaning it was unable to visualise the entire depth of a MTS.

Two and multi photon microscopy have been used for imaging 3D samples as they can give a two to three fold increase in penetration depth in comparison to one photon confocal microscopy.[20] Samples are probed with laser pulses of longer wavelengths but high intensities to stimulate multi photon excitation.[21] High intensities are required to increase the chance of non-linear multi photon excitations and the laser is generally operated by using long wavelength femtosecond pulses of high intensity to decrease phototoxicity and photobleaching.[22] Increased *z* penetration and contrast are achieved and only the point of interest is subjected to illumination so photobleaching and phototoxicity are minimised in the surrounding sample.[20–23]

Recent advances in microscopy to view MTS involve the use of optical coherence tomography (OCT) (Fig. 3b), optical projection tomography (OPT) (Fig. 3c) and light sheet microscopy (LSM) (Fig. 3d) to map MTS. In OCT back scattered or back reflected light is detected to provide cross sectional images through a 3D sample.[24] In OPT the sample is rotated and straight line projections are taken through it to generate 3D images.[25,26] The advantage of OCT and OPT are that much larger sample volumes can be imaged but resolution is much lower than that which can be obtained from sectioned samples viewed through standard high resolution microscopes or by using confocal microscopy.[27]

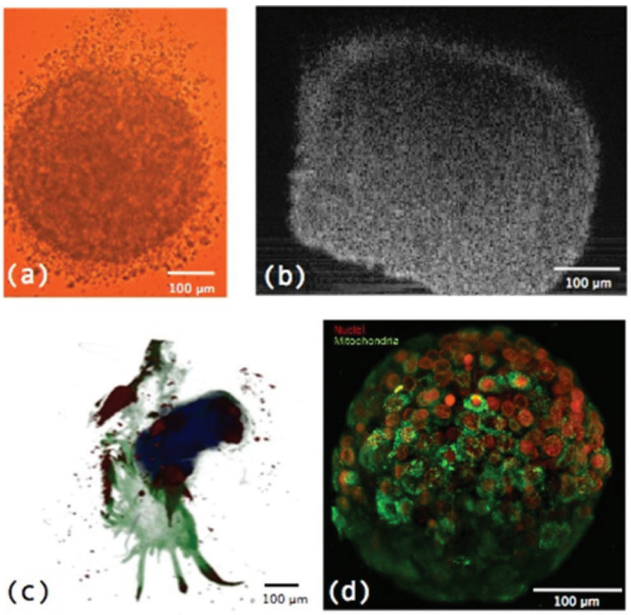

Fig. 3 (a) MTS imaged using a light microscope; (b) a cross section through the centre of an MTS using OCT; (c) an OPT image of an MTS derived from a primary cancer specimen where blue core = implanted MTS, green = outgrowth into culture in collagen and red = positive immunoreactivity for Her2; and (d) LSM image of a MTS.[8]

A more recent and very useful microscopy advancement for the analysis of MTS is LSM or single plane illumination microscopy (SPIM). This involves using a light sheet, a plane of light, to illuminate a sample as opposed to a single point. As well as providing an image of a whole specimen slice at once and therefore reducing acquisition time, this technique reduces the light exposure of areas of the sample and therefore reduces photobleaching and phototoxicity.[8] It is an ideal technique for analysis of MTS as it allows whole sections through MTS to be observed at once and *z* stacks to be built into a 3D image with better *z* resolution than confocal microscopy (Fig. 3d). A disadvantage of this technique is the general need to embed samples in a transparent gel material, usually agarose or low melting point agarose. Embedding in such materials can impact the growth, placing mechanical restraints on specimens and making growth time course experiments inaccurate. Recently, Desmaison, A. *et al.*[28] developed a sample holder allowing MTS to be mounted in hydrogel and a time course experiment of MTS growth to be performed.

Further advances have recently been made to LSM including the use of self-reconstructing Bessel beams and two-photon fluorescence excitation which saw an increase of nearly two fold in axial resolution and 5–10 fold increase in contrast in comparison to linear Bessel beam excitation and 3–5 fold increase in *z* penetration depth in comparison to Gaussian beam linear excitation.[29,30] Very recently LSM has been performed using an Airy beam to provide further advances in particular allowing a larger field of view with high contrast and high resolution.[31]

Open Access Article. Published on 23 April 2015. Downloaded on 04/09/2015 14:19:06.
This article is licensed under a Creative Commons Attribution 3.0 Unported Licence.

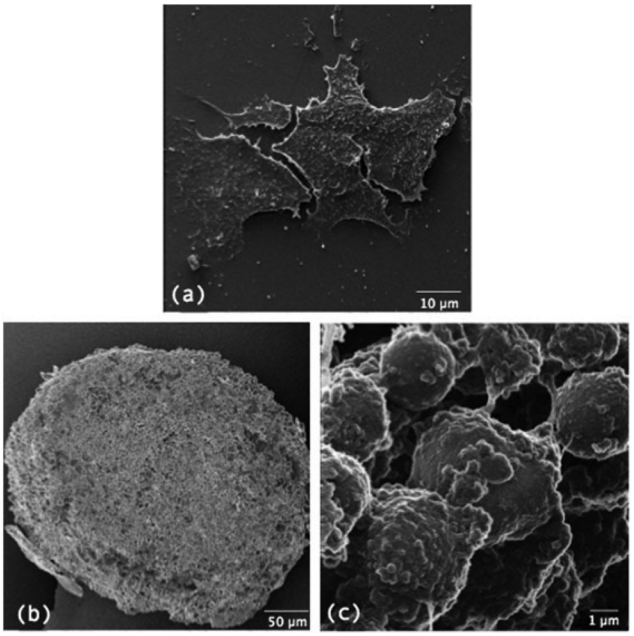

Fig. 4 comparison of the morphology of cells growing in (a) monolayer culture to (b) cells growing as MTS and (c) a magnified area of cells growing as MTS.

It is worth mentioning some additional microscopy techniques that can reveal morphological characteristics of MTS compared to monolayer culture. Transmission electron microscopy (TEM) has been used to visualise cell–cell[32] and cell–ECM[33] interactions in MTS while scanning electron microscopy (SEM) reveals high magnification and high resolution information about the surface characteristics of MTS including visualisation of cell–cell interactions and the morphology of cells.[34–36] Both techniques require cells to be fixed and processed and SEM only reveals surface topology, with samples often coated in gold removing a lot of surface detail. Helium ion microscopy (HIM) removes the need for coating and provides increased resolution compared to SEM.[37] Fig. 4 compares morphology of monolayer cultured cells to MTS using HIM. Table 1 summarises the microscopy techniques used when analysing MTS along with their advantages and limitations.

Measuring oxygen concentration and hypoxia

A significant characteristic of MTS in comparison to monolayer culture is variation in oxygen concentration mimicking *in vivo* tumours. As tumours and MTS grow the central regions become increasingly depleted in oxygen (and hypoxic) and eventually cells may die creating a necrotic core.[38] Hypoxia in tumours is incredibly significant as it can induce pro-survival signalling, leading to metabolic changes and resistance to therapy.[4,5,39,40]

It is desirable to chemically analyse variations in oxygen concentration and hypoxia through MTS. Oxygen concentration and hypoxia are highly interlinked but not identical characteristics. Oxygen concentration is singularly a measurement of the level of oxygen present while hypoxia is a more complex characteristic which can be defined in several ways including nitroreductase activity,[41] HIF activation[42] and expression of HIF associated genes[43] to name a few. This distinction is important since a hypoxic phenotype (HIF stabilisation, glycolytic metabolism) is a characteristic of many cancers irrespective of oxygen concentration (Warburg Effect).[44] When considering chemical analysis of MTS some techniques have been developed specifically to measure hypoxia as a function of, for example, nitroreductase activity, while other techniques directly measure oxygen concentration.

One of the first methods developed for measuring hypoxia uses small molecules such as 2-nitroimidazole that are metabolised under hypoxic conditions and subsequently detected.[45] An example is the commercially available Hypoxyprobe-1™ (PimonidazoleHCl)[46], where the metabolised product in hypoxic regions is detected by an antibody and subsequently visualized by either a fluorescent tag[47] or colorimetric detection (Fig. 5). This technique is limited to distinguishing cells below and above a hypoxic limit without giving truly quantitative information. Autoradiography was used in initial detection methods for these probes and extension to magnetic resonance spectroscopy (MRS) and positron emission tomography (PET) allowed non-invasive detection of hypoxia in living systems.[48–54] Hypoxyprobe-1™ has been used to visualise distributions of hypoxia in MTS, giving good spatial resolution, but its use is limited to fixed sections.

Direct measurement of oxygen concentration can be achieved using oxygen microelectrodes. These have been miniaturised to give increased spatial resolution of oxygen measurements both *in vivo* and *ex vivo*. The main disadvantage is that this is an invasive technique with the risk that the oxygen electrodes perturb their immediate environment and thus distort values obtained.[41,55]

Recent advances have been made to develop increasingly efficient O_2 sensing probes such as new cell-penetrating phosphorescent probes based on conjugates of Pt(II)-tetrakis(pentafluorophenyl)porphine (PtPFPP) dyes.[56] The Pt probe was conjugated with glucose which minimised aggregation and self-quenching for measurements in aqueous media and was used to perform high resolution phosphorescence lifetime based O_2 imaging (PLIM) in PC12 MTS. Nanoprobes have also been used *in vivo* to measure reactive oxygen species (ROS) concentrations and hypoxia and these techniques could potentially be applied to MTS models and, with the use of more advanced instrument technologies, allow live 3D imaging through the MTS.[57]

pH and nutrient concentration

Lactate accumulation is common in areas of low oxygen due to increased glycolysis, utilisation of the pentose phosphate pathway and decreased oxidative phosphorylation.[58] Therefore decreasing oxygen concentration and hypoxia tends to correlate with an increase in lactate accumulation and decreasing pH. Gradients in nutrient concentration including glucose and

 This journal is © The Royal Society of Chemistry 2015

Open Access Article. Published on 23 April 2015. Downloaded on 04/09/2015 14:19:06.
This article is licensed under a Creative Commons Attribution 3.0 Unported Licence.

Table 1 Summarises microscopy techniques used to visualise MTS along with advantages and limitations of each technique

Microscopy technique	Advantages	Limitations
Standard	Simple	No *z* depth Primarily fixed and sectioned samples
Confocal	*z* Depth possible	Limited to a maximum of 350 μM *z* depth
Two and multi-photon	Increased *z* depth and contrast Photobleaching and phototoxicity to surrounding sample minimised	*z* Depth still limited
OCT	Can image whole MTS	Resolution is poorer
OPT	Can image whole MTS	Resolution is poorer
LSM	Can image whole MTS Acquisition time reduced Photobleaching and phototoxicity reduced	Samples typically embedded in a transparent gel which can impact growth
TEM	High resolution to visualise cell–cell and cell–ECM interactions	Limited field of view Involves fixing and processing samples
SEM	High resolution and high magnification of surface characteristics	Involves fixing samples Only reveals surface information Samples often gold coated which removes surface detail
HIM	Increased resolution compared to SEM for revealing surface characteristics No requirement for coating	Involves fixing samples Only reveals surface information

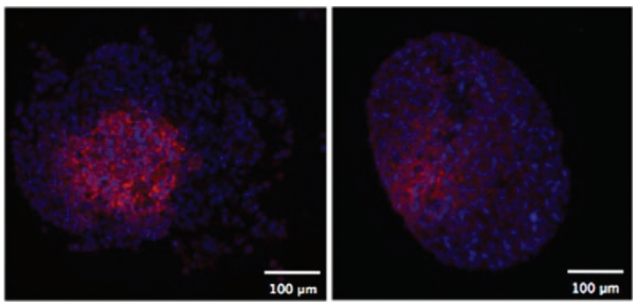

Fig. 5 Two fluorescent images of MTS stained with Hypoxyprobe-1™ (pink) where cell nuclei are stained blue.

ATP that are intimately linked to changes in metabolic pathways can also correlate with pH and oxygen gradients.

Methods for measuring pH and nutrient concentrations in MTS are limited and primarily based on monolayer techniques. Significantly, studies of pH in tumour cells have revealed that intracellular and extracellular pH differ significantly, with intracellular pH becoming neutral to alkaline and extracellular pH acidic.[5,59] This intra- and extracellular trend is attributed to ion pumps exporting protons from inside to outside cells which can become activated by certain growth factors which promote tumour angiogenesis, often associated with requirement for increased blood supply in areas of lower oxygen. This gradient of lower extracellular to intracellular pH is the opposite of that observed under normal tissue conditions. Detection of differences between intra- and extracellular environment requires very high resolution techniques which are currently limited.

Most methods to detect pH in culture employ fluorescence and can also be used in MTS, for example the intracellular monitoring dye BCECF.[60] One of the commonly used techniques to monitor nutrient and pH variations in MTS is bioluminescence imaging. Walenta, S. *et al.*[61] used the technique of bioluminescence of cryosectioned non-proliferating Rat 1 aggregates and MR1 MTS to determine variations in ATP, glucose and lactate. While bioluminescence imaging reveals detailed information about nutrient gradients in MTS with high spatial resolution, the resolution is not sufficient to distinguish intra- and extra-cellular compartments.

The more recent use of nanoprobes for pH imaging *in vivo* also has potential in live MTS. This technique is based on pH sensitive fluorescent probes conjugated to nanoprobes that can also be antibody-targeted to specific cells. Live cell imaging is possible but there is the drawback of limited range of pH detection.[57] Surface enhanced Raman scattering (SERS) has been used to measure intracellular pH using gold nanoshells functionalised with pH active molecules in monolayer culture.[62–66] This technique could be extended to MTS and has the potential for multiplexing to allow numerous characteristics, such as pH and redox, to be measured simultaneously.[67]

^{1}H magnetic resonance chemical shift imaging of MTS incubated with imidazole was used to provide information on pH variations in MTS with 32 × 32 μm resolution. While this resolution is not enough to distinguish intra- and extracellular pH variations it revealed a 0.6 pH unit difference between central and peripheral regions of the MTS.[68]

Spectroscopic imaging techniques have been used to map changes in chemical, elemental and nutrient concentrations in MTS. DLD-1 MTS have been analysed by scanning transmission ion microscopy (STIM), proton-induced X-ray emission (PIXE) mapping, scanning X-ray fluorescence microscopy (SXFM) and Fourier transform infrared (FT-IR). STIM revealed useful information regarding cell density where lower density was observed in central regions relating to the necrotic core. PIXE revealed elemental maps giving information of element density of P, S, Cl, K and Fe. Cu and Zn distribution were

Open Access Article. Published on 23 April 2015. Downloaded on 04/09/2015 14:19:06.
This article is licensed under a Creative Commons Attribution 3.0 Unported Licence.

mapped using SXFM while FT-IR revealed detailed information regarding the distribution of different biomolecules such as proteins, lipids and DNA as well as lactate.[69]

Proteins

Primarily as a result of the gradients of, for example, oxygen that develop in MTS, protein expression is often altered. Standard techniques for measuring protein expression such as Western Blotting can be difficult to perform with MTS samples due to the requirement for large numbers of cells, although this problem has been addressed to some extent by techniques such as in-cell westerns.[2] To overcome this problem multiple MTS for the same conditions can be used. An example study using western blotting shows that the multidrug resistance (MDR1) gene is hypoxia responsive and regulated by Hypoxia Inducible Factor-1 (HIF-1).[70] Both immunohistochemistry and immunofluorescence can be used to detect and quantify protein expression using specific antibodies. For example, proteins involved in cell–cell and cell–ECM interactions and components of ECM such as cadherins, integrins and collagens respectively can be immunochemically stained. It is also possible to perform quantitative immunofluorescence, for example using Automated Quantitative Analysis (AQUA), which allows quantitation of a target signal *e.g.* Her2 in Fig. 6 in cells stained for cytokeratin (tumour cells).[71] While spatial information can be acquired using these techniques there is the need to fix samples. A similar technique that is also often used and based on fluorescence is flow cytometry of trypsinised samples. While this is simple and can provide quantitative data, it removes the majority of spatial information.[72,73]

Bioluminescence has also been used to detect protein expression, protein–protein interactions and enzyme activity by employing different versions of the luciferase bioluminescence assay.[74,75] This is a promising technique as it has the potential to provide spatial information by live imaging of intact MTS. In comparison to fluorescence, bioluminescence has the advantage of a lower background and therefore better sensitivity, a larger range over which quantitative signal can be obtained and less perturbation by coloured compounds.[2]

Nanoprobes can be used for the detection of particular enzymes to analyse their expression. For example, a nanoprobe was developed to detect the activity of caspase-3, an enzyme involved in apoptosis, where nanoparticles were conjugated with a caspase-3 substrate and scattering colour varied as individual nanoparticles were released by the enzyme acting to digest the substrate.[57] This technique was used *in vivo* but has the potential for spatial analysis of differences in enzyme expression in MTS.

A novel demonstration of spatially resolved protein expression information was performed by McMahon,[76] where MTS layers were progressively trypsinised to isolate the outer proliferating layer, middle peri-necrotic layer and necrotic core. Mass spectrometry using an iTRAQ approach with MALDI-TOF-TOF and ESI-Q-TOF was used to analyse the protein content of each layer and compare and contrast. This new approach was also complemented with traditional techniques including immunohistological staining using GLUT-1 and CAIX antibodies. While this technique does not provide highly resolved spatial information it is the first technique to demonstrate spatial changes in protein expression through MTS.

Another recent and promising technique based on mass spectrometry that provides spatial information on proteins in MTS is mass spectrometry imaging (MSI). Matrix-assisted laser desorption/ionization mass spectrometry (MALDI) has been used to analyse frozen or fixed tissue sections for spatial imaging of protein and peptides as well as other species such as lipids and small molecules.[77] Typically frozen tissue sections are analysed,[78] however, this technique has also been performed on formalin-fixed, paraffin-embedded tissue sections.[79] To limit analyte spreading during preparation, matrix-free MSI has also been developed.[80] In addition to tissue sections MALDI imaging has been performed on sectioned MTS embedded in collagen to give information on protein variations through the structure. Proteins were identified using MALDI-TOF-TOF and nanoflow-LC-MS/MS of lysates from MTS and cytochrome C and histone H were both detected as two of the species mapped. This technique is useful as it provides spatially resolved information without the need for specific stains such as those used in immunohistochemistry and immunofluorescence. However it still requires samples to be fixed or frozen and sectioned and therefore live samples cannot be analysed.

Another emerging and promising technique for chemical analysis of MTS is Raman imaging. This technique is a label free and non-invasive technique for probing differences in chemical composition. Raman imaging probes the vibrational modes of molecules giving information on the chemical composition of the area being probed in a spatially resolved

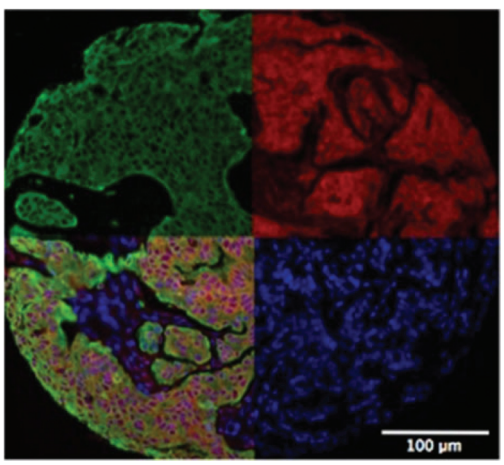

Fig. 6 Quantitative immunofluorescence using AQUA to quantify target signal (Her2, red, top right) in cells marked for cytokeratin (*i.e.* tumour cells, green, top left) in MTS. Nuclei are stained with DAPI (blue, bottom right). All fluorescent signals are combined in the bottom left image.

 This journal is © The Royal Society of Chemistry 2015

Open Access Article. Published on 23 April 2015. Downloaded on 04/09/2015 14:19:06.
This article is licensed under a Creative Commons Attribution 3.0 Unported Licence.

manner. This technique has been predominantly investigated in monolayer culture but recently it has been shown to be useful for the analysis of 3D MTS culture also.[81] While still in its initial stages of research, this technique is very promising for live and label free chemical imaging of MTS.

The techniques of MSI and confocal Raman imaging (CRI) have been combined to provide enhanced chemical information, combining information on integrity of cells and protein levels using CRI and small molecule location using MSI.[82] In this example, MTS were fixed, processed and sectioned for analysis. While CRI has potential for live cell imaging of whole MTS, MSI is only possible on sectioned samples.

Localisation of and cellular response to drugs

The development of the MTS model and techniques to chemically analyse and characterise MTS has provided a more realistic *ex vivo* model of cancer. In addition to increasing insight into physiological characteristics of MTS, this provides a platform for more effective testing of drug candidates and therapies.[83] Screening of drug candidates on MTS gives more reliable results saving time and money in later stages of drug trials. Recent developments in high throughput screening have allowed MTS to be used in place of monolayer culture, allowing drug candidates to be better selected for efficacy.[13,34,84]

The interesting technique of biodynamic imaging has been used to analyse cellular response to drugs toxic to mitochondria and B-Raf inhibitors.[85] This is an optical technique which monitors dynamic changes in cells over time and how these changes vary when treated with a particular drug. Biodynamic imaging detects dynamic light scattering using low-coherence digital holography to elucidate information on intracellular motions. Such motions include dynamic processes in cells including organelle movement and cytoskeletal changes that are often affected by drug treatment. The effect of drugs affecting the mitochondria and Raf kinase inhibitors on two colon cancer cell lines was investigated using this biodynamic imaging technique.

Nanomedicine is a rapidly advancing area of cancer research. It is apparent that when developing promising nanoparticle based techniques for cancer therapy, imaging technologies capable of successful visualising the 3D MTS structure are essential. As already discussed the advances in instrument technology, primarily with OCT, OPT and LSM, allows successful 3D images of MTS to be formed. Fluorescent LSM would be particularly useful for monitoring nanoparticle uptake if nanoparticles could be fluorescently labelled. Studies have investigated the use of techniques such as fluorescence lifetime imaging microscopy (FLIM) to examine the distribution of doxorubicin (DOX) functionalised iron oxide nanoparticles where native DOX released from the nanoparticles had a different fluorescence lifetime to DOX conjugated to the nanoparticles allowing distinction between released and conjugated DOX to be investigated.[86] In another study 3D multiphoton fluorescence microscopy was successfully employed to investigate the uptake of quantum dots and DOX encapsulated in micelles.[36]

MALDI imaging has also been used to monitor drug uptake in MTS. Both the drug irinotecan and its metabolites were imaged by MALDI in HCT 116 colon cancer MTS at various time points to investigate uptake and metabolism of the drug.[87] Raman imaging also has potential for use in drug uptake studies in MTS.[81]

Conclusions

MTS are now established as a valuable *in vitro* tool for investigation of tumour physiology and response to drugs and therapy. There is a need for these models due to the limitations of monolayer culture in displaying the complex characteristics found *in vivo* as a result of their 2D rather than 3D nature. This includes characteristics such as lack of cell–cell and cell–ECM interactions and failure to develop the gradients found in tumours where central regions become deprived of oxygen and nutrients – a very important characteristic as limited penetration to these areas by drugs and oxygen leads to resistance to many therapies. However, the increasing use of the more physiologically relevant MTS model has led to the requirement of more sophisticated functional imaging, in real time and in three dimensions, and chemical analysis techniques to characterise the physiological environment of these MTS and monitor responses to drugs and therapy, particularly for use in high throughput screening methods.

The fundamental consideration when chemically analysing MTS is choice of a suitable technique and instrumentation to obtain the desired spatial, chemical and 3D resolution. Conventional light and confocal fluorescence microscopy techniques can be used to successfully image whole MTS with limited z depth, whilst immunohistochemistry and immunofluorescence can be used to image processed and sectioned samples. Improvements to confocal microscopy along with the use of two- and multiphoton techniques allows increasing z penetration depth. The techniques of OCT, OPT and particularly LSM have allowed whole MTS samples to be viewed and advanced our understanding of MTS.

There is still huge potential for development in analysis of MTS as many of the techniques currently used are based on analysing lysed MTS which removes spatial information or fixing and processing MTS which can introduce artefacts and does not allow for real time imaging. Variants of traditional techniques including flow cytometry, immunohistochemistry, immunofluorescence, bioluminescence imaging and western blotting are currently the main techniques employed for monitoring various chemical characteristics of MTS. There is constant development of new techniques to allow real time analysis of live MTS and perhaps the most promising areas for development is in the use of nanoprobes and Raman imaging. The combination of new probes, new imaging techniques and improved culture techniques will help drive MTS use into the mainstream of drug discovery. This review has highlighted these latest areas pushing the limits of chemical analysis of MTS and enabling technologies for imaging results. Table 2

Open Access Article. Published on 23 April 2015. Downloaded on 04/09/2015 14:19:06.
This article is licensed under a Creative Commons Attribution 3.0 Unported Licence.

Table 2 Summarises the enabling technologies discussed for chemical analysis of MTS along with their uses and limitations

Enabling technology	Use	Limitations
Hypoxia probes *e.g.* Hypoxyprobe™	Hypoxia detection	Sample has to be fixed and sectioned Only detects above/below a certain hypoxic threshold
Oxygen microelectrodes	Measure oxygen concentration	Invasive so can perturb environment
Cell penetrating phosphorescent probes	O_2 sensing	Delivery of probes to cells
Nanoprobes	ROS detection pH detection Enzyme activity	Delivery of nanoprobes to cells
Fluorescent dyes	pH detection	Limited pH detection range
Bioluminescence imaging	pH and nutrient detection Protein expression protein–protein interactions Enzyme activity	Intra- and extra-cellular compartments cannot be distinguished
^{1}H magnetic resonance chemical shift imaging	pH detection	Intra- and extra-cellular compartments cannot be distinguished
Spectroscopic imaging	Cell density (STIM) Element density (PIXE and SXFM) Protein, lipid, DNA and lactate distribution (FT-IR)	Samples have to be frozen and sectioned Spatial information lost Samples have to be fixed and processed Spatial information limited Spatial resolution possible but limited Samples have to be frozen and sectioned
Western blotting	Protein expression	
Immunohistochemistry and immunofluorescence	Protein expression	
Flow cytometry	Protein expression	
Mass spectrometry	Protein expression	
Mass spectrometry imaging	Protein expression Lipid and small molecule expression Drug uptake and metabolism Chemical composition Molecule distribution	
Raman imaging	pH and redox potential measurement	Promising but limited research so far
SERS	Monitoring dynamic changes in response to drug Drug release	Delivery of nanoprobes to cells Monitors motions only Promising but limited use so far
Biodynamic imaging		
FLIM		

summarises the techniques discussed for chemical analysis of MTS.

Acknowledgements

The authors gratefully acknowledge Peter Mullen for providing the image in Fig. 2b and Fig. 5; Dr A Leeper for use of the image in Fig. 3c; Dr Pierre Bagnaninchi for acquisition of the OCT image in Fig. 3b; Dr S Langdon for use of the image in Fig. 2d; and Prof. Ernst Stelzer for permission to use the image I Fig. 3d. This research received support from the QNano Project http://www.qnano-ri.eu which is financed by the European Community Research Infrastructures under the FP7 Capacities Programme (grant no. INFRA-2010-262163), and its partner Trinity College Dublin.

Notes and references

1 H. Page, P. Flood and E. G. Reynaud, *Cell Tissue Res.*, 2013, **352**, 123–131.
2 G. Mehta, A. Y. Hsiao, M. Ingram, G. D. Luker and S. Takayama, *J. Controlled Release*, 2012, **164**, 192–204.
3 L. A. Kunz-Schughart, P. Heyder, J. Schroeder and R. Knuechel, *Exp. Cell Res.*, 2001, **266**, 74–86.
4 D. Hanahan and R. A. Weinberg, *Cell*, 2011, **144**, 646–674.
5 P. Vaupel, *Semin. Radiat. Oncol.*, 2004, **14**, 198–206.
6 A. S. Mikhail, S. Eetezadi, S. N. Ekdawi, J. Stewart and C. Allen, *Int. J. Pharm.*, 2014, **464**, 168–177.
7 R.-Z. Lin and H.-Y. Chang, *Biotechnol. J.*, 2008, **3**, 1172–1184.
8 F. Pampaloni, N. Ansari and E. H. K. Stelzer, *Cell Tissue Res.*, 2013, **352**, 161–177.
9 H.-G. Kang, J. M. Jenabi, J. Zhang, N. Keshelava, H. Shimada, W. A. May, T. Ng, C. P. Reynolds, T. J. Triche and P. H. B. Sorensen, *Cancer Res.*, 2007, **67**, 3094–3105.
10 J. Holtfreter, *J. Exp. Zool.*, 1944, **95**, 171–212.
11 A. Moscona and H. Moscona, *J. Anat.*, 1952, **86**, 287–301.
12 Using Perfecta3D™ *Hanging Drop Plates to Assess Chemosensitivity (White Paper)*, 3D Biomatrix™, https://3dbiomatrix.com/wp-content/uploads/downloads/2011/11/3D-Biomatrix-White-Paper-Hanging-Drop-Plate.pdf (accessed March 2015).
13 Y.-C. Tung, A. Y. Hsiao, S. G. Allen, Y. Torisawa, M. Ho and S. Takayama, *Analyst*, 2011, **136**, 473–478.
14 G. Hamilton, *Cancer Lett.*, 1998, **131**, 29–34.
15 F. Hirschhaeuser, H. Menne, C. Dittfeld, J. West, W. Mueller-Klieser and L. A. Kunz-Schughart, *J. Biotechnol.*, 2010, **148**, 3–15.
16 A. L. van Wezel, *Nature*, 1967, **216**, 64–65.
17 J. Comley, *Drug Discovery World*, 2010 (summer), 25–41.
18 H. Hardelauf, J.-P. Frimat, J. D. Stewart, W. Schormann, Y.-Y. Chiang, P. Lampen, J. Franzke, J. G. Hengstler, C. Cadenas, L. A. Kunz-Schughart and J. West, *Lab Chip*, 2011, **11**, 419–428.

This journal is © The Royal Society of Chemistry 2015

Open Access Article. Published on 23 April 2015. Downloaded on 04/09/2015 14:19:06.
This article is licensed under a Creative Commons Attribution 3.0 Unported Licence.

19 L. le Roux, D. Schellingerhout, A. Volgin, D. Maxwell, K. Ishihara and J. Gelovani, *Microsc. Microanal.*, 2008, **14**, 734–735.
20 R. M. Williams, W. R. Zipfel and W. W. Webb, *Curr. Opin. Chem. Biol.*, 2001, **5**, 603–608.
21 W. R. Zipfel, R. M. Williams and W. W. Webb, *Nat. Biotechnol.*, 2003, **21**, 1369–1377.
22 V. E. Centonze and J. G. White, *Biophys. J.*, 1998, **75**, 2015–2024.
23 K. König, A. Uchugonova and E. Gorjup, *Microsc. Res. Tech.*, 2011, **74**, 9–17.
24 J. G. Fujimoto, C. Pitris, S. A. Boppart and M. E. Brezinski, *Neoplasia*, 2000, **2**, 9–25.
25 J. Sharpe, *Annu. Rev. Biomed. Eng.*, 2004, **6**, 209–228.
26 J. Sharpe, U. Ahlgren, P. Perry, B. Hill, A. Ross, J. Hecksher-Sørensen, R. Baldock and D. Davidson, *Science*, 2002, **296**, 541–545.
27 M. Sharma, Y. Verma, K. D. Rao, R. Nair and P. K. Gupta, *Biotechnol. Lett.*, 2007, **29**, 273–278.
28 A. Desmaison, C. Lorenzo, J. Rouquette, B. Ducommun and V. Lobjois, *J. Microsc.*, 2013, **251**, 128–132.
29 F. O. Fahrbach, V. Gurchenkov, K. Alessandri, P. Nassoy and A. Rohrbach, *Opt. Express*, 2013, **21**, 13824–13839.
30 O. E. Olarte, J. Andilla, R. Jorand, B. Ducommun, C. Lorenzo and P. Loza-Alvarez, http://www.focusonmicroscopy.org/2013/PDF/392_Olarte.pdf (accessed March 2015).
31 T. Vettenburg, H. I. C. Dalgarno, J. Nylk, C. Coll-Lladó, D. E. K. Ferrier, T. Čižmár, F. J. Gunn-Moore and K. Dholakia, *Nat. Methods*, 2014, **11**, 541–544.
32 R. M. Sutherland, J. A. McCredie and W. R. Inch, *J. Natl. Cancer Inst.*, 1971, **46**, 113–120.
33 T. Nederman, B. Norling, B. Glimelius, J. Carlsson and U. Brunk, *Cancer Res.*, 1984, **44**, 3090–3097.
34 W. Y. Ho, S. K. Yeap, C. L. Ho, R. A. Rahim and N. B. Alitheen, *PLoS One*, 2012, **7**, e44640.
35 M. T. Santini, G. Rainaldi and P. L. Indovina, *Crit. Rev. Oncol. Hematol.*, 2000, **36**, 75–87.
36 H. Ma, Q. Jiang, S. Han, Y. Wu, J. C. Tomshine, D. Wang, Y. Gan, G. Zou and X.-J. Liang, *Mol. Imaging*, 2012, **11**, 487–498.
37 G. Hlawacek, V. Veligura, R. van Gastel and B. Poelsema, *J. Vac. Sci. Technol., B*, 2014, **32**, 020801.
38 T. Anada, J. Fukuda, Y. Sai and O. Suzuki, *Biomaterials*, 2012, **33**, 8430–8441.
39 A. Hunter, A. Hendrikse, M. Renan and R. Abratt, *Apoptosis*, 2006, **11**, 1727–1735.
40 H. Harada, *J. Radiat. Res.*, 2011, **52**, 545–556.
41 K. A. Krohn, J. M. Link and R. P. Mason, *J. Nucl. Med.*, 2008, **49**, 129S–148S.
42 M. W. Dewhirst, Y. Cao and B. Moeller, *Nat. Rev. Cancer*, 2008, **8**, 425–437.
43 G. L. Semenza, *Nat. Rev. Cancer*, 2003, **3**, 721–732.
44 W. H. Koppenol, P. L. Bounds and C. V. Dang, *Nat. Rev. Cancer*, 2011, **11**, 325–337.
45 A. J. Varghese, S. Gulyas and J. K. Mohindra, *Cancer Res.*, 1976, **36**, 3761–3765.
46 *HypoxyprobeTM-1 Plus Kit for the Detection of Tissue Hypoxia*, Chemicon International, http://webcache.googleusercontent.com/search?q=cache:8bxU7yy_OUoJ:www.ibrarian.net/navon/paper/HypoxyprobeTM_1_Plus_Kit_for_the_Detection_of_Tis.pdf%3Fpaperid%3D4633961+&cd=5&hl=en&ct=clnk&gl=uk (accessed March 2015).
47 J. A. Raleigh, G. G. Miller, A. J. Franko, C. J. Koch, A. F. Fuciarelli and D. A. Kelly, *Br. J. Cancer*, 1987, **56**, 395–400.
48 J. D. Chapman, A. J. Franko and J. Sharplin, *Br. J. Cancer*, 1981, **43**, 546–550.
49 J. D. Chapman, K. Baer and J. Lee, *Cancer Res.*, 1983, **43**, 1523–1528.
50 A. J. Franko and C. J. Koch, *Int. J. Radiat. Oncol. Biol. Phys.*, 1984, **10**, 1333–1336.
51 A. J. Varghese and G. F. Whitmore, *Int. J. Radiat. Oncol. Biol. Phys.*, 1984, **10**, 1341–1345.
52 J. A. Raleigh, A. J. Franko, C. J. Koch and J. L. Born, *Br. J. Cancer*, 1985, **51**, 229–235.
53 R. C. Urtasun, C. J. Koch, A. J. Franko, J. A. Raleigh and J. D. Chapman, *Br. J. Cancer*, 1986, **54**, 453–457.
54 J. A. Raleigh, D. P. Calkins-Adams, L. H. Rinker, C. A. Ballenger, M. C. Weissler, W. C. Fowler, D. B. Novotny and M. A. Varia, *Cancer Res.*, 1998, **58**, 3765–3768.
55 B. Bourrat-Floeck, K. Groebe and W. Mueller-Klieser, *Int. J. Cancer*, 1991, **47**, 792–799.
56 R. I. Dmitriev, A. V. Kondrashina, K. Koren, I. Klimant, A. V. Zhdanov, J. M. P. Pakan, K. W. McDermott and D. B. Papkovsky, *Biomater. Sci.*, 2014, **2**, 853–866.
57 H. Koo, M. S. Huh, J. H. Ryu, D.-E. Lee, I.-C. Sun, K. Choi, K. Kim and I. C. Kwon, *Nano Today*, 2011, **6**, 204–220.
58 C. Riganti, E. Gazzano, M. Polimeni, E. Aldieri and D. Ghigo, *Free Radicals Biol. Med.*, 2012, **53**, 421–436.
59 M. K. Danquah, X. A. Zhang and R. I. Mahato, *Adv. Drug Delivery Rev.*, 2011, **63**, 623–639.
60 D. Rotin, D. Steele-Norwood, S. Grinstein and I. Tannock, *Cancer Res.*, 1989, **49**, 205–211.
61 S. Walenta, J. Doetsch, W. Mueller-Klieser and L. A. Kunz-Schughart, *J. Histochem. Cytochem.*, 2000, **48**, 509–522.
62 A. Jaworska, L. E. Jamieson, K. Malek, C. J. Campbell, J. Choo, S. Chlopicki and M. Baranska, *Analyst*, 2015, **140**, 2321.
63 S. W. Bishnoi, C. J. Rozell, C. S. Levin, M. K. Gheith, B. R. Johnson, D. H. Johnson and N. J. Halas, *Nano Lett.*, 2006, **6**, 1687–1692.
64 J. Kneipp, H. Kneipp, B. Wittig and K. Kneipp, *Nano Lett.*, 2007, **7**, 2819–2823.
65 J. Kneipp, H. Kneipp, B. Wittig and K. Kneipp, *J. Phys. Chem. C*, 2010, **114**, 7421–7426.
66 M. A. Ochsenkuehn, P. R. T. Jess, H. Stoquert, K. Dholakia and C. J. Campbell, *ACS Nano*, 2009, **3**, 3613–3621.
67 L. E. Jamieson, A. Jaworska, J. Jiang, M. Baranska, D. J. Harrison and C. J. Campbell, *Analyst*, 2015, **140**, 2330.
68 J. Alvarez-Pérez, P. Ballesteros and S. Cerdán, *MAGMA*, 2005, **18**, 293–301.

Open Access Article. Published on 23 April 2015. Downloaded on 04/09/2015 14:19:06.
This article is licensed under a Creative Commons Attribution 3.0 Unported Licence.

69 J. Z. Zhang, N. S. Bryce, R. Siegele, E. A. Carter, D. Paterson, M. D. de Jonge, D. L. Howard, C. G. Ryan and T. W. Hambley, *Integr. Biol.*, 2012, **4**, 1072–1080.
70 K. M. Comerford, T. J. Wallace, J. Karhausen, N. A. Louis, M. C. Montalto and S. P. Colgan, *Cancer Res.*, 2002, **62**, 3387–3394.
71 R. L. Camp, G. G. Chung and D. L. Rimm, *Nat. Med.*, 2002, **8**, 1323–1328.
72 N.-C. Cheng, S. Wang and T.-H. Young, *Biomaterials*, 2012, **33**, 1748–1758.
73 J. M. Lee, P. Mhawech-Fauceglia, N. Lee, L. C. Parsanian, Y. G. Lin, S. A. Gayther and K. Lawrenson, *Lab. Invest.*, 2013, **93**, 528–542.
74 P. M. Tiwari, K. Vig, V. A. Dennis and S. R. Singh, *Nanomaterials*, 2011, **1**, 31–63.
75 E. Salomonnson, A. C. Stacer, A. Ehrlich, K. E. Luker and G. D. Luker, *PLoS One*, 2013, **8**, e51500.
76 K. Mcmahon, *PhD Thesis*, University of Bradford, 2011.
77 R. J. A. Goodwin, S. R. Pennington and A. R. Pitt, *Proteomics*, 2008, **8**, 3785–3800.
78 M. Stoeckli, P. Chaurand, D. E. Hallahan and R. M. Caprioli, *Nat. Med.*, 2001, **7**, 493–496.
79 M. C. Djidja, E. Claude, M. F. Snel, P. Scriven, S. Francese, V. Carolan and M. R. Clench, *J. Proteome Res.*, 2009, **8**, 4876–4884.
80 R. J. A. Goodwin, A. R. Pitt, D. Harrison, S. K. Weidt, P. R. R. Langridge-Smith, M. P. Barrett and C. L. MacKay, *Rapid Commun. Mass Spectrom.*, 2011, **25**, 969–972.
81 E. Zuser, *PhD Thesis*, Northeastern University, 2013.
82 D. R. Ahlf, R. N. Masyuko, A. B. Hummon and P. W. Bohn, *Analyst*, 2014, **139**, 4578–4585.
83 W. Fayad, L. Rickardson, C. Haglund, M. H. Olofsson, P. D'Arcy, R. Larsson, S. Linder and M. Fryknäs, *Chem. Biol. Drug Des.*, 2011, **78**, 547–557.
84 B. G. Reid, T. Jerjian, P. Patel, Q. Zhou, B. H. Yoo, P. Kabos, C. A. Sartorius and D. V. LaBarbera, *Curr. Chem. Genomics Transl. Med.*, 2014, **8**, 27–35.
85 R. An, D. Merrill, L. Avramova, J. Sturgis, M. Tsiper, J. P. Robinson, J. Turek and D. D. Nolte, *J. Biomol. Screening*, 2014, **19**, 526–537.
86 J. S. Basuki, H. T. T. Duong, A. Macmillan, R. B. Erlich, L. Esser, M. C. Akerfeldt, R. M. Whan, M. Kavallaris, C. Boyer and T. P. Davis, *ACS Nano*, 2013, **7**, 10175–10189.
87 X. Liu, E. M. Weaver and A. B. Hummon, *Anal. Chem.*, 2013, **85**, 6295–6302.

This journal is © The Royal Society of Chemistry 2015

Monolayer to MTS: using SEM, HIM, TEM and SERS to compare morphology, nanosensor uptake and redox potential in MCF7 cells

L. E. Jamieson[a], A. P. Bell[b], D. J. Harrison[c], C. J. Campbell*[a]
[a] EaStCHEM, School of Chemistry, University of Edinburgh, Edinburgh, EH9 3JJ, UK. E-mail: colin.campbell@ed.ac.uk; [b]Advanced Microscopy Laboratory, CRANN, Trinity College Dublin, Dublin 2, Ireland; [c]Medical and Biological Sciences Building, University of St Andrews, North Haugh, St Andrews, Fife, KY16 9TF.

ABSTRACT

Cellular redox potential is important for the control and regulation of a vast number of processes occurring in cells. When the fine redox potential balance within cells is disturbed it can have serious consequences such as the initiation or progression of disease. It is thought that a redox gradient develops in cancer tumours where the peripheral regions are well oxygenated and internal regions, further from vascular blood supply, become starved of oxygen and hypoxic. This makes treatment of these areas more challenging as, for example, radiotherapy relies on the presence of oxygen. Currently techniques for quantitative analysis of redox gradients are limited. Surface enhanced Raman scattering (SERS) nanosensors (NS) have been used to detect redox potential in a quantitative manner in monolayer cultured cells with many advantages over other techniques. This technique has considerable potential for use in multicellular tumour spheroids (MTS) – a three dimensional (3D) cell model which better mimics the tumour environment and gradients that develop. MTS are a more realistic model of the *in vivo* cellular morphology and environment and are becoming an increasingly popular *in vitro* model, replacing traditional monolayer culture. Imaging techniques such as transmission electron microscopy (TEM), scanning electron microscopy (SEM) and helium ion microscopy (HIM) were used to investigate differences in morphology and NS uptake in monolayer culture compared to MTS. After confirming NS uptake, the first SERS measurements revealing quantitative information on redox potential in MTS were performed.

Keywords: MTS, SERS, TEM, HIM, NS, redox, cancer, tumour

1. INTRODUCTION

Cell culture is used extensively for the *in vitro* study of cellular characteristics including morphology, chemical composition and response to drug and therapy treatment. Typically cells are cultured as a monolayer growing on a flat surface such as a petri dish or flask. While this simple setup has been used to provide invaluable cellular information, it suffers from the drawback that the cells are not growing in a realistic physiological environment. *In vivo* cells exist in a 3D environment where their primary physical contacts are with surrounding cells and the extracellular matrix (ECM).[1] In monolayer culture there is very little contact with other cells - the primary contacts being with the flat surface on which they are growing and the media they are growing in. The 3D environment *in vivo* gives rise to important differences in cellular characteristics compared to monolayer culture and for this reason 3D cell culture techniques are now being more frequently employed.[2] In particular 3D techniques are useful in the study of cancer as, when a tumour grows, gradients in characteristics such as oxygen concentration, pH and nutrient concentration develop as the central regions of a tumour mass become further from the well organised vasculature of the body providing oxygen and nutrients to cells.[3,4]

Multicellular tumour spheroids (MTS) are a 3D cell culture model for the study of cancer.[1,5] Due to the 3D nature of this model, techniques for analysis of cells grown in this way are complicated particularly by instrumental limitations in z imaging depths.[6,7] Traditional histology techniques have been used to analyse paraffin embedded and sectioned MTS for attributes such as growth characteristics[8]; changes in morphology; hypoxia using reporters such as Hypoxyprobe[TM9]; and protein expression using immunohistochemistry[10]. These techniques have

Biophotonics South America, edited by Cristina Kurachi, Katarina Svanberg, Bruce J. Tromberg, Vanderlei Salvador Bagnato, Proc. of SPIE Vol. 9531, 95311I · © 2015 SPIE
CCC code: 1605-7422/15/$18 · doi: 10.1117/12.2180944

Downloaded From: http://proceedings.spiedigitallibrary.org/ on 09/04/2015 Terms of Use: http://spiedigitallibrary.org/ss/TermsOfUse.aspx

limitations in that they cannot be performed on live cells and fixing, embedding and sectioning can introduce artefacts and deformities. Fluorescence[11] and bioluminescence[12] have also been used when analysing characteristics such as pH and nutrient concentration but imaging depth is still a limitation. Other techniques such as transmission electron microscopy (TEM)[13,14] and scanning electron microscopy (SEM)[15–17] have been used to analyse morphological characteristics of MTS but again require fixing and, in the case of TEM, sectioning of samples.

A characteristic of particular interest in cancer tumours is intracellular redox potential. This is a measure of the oxidising potential of the intracellular environment and exists as a delicate balance between oxidants such as reactive oxygen species (ROS), antioxidant enzymes and reductants such as NADH/NADPH.[18–22] Intracellular redox potential is tightly regulated in healthy cells and when this is disrupted disease can often progress.[23–25] Disease is often associated with excessive ROS and oxidative stress at one end of the scale and lack of oxygen and hypoxia at the other. This is an important characteristic to consider in cancer tumours as cells near the centre of a tumour mass become increasingly far from the organised blood supply carrying oxygen to cells. Currently techniques for measuring hypoxia in MTS as a tumour model are limited and the 'gold standard' technique is to use small molecules like Hypoxyprobe[TM26–29] which are reductively metabolized under hypoxic conditions and detected in paraffin embedded and sectioned samples by antibody detection and either colorometric or fluorescence detection. These probes give limited quantitative information however as they only report on whether the environment was above or below a certain limit. They also require fixing and sectioning MTS and therefore cannot be used for live cell dynamic measurements.

Our group has previously used SERS NS to monitor intracellular redox potential quantitatively in live cells in monolayer culture.[30–32] In this technique, NS are prepared by attaching redox sensitive probe molecules to gold nanoparticles (NPs) and delivered to cells, SERS spectra are then collected and allow redox potential to be determined by ratiometric analysis of resultant signals. In this paper we extend this technique to MTS to allow quantitative analysis of redox potential in 3D culture and combine it with imaging techniques for analysis of morphological differences between monolayer and MTS culture and NS uptake. Specifically, we used TEM to analyse NS uptake and probe morphological differences between monolayer culture and MTS; Helium Ion Microscopy (HIM)[33] (a relatively new technique that provides increased image resolution in comparison to SEM and removes the need for sample coating) to reveal morphological differences of MTS compared to monolayer culture and provide information on NS uptake at a surface level and SEM to reveal NS uptake below the surface of MTS.

2. METHODOLOGY

NS functionalisation

Aqueous suspensions of NPs (2.2×10^9 particles/ml, 3.65 pM) were purchased from Nanospectra Biosciences. NPs had a 150 nm diameter with a 125 nm silica core and 25 nm gold shell and were resonant at 782 nm. For NQ-NP (where NQ refers to a naphthaquinone reporter), NPs were functionalised with 100 μM NQ solution overnight in 10% EtOH solution. Functionalised NQ-NPs were washed 3 times with water. For AQ-NP (where AQ refers to an anthraquinone reporter), NPs were functionalised with 100 μM AQ solution overnight in 1% DMSO solution. Functionalised AQ-NPs were washed 2 times with water.

General Cell Culture Procedures

All cellular work was carried out using MCF7 human breast cancer cells. Cells were cultured in Dulbecco's Modified Eagle's Medium (DMEM; Gibco; 31885-023), supplemented with penicillin/streptomycin (Invitrogen, 10,000 units/ml) and 10% heat-inactivated Foetal Calf Serum (FCS, Sigma). Cells were incubated at 37 °C and 5% CO_2 in a humidified incubator.

For monolayer culture 1×10^5 cells were plated on a coverslip in a 6 well plate or 35 mm glass bottomed imaging dish. The following day, growth media was replaced with media without FCS or remained the same. After 1-2 hrs, functionalised NS were added at a concentration of approximately 170 fM and cells were incubated

Downloaded From: http://proceedings.spiedigitallibrary.org/ on 09/04/2015 Terms of Use: http://spiedigitallibrary.org/ss/TermsOfUse.aspx

overnight. The next day, media was removed, cells were washed and media was replaced with normal growth media before performing SERS measurements.

For MTS, cells were split into 25 cm^3 flasks. The following day growth media was replaced with media without FCS. After 1-2 hrs, functionalised NS were added at a concentration of approximately 200 fM and cells were incubated overnight. The next day cells were trypsinised and resuspended in growth media before forming 20 µl hanging drops of cell suspension on the lid of a petri dish. Growth media was added to the petri dish and the lid placed back on and MTS were grown for 6 days.

General SERS information

SERS spectra were recorded with a Reinshaw inVia Raman Microscope and Spectrometer. A 785 nm diode laser with ~6 mW power at the sample was used, along with a 10 × and 50 × Olympus objective to focus laser light onto the gold NS. SERS spectra were processed using WIRE™ 2.0 software and Origin 8.5.

Intracellular SERS measurements

When performing SERS measurements in cells a line focus laser was used. A rough map was firstly performed over a cell with an X step of 5.0 µm and a Y step of 3.56 µM, 1580 cm^{-1} center and 2 or 3 s acquisition time at 50% laser power. Where a signal was observed in the resulting spectra, coordinates were noted and a more detailed map with an X step of 1 µm and a Y step of 1.19 µm, 1580 cm^{-1} center and 30 s acquisition time at 10% laser power was recorded. This generated 147 spectra in just under 4 minutes.

SERS data processing

Spectra were analysed using Origin 8.5 software. Firstly all spectra from a single map were analysed by eye to determine the spectra with NQ-NP signals present. For all spectra with signals smoothing was performed 4 times using a Savitzky-Golay algorithm and 9 points of window. An 8 point baseline was then subtracted by manually placing the points. Peak intensities of peaks in the region of 1570-1588 cm^{-1} and 1630-1648 cm^{-1} were then determined using the peak finding function and the 1st derivative method. The ratio of the peak intensity at 1630-1648 cm^{-1} to that at 1570-1588 cm^{-1} was used along with calibration data from previous work in our group[30] to determine redox potential from each spectrum.

Transmission electron microscopy (TEM)

Cells or cell spheroids were fixed in 0.5% gluteraldehyde in 0.1 M sodium cacodylate or PBS for about 2 hrs. Cells in monolayer culture were scraped and transferred to an eppendorf tube where they were pelleted by centrifugation before removing fixative and adding PBS. Cell spheroids were fixed in an eppendorf tube before removing excess fixative and adding PBS.

Osmium tetroxide solution was prepared by mixing 1 part 4% osmium tetroxide, 1 part 6% potassium ferrocyanide, 1 part 0.4 M sodium cacodylate and 1 part dH_2O. Excess PBS supernatant was removed from the samples and osmium tetroxide solution (100 – 200 µl per sample) was added and cells incubated for 10-15 minutes. Osmium tetroxide solution was removed and the samples were washed with distilled water (3 x 5 min). Using a glass vial rotator for subsequent steps, 50% ethanol was added to the samples and they were transferred into small glass vials. After 10 mins, 50% ethanol was removed and 70% ethanol added to each sample, making sure the sample did not dry out during exchange. A further series of graded ethanol steps were carried out (80%, 90%, 95% and 2 x 100%) with 10 min incubation per step. Following this 2 x 15 min propylenoxide incubations were carried out, before adding a 1:1 mix of epoxy resin in propylenoxide and incubating overnight with a sealed lid. The next morning, lids were removed from the vials and the samples were incubated for a further 3 hours on the rotator until the propylenoxide had evaporated. Cell fragments were taken out, gently blotted on filter paper, placed inside the PVC lids and fresh epoxy resin added. After a further 4 hours incubation, the blotting of fragments was repeated and the fragments were placed in PVC capsules for making the final blocks and filled with fresh epoxy resin. Capsules were placed in oven at 60 ° for 24 hours.

Downloaded From: http://proceedings.spiedigitallibrary.org/ on 09/04/2015 Terms of Use: http://spiedigitallibrary.org/ss/TermsOfUse.aspx

70 nm sections were taken using a diamond knife. Sections were positioned on copper grids and stained with lead citrate before examining and photographing with a Jeol JEM transmission electron microscope connected to a digital camera.

Helium ion microscopy (HIM)

Monolayer cultured cells grown on a coverslip and incubated overnight with functionalised NPs as described previously or MTS grown as described previously were fixed in 0.5% gluteraldehyde in 0.1 M sodium cacodylate or PBS. Samples were mounted on a sticky carbon stub and analysed using a Zeiss Orion Plus Helium Ion Microscope running at 30 kV with 10 µm aperture, an Everhart Thornley detector and charge neutralization achieved using an electron flood gun.

Scanning electron microscopy (SEM)

Samples were prepared as for SEM and analysed using a Zeiss Ultra SEM.

3. RESULTS

Previously SERS NS functionalised with redox active molecules NQ and AQ have been used to measure intracellular redox potential in NIH/3T3 mouse fibroblast[30], A549[31] and EA.hy926[32] cells in monolayer culture. The primary goal of this research was to use these NS to measure intracellular redox potential in MTS, in particular MCF7 breast cancer MTS.

TEM

TEM was used primarily to confirm NS uptake but could also be used to reveal morphological differences over a restricted field of view. Figure 1 compares monolayer and MTS cell morphology by TEM where the primary difference is the increase in cell-cell interactions in MTS, mimicking better the *in vivo* environment.

TEM was used to confirm uptake by MCF7 cells in a similar way to previous work and secondly to confirm that NS remained in cells over extended periods of time up to 7 days after incubation with cells. Previous work with monolayer cells employed an overnight incubation with NS before taking SERS measurements the following day but as MTS take several days to grow, we used TEM to confirm that NS were maintained inside cells over a longer time period. To form MTS that contained NS, NS were added in monolayer culture before forming MTS from the resultant cell suspension and growing for 6 days in hanging drops - as a comparison between 2D and 3D we also examined cells that were incubated with NS overnight before growing for either a further 6 days in monolayer culture or as MTS.

Figure 2 shows TEM images of NQ-NPs in MCF7 cells in monolayer culture after 24 hours incubation with NQ-NPs before fixing. NQ-NPs were found both free in the cytosol (Figure 2(b)) and inside endosome structures (Figure 2(c)). This confirmed uptake of NS to MCF7 cells. Interestingly some NQ-NPs were found on the outside edge of cells (Figure 2(a)), as if in the process of being taken up.

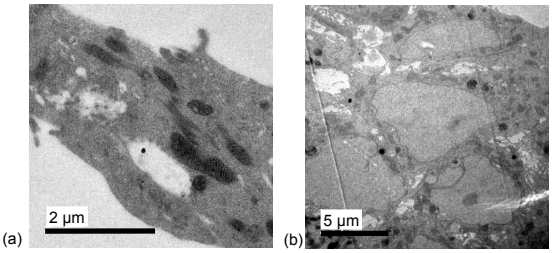

Figure 1 shows TEM images of MCF7 cells in monolayer culture (a) and MTS (b) where differences in cell morphology can be visualised.

Downloaded From: http://proceedings.spiedigitallibrary.org/ on 09/04/2015 Terms of Use: http://spiedigitallibrary.org/ss/TermsOfUse.aspx

TEM images from MCF7 cells which were incubated for 24 hours with NQ-NPs in monolayer culture before a further 6 days growth in 2D (Figure 3) and as MTS (Figure 4) revealed that NQ-NPs remained in the cells for this extended period of time. Again NQ-NPs were found both in the cytosol and endosome structures for cells grown over extended periods of time in monolayer and MTS.

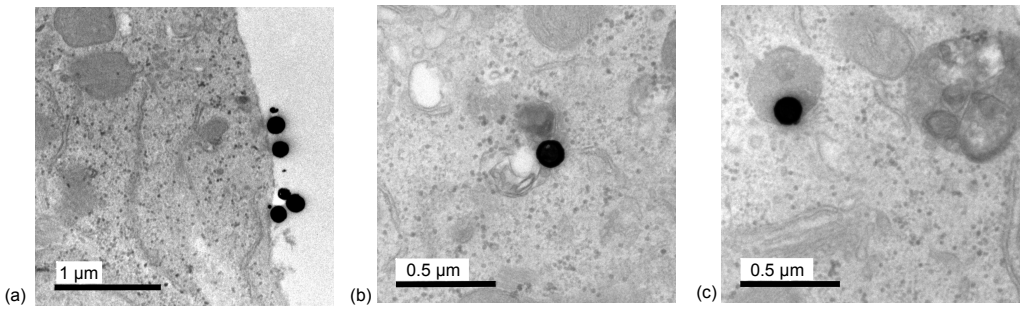

Figure 2 (a)-(c) illustrate TEM images obtained for MCF7 cells grown in monolayer culture and incubated with NQ-NPs for 24 hours before fixing.

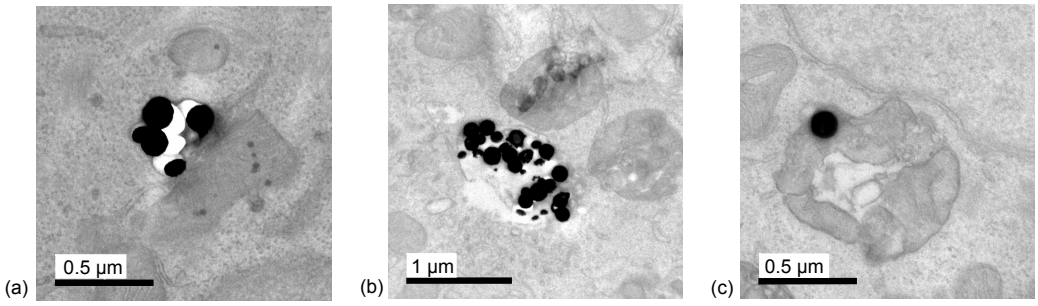

Figure 3 (a)-(c) illustrate TEM images obtained for MCF7 cells grown in monolayer culture and incubated with NQ-NPs for 24 hours followed by a further 6 days growth in monolayer culture before fixing.

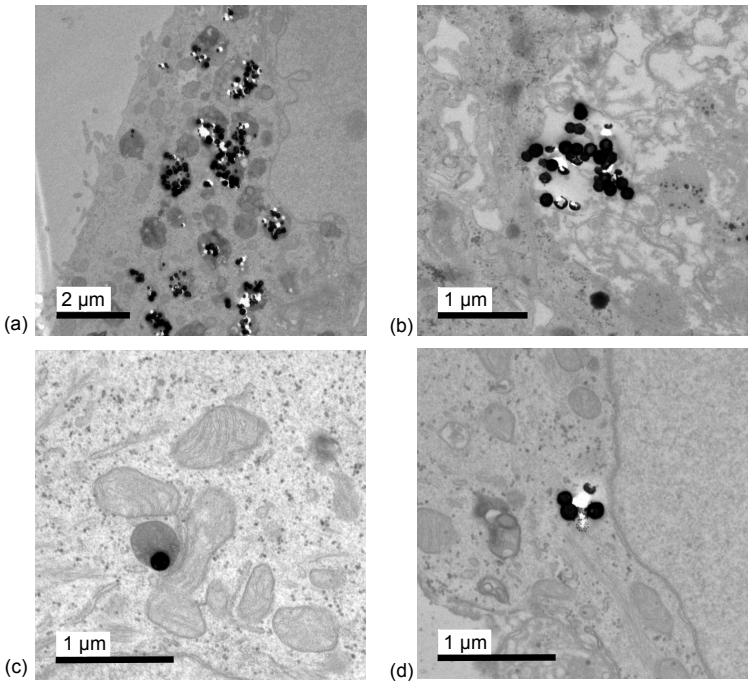

Figure 4 (a)-(d) illustrate TEM images obtained for MCF7 cells grown in monolayer culture and incubated with NQ-NPs for 24 hours followed by a further 6 days growth as MTS before fixing.

Downloaded From: http://proceedings.spiedigitallibrary.org/ on 09/04/2015 Terms of Use: http://spiedigitallibrary.org/ss/TermsOfUse.aspx

SEM & HIM

HIM provides increased resolution to SEM for comparison of morphological features of MTS and monolayer cultured cells.[33] While SEM often requires samples to be coated in gold prior to analysis, this is not required for HIM. As coating can remove a lot of surface features HIM allows surface detail to be more accurately visualised in comparison to SEM. Figure 5 compares cell morphology of monolayer cultured MCF7 cells (Figure 5(a)) to MTS over both a larger field of view to image the whole MTS (Figure 5(b)) and a smaller field of view showing cell-cell interactions (Figure 5(c)).

It is possible to use HIM to visualise the interaction of NS with cells. Figure 6 shows NS interacting with cells in monolayer culture. This is limited to visualizing NS on the surface of cells as this technique is highly surface sensitive. Interestingly NS with different functionalities appeared to interact differently with cells. Figure 6(a) and (b) show the interaction of AQ-NPs with cells and Figure 6(c) and (d) show the interaction of NQ-NPs with cells. AQ-NPs appear to be more aggregated and it is possible that cells are either releasing clumps of NS that have been coated in protein within the cell, or depositing extra cellular matrix onto NS outside the cell – Figure 6(b) shows some extracellular material encapsulating AQ-NPs. Aggregates of NQ-NPs are also visible as in Figure 6(d) however they are fewer and often only single NQ-NPs are seen as in Figure 6(c). This is likely due to the differing properties of NQ and AQ – AQ is more hydrophobic.

While HIM provided some information regarding NS interaction with the surface of cells in monolayer culture it was difficult to extend this technique into MTS as there were fewer instances of NS being present on the surface of cells on the outside of MTS. In order to try and visualise NS in MTS, SEM was performed using backscattered electron detection to detect NS just below the surface of cells (Figure 7). This technique allowed NS to be visualised successfully however it was only possible to see NS just below the surface of cells so had limited applicability for looking at distribution over the whole MTS. These images also allowed comparison of resolution to those captured using HIM where much greater resolution was achieved in HIM.

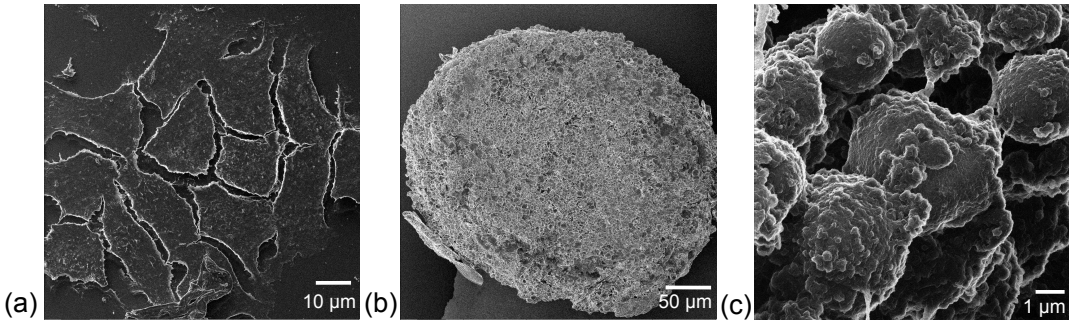

Figure 5 shows HIM images of MCF7 cells growing in monolayer culture (a) and as MTS with a larger field of view to image a whole MTS (b) and smaller field of view to image more detailed cell-cell interactions in MTS (c).

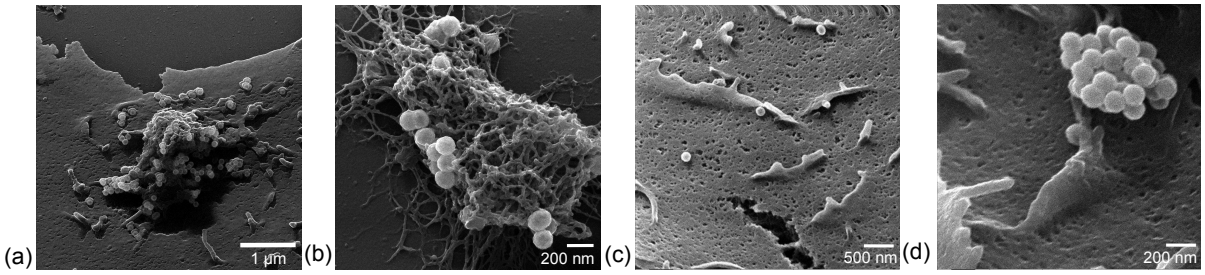

Figure 6 shows HIM images of AQ-NPs interacting with the surface of MCF7 cells grown in monolayer culture (a), as well extracellular material (b) and NQ-NPs interacting with the surface of MCF7 cells (c and d).

Downloaded From: http://proceedings.spiedigitallibrary.org/ on 09/04/2015 Terms of Use: http://spiedigitallibrary.org/ss/TermsOfUse.aspx

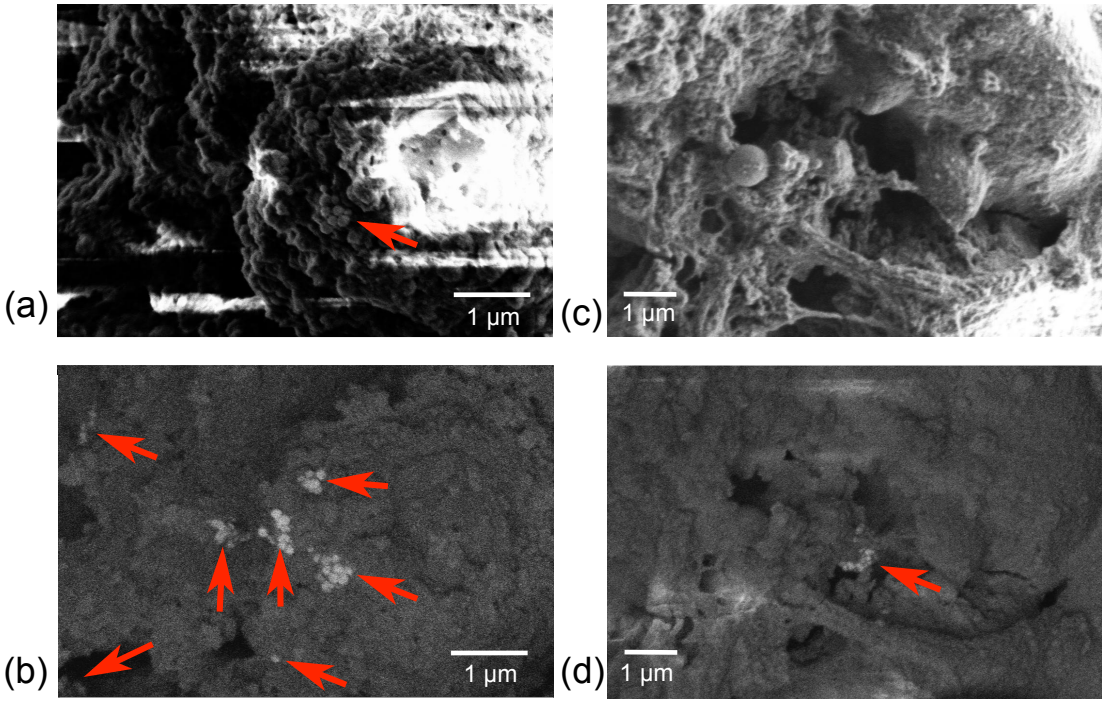

Figure 7 shows SEM images of regions of MCF7 cell MTS where the same area was imaged with secondary (a and c) and backscattered (b and d respectively) electrons. Red arrows point to areas where NS are visible.

SERS

After confirming NS uptake in both monolayer culture and MTS, SERS was used to investigate redox potential in both cases using the probe NQ-NP (Figure 8(a)).[30] For calibration, spectra of NQ-NPs dried onto a slide and covered by buffer were recorded at different redox potential values set using a potentiostat (as previously published). The ratiometric response of signals in the spectrum assigned to C=O stretching at 1630-1648 cm^{-1} and aromatic ring breathing at 1577-1600 cm^{-1} was used to construct a calibration plot and equation for determining redox potential. The C=O stretching signal increases in intensity with increasing oxidising potential of the environment due to an increased proportion of NQ being present in the oxidised form where C=O bonds are present.

For monolayer culture MCF7 cells were plated and incubated with NQ-NPs overnight as described in the experimental section before carrying out SERS on the cells. Figure 8(b) shows a typical SER spectrum of NQ-NPs from a cell in monolayer culture, which gave a redox potential of –260 mV. Figure 9 summarises redox potential obtained in monolayer culture cells giving a mean potential of –260 ± 4.5 mV.

After applying the previously established technique to the MCF7 cells of choice in monolayer culture, resulting in redox potential values expected, work began to expand this technique to samples prepared in 3D as MTS. As already discussed and detailed in the experimental section, cells were incubated with NQ-NPs in monolayer culture before growing the resultant cell suspension in hanging drops to form MTS. Regions of MTS were then mapped in a similar way to monolayer cultured cells as detailed in the experimental section. As MTS are much larger, this meant only small regions of MTS could be mapped at a time and at this stage, detection of whole MTS variations in redox potential were not possible. The number of spectra obtained for a single map was much greater than that for monolayer cultured cells, possibly due to the additional z direction from which signals could be obtained. Figure 9 illustrates the distribution of redox potential values obtained from a single map of NQ-NPs from an MTS compared to the previously obtained values for monolayer culture. The average redox potential of –268 ± 5.9 mV was more negative than that for the values obtained in monolayer culture, which would be expected from the more hypoxic nature of MTS. Some spectra had no C=O stretching peak (fully reduced NQ). A one way ANOVA confirmed that redox potential values in monolayer culture compared to MTS were

Downloaded From: http://proceedings.spiedigitallibrary.org/ on 09/04/2015 Terms of Use: http://spiedigitallibrary.org/ss/TermsOfUse.aspx

significantly different at the 0.05 level. Not only was mean redox potential different between monolayer culture and MTS but MTS showed a higher standard deviation and more widespread redox potential values. This was expected as a gradient develops in MTS so a wider range of redox values would be expected across this gradient.

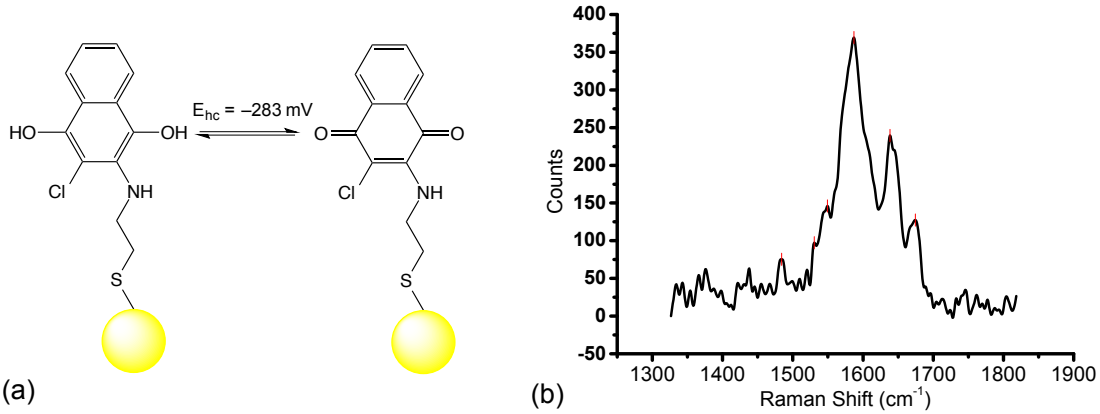

Figure 8 shows a typical SERS spectrum obtained from NQ-NPs in MCF7 cells with peaks at 1638 cm^{-1} and 1587 cm^{-1} assigned to C=O stretch and ring breathing respectively.

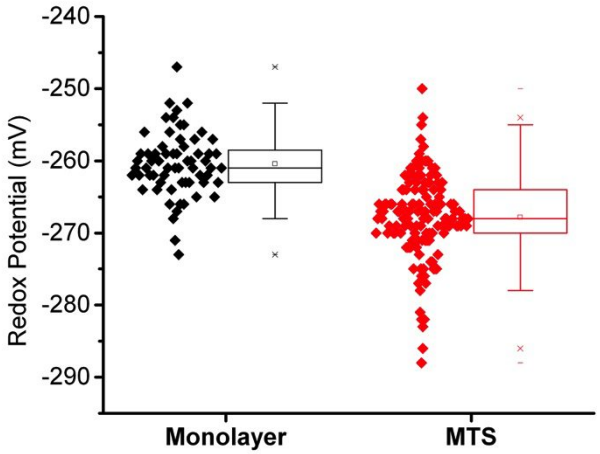

Figure 9 illustrates the distribution of redox potential values obtained using SERS of NQ-NPs in MCF7 cells in monolayer culture and grown as MTS. A one way ANOVA confirmed that the two sets of data were significantly different at the 0.05 level.

4. CONCLUSIONS

MTS are becoming increasingly important as a cell culture model that mimics the *in vivo* environment better than the traditional monolayer culture and these results reveal some of the important characteristics that develop in this 3D environment. Cell morphology and NS uptake were measured and monitored using TEM, SEM and HIM. TEM was used primarily to confirm both the uptake of functionalised NPs to MCF7 cells in monolayer culture for the first time and that they remained present in cells in both monolayer culture and MTS over extended periods of time up to one week. HIM is a relatively new technique that was used for the first time to study NS uptake in MCF7 cells in monolayer and MTS culture and reveal significant morphological differences between cells in monolayer culture and MTS. While it provided little information about NS uptake in MTS, detection of backscattered electrons by SEM allowed some NS to be visualised in MTS but also revealed the much greater image resolution of HIM compared to SEM. SERS has been used for the first time to reveal quantitative

Downloaded From: http://proceedings.spiedigitallibrary.org/ on 09/04/2015 Terms of Use: http://spiedigitallibrary.org/ss/TermsOfUse.aspx

information regarding intracellular redox potential in MCF7 MTS. These initial experiments used the redox probe NQ-NP, previously developed in our group, to probe intracellular redox potential in MCF7 cells in both monolayer culture and MTS. As expected, results revealed a significantly lower and more varied intracellular redox potential state in MTS compared to monolayer culture. All techniques collectively revealed increased information on NS uptake in monolayer culture and MTS, important differences in morphology between monolayer culture and MTS and important quantitative differences in characteristics of MTS, specifically intracellular redox potential, in comparison to monolayer culture.

ACKNOWLEDGEMENTS

The authors gratefully acknowledge the School of Chemistry at the University of Edinburgh and The School of Medicine at the University of St Andrews. This research received support from the QNano Project http://www.qnano-ri.eu which is financed by the European Community Research Infrastructures under the FP7 Capacities Programme (Grant No. INFRA-2010-262163), and its partner Trinity College Dublin. The authors thank Dr John Lucocq and Dr Christian Hacker at the University of St Andrews for TEM work.

REFERENCES

[1] Page, H., Flood P. and Reynaud, E. G., " Three-dimensional tissue cultures: current trends and beyond", Cell Tissue Res., 352, 123–131 (2013).

[2] Hirschhaeuser, F., Menne, H., Dittfeld, C., West, J., Mueller-Klieser, W. and Kunz-Schughart, L.A. " Multicellular tumor spheroids: An underestimated tool is catching up again", J. Biotechnol., 148, 3–15 (2010).

[3] Hanahan, D. and Weinberg, R.A., " Hallmarks of Cancer: The Next Generation", Cell, 144, 646–674 (2011).

[4] Vaupel, P. " Tumor Microenvironmental Physiology and Its Implications for Radiation Oncology", Semin. Radiat. Oncol., 14, 198–206 (2004).

[5] Lin, R.-Z. and Chang, H.-Y, " Recent advances in three-dimensional multicellular spheroid culture for biomedical research", Biotechnol. J., 3, 1172–1184 (2008).

[6] Jamieson, L. E., Harrison, D.J. and Campbell, C. J. "Chemical Analysis of Multicellular Tumour Spheroids", Analyst (2015) (accepted).

[7] Pampaloni, F., Ansari, N., and Stelzer, E. H. K, " High-resolution deep imaging of live cellular spheroids with light-sheet-based fluorescence microscopy", Cell Tissue Res., 352, 161–177 (2013).

[8] K. Groebe, 1991, **799**, 792–799.

[9] Anada, T., Fukuda, J., Sai, Y. and Suzuki, O., " An oxygen-permeable spheroid culture system for the prevention of central hypoxia and necrosis of spheroids", Biomaterials, 33, 8430–8441 (2012).

[10] Lee, J. M., Mhawech-Fauceglia, P., Lee, N., Parsanian, L. C., Lin, Y. G., Gayther, S. A. and Lawrenson, K., " A three-dimensional microenvironment alters protein expression and chemosensitivity of epithelial ovarian cancer cells in vitro", Lab. Invest., 93, 528–542 (2013).

[11] Rotin, D., Steele-Norwood, D., Grinstein, S. and Tannock, I., " Requirement of the Na^+/H^+ Exchanger for Tumor Growth", 49, 205–211 (1989).

[12] Walenta, S., Doetsch, J., Mueller-Klieser, W. and Kunz-Schughart, L. A., " Metabolic Imaging in Multicellular Spheroids of Oncogene-transfected Fibroblasts", J. Histochem. Cytochem., 48(4), 509–522 (2000).

[13] Sutherland, R. M., McCredie, J. A. and Inch, W. R., "Growth of Multicell Spheroids in Tissue Culture as a Model of Nodular Carcinomas", J. Natl. Cancer Inst., 46, 113–120 (1971).

[14] Nederman, T., Norling, B., Glimelius, B., Carlsson, J. and Brunk, U., "Demonstration of an Extracellular Matrix in Multicellular Tumor Spheroids", 44(7), 3090–3097 (1984).

[15] Ho, W. Y., Yeap, S. K., Ho, C. L., Rahim, R. A. and Alitheen, N.B., "Development of Multicellular Tumor Spheroid (MCTS) Culture from Breast Cancer Cell and a High Throughput Screening Method Using the MTT Assay", PLoS One, 7(9), e44640 (2012).

Downloaded From: http://proceedings.spiedigitallibrary.org/ on 09/04/2015 Terms of Use: http://spiedigitallibrary.org/ss/TermsOfUse.aspx

[16] Santini, M. T., Rainaldi, G. and Indovina, P. L., "Apoptosis, cell adhesion and the extracellular matrix in the three-dimensional growth of multicellular tumor spheroids", Crit. Rev. Oncol. Hematol., 36, 75–87 (2000).
[17] Ma, H., Jiang, Q., Han, S., Wu, Y., Tomshine, J. C., Wang, D., Gan, Y., Zou, G. and Liang, X.-J., "Multicellular Tumor Spheroids as an In Vivo–Like Tumor Model for Three-Dimensional Imaging of Chemotherapeutic and Nano Material Cellular Penetration", Mol. Imaging, 11(6), 487–498 (2012).
[18] Kemp, M., Go, Y.-M. and Jones, D. P., " Nonequilibrium thermodynamics of thiol/disulfide redox systems: A perspective on redox systems biology", Free Radic. Biol. Med., 44, 921–937 (2008).
[19] Zhang, Y., Hong, H. and Cai, W., " Imaging with Raman Spectroscopy", Curr. Pharm. Biotechnol., 11(6), 654–661 (2011).
[20] Schafer, F. Q. and Buettner, G. R., "Redox Environment of the Cell as Viewed Through the Redox State of the Glutathione Disulfide/Glutathione Couple", Free Radic. Biol. Med., 30(11), 1191–1212 (2001).
[21] Filomeni, G., Rotilio, G. and Ciriolo, M. R., " Disulfide relays and phosphorylative cascades: partners in redox-mediated signaling pathways", Cell Death Differ., 12, 1555–1563 (2005).
[22] Mallikarjun, V., Clarke, D. K. and Campbell, C. J., " Cellular redox potential and the biomolecular electrochemical series: A systems hypothesis", Free Radic. Biol. Med., 53, 280–288 (2012).
[23] Waris, G. and Ahsan, H., " Reactive oxygen species: role in the development of cancer and various chronic conditions", J. Carcinog., 5(14), (2006).
[24] Go, Y.-M. and Jones, D. P., " Cysteine/cystine redox signaling in cardiovascular disease", Free Radic. Biol. Med., 50, 495–509 (2011).
[25] Dewhirst, M. W., Cao, Y. and Moeller, B., " Cycling hypoxia and free radicals regulate angiogenesis and radiotherapy response", Nat. Rev. Cancer, 8, 425–437 (2008).
[26] Chemicon International, "Hypoxyprobe™-1 Plus Kit for the Detection of Tissue Hypoxia", accessed March 2015, http://webcache.googleusercontent.com/search?q=cache:8bxU7yy_OUoJ:www.ibrarian.net/navon/paper/HypoxyprobeTM_1_Plus_Kit_for_the_Detection_of_Tis.pdf%3Fpaperid%3D4633961+&cd=5&hl=en&ct=clnk&gl=uk.
[27] Raleigh, J. A., Calkins-Adams, D. P., Rinker, L. H., Ballenger, C. A., Weissler, M. C., Fowler, W. C., Novotny, D. B. and Varia, M. A., " Hypoxia and Vascular Endothelial Growth Factor Expression in Human Squamous Cell Carcinomas Using Pimonidazole as a Hypoxia Marker", Cancer Res., 58, 3765–3768 (1998).
[28] Varghese, A. J., Gulyas, S. and Mohindra, J. K., " Hypoxia-dependent Reduction of 1-(2-Nitro-1-imidazolyl)-3-methoxy-2-propanol by Chinese Hamster Ovary Cells and KHT Tumor Cells in Vitro and in Vivo", 36, 3761–3765 (1976).
[29] Raleigh, J. A., Miller, G. G., Franko, A. J., Koch, C. J., Fuciarelli, A. F. and Kelly, D. A., " Fluorescence immunohistochemical detection of hypoxic cells in spheroids and tumours", Br. J. Cancer, 56, 395–400 (1987).
[30] Auchinvole, C. A. R., Richardson, P., McGuinnes, C., Mallikarjun, V., Donaldson, K., McNab, H. and Campbell, C. J., " Monitoring Intracellular Redox Potential Changes Using SERS Nanosensors", ACS Nano, 6(1), 888–896 (2012).
[31] Jiang, J., Auchinvole, C., Fisher, K. and Campbell, C. J., " Quantitative measurement of redox potential in hypoxic cells using SERS nanosensors", Nanoscale, 6, 12104–12110 (2014).
[32] Jamieson, L. E., Jaworska, A., Jiang, J., Baranska, M., Harrison, D. J. and Campbell, C. J., " Simultaneous intracellular redox potential and pH measurements in live cells using SERS nanosensors", Analyst, 140(7), 2330-2335 (2015).
[33] Hlawacek, G., Veligura, V., van Gastel, R. and Poelsema, B., " Helium ion microscopy", J. Vac. Sci. Technol. B Microelectron. Nanom. Struct., 32(2), 020801 (2014).

Downloaded From: http://proceedings.spiedigitallibrary.org/ on 09/04/2015 Terms of Use: http://spiedigitallibrary.org/ss/TermsOfUse.aspx

Analyst

PAPER

View Article Online
View Journal | View Issue

Published on 08 December 2014. Downloaded by University of Edinburgh on 04/09/2015 14:20:40.

Cite this: *Analyst*, 2015, **140**, 2321

SERS-based monitoring of the intracellular pH in endothelial cells: the influence of the extracellular environment and tumour necrosis factor-α†

Aleksandra Jaworska,[a,b] Lauren E. Jamieson,[c] Kamilla Malek,*[a,b] Colin J. Campbell,[c] Jaebum Choo,[d] Stefan Chlopicki[b,e] and Malgorzata Baranska[a,b]

Received 30th October 2014,
Accepted 20th November 2014

DOI: 10.1039/c4an01988a

www.rsc.org/analyst

The intracellular pH plays an important role in various cellular processes. In this work, we describe a method for monitoring of the intracellular pH in endothelial cells by using surface enhanced Raman spectroscopy (SERS) and 4-mercaptobenzoic acid (MBA) anchored to gold nanoparticles as pH-sensitive probes. Using the Raman microimaging technique, we analysed changes in intracellular pH induced by buffers with acid or alkaline pH, as well as in endothelial inflammation induced by tumour necrosis factor-α (TNFα). The targeted nanosensor enabled spatial pH measurements revealing distinct changes of the intracellular pH in endosomal compartments of the endothelium. Altogether, SERS-based analysis of intracellular pH proves to be a promising technique for a better understanding of intracellular pH regulation in various subcellular compartments.

Introduction

Intracellular pH (pH_i) regulation is critical for most cellular processes including cell volume regulation, vesicle trafficking, cellular metabolism, cell membrane polarity, muscular contraction, and cytoskeletal interactions.[1] In addition, some growth-stimulating signals including epidermal growth factor, platelet-derived growth factor, insulin, vasopressin, and serum activate the sodium–proton exchange activity to induce cellular alkalinisation and are thus important in cell activation, growth, and proliferation.[1] The endothelium, lining the interior of the whole circulation, which may be regarded as the largest functional organ in the human body, plays an active role in vasoregulation, coagulation, inflammation, and microvascular permeability.[2] In most if not all of these processes changes in the intracellular pH may be of importance. Indeed, it was demonstrated that endothelial alkalinisation inhibits gap junction communication and endothelium-derived hyperpolarisation.[3] In turn, a decrease in pH_i may result in the diminished production of nitric oxide.[4]

Tumour necrosis factor-α (TNFα) induces endothelial inflammation.[5] It inhibits the anticoagulatory mechanism and promotes thrombotic processes, which are responsible for venous thrombosis, arteriosclerosis, vasculitis, and disseminated intravasal coagulation.[5] Moreover, several chronic and acute human pathologies are associated with various degrees of endoplasmatic acidosis.[6] Failure of intracellular pH regulation may result in malfunction of various other enzymes and transduction pathways and may well contribute to various facets of the phenotype of endothelial dysfunction.[6]

There are only a few techniques that can be employed for the determination of pH_i such as pH-sensitive microelectrodes, nuclear magnetic resonance and fluorescence.[1] Until now, fluorescence spectroscopy has been shown to be the most sensitive and commonly used technique to measure pH_i.[1,7–9] In addition, pH-sensitive organic probes or fluorescent proteins can be functionalized to target specific cellular compartments, detecting pH from 4.7 (in lysosomes) to 8 in mitochondria.[7–10 and therein] However, low sensitivity, signal from background and photobleaching of fluorophores limit the application of fluorescence microscopy. An alternative technique is surface enhanced Raman spectroscopy. Briefly, nanoparticles (gold, silver, and carbon nanotubes *etc.*) are conjugated to pH-sensitive Raman reporters. The most commonly used compounds in the current approaches are 4-mercaptobenzoic acid,[11–17] 2-aminothiophenol[18] or 4-mercaptopyridine.[19] In an early application of SERS for measurements of pH_i, Talley *et al.*[11] have shown that the SERS signal from MBA adsorbed on silver nanoparticles is sensitive within 1 unit on the pH scale. The use of hollow gold nanoparticles as a SERS support improved the sensitivity to *ca.* 0.5 unit of pH as shown in SERS studies on pH_i in Chinese

[a]*Faculty of Chemistry, Jagiellonian University, 3 Ingardena Str., 30-060 Krakow, Poland. E-mail: malek@chemia.uj.edu.pl; Fax: +48-12634-0515; Tel: +48-12663-2064*
[b]*Jagiellonian Centre for Experimental Therapeutics (JCET), Jagiellonian University, 14 Bobrzynskiego Str., 30-348 Krakow, Poland*
[c]*EaStCHEM, School of Chemistry, University of Edinburgh, Edinburgh, EH9 3JJ, UK*
[d]*Department of Bionano Engineering, Hanyang University, Sa-1-dong 1271, Ansan 426-791, South Korea*
[e]*Department of Experimental Pharmacology, Jagiellonian University Medical College, Grzegorzecka 16, 31-531 Krakow, Poland*
†Electronic supplementary information (ESI) available. See DOI: 10.1039/c4an01988a

Published on 08 December 2014. Downloaded by University of Edinburgh on 04/09/2015 14:20:40.

hamster ovary cells.[12] Scaffidi and co-workers[13] have applied pH-sensitive plasmonic-active fiber-optic nanoprobes to measure the intracellular pH in human mammary epithelial (HMEC-15/hTERT) and PC-3 human prostate cancer cells, showing that such *in situ* pH_i measurements correctly determine the intracellular acidity. The most innovative application of SERS for pH measurements has been reported by Cong and others[20] where the intracellular pH was measured using MBA-coated AuNPs embedded into silica nanopeapods *in vitro* and *in vivo*.

In our work, we evaluate the usefulness of SERS imaging with MBA-AuNP probes for monitoring pH_i dysregulation due to pH stress from the extracellular environment. In addition, we investigate the *in vitro* pH response in human umbilical vein endothelial cells (EA.hy926) upon their stimulation with tumour necrosis factor (TNFα).

Experimental

Materials

All compounds used in the fabrication of Au nanoparticles and preparation of buffers and 4-mercaptobenzoic acid (MBA) were purchased from Sigma-Aldrich and were of analytical grade. Deionized water (Millipore Milli-Q grade) with a resistivity of 18.2 MΩ was used in all the experiments. A solution of 4-mercaptobenzoic acid at a concentration of 1×10^{-3} M was prepared by diluting an appropriate mass of the solid in ethanol. Gold nanoparticles (AuNPs) with an average diameter of 40 nm were prepared according to the Frens procedure.[21] UV-Vis spectra, DLS (Dynamic Light Scattering) and AFM measurements confirmed the size of nanoparticles and excluded their aggregation due to interactions with MBA, similar to our previous work.[22] We applied 40 nm gold nanoparticles to EA.hy926 endothelial cells for which the uptake mechanism has been well-established in our previous studies.[22,23] For the collection of SERS spectra, 100 μL of 1×10^{-3} M solution of MBA was mixed with 1 mL of gold colloid. After 5 min vortexing, the mixture was centrifuged for 10 min at 3000 rpm and the supernatant was re-dissolved in DPBS (Dulbecco's phosphate-buffered saline). 0.1 M aqueous solutions of sodium hydroxide, sodium phosphate, disodium hydrogen phosphate, sodium dihydrogen phosphate and phosphate acid were used for preparing buffers in the pH range of 1–12.

To determine pH calibration curves, MBA-AuNP solution was mixed with a phosphate buffer of a given pH (5 : 1 v/v), then placed in a 96-well plate and SERS spectra were collected. The relative intensity of SERS bands assigned to the stretching modes of the carboxylate group and aromatic ring was calculated using OPUS 7.2 software by using unprocessed SERS spectra and plotted against pH. Finally, an equation was fitted to a calibration curve using Gnuplot software.

Cell culture

Experiments were conducted for EA.hy926 cells, a line derived from human umbilical vein endothelial cells fused with the A549 line. Cells were grown in plastic wells in DMEM supplemented with 10% fetal bovine serum, 2 mM L-glutamine, penicillin, streptomycin, and 2% HAT. Where cells were treated with TNFα, the medium was replaced with a medium containing 10 ng mL^{-1} TNFα and cells were incubated for 12 hours. Then, for all cells, the medium was replaced by a medium containing a solution of MBA-AuNPs. Briefly, the medium was mixed with the MBA-AuNP solution in the ratio of 10 : 1 (v/v). The final concentration of MBA-AuNPs in the medium was 1×10^{-11} M. Cells were incubated in the medium containing pH sensors for 0.5, 1, 2, 4 and 12 hours. Next, the cells were washed three times with DPBS to eliminate most of the residual nanoparticles left outside of the cell. In the next step, cells were stressed by incubation (10 min) in buffers with a pH of 3.93, 6.21, 7.20, 8.60 and 11.35. Then, SERS maps of live cells were immediately collected. For each buffer, SERS maps from 5 cells were collected, as under these conditions we could observe relatively fast progression in the loss of cell viability (up to 1 h). The total time of mapping of one cell was *ca.* 5 min, and only live and healthy cells were selected for the measurement, determined by their morphological characteristics such as shape and adhesion.

Instrumentation

Electronic absorption spectra of the gold colloid, 4-mercaptobenzoic acid and the gold colloid functionalised with MBA were recorded with a UV-Vis-NIR Perkin Elmer spectrophotometer (model Lambda 35) in the range of 200–1100 nm with a resolution of 2 nm using quartz cells of 1 cm path length. SERS mapping of cells and SERS spectra of MBA in buffers were recorded by using a WITec system, equipped with a He–Ne laser (632.8 nm). For all measurements, the integration time was 0.04 s with a single accumulation and laser power of 10 mW. The recorded spectral range for grating 600 g mm^{-1} was 0–2400 cm^{-1}. SERS spectra of MBA-AuNPs were recorded by placing a sample in a plastic 96-well plate and using an air objective (20×). Three SERS spectra were acquired, each for freshly prepared samples. For Raman mapping, raster scans over single living cells were carried out with a computer-controlled *x*,*y*-stage under an immersion objective with a magnification of 60×. The mapping step was 1 μm.

Analysis of SERS maps

Hierarchical K-means cluster analysis of SERS maps was performed using WITec Project 2.06 software. The spectra were analysed in the region of 200–1800 cm^{-1} after a routine procedure for cosmic ray removal and smoothing (13 points) using a Savitzky–Golay algorithm which improves the signal to noise ratio. A number of classes were chosen by the comparison of spectral profiles of their mean spectra. We started our analysis from 10–12 classes and then, if mean spectra were identical in the region of the marker bands, classes were merged. Cluster analysis was performed for each cell separately. pH_i values presented in the work were calculated from mean SERS spectra.

 This journal is © The Royal Society of Chemistry 2015

Published on 08 December 2014. Downloaded by University of Edinburgh on 04/09/2015 14:20:40.

Results and discussion

pH calibration curves

Calibration curves were determined in the range of pH from 1 to 12. As discussed in detail previously,[11,24] the two SERS bands are sensitive to pH changes and this agrees with our SERS spectra of MBA shown in Fig. 1A. They are assigned to the symmetric stretching of the COO^- group [$\nu_s(COO)^-$] and the stretching vibration of the C=O bond in the COOH group at ~1420 and ~1720 cm^{-1}, respectively. Going toward acidic pH, the intensity of the 1720 cm^{-1} band increases, whereas the neutral and alkaline environments cause deprotonation of the COOH group resulting in an increase in the intensity of the $\nu_s(COO)^-$ mode along with its shifting from *ca.* 1400 to *ca.* 1420 cm^{-1}, *cf.* the inset in Fig. 1A. The strongest SERS bands at 1070 and 1580 cm^{-1}, attributed to the ν_{12} and ν_{8a} aromatic ring vibrations, respectively, are not sensitive to pH changes and were used for calculation of the relative intensities. We determined calibration curves representing the spectral changes as a function of pH by calculating heights as well as integral intensities of SERS bands at 1070, 1400–1420, 1580 and 1720 cm^{-1} individually for each raw spectrum. Fig. 1B illustrates exemplary calibration curves for the ratios $I_{1400-1420}/I_{1070}$ and I_{1720}/I_{1070}. They represent typical Henderson–Hasselbalch plots.[25] Several reports have shown similar calibration curves for the pH dependence of SERS signals of MBA but they usually estimate pH_i values by comparing calibration spectra with SERS spectra from cells.[11,13,15,17] Therefore, we additionally fitted an equation to the curves to give a simple mathematical formulation for the determination of pH based on spectral changes of 4-mercaptobenzoic acid, see Table 1. Slopes of both the plots in Fig. 1B show noticeable spectral changes in the pH range of 5–9 that corresponds to the natural pH range determined in the cellular compartments, *i.e.* from 4.7 in lysosomes to 8 in mitochondria.[26] The error calculated for eqn (1) was ±0.15 of pH value. For comparison, the error of pH measurements by using fluorescence labels is *ca.* ±0.3 according to Wu and co-workers.[27]

In vitro SERS-based pH_i imaging

In our previous study on the cellular uptake of R6G-AuNPs by EA.hy926 cells (R6G – rhodamine 6G), we observed the SERS signal of the Raman reporter just after 0.5 h of incubation and then saturation of the nanoparticles appeared after 2 h incubation.[23] A longer incubation time of more than 2 hours resulted in a slow process of de-attaching molecules of the dye from the gold surface. Since the MBA molecules interact with the

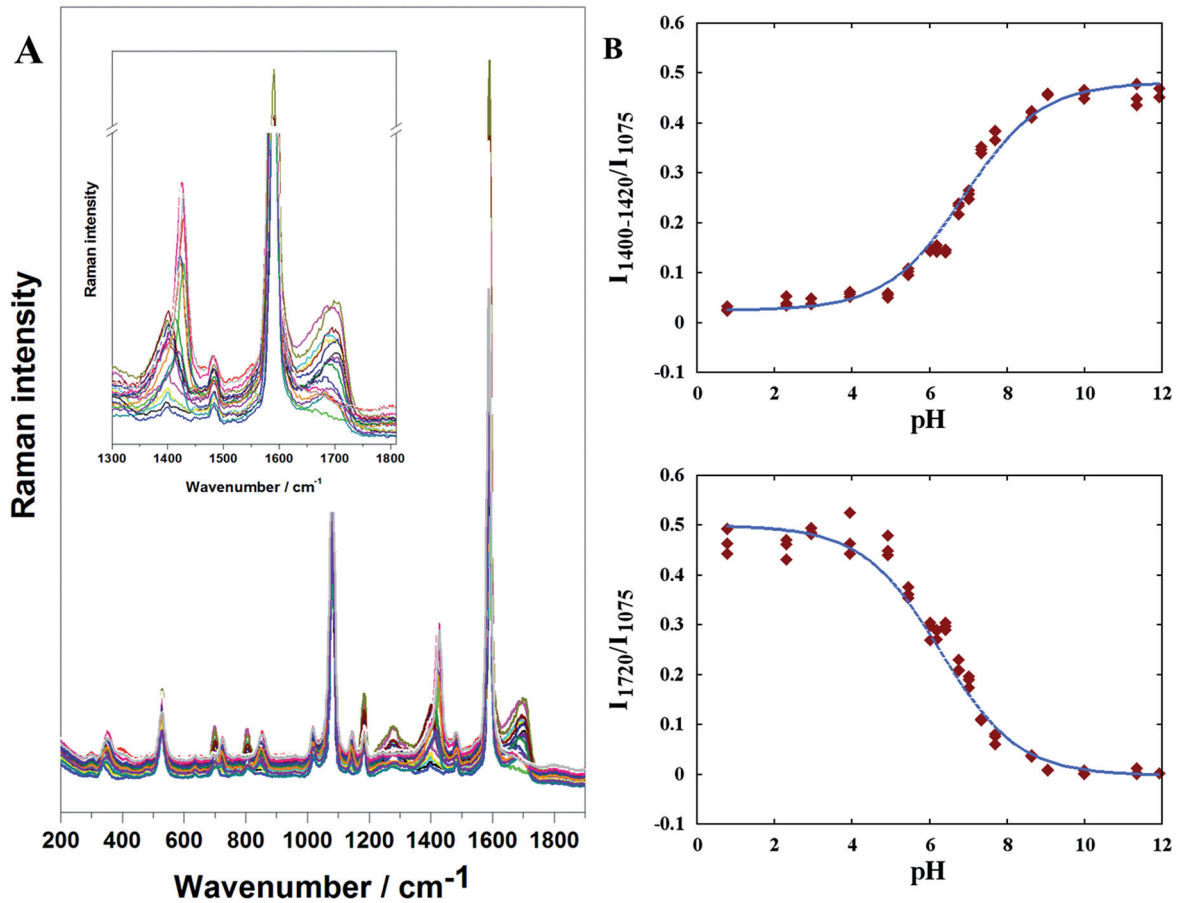

Fig. 1 (A) SERS spectra of MBA at different pH values from 1 to 12. The inset shows the region of 1300–1800 cm^{-1} associated with pH-sensitive bands at *ca.* 1400–1420 and 1720 cm^{-1}; (B) Henderson–Hasselbalch plots for band ratios: $I_{1400-1420}/I_{1070}$ (top) and I_{1720}/I_{1070} (bottom).

Published on 08 December 2014. Downloaded by University of Edinburgh on 04/09/2015 14:20:40.

metal surface in a different way than rhodamine 6G, we optimized the incubation time for MBA-AuNPs to examine saturation of cells by nanoprobes and to avoid incubation resulting in their substitution by cellular biomolecules. Fig. 2 displays SERS maps showing the intensity of the 1070 cm^{-1} band in endothelial cells incubated with MBA-AuNPs for 0.5–12 hours and SERS spectra randomly chosen from these maps. They illustrate that the overall intensity of the SERS signal increases upon elongation of incubation time and the largest number of nanosensors entered the intercellular space after overnight incubation. Kneipp and co-workers have shown that MBA-AuNPs are distributed all over the cytosol in mouse fibroblast cells after 4.5 h and a longer incubation time does not change the distribution of nanosensors[14] while the 6 h and 12 h incubation were applied in experiments with mouse macrophage and Chinese hamster ovary cells, respectively.[11,15] This indicates that the optimal incubation time should be determined for each cell type as it may considerably differ.

No SERS bands originating from cellular biocomponents were found in spectra indicating the stability of interactions between MBA and the gold while SERS marker bands for pH were not observed before the 4 h incubation however, they exhibited a low signal to noise ratio. Therefore, the 12 h incubation was applied in the further experiments. Moreover, apart from typical SERS features of 4-mercaptobenzoic acid observed in spectra displayed in Fig. 1A, we found the presence of anomalous bands in SERS spectra at ~1000 and ~1025 cm^{-1}, *cf.* Fig. 2. The other reports regarding the application of MBA for determination of pH_i have also shown the presence of these bands when the sensor molecules were anchored to AgIF fiber-optic nanoprobes,[13] hollow gold nanospheres,[12] silver nanoparticles[11] whereas they were absent when MBA-AgNPs were encapsulated in silica[15] and when MBA-AgNPs in cells were probed using surface enhanced hyper-Raman scattering (SEHRS).[28] This indicates that the appearance of these bands does not depend on the properties of the metal surface. Michota and Bukowska have shown in their studies on the adsorption process of MBA on silver and gold roughened electrodes that the 1000 and ~1025 cm^{-1} bands are typical for monosubstituted benzene derivatives and their presence in SERS spectra of MBA may result from the decarboxylation process of these molecules.[24] This process can be additionally accelerated in an alkaline environment and appears even after 20 minutes after adsorption. Since our calibration spectra do not show the

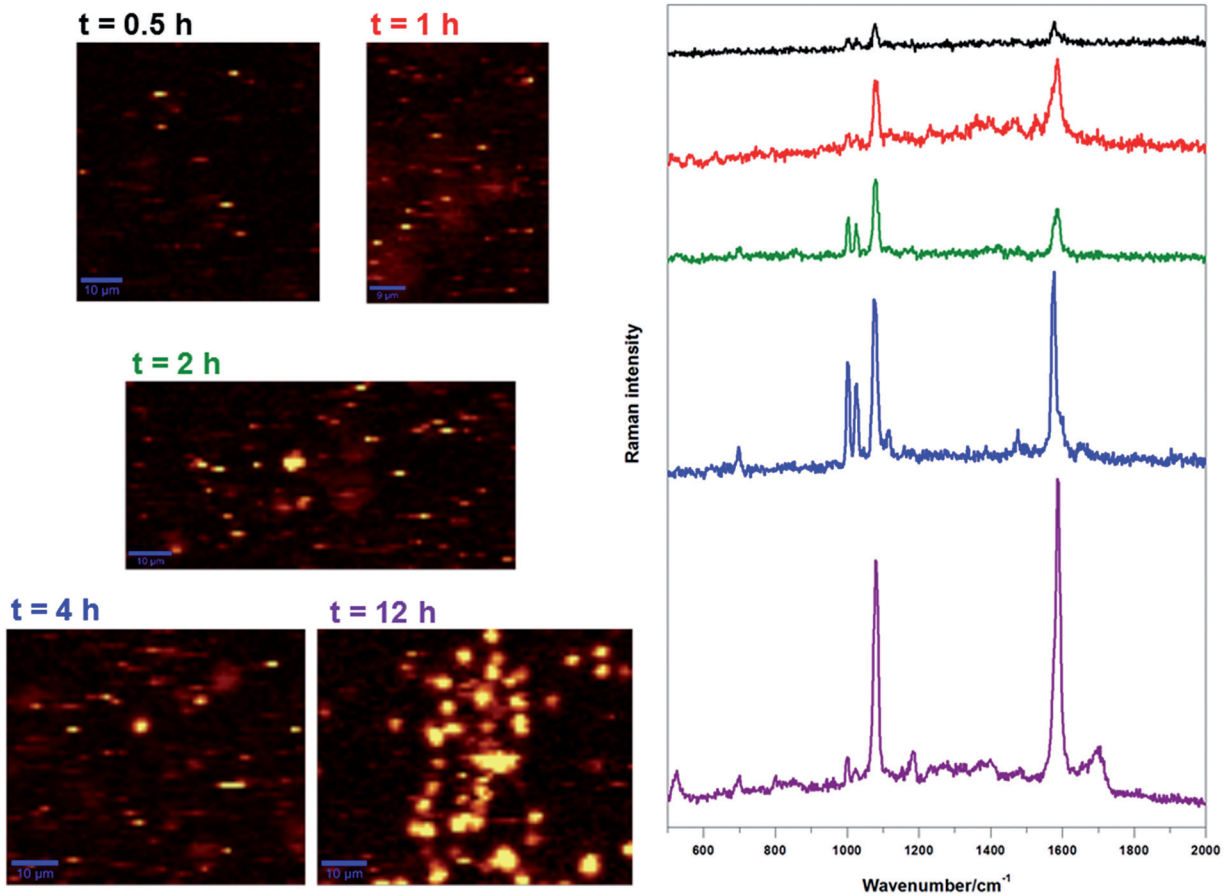

Fig. 2 SERS maps constructed by integration of the 1070 cm^{-1} band for EA.hy926 cells incubated in medium (pH = 7.20) containing MBA-AuNPs for 0.5, 1, 2, 4 and 12 h. The same intensity scale is applied for each map. SERS spectra of MBA (right) were extracted from pixels of the maps representing the highest intensity of the 1070 cm^{-1} band. Colours of spectra correspond to the incubation time of 0.5 (black), 1 (red), 2 (green), 4 (blue) and 12 h (purple). Microphotographs of cells for the SERS maps are displayed in Fig. S2 (in the ESI†).

 This journal is © The Royal Society of Chemistry 2015

Published on 08 December 2014. Downloaded by University of Edinburgh on 04/09/2015 14:20:40.

presence of these bands while some SERS spectra of cells do, we speculate that decarboxylation of MBA molecules anchored to AuNPs can result from the microenvironment process, *e.g.* interactions of nanosensors with other molecules through the MBA carboxylate group.

Next, we investigated the effects of extracellular pH changes on SERS nanosensors and consequently on the intracellular pH in endothelial cells. The incorporation of MBA-AuNPs did not bring a significant change to the cell morphology and no obvious cell death was found. This is not surprising since similar nanosensors have been shown to be non-toxic using biochemical assays.[22,29–31] Fig. 3 shows the presence of the targeted nanosensors in EA.hy926 cells incubated in the buffers with pH 3.9, 6.2, 8.6 and 11.3. The control cells were incubated only in DPBS (pH: 7.2), see Fig. 3C. To simplify our analysis, we performed K-means cluster analysis and a number of classes were chosen based on spectral differences in the pH-sensitive spectral region. Then pH values were calculated for the mean spectra from cluster analysis according to eqn (1) in Table 1.

For control cells, we observed changes in pH_i from 6.5 to 9.8. Pixels decoding pH values are unevenly distributed within the intercellular space of the endothelial cells, *cf.* Fig. 3C. The observed range of pH indicates that the 12 h uptake of the nanosensors results in a marked lack of delivery to low pH (4.7–6.3) compartments like early stage endosomes and lysosomes. The red and blue classes, pH values of 6.5 and 6.8, respectively, can correspond to recycling of endosomes.[26,32] In turn, the green and grey classes for which pH values vary from 7.2 to 7.6 exhibit the environment of cytosol. Although the current studies on the internalisation of particles through formation and maturation of the endocytic system do not predict a direct release of nanoparticles from vesicles to the cytosol, except a specific process of backfusion, in which lysosomal degradation can appear,[33] TEM and fluorescence studies on intracellular trafficking of various nanoparticles have implicated their presence in the cytosol, mitochondria and Golgi apparatus.[34–36] This may be associated with saturation of the endosomal–lysosomal compartments by nanoparticles and their leakage to the cytosol. The cluster analysis also differentiated a cellular area with pH in the range of 8.8–9.8, the black and purple classes. This unusual H^+/OH^- balance for the healthy cells can result from variation in the adsorption process and/or decomposition of 4-mercaptobenzoic acid on the gold surface hence we observed intensification of the anomalous bands in mean SERS spectra corresponding to these pH values, *cf.* Fig. S2C (in the ESI†).

Stimulating extreme stress conditions for cells by keeping them in a relatively acidic (pH: *ca.* 4) or alkaline environment (pH: *ca.* 11) resulted in inducing appropriate changes in pH_i in a very narrow range of values in comparison to other experimental conditions applied in our work, *cf.* Fig. 3A and E. Reducing the extracellular pH from 7.2 typical for the medium solution to 3.9 led to a high uptake of the pH sensors and decreasing the pH_i of cytoplasm to 5.4 (pink class in Fig. 3A). This remarkable accumulation of nanosensors can be associated with increased acidification of early and recycling endosomes that shifts the balance from recycling endosomes to the lysosome formation as shown previously by the effects of inhibition of the Na^+/H^+ exchanger by amiloride in the RBL-2H3 mast cell line.[32] The blue class surrounding the pink area and located close to the cellular membrane indicates an increase of pH to 6.3. It is well-known that nanoparticles enter the intercellular space through the process of endocytosis and that accumulated endosomes are converted into lysosomes. Thus, the observed pH of 6.3 likely corresponds to early sorting of endosomes which then accumulate in the cytosol of the cell in the form of late endosomes that in turn exhibit an average pH of 5.4.[26,37,38] Interestingly, a range of pH typical for the endosomes–lysosome conversion (4.7–6.5) was not found when the endothelial cells were exposed to the highly alkaline environment (Fig. 3E). The concentration of the nanoparticles functionalised with MBA is much lower in this case than for the acidic conditions of cell culture. The MBA-AuNPs are distributed along the cellular membranes of the three endothelial cells in cellular compartments with pH 8.4 with a small contribution of pH 8.5. The cluster analysis discriminated also the blue class for a SERS spectrum exhibiting the spectral profile of the decarboxylated MBA molecules.[24] According to the literature,[26] pH of *ca.* 8 is likely to be found in mitochondria however, we do not expect that the SERS imaging reports directly on these cellular compartments. It seems more likely that the endosomal–lysosomal system responds to increasing pH through inhibition of the H^+ ATPase pump as shown in numerous reports.[26,32,39,40] The other reason could be an increase in cytosolic pH due to the alkaline buffer, affecting the overall H^+/OH^- equilibrium in all cellular compartments. We also investigated a mild effect of the extracellular environment on the regulation of pH_i. For this purpose, the endothelial cells were exposed to buffer solutions with pH different from the typical culture conditions by 1 unit, see Fig. 3B and D. The range of pH for the cells incubated in the buffer with pH 6.2 is 6.9–8.1 and the concentration of the nanoprobes in a cell is relatively low in comparison to strongly acidic and physiological conditions, *cf.* Fig. 3A and C. The qualitative assessment of the distribution of pH_i in the cluster map shown in Fig. 3B indicates that the highest pH, 7.6 and 8.1, is spatially localised within a few pixels of the SERS image of the cells. This observation suggests that exposing endothelial cells to a mildly acidic environment does not strongly affect the cellular processes of endocytosis or the SERS technique is not sensitive enough to determine such a cellular response. The latter is more possible, as pH 7.0 inhibits chemically induced apoptosis in a specific endothelial cell line, suggesting that the effects of altered extracellular pH may be cell type dependent.[41] On the other hand, our results agree well with fluorescence spectroscopy studies on endothelial cells from rat aorta.[7] In contrast, increasing the extracellular pH to 8.6 discriminates pH_i from 5.8 to 9.1 related mainly to early and late endosomes (pH: 5.8–6.8). An increase of pH_i to 7.5 and 9.1 correlates well with a high intensity of a SNARF-1 fluorophore used in confocal fluorescence measurements of the endothelial layer in the animal aorta cross-sections.[7] In this report, extracellular alkalinisation to pH 8.6 was also associated with an increase of the NO concentration which serves as a specific biochemical marker for the

Published on 08 December 2014. Downloaded by University of Edinburgh on 04/09/2015 14:20:40.

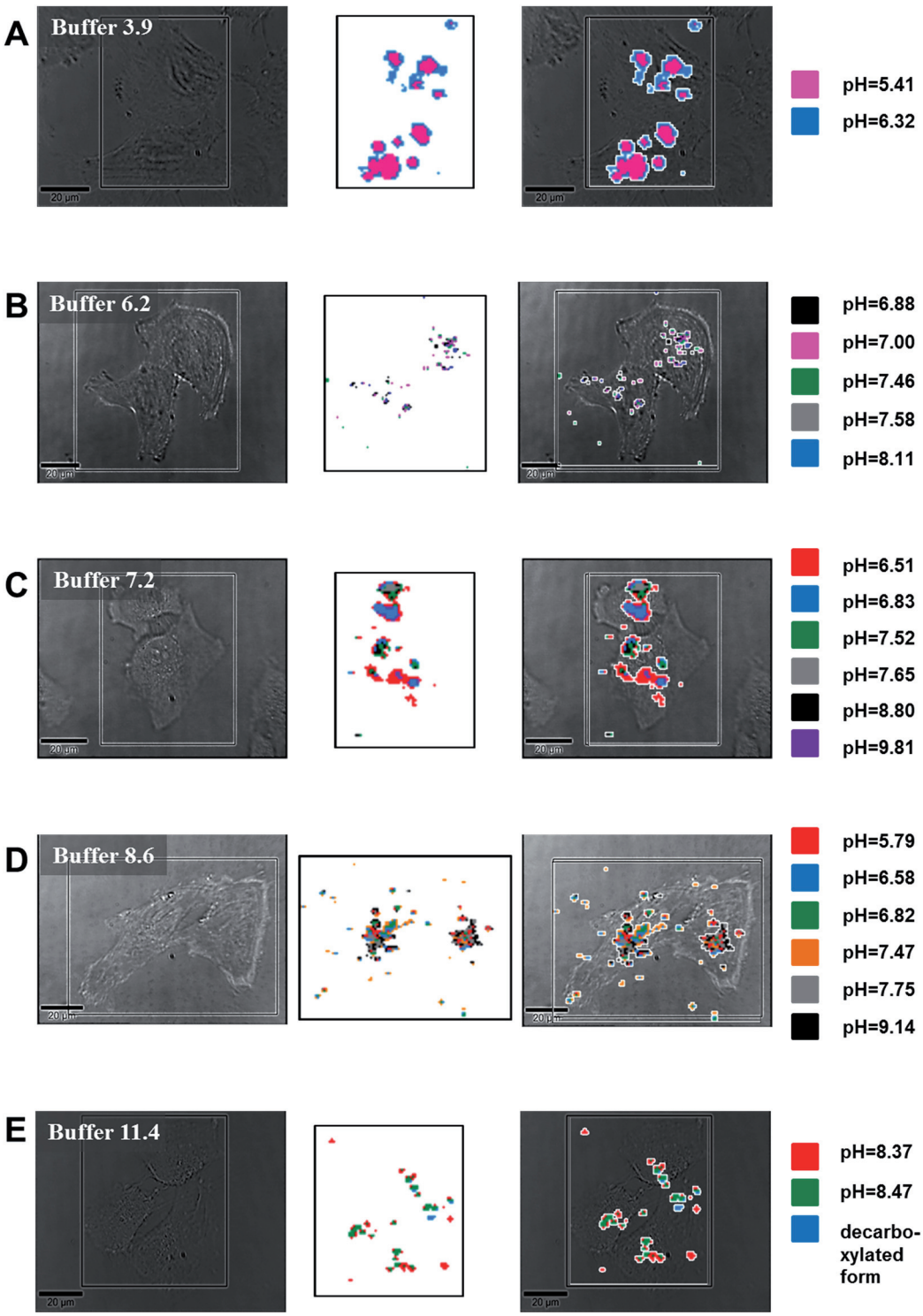

Fig. 3 Microphotographs and cluster maps of SERS-based pHi imaging for EA.hy926 cells incubated with MBA-AuNPs in buffers with pH 3.9 (A), 6.2 (B), 7.2 (C), 8.6 (D) and 11.4 (E). The colours decoded in the cluster maps correspond to pH values labelled by squares.

endothelial dysfunction.[42] Endothelial inflammation may be induced by tumour necrosis factor-α.[5,42] Fig. 4 displays the distribution of pH-sensitive nanosensors in TNFα incubated endothelial cells. First of all, the cluster maps show a high accumulation of the functionalised gold nanoparticles in the impaired endothelial cells similar to those found for cells exposed to the highly acidic extracellular environment (see Fig. 3A) and to cancerous cells.[43] Oku *et al.* showed that under certain conditions TNFα may increase the membrane permeability,[44] which can explain the relatively pronounced uptake

 This journal is © The Royal Society of Chemistry 2015

Published on 08 December 2014. Downloaded by University of Edinburgh on 04/09/2015 14:20:40.

Table 1 The Henderson–Hasselbalch equation determined from calibration curves shown in Fig. 1B along with calculated coefficients[a] and their root mean square error (RMSE, in %)

r	$I_{1400-1420}/I_{1070}$	RMSE	I_{1720}/I_{1070}	RMSE
$\mathrm{pH} = d + \ln\frac{r-a}{b-r}$ (1)				
a	0.024	2.26	0.499	0.76
b	0.481	0.53	0.0027	65.0
d	6.876	2.00	6.273	2.65

[a] r – relative intensity of the selected bands; a, b and d – equation coefficients.

of nanoparticles to the TNFα-treated cells. It was shown that TNFα induced mitochondrial membrane depolarisation, increased intracellular Ca^{2+} concentration, released cytochrome c resulting in disruption of cytosolic pH.[45,46] Fig. 4 shows TNFα treated cells that display the characteristic rounding and blebbing. The cluster analysis shows a more uniform distribution of nanosensors throughout the cytosol – this suggests a disruption of the endocytic pathway leading to nanosensor release into the cytosol or high increase in formation of endosomes in TNFα – activated cells. Cluster maps in Fig. 4 show that the pH_i varies from 5.5 to 7.2. This reflects endocytic recycling pathways.[47] In Fig. 4A, we observe a conversion between late endosomes (red class, pH 5.5) and endocytic recycling compartments[47] or early endosomes[19] (blue class, pH 6.4) localized along the cellular membrane. Next, the response for the TNFα-induced intracellular imbalance may also result in lowering of cytosol pH, observed in the beige class (pH 7.1). A slightly different picture is illustrated in Fig. 4B, for which we do not observe pH typical for late endosomes.

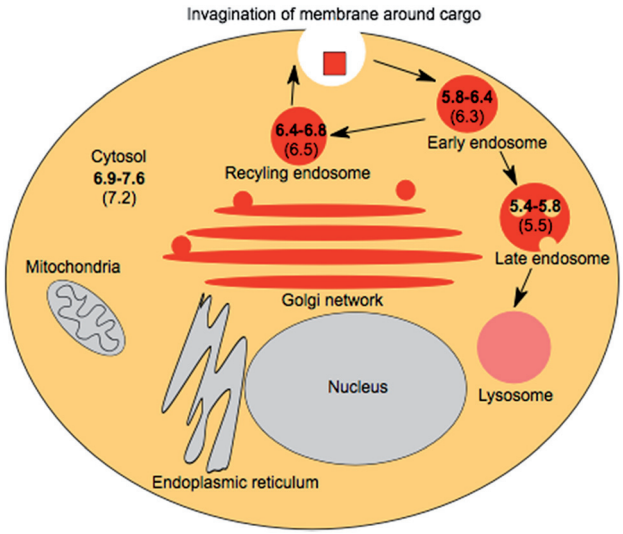

Fig. 5 A scheme of cell regions and pH determined in this work (in bold) along with the pH of cell compartments from ref. 26 (in brackets).

Conclusions

These experiments demonstrated that using targeted gold nanoparticles functionalized with 4-mercaptobenzoic acid allowed the detection of changes in pH_i induced by short-term alkalization or acidification of the extracellular environment of endothelium. Using SERS-based pH_i mapping, we also demonstrated that the TNFα-induced response in the endothelium was associated with intracellular acidosis. In all experiments, we were able to follow the endocytic pathway in cells, as calcu-

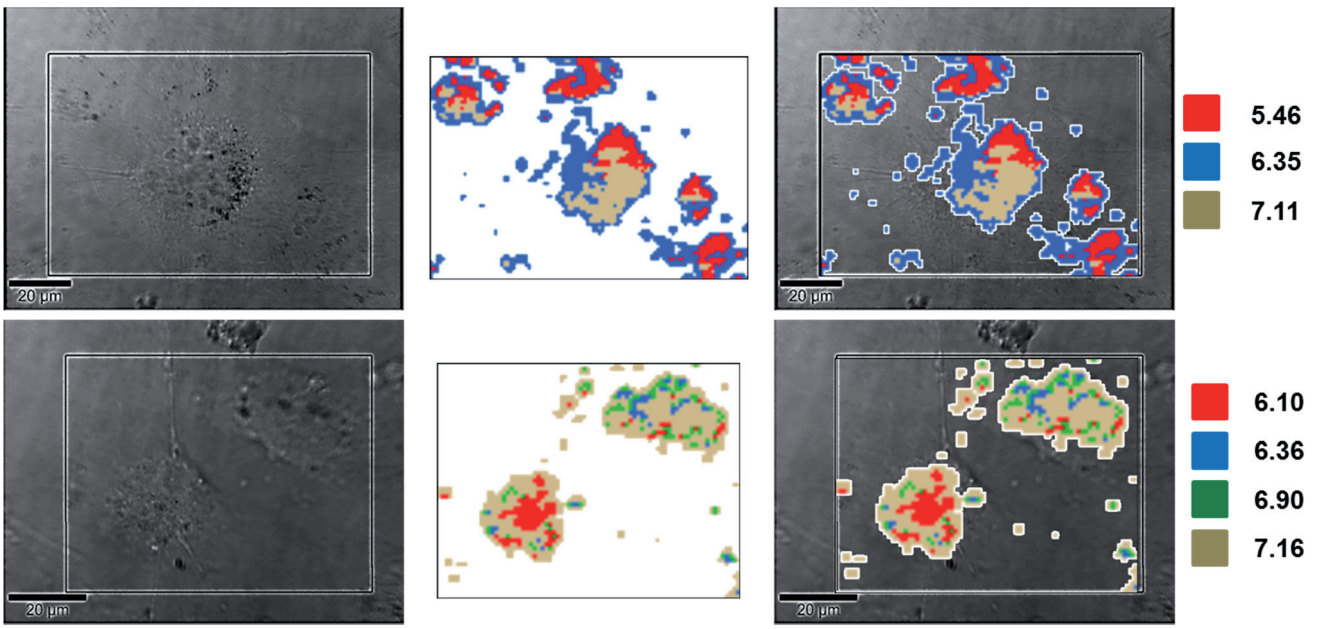

Fig. 4 Microphotographs and cluster maps of SERS-based pHi imaging for TNFα-incubated EA.hy926 cells. The colours decoded in the cluster maps correspond to pH values labelled by squares. SERS maps of control cells for this experiment are shown in Fig. 3C.

Published on 08 December 2014. Downloaded by University of Edinburgh on 04/09/2015 14:20:40.

lated pH values were correlated with the pH of endosomes at different stages of maturation. We summarised our findings in Fig. 5. Moreover, we observed the differences between MBA-AuNPs' uptake by healthy and inflamed cells, which suggested TNFα-induced activation of uptake. In contrast to the determination of pH by fluorescence spectroscopy,[1] the MBA-AuNPs' uptake appears through endocytosis, which makes SERS a valuable tool to study different stages of this process. Altogether, SERS spectra of MBA exhibit a spectral signature suited for differentiation of pH_i values between 5 and 9, enabling probing of a variety of subcellular compartments and their response to environmental and pathological stimuli.

Acknowledgements

This work was supported by the National Center of Science (grant PRELUDIUM DEC-2012/05/N/ST4/00218) and by the European Union from the resources of the European Regional Development Fund under the Innovative Economy Programme (grant coordinated by JCET-UJ, no. POIG.01.01.02-00-069/09). We also thank the University of Edinburgh School of Chemistry for the Neil Campbell Travel Award for supporting LJ. We also thank Joanna Jałmużna from the Department of Mathematics and Computer Sciences, Jagiellonian University in Krakow for fitting the calibration curve using Gnuplot software.

References

1 F. B. Loiselle and J. R. Casey, in *Membrane Transporters in Drug Discovery and Development, Methods in Molecular Biology*, ed. Q. Yan, Springer Science + Business Media, LLC, 2010, vol. 637.
2 P. F. Davies, *Physiol. Rev.*, 1995, **75**(3), 519.
3 E. Boedtkjer, S. Kim and C. Aalkjaer, *J. Physiol.*, 2013, **591**(6), 1447.
4 E. Schulz and T. Münzel, *Circulation*, 2011, **124**, 1806.
5 K. Chatzantoni and A. Mouzaki, *Curr. Top. Med. Chem.*, 2006, **6**, 1707.
6 E. Crimi, F. S. Taccone, T. Infante, S. Scolletta, V. Crudele and C. Napoli, *J. Crit. Care*, 2012, **27**, 108.
7 V. K. Capellini, C. B. A. Restini, L. M. Bendhack, P. R. B. Evora and A. C. Celotto, *PLoS One*, 2013, **8**(5), e62887.
8 J. Zhou, C. Fang, T. Chang, X. Liu and D. Shangguan, *J. Mater. Chem. B*, 2013, **1**, 661.
9 P. Li, H. Xiao, Y. Cheng, W. Zhang, F. Huang, W. Zhang, H. Wang and B. Tang, *Chem. Commun.*, 2014, **50**, 7184.
10 K. Galler, K. Brautigam, C. Große, J. Popp and U. Neugebauer, *Analyst*, 2014, **139**, 1237.
11 C. E. Talley, L. Jusinski, C. W. Hollars, S. M. Lane and T. Huser, *Anal. Chem.*, 2004, **76**, 7064.
12 A. M. Schwartzberg, T. Y. Oshiro, J. Z. Zhang, T. Huser and C. E. Talley, *Anal. Chem.*, 2006, **78**, 4732.
13 J. P. Scaffidi, M. K. Gregas, V. Seewaldt and T. Vo-Dinh, *Anal. Bioanal. Chem.*, 2009, **393**, 1135.
14 J. Kneipp, H. Kneipp, B. Wittig and K. Kneipp, *J. Phys. Chem. C*, 2010, **114**, 7421.
15 F. Wang, R. Widejko, Z. Yang, K. T. Nguyen, H. Chen, L. P. Fernando, K. A. Christensen and J. N. Anker, *Anal. Chem.*, 2012, **84**, 8013.
16 S. W. Bishnoi, C. J. Rozell, C. S. Levni, M. K. Gheith, B. R. Johnson, D. H. Johnson and N. J. Halas, *Nano Lett.*, 2006, **6**(8), 1687.
17 S. Balint, S. Rao, M. Maroo, P. Miskovsky and D. Petrov, *J. Raman Spectrosc.*, 2011, **42**, 1215.
18 Z. Wang, A. Bonoiu, M. Samoc, Y. Cui and P. N. Prasad, *Biosens. Bioelectron.*, 2008, **23**, 886.
19 K. L. Nowak-Lovato and K. D. Rector, *Appl. Spectrosc.*, 2009, **63**(4), 387.
20 V. T. Cong, E. O. Ganbold, J. K. Saha, J. Jang, J. Min, J. Choo, S. Kim, N. W. Song, S. J. Son, S. B. Lee and S. W. Joo, *J. Am. Chem. Soc.*, 2014, **136**, 3833.
21 G. Frens, *Nature Phys. Sci.*, 1973, **241**, 20.
22 A. Jaworska, T. Wojcik, K. Malek, U. Kwolek, M. Kepczynski, A. A. Ansary, S. Chlopicki and M. Baranska, *Microchim. Acta*, 2014, DOI: 10.1007/s00604-014-1307-5.
23 A. Jaworska, K. Malek, N. Kachamakova-Trojanowska, S. Chlopicki and M. Baranska, *Biomed. Spectrosc. Imaging*, 2013, **2**, 183.
24 A. Michota and J. Bukowska, *J. Raman Spectrosc.*, 2003, **34**, 21.
25 N. Radić and A. Prkić, *Rev. Anal. Chem.*, 2012, **31**, 93.
26 J. R. Casey, S. Grinstein and J. Orlowski, *Nat. Rev. Mol. Cell Biol.*, 2010, **11**, 50.
27 M. M. Wu, J. Llopis, S. Adams, J. M. McCaffery, M. S. Kuloma, T. E. Machen, H. H. Moore and R. Y. Tsien, *Chem. Biol.*, 2000, **7**, 197.
28 J. Kneipp, H. Kneipp, B. Wittig and K. Kneipp, *Nano Lett.*, 2007, **7**(9), 2819.
29 C. A. R. Auchinvole, P. Richardson, C. McGuinnes, V. Mallikarjun, K. Donaldson, H. McNab and C. J. Campbell, *ACS Nano*, 2012, **6**, 888–896.
30 J. Jiang, C. Auchinvole, K. Fisher and C. J. Campbell, *Nanoscale*, 2014, **6**, 12104–12110.
31 M. A. Ochsenku, P. R. T. Jess, H. Stoquert, K. Dholakia and C. J. Campbell, *ACS Nano*, 2009, **3**, 3613–3621.
32 K. L. Nowak-Lovato, B. S. Wilson and K. D. Rector, *Anal. Bioanal. Chem.*, 2010, **398**, 2019.
33 J. Huotari and A. Helenius, *EMBO J.*, 2011, **30**, 3481.
34 M. Ekkapongpisit, A. Giova, C. Follo, G. Caputo and C. Isidoro, *Int. J. Nanomed.*, 2012, **7**, 4147.
35 J. Huang, C. Zong, H. Shen, M. Liu, B. Chen, B. Ren and Z. Zhang, *Small*, 2012, **8**, 2577.
36 R. R. Sathuluri, H. Yoshikawa, E. Shimizu, M. Saito and E. Tamiya, *PLoS One*, 2011, **6**, e22802.
37 S. H. Hansen, K. Sandvig and B. Van Deurs, *J. Cell Biol.*, 1991, **113**, 731.
38 S. Mukherjee, R. N. Ghosh and F. R. Maxfield, *Physiol. Rev.*, 1997, **77**, 759.

 This journal is © The Royal Society of Chemistry 2015

Published on 08 December 2014. Downloaded by University of Edinburgh on 04/09/2015 14:20:40.

39 M. Bradley, L. Alexander, K. Duncan, M. Chennaoui, A. C. Jones and R. M. Sanchez-Martin, *Bioorg. Med. Chem. Lett.*, 2008, **18**, 310.
40 J. Liu, W. Lu, D. Reigada, J. nquyen, A. M. Laties and C. H. Mitchell, *Invest. Ophthalmol. Visual Sci.*, 2008, **49**(2), 772.
41 C. Terminella, K. Tollefson, J. Kroczynski, J. Pelli and M. Cutaia, *Am. J. Physiol.: Lung Cell. Mol. Physiol.*, 2002, **283**, L1291.
42 J. de Haro Miralles, E. Martınez-Aguilar, A. Florez, C. Varela, S. Bleda and F. Acin, *Interact. Cardiovasc. Thorac. Surg.*, 2009, **9**, 107.
43 S. Jung, J. Nam, S. Hwang, J. Park, J. Hur, K. Im, N. Park and S. Kim, *Anal. Chem.*, 2013, **85**, 7674.
44 N. Oku, R. Araki, H. Araki, S. Shibamoto, F. Ito, T. Nishihara and M. Tsujimoto, *J. Biochem.*, 1987, **102**(5), 1303.
45 Z. Jin, L. Pei and D. Wang, *Zhonghua Fuchanke Zazhi*, 2000, **35**, 657.
46 J. Cheng, W. Tang, Z. Su, J. Guo, L. Tong and Q. Wei, *Cancer Lett.*, 2012, **321**(2), 169.
47 F. R. Maxfield and T. E. McGraw, *Nat. Rev. Mol. Cell Biol.*, 2004, **5**, 121.

Analyst

PAPER

View Article Online
View Journal | View Issue

CrossMark click for updates

Cite this: *Analyst*, 2015, **140**, 2330

Simultaneous intracellular redox potential and pH measurements in live cells using SERS nanosensors†

L. E. Jamieson,[a] A. Jaworska,[b,c] J. Jiang,[a] M. Baranska,[b,c] D. J. Harrison[d] and C. J. Campbell*[a]

Received 23rd December 2014,
Accepted 11th February 2015

DOI: 10.1039/c4an02365j

www.rsc.org/analyst

Intracellular redox potential is a highly regulated cellular characteristic and is critically involved in maintaining cellular health and function. The dysregulation of redox potential can result in the initiation and progression of numerous diseases. Redox potential is determined by the balance of oxidants and reductants in the cell and also by pH. For this reason a technique for quantitative measurement of intracellular redox potential and pH is highly desirable. In this paper we demonstrate how surface enhanced Raman scattering (SERS) nanosensors can be used for multiplexed measurement of both pH and redox potential in live single cells.

Open Access Article. Published on 20 February 2015. Downloaded on 04/09/2015 14:20:06.
This article is licensed under a Creative Commons Attribution 3.0 Unported Licence.

Introduction

Intracellular redox potential is a measure of the oxidising or reducing potential of the environment within a cell. It is a delicate balance between a number of species including reactive oxygen species (ROS), antioxidant enzymes and small molecules that exist as redox couples.[1,2] These numerous intracellular species interact with each other to maintain a tightly regulated redox potential.[3] Cellular redox potential and its regulation is critically important for maintaining cellular health and integrity and is involved in the regulation of numerous essential processes.[4–7] When the delicate balance of intracellular redox potential is disrupted the resulting consequences include the initiation and progression of numerous diseases including neurodegeneration,[8] cardiovascular diseases[9] and cancer.[8,10]

The importance of redox potential in vital aspects of cell function and the implication of disruption of redox potential on disease makes establishing an effective method for measuring intracellular redox potential an important goal. Techniques such as the glutathione recycling assay allow an estimate of redox potential to be made in a population of cells, but lack any information about dynamics or cell-to-cell variability.[11] Fluorescent dyes such as DCFH[12] allow the measurement of ROS, but not a quantitative measurement of potential. More recently dyes such as Redoxfluor-1 (RF1)[13] have been used to report reversibly on intracellular redox potential. These dyes have the disadvantage that they act as 'switches' only determining whether the redox potential is above or below a certain value, the half-cell potential of the dye, thus failing to give quantitative determination of intracellular redox potential. The current 'gold standard' technique for measuring intracellular redox potential is the use of redox active Green Fluorescent Proteins (roGFPs).[14–16] Various roGFPs have been engineered with specific cysteine residues, which allow the protein to exist as a redox couple either with two free thiols or a disulfide (cystine). Depending on the oxidation state of the residues the fluorescence excitation maxima of the roGFP changes and therefore the ratio of reduced to oxidised roGFP can be determined and thus the redox potential is calculated. This technique allows *in vivo* real time and reversible monitoring of intracellular redox potential. It also has the advantage that the engineered roGFPs can be designed to target particular organelles and therefore report on intracellular variations.[14] While this technique has many advantages over the previous techniques developed roGFPs have been reported to primarily respond to glutathione concentration[17] and thus the range over which they can report is relatively small and, while recent developments have seen improvements in this area, there is a need for a complementary approach that allows quantification of a larger range of potentials.

Our group has developed a technique which involves using surface enhanced Raman scattering (SERS) nanosensors that report on intracellular redox potential in live cells. We used

[a]*EaStCHEM, School of Chemistry, University of Edinburgh, Edinburgh, EH9 3JJ, UK. E-mail: colin.campbell@ed.ac.uk*
[b]*Faculty of Chemistry, Jagiellonian University, 3 Ingardena Str., 30-060 Krakow, Poland*
[c]*Jagiellonian Centre for Experimental Therapeutics (JCET), Jagiellonian University, 14 Bobrzynskiego Str., 30-348 Krakow, Poland*
[d]*Medical and Biological Sciences Building, University of St Andrews, North Haugh, St Andrews, Fife, KY16 9TF, UK*
†Electronic supplementary information (ESI) available. See DOI: 10.1039/c4an02365j

This journal is © The Royal Society of Chemistry 2015

Open Access Article. Published on 20 February 2015. Downloaded on 04/09/2015 14:20:06.
This article is licensed under a Creative Commons Attribution 3.0 Unported Licence.

redox sensitive probe molecules attached to gold nanoparticles (NPs) which are delivered to cells and whose SERS spectra report in a ratiometric manner on the redox potential of their intracellular environment.[18,19]

When making a redox potential measurement it is also necessary to measure pH as the calculation of redox potential is pH dependent.[19] Since SERS has previously been used to make intracellular pH measurements[20–23] we consider that there is an opportunity to combine these nanosensors to make a multiplexed measurement of redox potential and pH and therefore gain a more accurate measure of the microenvironment within the cell.

Results and discussion

Nanosensor calibration

MBA has been well documented as a pH sensitive SERS reporter.[20–24] MBA nanosensors (NS) (Fig. 1A) have pH responsive signals in their SERS spectra, most significantly signals at approximately 1400 cm^{-1} and approximately 1700 cm^{-1}, assigned to COO^- stretching and C═O stretching respectively. The COO^- stretching mode signal intensity increases with increasing pH, due to increased MBA deprotonation and the C═O stretching mode signal intensity increases with decreasing pH. The strong signals at approximately 1080 cm^{-1} and approximately 1590 cm^{-1} are attributed to pH independent aromatic ring vibration and can therefore be used as reference signals.

Calibration of MBA nanoparticles (MBA-NPs) is generated by plotting pH *vs.* relative intensity of selected signals. The expected sigmoid is centred around the pKa of the MBA and demonstrates that MBA-NPs are most sensitive to changes in pH between 6 and 8 (Fig. 1B). This shape of curve is to be expected since the transition between acid and base is expected to follow the Henderson–Hasselbach equation. The pH range offered by the MBA-NPs is well suited to the measurement of intracellular pH and we have previously demonstrated that MBA-NPs can accurately report on changes to the cytosolic pH.[23] Representative spectra of fully protonated and deprotonated MBA-NPs are shown in Fig. 1C.

We have previously reported that *N*-[2-({2-[(9,10-dioxo-9,10-dihydroanthracen-2-yl)formamido]ethyl}disulfanyl)ethyl]-9,10-dioxo-9,10-dihydroanthracene-2-carboxamide (referred to as AQ) can be used as a redox sensitive SERS reporter when conjugated to gold nanoparticles (Fig. 2A).[19] The signal at 1666 cm^{-1}, corresponding to C═O stretching reports on the oxidation state of the reporter and can be plotted relative to the non redox sensitive signal at 1606 cm^{-1} corresponding to C═C stretching. Calibration of AQ-NPs is described in the Experimental section and the resultant calibration plot is given in Fig. 2B. The resultant calibration is a stretched sigmoid centred around the $E_{1/2}$ of AQ. The stretched nature of the plot has been seen before[25] and is probably the result of hindered electron or proton transfer between the solution and the nanosensor. We have demonstrated that AQ can be used to report on redox potentials that span from normoxia to hypoxia.[18,19] Representative spectra of fully oxidised and fully reduced AQ-NPs are shown in Fig. 2C.

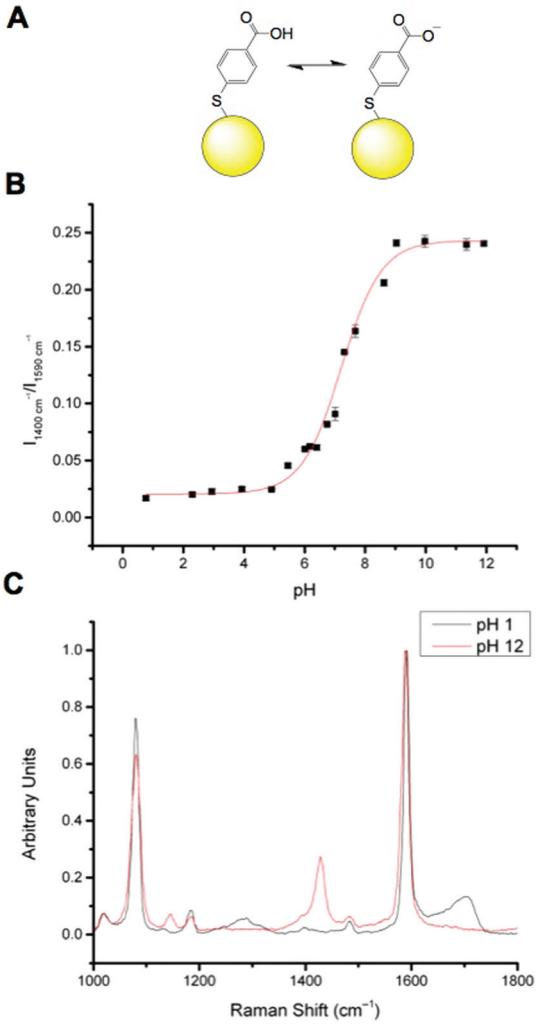

Fig. 1 MBA-NP nanosensor. (A): Equilibrium between protonated and deprotonated MBA attached to a gold NP (yellow sphere, not to scale). (B): Calibration curve for MBA-NP nanosensors (R^2 = 0.98687). (C): Representative spectra of fully protonated (pH 1) and fully deprotonated (pH 12) MBA-NPs.

Intracellular SERS measurements

In previous work MBA-NPs have been used to monitor intracellular pH[23,24] and AQ-NPs have been used to monitor intracellular redox potential.[19] Our study investigates the data processing necessary to combine these two measurements. Cells were incubated with MBA-NPs and AQ-NPs as described in the Experimental section. Cells were located and imaged and then Raman mapping was performed with acquisitions in 1 μm steps in *x* and *y*. Hierarchical *k*-means cluster analysis was performed on the resultant maps (Fig. 3). This grouped similar spectra together into a single cluster represented by a colour on the false colour images and identified regions that contained NPs. The colours chosen do not indicate the magni-

Open Access Article. Published on 20 February 2015. Downloaded on 04/09/2015 14:20:06.
This article is licensed under a Creative Commons Attribution 3.0 Unported Licence.

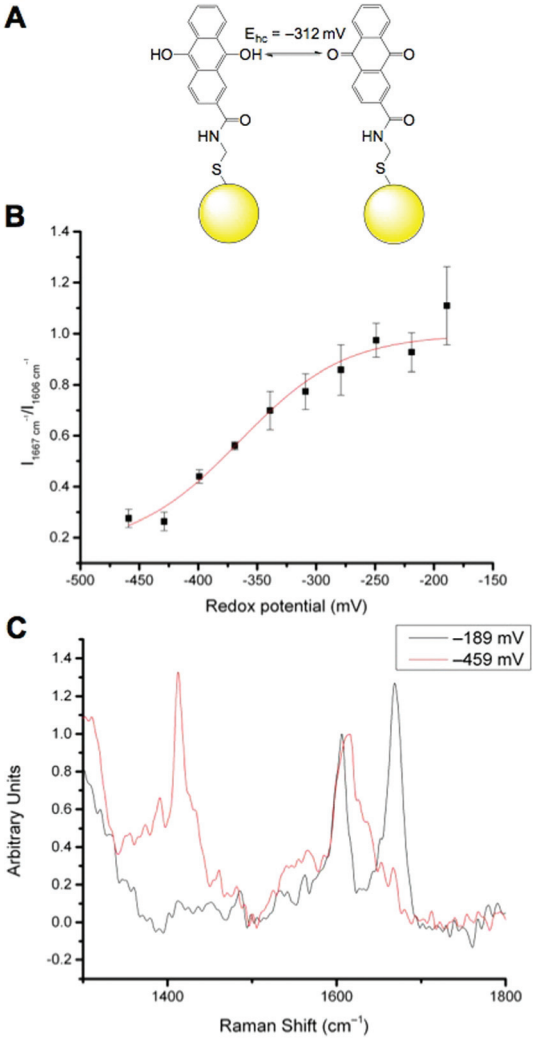

Fig. 2 AQ-NP nanosensor. (A): Equilibrium between oxidised and reduced AQ attached to a gold NP (yellow sphere, not to scale). (B): Calibration curve for AQ-NP nanosensors (R^2 = 0.96855). (C): Representative spectra of fully oxidised (–189 mV) and fully reduced (–459 mV) AQ-NPs.

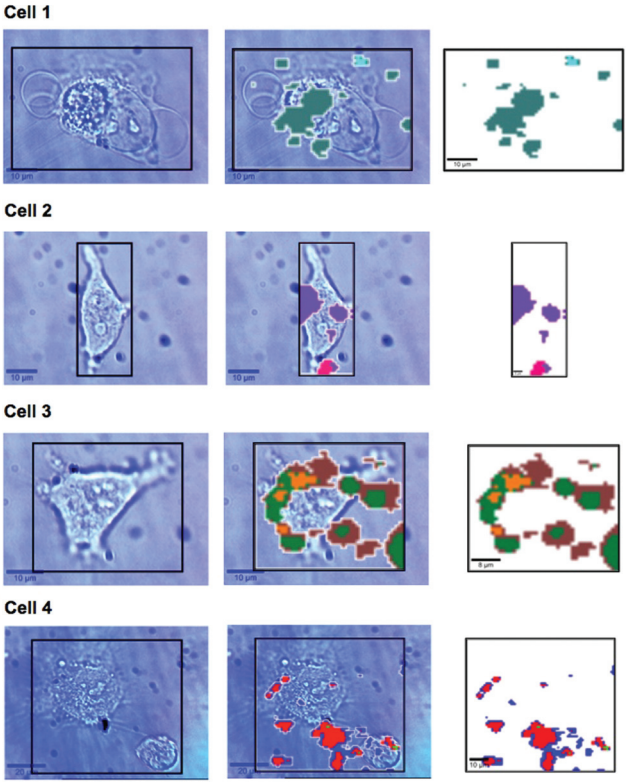

Fig. 3 Photographs of SERS mapped cells (left column), area highlighted with black box corresponds to the Raman mapped area represented by the corresponding *k*-means cluster map (right hand column). Photographs and cluster maps are overlaid in the middle column. Each cluster from *k*-means cluster analysis is represented by a different colour. Cell 1 – turquoise cluster corresponds to a singleplex spectrum of MBA-NPs giving pH 7.1, cyan cluster corresponds to a multiplex spectrum of MBA-NPs and AQ-NPs from which redox potential –304 mV was extracted by peak fitting (pH-adjusted to –297 mV). Cell 2 – purple cluster corresponds to a singleplex spectrum of MBA-NPs giving pH 6.9 and the pink cluster corresponds to a multiplex spectrum of MBA-NPs and AQ-NPs from which redox potential –258 mV was extracted by peak fitting (pH-adjusted to –241 mV). Cell 3 – green cluster corresponds to a singleplex spectrum of MBA-NPs giving pH 7.0 and the yellow and brown clusters correspond to multiplex spectra of MBA-NPs and AQ-NPs from which redox potentials of –276 mV and –345 mV were extracted respectively by peak fitting (pH-adjusted to –272 mV and –332 mV respectively). Cell 4 – light green cluster corresponds to a singleplex spectrum of MBA-NPs giving pH 7.1 and the blue and red clusters correspond to multiplex spectra of MBA-NPs and AQ-NPs from which redox potentials of –337 mV and –306 mV were extracted respectively by peak fitting (pH-adjusted to –320 mV and –300 mV respectively).

tude of pH or redox potential only that a group of spectra have similar features. An average spectrum representative of the cluster was generated for each colour. Cluster spectra were processed manually by subtracting a baseline (8 points) in order to give an average spectrum for the cell. Of all spectra collected signals from MBA-NPs were predominant, with fewer AQ-NP signals in comparison. All cluster spectra with AQ-NP signals were multiplexed with MBA-NP signals while other clusters gave singleplex MBA-NP signals. For this reason, data analysis was simplified by determining only redox potential from multiplexed spectra and using the abundant singleplex MBA-NP signals for simplified processing for pH determination. This approach allowed intracellular redox potential and pH predominantly to be simultaneously measured on a whole cell basis. From the 4 mapped cells, cluster analysis for Cell 1 and 2 gave 2 clusters. Analysis of the spectra revealed that one cluster gave a singleplex spectrum with only MBA-NP signals and the other gave a multiplex spectrum with evidence of both MBA-NP and AQ-NP signals. The remaining cells (3 and 4) revealed 3 clusters. In each case one cluster contained a singleplex spectrum with MBA-NP signals in isolation and the other 2 contained multiplexed signals at different ratios.

For spectra with only MBA-NP signals peak finding was performed to determine the intensity of the peak at 1400 cm^{-1} relative to the peak at 1590 cm^{-1} and subsequently determine

This journal is © The Royal Society of Chemistry 2015

Open Access Article. Published on 20 February 2015. Downloaded on 04/09/2015 14:20:06.
This article is licensed under a Creative Commons Attribution 3.0 Unported Licence.

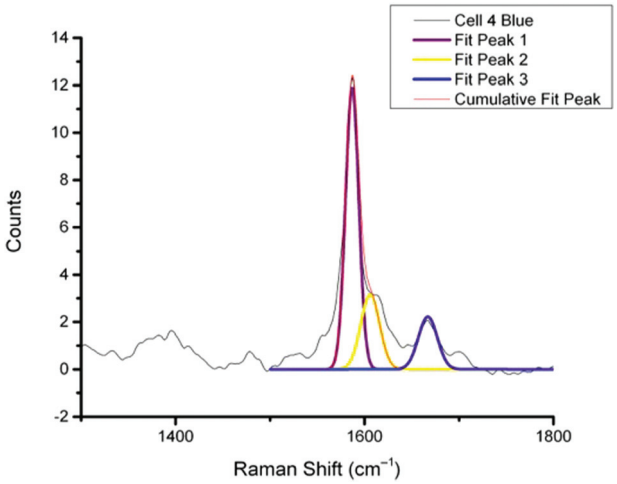

Fig. 4 Representative example of peak fitting for a multiplex spectrum generated from *k*-means cluster analysis (cell 4 blue cluster). Peaks were fitted using a GaussAmp function with constrained parameters resulting in the 3 individual peak fits, Fit 1, 2 and 3 and the overall resultant Cumulative Fit Peak shown overlaid on the original spectrum (black line).

pH from the calibration data. For spectra with multiplexed signals, peak fitting, as described in the Experimental section, was performed to extract the intensity of the peak at 1667 cm^{-1} relative to that at 1606 cm^{-1} and subsequently determine redox potential from the calibration data. Fig. 4 illustrates one example of peak fitting for the blue cluster in cell 4. A GaussAmp function was used with fixed *y*0, peak widths and peak centres and peak intensities of the fitted peaks from AQ-NPs were obtained. All singleplex cluster spectra analysed for pH measurements are overlaid in Fig. 5A and all multiplex cluster spectra analysed for redox measurements are overlaid in Fig. 5B.

Table 1 documents pH and redox potential values determined from each cluster from each cell in Fig. 3. The significance of multiplexing pH and redox potential measurements is to allow for redox potential values to be corrected relative to pH. Jiang *et al.*[19] demonstrated that the half-cell potential of AQ relative to pH changed as expected from theory, by 60 mV per pH unit (Fig. S1†). Therefore the redox potential values determined from each cell could be corrected based on the pH determined from the same cell to give both pH and pH-corrected redox potential on a whole cell basis.

A more detailed analysis of Fig. 3. reveals that in some cases the colours representing clusters from NPs do not always overlay cell location. It is likely that this is a result of drift during measurements of live cells and not signals from extracellular particles as we used well established NP delivery protocols and the cells were washed multiple times before map acquisition.[18,23,24,26–29] It is unlikely but possible that some NP remained outside cells after washing which could introduce error to cluster measurements however if this was the case the contribution from NP signals outside cells should have been minimal to the overall cluster. Both pH and redox potential differences between cells are apparent and in the case of cell 3

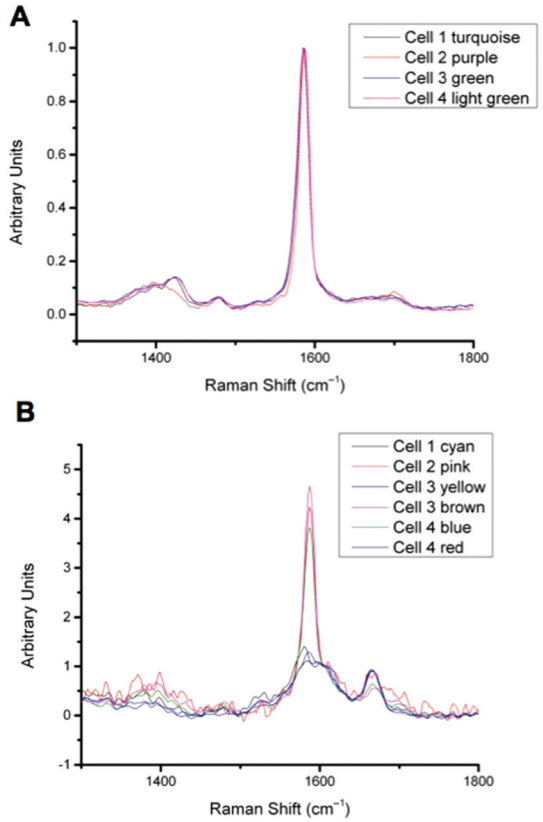

Fig. 5 A: Overlay of all singleplex spectra from cells 1–4 corresponding to the clusters indicated. Spectra show MBA-NP signals corresponding to the pH values given in Table 1, calculated by taking the intensity ratio of the peaks around 1400 cm^{-1} and 1590 cm^{-1}. B: Overlay of all multiplex spectra from cells 1–4 corresponding to the clusters indicated. Spectra show both MBA-NP and AQ-NP signals overlapping. Peaks were fitted to extract the intensity ratio of peaks at 1670 cm^{-1} and 1600 cm^{-1} to give redox potential values given in Table 1.

Table 1 Calculated pH, redox potential and pH-adjusted redox potential values for clusters from cells 1–4

Cell	pH (colour)	Redox potential (mV) (colour)	pH-adjusted redox potential (mV) (colour)
1	7.1 (turquoise)	−304 (cyan)	−297 (cyan)
2	6.9 (purple)	−258 (pink)	−241 (pink)
3	7.0 (green)	−276 (yellow)	−272 (yellow)
		−345 (brown)	−332 (brown)
4	7.1 (light green)	−337 (blue)	−320 (blue)
		−306 (red)	−300 (red)

and cell 4 intracellular redox potential differences are also apparent. Intercellular pH variations were minimal, as expected for healthy cells, which maintain a pH around 7.2. Calculated pH varied by 0.2 pH units between 6.9 and 7.1. This is in agreement with measurements assigned to cytosolic pH when the same MBA-NP reporter was used independently.[23] Redox variations were more substantial, with adjusted potential varying by 91 mV from −241 mV to −332 mV. This is in line with the normoxic range in A549 cells determined

Open Access Article. Published on 20 February 2015. Downloaded on 04/09/2015 14:20:06.
This article is licensed under a Creative Commons Attribution 3.0 Unported Licence.

using AQ-NP[19] and the large range could be attributed to varying stages of cell life-cycle. In the future this technique could be used to investigate more significant changes in response to, for example, disease and drug treatments.

Our results are the first demonstration of simultaneous measurement of redox potential and pH and this greatly improves our ability to analyse intracellular microenvironments. Cluster analysis provides a simple way of condensing large volumes of information for analysis of average redox potential and pH on a cell by cell basis, providing a platform for detailed analysis of whole cell differences and response to treatment. Continued improvements in reporter design will allow for improved multiplexing of spectra with potential to include markers for other biochemical parameters.

Experimental

Nanoparticle synthesis

Mercaptobenzoic acid (MBA), gold(III) chloride trihydrate, sodium citrate tribasic dehydrate and methanol were purchased from Sigma and were of analytical grade. Gold nanoparticles (GNPs) were prepared according to the Frens procedure.[30] In this synthesis Au ions are reduced by citrate ions. A stock solution of MBA at the concentration of 1 mM was prepared by diluting an appropriate mass of the solid in ethanol. A stock solution of AQ at the concentration of 100 μM was prepared by diluting an appropriate mass of the solid in DMSO to a concentration of 10 mM and diluting the resultant solution with PBS to 100 μM.

MBA-NP and AQ-NP solutions were prepared by mixing 100 μl of the 1 mM solution of MBA and 400 μl of 100 μM solution of AQ respectively with 1 ml of the gold colloid. After 5 min, mixtures were centrifuged for 10 min at 3000 rpm. For MBA-NPs supernatant was removed and NPs were re-dissolved in PBS.

Nanosensor calibration AQ

SERS spectroelectrochemistry was carried out as described by Jiang *et al.*[19] Analysis was performed using Origin 9. After smoothing (9 points, Savitzky–Golay) and manual baseline subtraction (8 points), two peaks were fitted in the region from 1500 cm^{-1} to 1800 cm^{-1} using the GaussAmp function. Peak centres were fixed to approximately 1606 cm^{-1} (C=C stretching) and 1667 cm^{-1} (C=O stretching), $y0$ was fixed to 0, and peak widths were fixed to 10 (for representative peak fitting see Fig. S2†). The relative intensity of the fitted peaks at 1667 cm^{-1} and 1606 cm^{-1} were plotted against redox potential and Origin 9 was used to fit a Boltzmann equation to the resulting calibration curve.

Nanosensor calibration MBA

Solutions of MBA-NPs were mixed with buffers in the pH range 0–12 (5 : 1 v/v) and solutions were placed in a 96 well plate. Multiple spectra for each pH were acquired directly from the wells. The relative intensity of bands corresponding to COO^- stretching (approximately 1400 cm^{-1}) and aromatic ring stretching (approximately 1590 cm^{-1}) were calculated using OPUS software and plotted against pH. Origin 9 was used to fit a Boltzmann equation to the calibration curve.

Buffers were prepared by firstly dissolving appropriate masses of solid analytes in deionised water to make 0.1 M solutions of sodium hydroxide, sodium phosphate, disodium hydrogen phosphate and phosphate acid purchased from Sigma-Aldrich and of analytical grade. Appropriate volumes of each of these solutions were mixed to prepare buffer solutions and pH was measured using a pH meter.

pH dependence of AQ half-wave potential

The half-wave potential of AQ at different pH values was determined by cyclic voltammetry as described by Jiang *et al.*[19] and agreed with theoretical predications (Fig. S1†).

Cellular delivery

Experiments were conducted using the EAhy926 cell line. Cells were grown in plastic wells with glass bottom in DMEM supplemented with 10% fetal bovine serum, 2 mM L-glutamine, penicillin, streptomycin, and 2% HAT. Cells were incubated at 37 °C and 5% CO_2 in a humidified incubator. 24 h after passaging medium was replaced by medium without serum and left for 1 hour. Then, 200 μl of MBA-NP solution and 400 μl of AQ-NP solution were added to the serum-free medium in the wells and left for approximately 2 hours. Media was removed, cells washed with PBS and Raman measurements were carried out immediately.

Instrumentation

The electronic absorption spectra of the gold colloid, the gold colloid mixed with MBA and gold colloid mixed with AQ were recorded with a UV-Vis-NIR Perkin Elmer spectrophotometer (model Lambda 35) in the range of 190–1100 nm with a resolution of 2 nm. Quartz cells of 1 cm were used.

SERS mapping of cells was carried out by using a WITec system, equipped with an immersive objective with magnification of 60× and a He–Ne laser (632.8 nm). For all measurements, integration time was 0.03 s with a single accumulation, laser power of 10 mW and grating 600 g mm^{-1}. SERS spectra of MBA-NPs and AQ-NPs as a reference for cell mapping were recorded by placing a sample in a glass cuvette and using an air objective (20×). Three SERS spectra were acquired for each freshly prepared sample. The latter was prepared by mixing 500 μL of the Au colloid with 5 μL of a 1×10^{-3} M MBA/AQ solution in a glass cuvette. For Raman mapping, raster scans over single living cells were carried out with a computer-controlled x,y-stage. The mapping step was 1 μm.

Data processing for intracellular measurements

Hierarchical k-means cluster analysis of SERS maps was performed by using WITec Project 2.06 software. The spectra were analysed in the region of 400–1800 cm^{-1} after a routine procedure for cosmic rays removal and smoothing (13 points) using a Savitzky–Golay algorithm.

 This journal is © The Royal Society of Chemistry 2015

Open Access Article. Published on 20 February 2015. Downloaded on 04/09/2015 14:20:06.
This article is licensed under a Creative Commons Attribution 3.0 Unported Licence.

Spectra of resultant clusters were analysed using Origin 9 software. An 8 point baseline was subtracted from all spectra in the region 1000–1800 cm^{-1}. For spectra with only MBA signals, peak heights were determined using the peak finding function and the 1st derivative method. For spectra with both MBA and AQ signals, three peaks were fitted in the region from 1500 cm^{-1} to 1800 cm^{-1} using the GaussAmp function. Peak centres were fixed to approximately 1587 cm^{-1} and width 7 (MBA ring breathing), 1606 cm^{-1} and width 10 (AQ C=C stretching) and 1667 cm^{-1} and width 10 (AQ C=O stretching) and $y0$ was fixed to 0. Relative intensities of the signals at 1667 cm^{-1} and 1606 cm^{-1} were used to determine redox potential.

Conclusions

In this paper we have presented the first example of multiplexing pH and redox responsive SERS nanosensors for intracellular live single cell measurement on a cell by cell basis. This provides quantitative information on the cell microenvironment, superior to previous techniques used for intracellular redox potential or pH measurements independently or together. MBA-NPs were calibrated and shown to be responsive in the pH range 6–8. AQ-NPs were calibrated and shown to be responsive in the range from −250 mV to −400 mV. Analysis of SERS maps of single cells incubated with both SERS reporters by *k*-means cluster analysis followed by spectral processing revealed detailed quantitative information on intracellular pH and redox potential on a whole cell basis. Redox potential measurements could be accurately corrected for pH and both inter- and intra- cellular differences were observed.

Acknowledgements

The authors gratefully acknowledge the School of Chemistry at the University of Edinburgh, a Neil Campbell Travel Award, the Faculty of Chemistry at Jagiellonian University and Jagiellonian Centre for Experimental Therapeutics (JCET). A. J.'s work was supported by National Center of Science (grant PRELUDIUM DEC-2012/05/N/ST4/00218) and by the European Union from the resources of the European Regional Development Fund under the Innovative Economy Programme (grant coordinated by JCET-UJ, No POIG.01.01.02-00-069/09).

Notes and references

1 M. Kemp, Y.-M. Go and D. P. Jones, *Free Radicals Biol. Med.*, 2008, **44**, 921–937.
2 Y.-M. Go and D. P. Jones, *Biochim. Biophys. Acta*, 2008, **1780**, 1273–1290.
3 F. Q. Schafer and G. R. Buettner, *Free Radicals Biol. Med.*, 2001, **30**, 1191–1212.
4 G. Filomeni, G. Rotilio and M. R. Ciriolo, *Cell Death Differ.*, 2005, **12**, 1555–1563.
5 D. P. Jones, *J. Intern. Med.*, 2010, **268**, 432–448.
6 H. Liu, R. Colavitti, I. I. Rovira and T. Finkel, *Circ. Res.*, 2005, **97**, 967–974.
7 V. Mallikarjun, D. J. Clarke and C. J. Campbell, *Free Radical Biol. Med.*, 2012, **53**, 280–288.
8 G. Waris and H. Ahsan, *J. Carcinog.*, 2006, **5**, 14.
9 Y.-M. Go and D. P. Jones, *Free Radicals Biol. Med.*, 2011, **50**, 495–509.
10 M. W. Dewhirst, Y. Cao and B. Moeller, *Nat. Rev. Cancer*, 2008, **8**, 425–437.
11 I. H. Shaik and R. Mehvar, *Anal. Bioanal. Chem.*, 2006, **385**, 105–113.
12 R. P. Rastogi, S. P. Singh, D.-P. Häder and R. P. Sinha, *Biochem. Biophys. Res. Commun.*, 2010, **397**, 603–607.
13 E. W. Miller, S. X. Bian and C. J. Chang, *J. Am. Chem. Soc.*, 2007, **129**, 3458–3459.
14 C. T. Dooley, T. M. Dore, G. T. Hanson, W. C. Jackson, S. J. Remington and R. Y. Tsien, *J. Biol. Chem.*, 2004, **279**, 22284–22293.
15 G. T. Hanson, R. Aggeler, D. Oglesbee, M. Cannon, R. A. Capaldi, R. Y. Tsien and S. J. Remington, *J. Biol. Chem.*, 2004, **279**, 13044–13053.
16 H. Ostergaard, A. Henriksen, F. G. Hansen and J. R. Winther, *EMBO J.*, 2001, **20**, 5853–5862.
17 M. Gutscher, A. Pauleau, L. Marty, T. Brach, G. H. Wabnitz, Y. Samstag, A. J. Meyer and T. P. Dick, *Nat. Methods*, 2008, **5**, 553–559.
18 C. A. R. Auchinvole, P. Richardson, C. McGuinnes, V. Mallikarjun, K. Donaldson, H. McNab and C. J. Campbell, *ACS Nano*, 2012, **6**, 888–896.
19 J. Jiang, C. Auchinvole, K. Fisher and C. J. Campbell, *Nanoscale*, 2014, **6**, 12104–12110.
20 J. Kneipp, H. Kneipp, B. Wittig and K. Kneipp, *J. Phys. Chem. C*, 2010, **114**, 7421–7426.
21 J. Kneipp, H. Kneipp, B. Wittig and K. Kneipp, *Nano Lett.*, 2007, **7**, 2819–2823.
22 S. W. Bishnoi, C. J. Rozell, C. S. Levin, M. K. Gheith, B. R. Johnson, D. H. Johnson and N. J. Halas, *Nano Lett.*, 2006, **6**, 1687–1692.
23 A. Jaworska, L. E. Jamieson, K. Malek, C. J. Campbell, J. Choo, S. Chlopicki and M. Baranska, *Analyst*, 2015, DOI: 10.1039/c4an01988a.
24 M. A. Ochsenkuhn, P. R. T. Jess, H. Stoquert, K. Dholakia and C. J. Campbell, *Nano Lett.*, 2009, **3**, 3613–3621.
25 W. J. Albery, M. G. Boutelle, P. J. Colby and A. R. Hillman, *J. Electroanal. Chem. Interfacial Electrochem.*, 1982, **133**, 135–145.
26 M. Ekkapongpisit, A. Giovia, C. Follo, G. Caputo and C. Isidoro, *Int. J. Nanomed.*, 2012, **7**, 4147–4158.
27 R. R. Sathuluri, H. Yoshikawa, E. Shimizu, M. Saito and E. Tamiya, *PLoS One*, 2011, **6**, e22802.
28 J. Huang, C. Zong, H. Shen, M. Liu, B. Chen, B. Ren and Z. Zhang, *NanoSmallMicro*, 2012, **10**, 2577–2584.
29 A. Jaworska, T. Wojcik, K. Malek, U. Kwolek, M. Kepczynski, A. A. Ansary, S. Chlopicki and M. Baranska, *Microchim. Acta*, 2014, 8–11.
30 G. Frens, *Nat. Phys. Sci.*, 1973, **241**, 20.